The Properties of Giant Molecular Clouds in Nearby Galaxies and their Environmental Variation

Saul Paul Phiri

A thesis submitted in partial fulfilment
of the requirements for the degree of
Doctor of Philosophy

Jeremiah Horrocks Institute for Maths, Physics and Astronomy
University of Central Lancashire

August 2022

Declaration

Declaration

Type of Award: Doctor of Philosophy

School: Natural Sciences

I declare that while registered as a candidate for the research degree, I have not been a registered candidate or enrolled student for another award of the University or other academic or professional institution.

I declare that no material contained in the thesis has been used in any other submission for an academic award and is solely my own work.

No proof-reading service was used in the compilation of this thesis.

Saul Paul Phiri

Abstract

Investigating giant molecular clouds (GMC) in external galaxies presents the opportunity to examine how the distribution, density structure and dynamical state of star forming clouds depend on the galactic environment. This thesis has focused on determining the physical properties and distribution of GMCs and clumps in M33 and compare them to other nearby galaxies including the Milky Way.

We have used archival data from the Atacama Millimeter/sub-millimeter Array (ALMA). For the first time, we have resolved and uncovered physical properties of molecular clouds at clump level in M33 at a distance of 840 kpc. We began with resolving NGC 604 GMCs into smaller molecular clouds using $^{13}CO(1-0)$ ALMA Band 3 data. Further, three GMCs at different evolutionary stages (NGC 604, GMC 16 and GMC 8) were resolved down to clump level using $^{12}CO(2-1)$ and $^{13}CO(2-1)$ ALMA Band 6 data. Using the Astrodendro algorithm, we identified molecular clouds and clumps in M33 from ^{12}CO and ^{13}CO emission. We identified a total of 15 molecular clouds from ALMA Band 3 data. With Band 6 data we identified a total of 714 ^{12}CO clumps and 457 ^{13}CO clumps. Physical properties (size, linewidths, mass, etc) were computed and a catalog has been created which is the first at this resolution in M33.

The emission distribution in NGC 604 both in Band 3 and Band 6 show spatial offsets at their peaks between line emission and continuum emission. The detected continuum emission is near the centre of the HII region. The identified

molecular clouds in Band 3 data have sizes ranging from 5-21 pc, linewidths of 0.3 - 3.0 km/s and luminosity-derived masses of 4.0×10^2 $M_\odot$ $-$ 8.1×10^4 $M_\odot$. Using band 6 data we have identified molecular clumps with sizes below 10 pc for ^{12}CO and below 3 pc for ^{13}CO, linewidths ranging from 0.3 – 2.6 km/s, luminosity-derived masses ranging from 10 $M_\odot$ to 10^4 $M_\odot$

Band 3 molecular clouds are in near virial equilibrium, with a spearman correlation coefficient of 0.98 for virial mass vs luminosity mass. The clumps size - linewidth relations for NGC 604 and GMC 16 generally follow the Galactic and Large Magellanic Clouds relation but this is not so for GMC 8. We find that clumps in all GMCs are in sub - virial equilibrium. In all the three clouds, mass - size relations show a constant surface density with power law exponents ranging from 2.5 to 4.0 which is the range of slopes in Large Magellanic clouds and the Milky Way. We show a cumulative mass distribution of our clump masses and found a power - law exponent ranging from -1.23 to -1.97 which is comparable to that which is found in similar studies in other galaxies.

We have shown that the physical properties of molecular clouds and clumps in M33 are comparable to those in the Large Magellanic Cloud, NGC 6822 and the Milky Way except those from GMC 8 which show different characteristics. Further studies are still needed to probe such results from GMC 8 and other properties and some assumptions made in estimating masses.

Contents

List of Tables

List of Figures

Abbreviations

Acknowledgements

I am extremely grateful to my supervisor, Dr. Jason Kirk, for granting me the opportunity to carry out this research and for the knowledge imparted along the way as well as the guidance. His advice has been invaluable and uplifting, both of which are greatly appreciated.

My gratitude to professor Derek Ward-Thompson and Dr. Anne E. Sansom for the invaluable knowledge imparted along the way, the series of discussions we had which shaped my studies greatly. Many thanks to star formation group at the Jeremiah Horrocks Institute (JHI) for the platform that granted me great advice and endless support throughout my journey. Thanks to the JHI staff and post-graduates for the great memories created together. Particular gratitude goes to Raeesa Parker and David Glass for the endless support throughout my journey and making sure I settled easily in school. The journey of becoming a radio astronomer was really fun with them.

Many thanks to Dr. George Bendo at the University of Manchester for guidance in radio interferometry data reduction. Furthermore, thanks to the workshops provided by UK ALMA Archnode, without whom the analysis of this thesis could not have been done.

I would like to acknowledge the Development in Africa with Radio Astronomy (DARA) through Newton fund for the sponsorship granted to me. This paved way for me to pursue my passion of exploring the universe.

Special thanks to my wife, Florence. Am greatly humbled for sacrificing everything just to see me pursue the career I so much love. You allowed me to travel thousands of miles away from home while you remained to take care of the kids at home which gave me an opportunity to only concentrate on my studies. Thank you so much for being such a great supporter. I would like to say thank you to my daughter, Taonga and my son Mphatso for enduring the ever absence of your father while I was studying.

To my family and friends I say thank you for your continuous encouragements in this journey. In particular, Lubinda, Jackson and Cedric for always reminding me that every journey that starts surely has its destination and regardless the storms along the way, resilience takes one to the end. Surely I am proud to have had you guys throughout this journey. To my late Father, Lyson Harrison John Phiri (MYSCRIP), I say thank you for the words of wisdom you gave me have guided me this far.

Finally, and most importantly, many thanks and lots of love to my mother Agness Phiri; to whom this thesis is dedicated. She has been the pillar in my life and without her prayers and counsel this thesis would not have been possible.

Chapter 1

Introduction

1.1 The Interstellar Medium

The space in between stars is not empty as one may assume, it contains dust particles, rarefied gas, a magnetic field, relativistically moving electrons and other atomic nuclei which form a dynamic entity called the interstellar medium or ISM (Binney J. 2014, and references therein). Most of the ISM components are detected in the discs of spiral galaxies. The interstellar medium is thin enough to qualify as a vacuum on the Earth, but it plays an important role in the evolution of the galaxies. Stars are born and die in the interstellar medium. When stars die, some of their materials are recycled back into the ISM.

The models of McKee & Ostriker (1977) and Krumholz & McKee (2005), presented in the schematic diagram in Figure 1.1, shows that the ISM consists of three separate and distinct gas phases: a hot tenuous medium at a temperature about 10^6 K, a warm medium with temperature of 10^4 K, and cold, dense molecular clouds at temperatures ≤ 100 K. In the Milky Way (MW) about 70-80 % of the volume consists of hot medium with a small percentage of the volume being cold and dense clouds (McKee & Ostriker 1977). The abbreviations presented in the schematic diagram in Figure 1.1 represent the following: HIM - hot interstellar medium, WIM - warm interstellar medium, WNM - warm neutral medium and

CNM - cold neutral medium. T, n and x represent their temperature, density of hydrogen atoms, and ionisation fraction respectively. Across the cold, warm, and hot phases of the ISM, the gas is isobaric in total pressure with the turbulent pressure component increasingly dominant at high star formation rates (Joung et al. 2009; Walch et al. 2015).

Below we discuss briefly the three ISM phases which are shown in the schematic diagram in Figure 1.1.

1.1.1 Hot Medium

In the ISM, hydrogen gas has been highly ionized (Fan et al. 2006). The most dominant sources of ionization of the ISM gas are cosmic rays from active galactic nuclei, quasars and gamma-ray bursts in galaxies which passes through the ISM. Another source of ionization is the feedback from stars and star clusters (Costa et al. 2021). The other process in which gas in the ISM gets ionized is through supernovae explosions from the death of massive stars.

1.1.2 Warm Medium

The warm medium with temperature of 10^4 K is confined to small clouds and envelopes which surround cold clouds. This exists as a natural consequence of immersing the cold clouds' envelopes in the ultraviolet and soft X-ray radiation emitted by stars and supernovae remnants. Consequently, with high exposure to radiation, it gets ionized.

Hydrogen gas in and around galaxies is the main diagnostic for understanding galaxy formation and evolution (Rhee et al. 2013). Different techniques are employed to observe the different components, with radio observations probing rotational - vibrational transitions of molecules (mainly carbon monoxide-CO), the hydrogen 21-cm line probing atomic hydrogen, and ultraviolet (UV) and X-ray observations probing the hot component. The fact that different techniques are employed to observe different gas components may exaggerate the degree to which

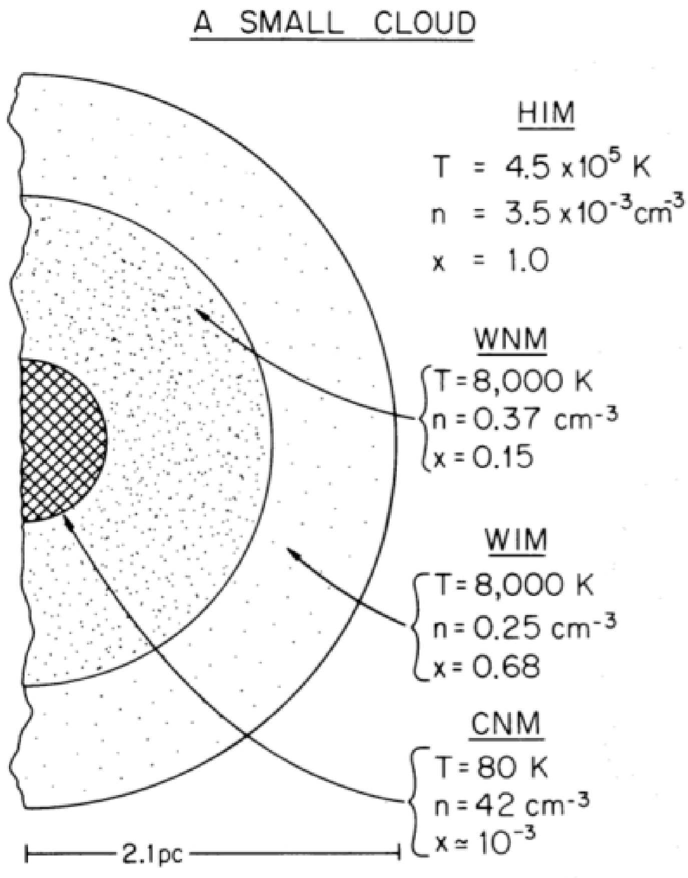

Figure 1.1: A schematic of steps for the three phase interstellar medium. HIM represents hot interstellar medium, WIM for warm interstellar medium, WNM for warm neutral medium and CNM for cold neutral medium. T, n and x represents their temperature, density of hydrogen atoms, and ionisation fraction respectively. Image credit from McKee & Ostriker (1977).

these phases are really different.

1.1.3 Cold Medium

About 5% of the interstellar medium is in the form of neutral hydrogen gas (HI). This neutral hydrogen gas in galaxies is linked to being the reservoir of star formation fuel and indeed star formation itself (Rhee et al. 2013). The typical density of neutral hydrogen in the Galaxy is one atom per cubic centimeter. This gas is cold and the electron is usually in its ground state.

Regions in the ISM where the gas is molecular are called molecular clouds. Hydrogen is the most abundant element in the universe and in this regard the most abundant molecule is H_2 (Weinreb et al. 1963; Wilson et al. 1970). H_2 is a homonuclear diatomic molecule with no permanent electric dipole moment, which means that radiative transitions in hydrogen molecule are too weak to be detected (Wilson et al. 2013). This makes it difficult to observe and, in place of it, carbon monoxide (CO) is often used as a tracer of molecular gas. Molecular gas is critical in the determination of both the morphology and evolution of galactic disks. It is within GMCs in the galactic discs where some of the ISM gas gets recycled into the next generation of stars and very massive young stars generate a major part of the galactic luminosity (Young & Scoville 1991). This thesis is based on this component of the ISM.

1.1.4 Dust

The other major component of the ISM is the dust. The dust grains are solid particles with size ranging from 0.3 nm to about 0.3 μm that are mixed with the gas (Galliano et al. 2011; Thirlwall et al. 2020, and references therein). Despite the dust accounting for only 1% of the ISM mass, dust grains have a great effect on galaxies as they scatter and absorb light from stars. These dust grains are responsible for the heating of gas in photodisociation regions through a photoelectric effect caused by the far ultra-violet radiation from newly born stars (Draine

1978). Dust grains are catalysts of several chemical reactions such as the ones for the formation of the most abundant molecule in the universe, H_2 (Gould & Salpeter 1963). An understanding of the grain properties is extremely important for studying the life cycle of the ISM as well as the evolution of galaxies (Galliano et al. 2011).

1.1.5 Metals in the ISM

Metals, both in the gas phase and in the form of interstellar dust affect processes within star forming clouds. Gas-phase metals act as important coolants while dust shields cloud interiors from external radiation, which would heat the gas and dissociate molecules. Interstellar dust also facilitates molecule formation through reactions on grain surfaces. Since low temperatures make the gas clouds more susceptible to gravitational collapse, both cooling and shielding are important to the ability of gas to form stars. Schruba et al. (2017), note that if the formation of cold, dense gas depends on the abundance of metals, then low-metalicity environments may be inefficient or unable to form stars. More observations are needed to test how metals affect molecular cloud structure and star formation.

1.1.6 ISM Tracers

There exist a number of ways to detect the interstellar matter across the electromagnetic spectrum as earlier indicated and one of them is through radio observations. Rotational transitions of hetero-nuclear molecules at mm wavelengths constitute powerful probes of the denser and colder components of the ISM. Important lines include those of carbon monoxide (CO) at wavelengths of 2.6 mm and 1.3 mm. CO is a hetero-nuclear molecule with a net dipole moment which can therefore radiate as it spins due to transitions between quantised rotational energy levels (Binney J. 2014). Giant Molecular clouds (GMCs) are traced by emission from the low rotational (low J) states of CO molecules, which are excited via collisions at temperatures ranging from $5 - 20$ K (van Dishoeck & Black 1988).

In our own Galaxy (the Milky Way), molecular cloud structure is mapped by observing dust extinction, dust emission, and molecular line emission. H_2 molecules are very inefficient emitters in the cold interstellar medium (ISM) and absorption measurements require a bright background source. Carbon monoxide, is used to trace H_2. Both dust and CO are made of metals which complicates their use in tracing gas in metal-poor regions. The abundance of CO depends on shielding by dust or H_2 from dissociating radiation. Due to its low abundance, CO cannot effectively self-shield and persists only in regions where H_2 has absorbed all dissociating radiation in the Lyman-Werner bands (Wolfire et al. 2010). Therefore, CO emission traces only the dense (particle density $\geq$ 100 cm^{-3}) or most opaque parts of a molecular cloud while H_2 remains filling most of the cloud volume (Hughes et al. 2016).

CO remains the second most abundant molecule in metal-poor galaxies and an indispensable tool in detecting cold, dense clouds and mapping their structure (Schruba et al. 2017). For decades now, CO and dust emission have been very successful tracers of GMCs in both the Milky Way and external galaxies (Solomon et al. 1979; Dame et al. 1986; Heyer et al. 2001; Draine 2003; Rosolowsky et al. 2003; Tosaki et al. 2007; Bolatto et al. 2008; Hughes et al. 2010; Colombo et al. 2014; Kirk et al. 2015; Faesi et al. 2018; Schinnerer et al. 2019, and references therein). Dust continuum is a good tracer of active star forming regions and dust mass estimation needs knowledge of the dust opacity. Carbon monoxide (CO) is the most commonly used tracer of molecular gas because its lines are the strongest and therefore easiest to observe. This work uses mainly CO as a tracer to probe structural properties of GMCs and clumps.

CO has three important isotopologues whose emission properties allow them to trace different components of star forming regions: ^{12}CO, ^{13}CO, and C^{18}O which are the three forms tracing relatively diffuse molecular clouds, relative denser molecular clouds and the densest regions of molecular clouds respectively.

1.2 Star Formation

Understanding star formation starts with understanding molecular clouds. Molecular clouds have temperatures in the range 10 - 20 K. The regions which are extremely cold allows the gas to clump to high densities and become opaque to visible light. Despite being opaque to optical light, clumps can be observed using IR and radio telescopes. The denser part of the cloud is where star formation starts from (Stutzki & Guesten 1990). This happens when denser parts of the cloud collapse under their own gravity (Prialnik 2010). The clumps are denser than the outer parts of the molecular cloud, hence, they are the first to collapse. There is fragmentation of the clumps into dense cores with typical sizes of 0.1 pc and 10 to 50 $M_\odot$ in mass. It is from dense cores that protostars are formed. A protostar is a young star which is still gathering mass from its parent molecular cloud core and its interior is not yet hot enough for fusion to take place (Ward-Thompson & Whitworth 2011).

Figure 1.2 shows the schematic of the steps discussed above, from molecular cloud to protostars. After a few million years, thermonuclear fusion begins in the core and strong stellar winds stop the infall of new mass. At this stage the protostar is considered to be a young star with a fixed mass and its future evolution is set. [1] Figure 1.3 shows summary of the physical processes that operate in the ISM. Atomic clouds form out of the diffuse ISM spontaneously like clouds in our atmosphere. These clouds collide due to there random motions, fuse and grow in size. As the particle density increases, molecules form and thus GMCs are formed. Both atomic and molecular clouds are destroyed by hard radiation.

[1] http://abyss.uoregon.edu/ js/ast122/lectures/lec13.html

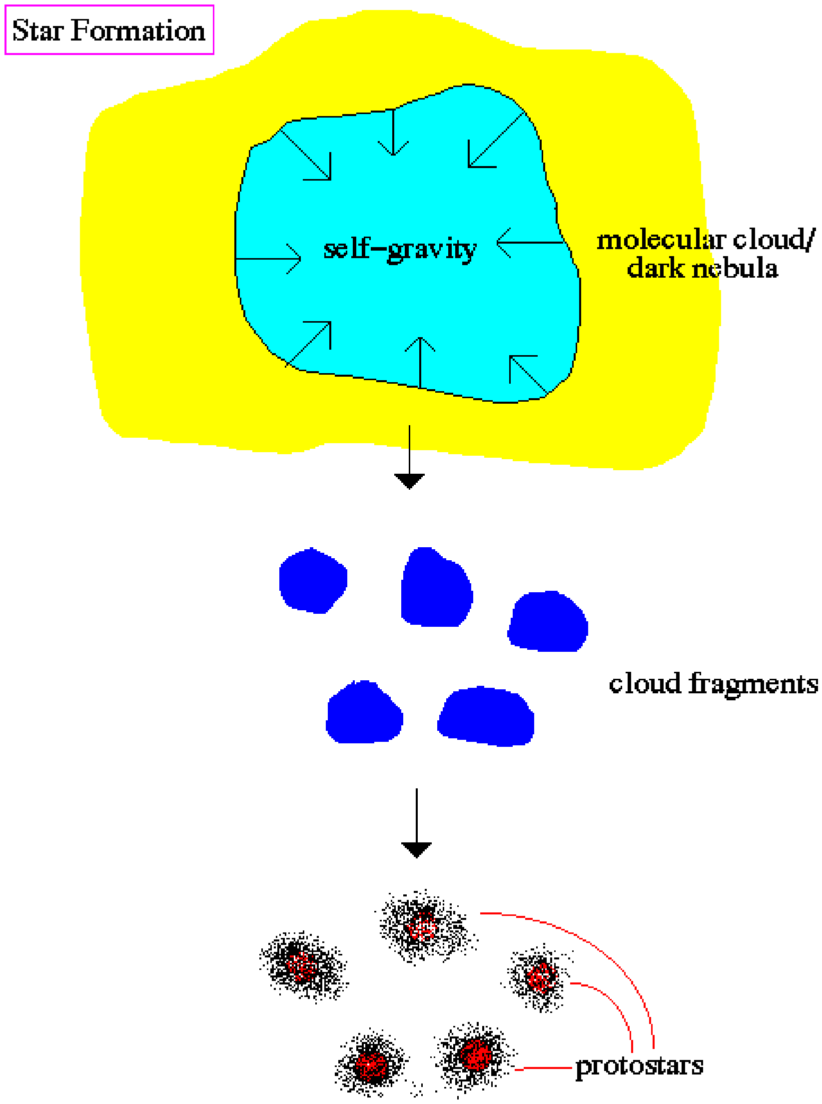

Figure 1.2: The schematic of steps during fragmentation of molecular cloud to protostars. Image credit: Schneider & Arny lecture notes[1].

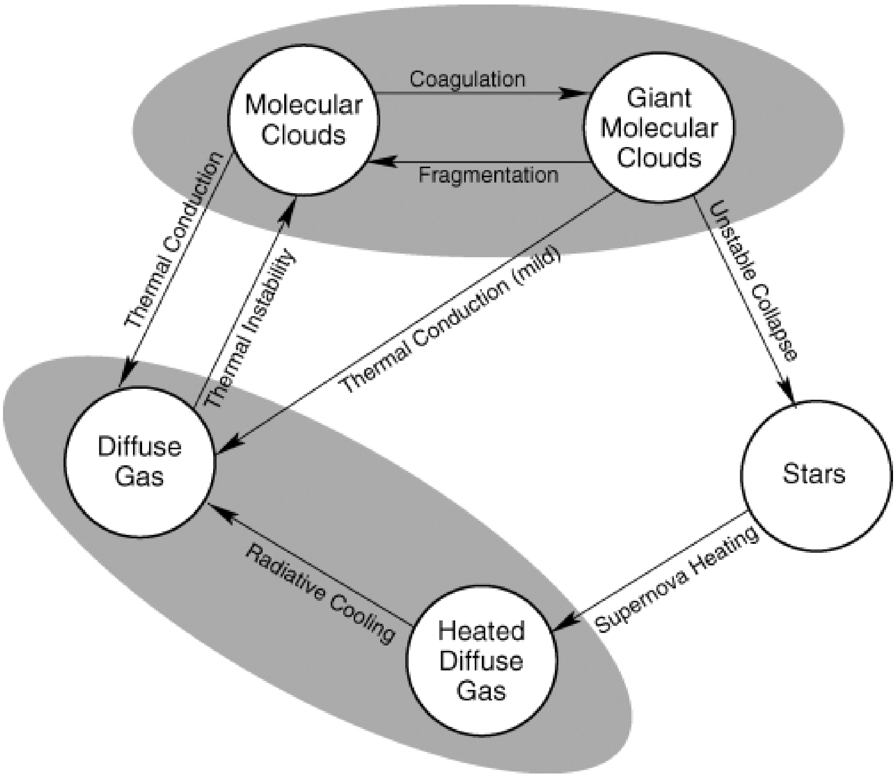

Figure 1.3: The schematic of processes at play in the ISM which depicts the formation and destruction of giant molecular clouds. The boundaries between molecular clouds and GMCs and between the heated and non-heated diffuse gas are just arbitrary, they are out in this figure to highlight the different physical mechanisms that are operating at any given time. This image is taken from the two-phase ISM model by Booth et al. (2007).

1.2.1 Star Formation in Both Galactic and Extra-galactic Context

Observations of star formation in our galaxy, the Milky Way, show that most stars form in groups, either as gravitaionally bound clusters or as unbound associations in giant molecular clouds (GMCs) (Booth et al. 2007). It has been discovered through observations that GMCs turn a small fraction of their mass ($0.03 - 0.1$) (Chevance et al. 2020, and references therein) into stars before they disperse again. This low star formation efficiency of clouds is attributed to the fact that they are short lived as they are dispersed by the very stars they produce (Booth et al. 2007).

Seo et al. (2019) proposed that star formation can be described by three different modes as shown in Figure 1.4. The first (fast) mode describes the star formation at a hub where the column density is highest and the global gravitational potential well is deepest. Large-scale flows drive continuous star formation on relatively short time scales and form a stellar cluster/association. The second (slow) mode describes the formation of the dense core chains within filaments due to gravitational fragmentation and localized star formation within each core. The third (isolated) mode describes formation of an isolated dense core and localized star formation removed from filamentary structures.

1.2.2 Giant Molecular Clouds

Giant molecular clouds (GMC) are cold, dense, and turbulent structures of the interstellar medium (ISM) composed mainly of molecular hydrogen (H_2). Observations show that stars form within these dense regions. They are large and massive molecular clouds, self-gravitating and magnetized. The densest molecular clouds have a particle density of approximately 100 cm^{-3}. Their internal temperatures are $\sim$ 10 K due to the attenuation of the interstellar radiation field. They can be typically $10 - 100$ pc across and have typical masses of 10^7 solar masses

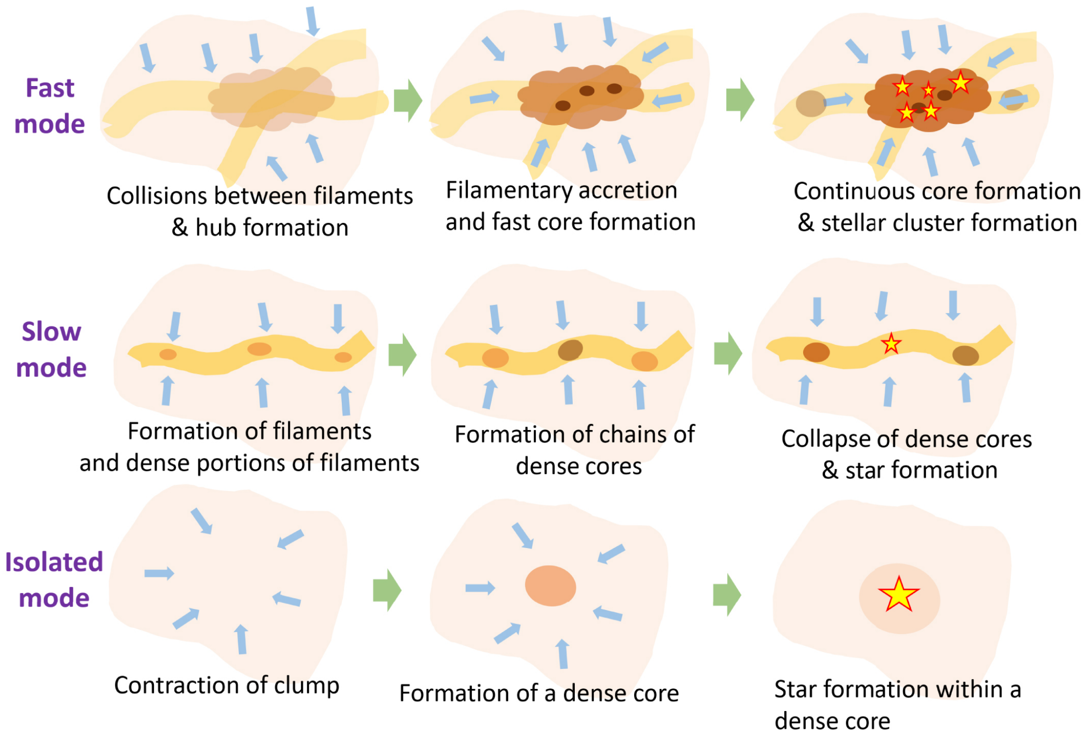

Figure 1.4: The three modes of star formation from Seo et al. (2019). The first mode describes star formation at the hub, where the column density is highest and the global gravitational potential well is deepest. The second mode describes the formation of the dense core chains within filaments due to gravitational fragmentation and localized star formation within each core. The third mode describes formation of an isolated dense core and localized star formation removed from filamentary structures, which is often discussed as conventional star formation (e.g., L1544, Bok globules). See text for a discussion.

(Kirk et al. 2015; Leroy et al. 2015). Their masses are dominated by molecular hydrogen (H_2) and a varying contribution from atomic hydrogen (HI), helium (He) and trace elements (Beuther et al. 2014, and references therein). The first catalogs of GMCs were made in the Milky Way as dark nebulae seen against a bright background starfield (Barnard 1919; Lynds 1962).

Large surveys of GMCs first became possible in the 1980s and have provided insight into the processes that govern their formation. These observations which were conducted in the Milky Way show that stars form in groups, either as gravitationally bound clusters or as unbound associations, in the GMCs (Blitz & Thaddeus 1980; Lada & Lada 2003). Figure 1.5 shows examples of single dish dust continuum observations of GMC complexes of an external galaxy (M33; Williams et al. 2019). Leroy et al. (2015) showed that limited sensitivity and resolution of single-dish millimeter-wave telescopes limit the understanding of the resolved properties of the star forming molecular structures such as clumps and cores in external galaxies. However, interferometers like ALMA have the power to resolve star forming structures due to their high angular resolution and high sensitivity. Molecular clouds contain supersonic turbulence and random motions which cause shocks. Passot et al. (1995) noted that the gas properties derived for galaxies are quite sensitive to the spatial scale over which measurements are made. Hence, to measure the properties of star forming clouds of galaxies, the measurements must be made over similar linear scales with high angular resolution being desirable in order to isolate individual dense cloud complexes. Interferometric observations combined with the use of consistent cloud identification and analysis techniques is essential for such studies. Figure 1.6 shows an example of ^{12}CO$(2-1)$ interferometric observations of internal structures of the GMC complexes in M33 mapped by the ALMA interferometer (Sano et al. 2021).

Most of our understanding of molecular clouds and the processes in the ISM which explain the formation of stars is based on the Galactic studies (Corbelli et al. 2019). The improvements in spatial resolution and sensitivity of modern

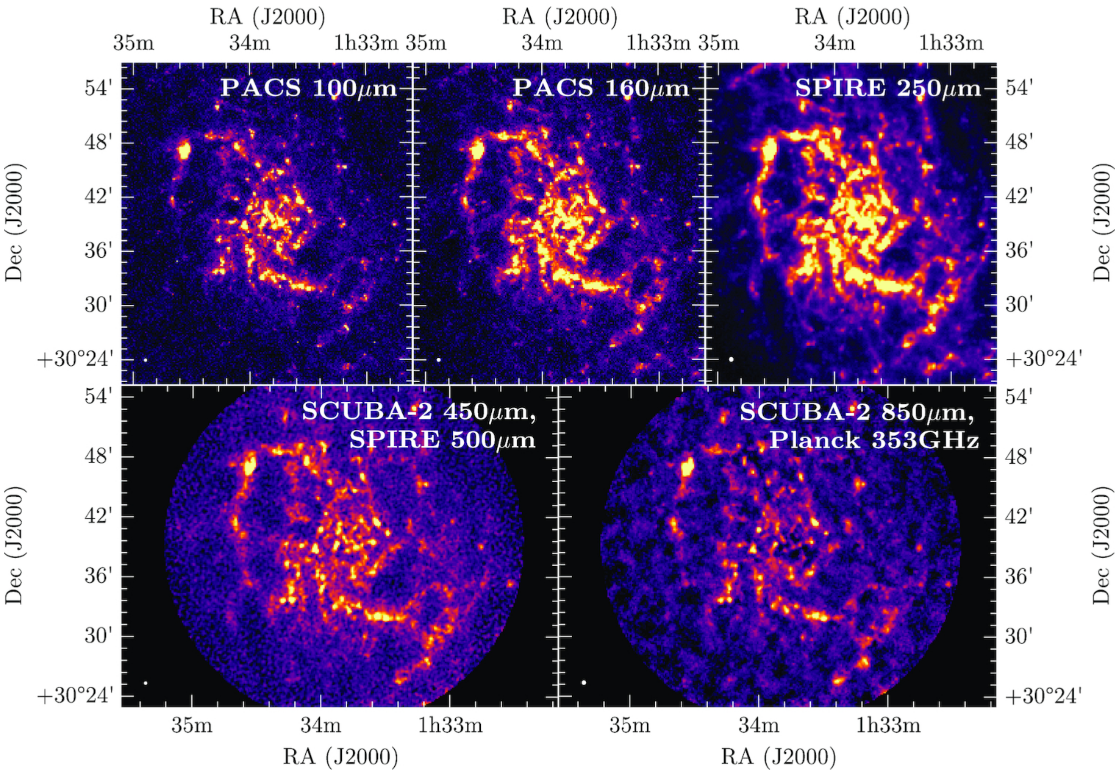

Figure 1.5: GMCs in M33 mapped in continuum emission. From the top left, PACS 100 μm and 160 μm data, SPIRE 250 μm map, and SCUBA-2 data 450 μm (combined with the SPIRE 500 μm map) and 850 μm (combined with Planck 353 GHz data). The image is taken from Williams et al. (2019).

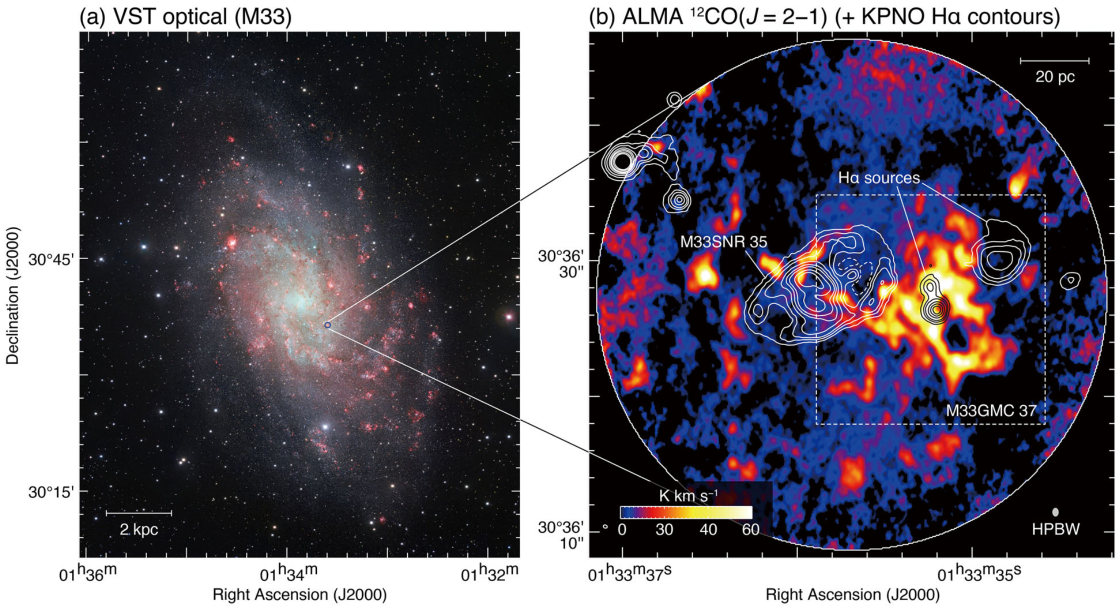

Figure 1.6: (a) False color image of M33 obtained with VLT Survey Telescope (VST, credit:ESO). (b) An integrated intensity map of ^{12}CO$(2-1)$ obtained with ALMA. The superposed white and black contours indicate the H_α intensity obtained by the Kitt Peak National Observatory. The entire image is taken from Sano et al. (2021)

instruments, have enabled extragalactic studies to be done (Engargiola et al. 2003; Rosolowsky et al. 2003; Pineda et al. 2009a; Gratier et al. 2012; Miura et al. 2012; Druard et al. 2014; Colombo et al. 2014; Kirk et al. 2015; Wong et al. 2017, 2019; Faesi et al. 2018, and references therein).

Individual GMCs have been resolved in external galaxies before but limited to Large and Small Magellanic Clouds and at above 10 pc resolution (Mizuno et al. 2001; Bolatto et al. 2003; Wong et al. 2011). With the emergence of modern (sub)millimeter interferometers, it has become possible to resolve individual GMCs in nearby galaxies down to clump level (Indebetouw et al. 2013; Rubio et al. 2015; Schruba et al. 2017; Wong et al. 2017, 2019).

Studies of molecular clouds in external galaxies have revealed that processes that govern star formation at GMC level are similar to those found in our Galaxy (Kirk et al. 2015; Williams et al. 2019, and references therein). Figure 1.7 shows the slope of the ^{12}CO luminosity vs. total dust mass relationship of 0.82 ± 0.05 for M31 GMCs measured by Kirk et al. (2015) to be is similar to the Milky Way value of 0.81 (Solomon et al. 1987). Figure 1.8 presents a slope of 1.21 for the cloud mass function of GMCs in M31 which is comparable to the Galactic value of 1.5. This indicates that properties of molecular clouds in external galaxies are similar to our Galaxy.

1.2.3 Giant Molecular Cloud Formation

The formation of GMCs is not well understood but there are some proposed mechanisms that try to explain how these fundamental sites of star formation are formed. The mechanisms that have been proposed include converging flows of gas and other ISM materials driven by stellar feedback or turbulence (Bania & Lyon 1980; Passot et al. 1995), agglomeration of smaller clouds (Colombo et al. 2014), gravitational instability, magneto-gravitational instabilities (Elmegreen & Elmegreen 1983; La Vigne et al. 2006) and instabilities involving differential buoyancy (Beuther et al. 2014). These mechanisms act on different sizes and time scales and hence they may

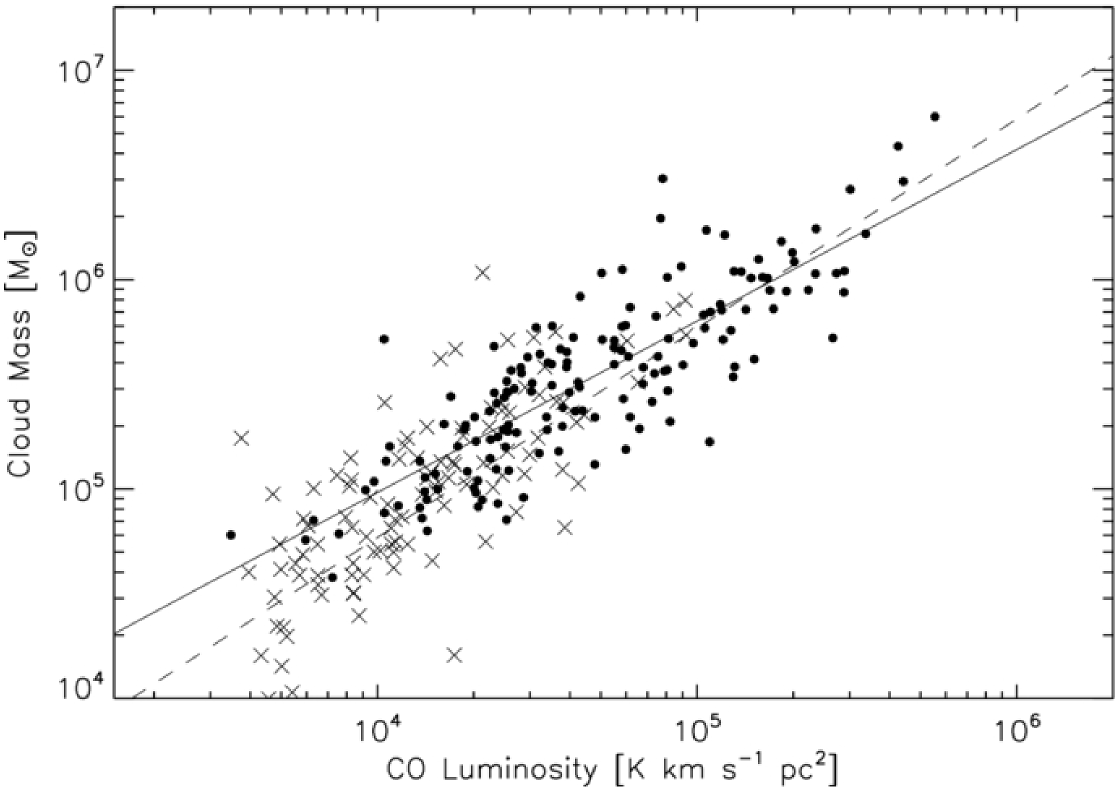

Figure 1.7: ^{12}CO luminosity vs. total dust mass derived from the Herschel FIR clouds in M31. The solid line shows a best-fit power law with an exponent of 0.82 ± 0.05. The dashed line shows the $\alpha_{\rm CO}$ relationship from M31 by Smith et al. (2012). Image taken from Kirk et al. (2015).

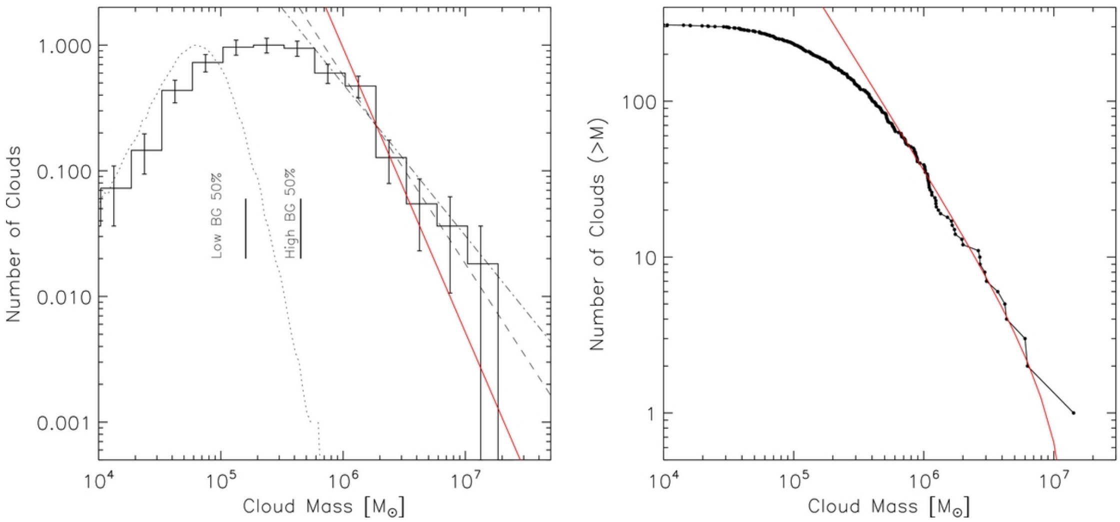

Figure 1.8: Mass distribution of clouds in M31. The solid red curves in both plots show mass distributions calculated from a truncated power law with an exponent $\alpha_{\rm M} = 2.34 \pm 0.12$ (equivalent to an exponent of 2.34–1 in the cumulative case). Left: histogram of $M_{\rm cloud}$. The dot–dashed power law has an exponent of 1.21. This is significantly different than that found via the modified maximum likelihood estimator method (i.e., 2.34). The dashed power law shows the equivalent $\alpha = 1.5$, power law for Milky Way clouds. The bars along the bottom edge show the 50% point-source completeness for low and highly structured background. The dotted line shows the equivalent point-source sensitivity once variations of dust temperature and properties have been accounted for. Right: cumulative histogram of total cloud mass for the M31 clouds. Image taken from Kirk et al. (2015).

dominate in different environments which may lead to different cloud properties.

1.2.4 Filaments

Filaments are part of the hierarchical structure of the ISM. Figure 1.9 shows filaments in Taurus molecular cloud traced with different cloud tracers from Seo et al. (2019). Filaments form in the ISM through magneto-hydrodymamical turbulence and shocks as well as convergent flows (Padoan et al. 2001; Vázquez-Semadeni et al. 2006). They are the initial step towards core and star formation (André et al. 2010). They have been observed both in our galaxy and external galaxies with different tracers ranging from extinction maps, optical, infrared wavelengths (Schneider et al. 1979; Jackson et al. 2010, and references therein), far-infrared/submillimeter dust maps (André et al. 2010; Hennemann et al. 2012) and CO maps (Goldsmith et al. 2008; Tokuda et al. 2020). They are typically about 5 - 6 pc in width and 50 - 80 pc in length and masses ranging from $10^4 - 10^5$ $M_\odot$ (Jackson et al. 2010; Tokuda et al. 2020, and references therein).

1.2.5 Clumps

The substructure of a GMC is a complex pattern of sheets, bubbles, and irregular clumps. A goal of this thesis is to resolve extragalactic GMCs down to clump scales. The densest parts of the filaments and clumps are referred to as molecular cores with the densest molecular cores having densities ranging from 10^4 to 10^6 particles per cubic centimeter (Beuther et al. 2014). Internal structures of GMCs have been extensively explored in our own galaxy by surveys such as the Herschel Infrared Galactic (Hi-Gal) survey (Elia et al. 2017, and references therein). Figure 1.10 shows Hi-GaL clump diameters and their distribution in the Hi-Gal survey as presented in Elia et al. (2017) on their Figure 4. The left panel shows clump linear diameters plotted against their distance at 250 μm and the right panel shows the distribution of source diameters. Most of the clumps in Hi-Gal survey have sizes ranging from 0.2 pc to 3 pc and masses ranging from 1 $M_\odot$ to 315 $M_\odot$.

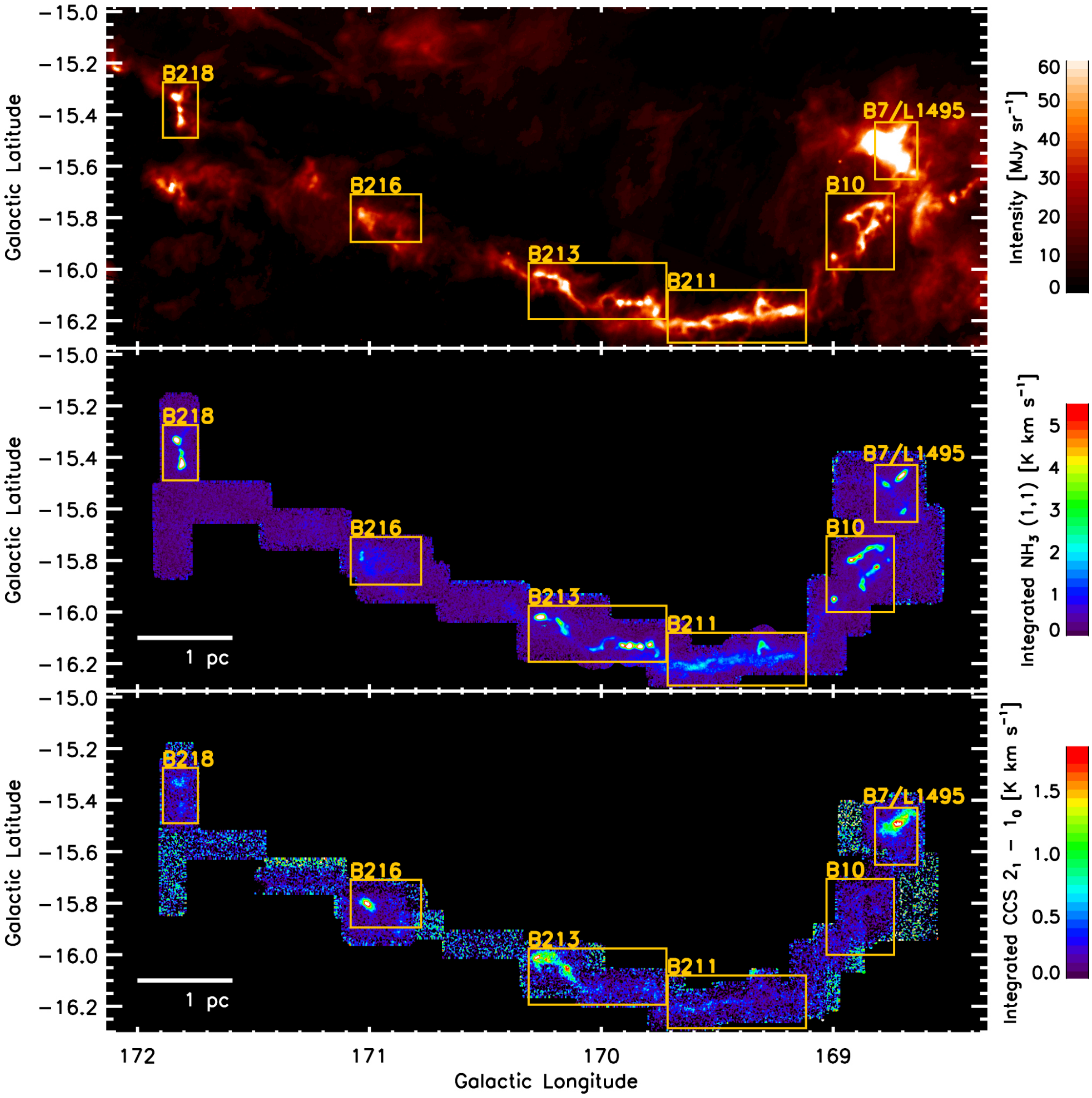

Figure 1.9: Top: 500 μm dust continuum emission in Taurus seen by the SPIRE instrument on the Herschel Space Observatory (Palmeirim et al. 2013). Middle: map of integrated intensity of NH_3 $(1, 1)$ (Seo et al. 2015). Bottom: map of integrated intensity of CCS $J_N = 2_1 - 1_0$ (Seo et al. 2019). The entire image is taken from Seo et al. (2019).

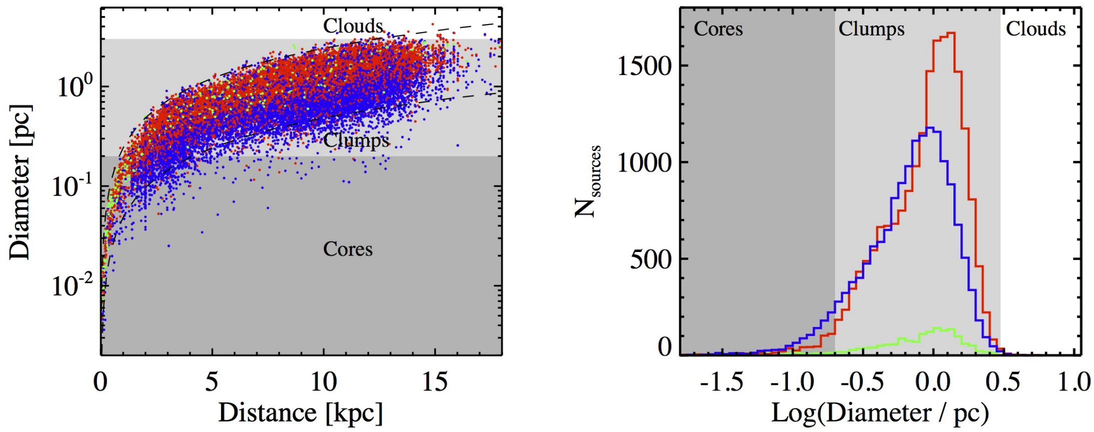

Figure 1.10: *Left-hand panel:* Hi-GAL clump diameters, estimated at 250 μm, versus distance (blue: protostellar; red: pre-stellar; green: starless unbound). Different background levels of grey indicate size ranges corresponding to different object typologies. The upper and lower dashed lines represent an angular size of 50 and 10 arcsec, respectively. *Right-hand panel:* distribution of source diameters from protostellar, pre-stellar and starless unbound source. Line and background colours, are the same as in the left-hand panel. Image taken from Elia et al. (2017).

The blue points represent protostellar clumps, red represent prestellar clumps and green represent unbound clumps. These are regions within molecular clouds with higher densities where large quantities of dust and gas cores reside, representing the collapse phase, just before the collapse phase and where there is no sign of star formation at all, respectively.

Despite a lot of work being done on GMCs in external galaxies for decades, the lack of high resolution observations has hampered the detection of clumps comparable to those in the Milky Way. With the advent of ALMA, these GMCs can now be resolved down to clump level in the Local Group of galaxies (Schruba et al. 2017). ALMA studies of clumps have been done in the Local Group in WLM (Rubio et al. 2015), NGC 6822 (Schruba et al. 2017) and Magellanic Clouds (Wong et al. 2017, 2019).

Surveys have mapped GMCs, filaments and clumps with similar physical properties (mass, size, linewidth, e.t.c) to those measured in the Milky way (Kirk et al. 2015; Faesi et al. 2018; Wong et al. 2017).

1.2.6 Cores

The substructures within clumps are known as cores. Cores are more compact and typically bound by gravity. They may collapse under their own gravity subsequently forming stars. These cores have sizes which are $\leq$ 0.2 pc based on the subdivision scheme proposed by Bergin & Tafalla (2007) of starless and star-containing based on whether there is an embedded young stellar object or not in the core.

1.3 Mass Estimates

Masses of molecular clouds can be estimated through both theoretical and observational means. Below we briefly discuss these methods of estimating masses of molecular clouds.

1.3.1 Theoretical Mass Estimate

As alluded to in the previous section, molecular cloud masses can be estimated in a number of ways. One is using linewidths as a measure of the cloud velocities following the argument of Solomon et al. (1987).

Let us assume that the cloud is spherically symmetric with radius R and mass M. We calculate the total energy which includes kinetic and potential of such a cloud. It is enough to calculate only the potential energy because of the virial theorem,

$$2\mathrm{K} + \mathrm{U} = 0 \tag{1.1}$$

where K is kinetic energy and U is potential energy. Therefore, the total energy of the cloud is given by,

$$E = K + U \tag{1.2}$$

using the virial theorem;

$$2K = -U \tag{1.3}$$

$$K = -\frac{U}{2} \tag{1.4}$$

Replacing Equation 1.4 into Equation 1.2 we get:

$$E = -\frac{U}{2} + U = \frac{U}{2} \tag{1.5}$$

To obtain the total potential energy, we will start by considering the potential du of a mass element dm inside the cloud at a distance r from the center. The gravitational forces from a spherical shell of matter add to zero outside this shell. Therefore, we only consider the gravitational attraction on the mass dm from the sphere of matter inside the position of the mass. This is the sphere of radius r and mass m(r). Being a sphere, Newton's law of gravitation applies as if it were a point mass allocated at the center with mass m(r). Therefore, the potential energy between the particle dm and the rest of the cloud (the part inside the particle) is

$$du = -\frac{Gm(r)dm}{r} \tag{1.6}$$

Integrating Equation 1.6 over all masses dm in the shell of thickness dr at distance r from the center, we assume that the mass density in the shell is given by $\rho(r)$. This results in obtaining the potential energy dU between the shell and the spherical mass m(r) inside the shell.

$$dU = -\frac{Gm(r)4\pi r^2 \rho(r)dr}{r} \tag{1.7}$$

To obtain the total potential energy U, the equation needs to be integrated over all radii r out to the edge of the cloud at r=R.

$$U = -4\pi G \int_0^R m(r)\rho(r) r dr \tag{1.8}$$

We would generally need to know the density $\rho(r)$ in order to obtain m(r) and to integrate this equation. Here, we assume that the density is constant with a value equal to the mean density of the cloud,

$$\rho = \frac{m}{\frac{4}{3}(\pi R^3)} \tag{1.9}$$

this gives $m(r) = \frac{4}{3}(\pi r^3)\rho$ and we integrate the equation;

$$U = -4\pi G \left(\frac{m}{\frac{4}{3}(\pi R^3)}\right)^2 \frac{4}{3}\pi \int_0^R r^4 dr = -4\pi G \left(\frac{m}{\frac{4}{3}(\pi R^3)}\right)^2 \frac{4\pi}{3}\frac{1}{5}\left[r^5\right]_0^R \tag{1.10}$$

$$U = -\frac{3Gm^2}{5R} \tag{1.11}$$

Therefore, from the virial theorem, Equation 1.11 into Equation 1.5;

$$E = \frac{U}{2} = \frac{1}{2}\left(-\frac{3GM^2}{5R}\right) = -\frac{3GM^2}{10R} \tag{1.12}$$

This is the total energy of a cloud of gas with mass M and radius R.

For a spherical cloud of mass M, radius R and velocity dispersion σ_v, we have kinetic energy, $K = \frac{3M\sigma_v^2}{2}$, with 3/2 arising from the projection of the 3-D velocity distribution onto the plane of the sky and potential energy $U = -\frac{3GM^2}{5R}$.

Substituting in virial theorem;

$$E = 2K + U = 2\left(\frac{3M\sigma_v^2}{2}\right) - \frac{3GM^2}{5R} = 0 \tag{1.13}$$

$$\frac{GM}{5R} = \sigma_v^2 \tag{1.14}$$

Therefore the virial mass becomes,

$$M_{\mathrm{vir}} = \frac{5R\sigma_{\mathrm{v}}^2}{G} \tag{1.15}$$

If the mass of a cloud is roughly equal to its virial mass, then it is close to virial equilibrium. If a cloud has a mass greater than its virial mass, then it will collapse unless supported by some other mechanism. If a cloud has mass less than its virial mass, then it is not gravitationally bound and will probably disperse under the action of its own internal motions, unless it is confined by external pressure (Ward-Thompson & Whitworth 2011).

1.3.2 Observational Mass Estimate

There are a number of ways to estimate molecular cloud mass from observations which depends on the tracer involved. We discuss some of the methods below and mostly the ones we use or those connected to our work.

1.3.2.1 The X_{CO} Conversion Factor

An understanding of interstellar physics and star formation in galaxies comes from the determination of molecular hydrogen mass (Arimoto et al. 1996). This is done by the principal method of converting the intensity or luminosity of the CO molecular line emission (I_{CO} or L_{CO}) into the column density or mass of H_2 molecules (N_{H_2} or M_{H_2}). This requires the use of a CO conversion factor X_{CO}.

The conversion factor $X_{CO} = X^* \times 10^{20}$ $\mathrm{cm^{-2}(Kkms^{-1})^{-1}}$, has been derived in the solar neighbourhood from molecular clouds using the assumption that individual clouds are in virial equilibrium following the large-velocity gradient approximation of the CO line (Goldsmith et al. 2008; Bolatto et al. 2013). The value derived from several studies for our galaxy is around $X^* = 2 - 3$. The X_{CO} factor derived from virial method is consistent with the one derived from $\gamma -$ ray method (Bloemen 1996) and extinction (A_v) method (Solomon et al. 1987). The pattern is the same for similar environment in other galaxies as Milky Way (Kuno et al. 1995).

There is a scatter on the X_{CO} value for low metallicity galaxies which shows that the value is dependent on metallicity. The lower the metallicity the higher the value of X_{CO}. In other galaxies with lower metallicities like M33 with half solar metallicity the conversion factor for $^{12}CO(1-0)$ is 4×10^{20} cm^{-2}(Kkms^{-1})$^{-1}$ (Gratier et al. 2012; Druard et al. 2014). In terms of $^{13}CO(1-0)$, the equivalent value of 2×10^{20} cm^{-2} (Kkms^{-1})$^{-1}$ translates to 8×10^{20} cm^{-2}(Kkms^{-1})$^{-1}$ (Rosolowsky et al. 2008) and for half solar metallicities the same gives the value of 1×10^{21} cm^{-2}(Kkms^{-1})$^{-1}$ (Cormier et al. 2018). The errors on this conversion factor value are about 30% (Bolatto et al. 2013). The X_{CO} is widely used and still remains subject of much study and debate.

Generally, the value of X_{CO} differs from galaxy to galaxy as well as within the galaxy from the centre going out. This is due to different environments which have different metallicities. In environments where the metallicities are less than solar we get higher values of X_{CO} conversion factor. Hence, understanding the metallicities in the target galaxy or source withing the galaxy helps determine the value of X_{CO} which in turn leads to more accurate estimation of masses for the sources.

1.3.2.2 Luminosity Derived Mass

The ISM contains oxygen and carbon which combine and form carbon monoxide (CO) under the conditions prevailing in molecular clouds (Bolatto et al. 2013). CO has a weak permanent dipole moment as well as a ground rotational transition with a low excitation energy of $h\nu \sim 5.53$ K (Bolatto et al. 2013, and references therein). This makes CO easily excited even in cold molecular clouds and allows it to be used as a tracer of H_2 distribution in galaxies.

Since CO and H_2 formation are closely linked chemically, a simple relation could convert CO emission into H_2 column density. The CO conversion factor (X_{CO}) relation is used to obtain the column density of H_2 by using the equation:

$$N_{H_2} = X_{CO} W_{CO(J=1-0)} \tag{1.16}$$

where $W_{CO(J=1-0)}$ is the integrated intensity of the first rotational emission line of CO, N_{H_2} is the column density of H_2 and X_{CO} is the empirically derived conversion factor with an accepted value of $X_{CO} = 2 \times 10^{20}$ cm^{-2}(Kkms^{-1})$^{-1}$ with 30% uncertainty with others ranging from $(1-3) \times 10^{20}$ cm^{-2}(Kkms^{-1})$^{-1}$ in the Milky Way (Bolatto et al. 2013). There are different methods through which the value for X_{CO} can be derived empirically. The first is by using the assumption that GMCs are in virial equilibrium. If this is the case equation 1.15 is used to estimate the total virial mass. This requires observations that are highly resolved, both in space and velocity, in order to accurately quantify the dynamical state of the cloud. Comparing the total CO luminosity (L_{CO}) with M_{vir} a strong correlation is found, this leads to the empirical relation $M_{CO} = \alpha_{CO} L_{CO}$. The accepted value is $\alpha_{CO} = 4.3$ $M_{\odot}$(Kkms^{-1}pc^{-2})$^{-1}$. corresponding to $X_{CO} = 2 \times 10^{20}$ cm^{-2}(Kkms^{-1})$^{-1}$ (Bolatto et al. 2013).

Therefore, molecular cloud masses derived from CO-based mass estimators can be computed based on the integrated CO flux assuming an X_{CO} conversion factor (luminosity mass) or virial mass which is derived from the size and linewidth of the observed molecular cloud (Solomon et al. 1987; Rosolowsky et al. 2003; Faesi et al. 2018).

1.3.2.3 Local Thermodynamics Equilibrium Derived Mass

In concluding that molecular clouds and their clumps are near virial equilibrium, there is a risk of circularity given that luminosity-to-mass conversion factor is calibrated in part by assuming virial equilibrium (Wong et al. 2017).

^{13}CO is used as a mass tracer by assuming that ^{12}CO and ^{13}CO are in local thermal equilibrium (LTE) at a common excitation temperature (Nishimura et al. 2015; Wong et al. 2017, and references therein). The assumption is that ^{12}CO line is optically thick at the line center and not subjected to beam dilution such that for a given line-of-sight, the excitation temperature is uniform. Following the derivation presented by Wong et al. (2017) LTE masses are derived as shown below. The ^{12}CO excitation temperature is given by:

$$\mathrm{T_{ex}^{J=1-0}} = 5.53 \left[\ln \left(1 + \frac{5.53}{\mathrm{T_{peak}^{12}} + 0.83} \right) \right]^{-1}. \quad (1.17)$$

where $\mathrm{T_{peak}^{12}}$ is the peak temperature of the ^{12}CO profile. ^{13}CO optical depth is therefore calculated from the brightness temperature $\mathrm{T_{13}}$ at each position and velocity in the cube using,

$$\tau_{13}^{\mathrm{J=1-0}} = -\ln \left[1 - \frac{\mathrm{T_{13}^{1-0}}}{5.29} \left(\frac{1}{\exp(\frac{5.29}{\mathrm{T_{ex}^{1-0}}}) - 1} - 0.17 \right)^{-1} \right]. \quad (1.18)$$

τ_{13} varies linearly with $\mathrm{T_{13}}$ in the optically thin limit.

Having established the excitation temperature and the optical depth, the total ^{13}CO column density in cm^{-2} summed over all rotational levels is computed using,

$$\mathrm{N(^{13}CO)_{J=1-0}} = 1.98 \times 10^{16} \left[\exp \left(\frac{5.29}{\mathrm{T_{ex}}} \right) - 1 \right]^{-1} \int \tau_{13}(\nu) \mathrm{d}\nu. \quad (1.19)$$

The LTE-based estimated mass ($\mathrm{M_{LTE}}$) is derived by scaling ^{13}CO column density, ($\mathrm{N^{13}CO}$), to molecular hydrogen column density, $\mathrm{N(H_2)}$ using an abundance ratio of $\mathrm{H_2}/^{13}$CO (Indebetouw et al. 2013; Wong et al. 2017). This method can be used to derive mass from other higher transitions of ^{13}CO and C^{18}O lines.

1.3.2.4 Dust Mass

In the ISM, emission from dust provides an opportunity to calculate mass of the emitting dust (Ward-Thompson & Whitworth 2011). Below is the derivation of the dust mass estimate following Ward-Thompson & Whitworth (2011).

A spherical grain of radius a has a monochromatic luminosity, L_ν as follows:

$$\mathrm{L_\nu} = 4\pi \mathrm{a^2 B_\nu(T_d) Q_\nu}. \quad (1.20)$$

where $4\pi\mathrm{a}^2$ is the surface area of the grain, $\pi\mathrm{B_\nu(T_d)}$ is the monochromatic flux at frequency ν from a blackbody-like surface with temperature $\mathrm{T_d}$ and $\mathrm{Q_\nu}$ is the emission efficiency of the grain (how well it approximates to a blackbody at frequency ν).

If we take the total mass of dust in the cloud to be $\mathrm{M_d}$ and the mass of a single dust grain is $\mathrm{m_d}$, then the total number of dust grains in the cloud, $\mathrm{N_d}$, is given by,

$$\mathrm{N_d} = \frac{\mathrm{M_d}}{\mathrm{m_d}} = \frac{3\mathrm{M_d}}{4\pi \mathrm{a}^3 \rho_\mathrm{d}}. \tag{1.21}$$

since $\mathrm{m_d} = 4\pi \mathrm{a}^3\rho/3$, where ρ_d is the density of the material in a single dust grain. When the dust emission is optically thin, the flux density F_ν, received by an observer at distance D is

$$\mathrm{F}_\nu = \frac{\mathrm{N_d L_\nu}}{4\pi \mathrm{D}^2}. \tag{1.22}$$

Substituting equations 1.20 and 1.21 into 1.22 we get

$$\mathrm{F}_\nu = \frac{3\mathrm{M_d B_\nu(T_d) Q_\nu}}{4\mathrm{a}\rho \mathrm{D}^2}. \tag{1.23}$$

and making $\mathrm{M_d}$ subject, we get

$$\mathrm{M_d} = \frac{4\mathrm{a}\rho_\mathrm{d} \mathrm{F}_\nu \mathrm{D}^2}{3\mathrm{B}_\nu(\mathrm{T_d})\mathrm{Q}_\nu}. \tag{1.24}$$

With this equation, we can estimate the mass of emitting dust. This is written as

$$\mathrm{M_d} = \frac{\mathrm{k}_\nu \mathrm{F}_\nu \mathrm{D}^2}{\mathrm{B}_\nu \mathrm{T_d}}. \tag{1.25}$$

where k_ν is the dust mass opacity coefficient given by,

$$\mathrm{k}_\nu = \frac{4\mathrm{a}\rho_\mathrm{d}}{3\mathrm{Q}_\nu}. \tag{1.26}$$

Therefore, measuring the flux density from the dust in a molecular cloud, provides a way to calculate the total mass of dust in that cloud. The total cloud mass is derived by multiplying the dust mass by the dust-to-gas ratio. This ratio is normally taken to be 100 but changes with metallicity.

1.4 Scaling Relations of the Physical Properties

Based on the studies conducted on turbulence and star formation in molecular clouds by Larson (1981) three scaling relations were discovered from their properties measured (i.e., size, linewidths). He based his studies on Galactic clouds as did Solomon et al. (1987). These two works laid the foundation for studies of molecular clouds physical properties. Thereafter, several studies have been done from the scales of GMC complexes down to cores in the process of star formation in the Milky Way (Goodman et al. 1998; Heyer et al. 2001; Elia et al. 2017, and references therein). These studies have generally found that three scaling relations hold for different hierarchical structures of the molecular clouds ranging from GMC complexes, GMCs, filaments, clumps to cores.

The size-linewidth relation is commonly known as Larson's first law. $\Delta \mathrm{v} \propto \mathrm{R}^{0.5}$ relates the line-width in kms^{-1} to the radius in parsecs (Larson 1981; Solomon et al. 1987). A version is shown in Figure 1.11. Large CO linewidths seen at parsec scales are evidence that these clouds are turbulent. Through whatever mechanisms that form clouds, turbulent kinetic energy appropriate for their sizes is inherited. It then follows from the size-linewidth relationship that there is a turbulent cascade of energy through the ISM and that the form of this turbulence is described by its power law slope of 1/2 for a compressible medium, 1/3 for an incompressible medium, (McKee & Ostriker 2007). Interstellar turbulence transfers energy across spatial scales and hence the size-linewidth relation can be studied on many scales from GMCs down to 0.1 pc scales (Goodman et al. 1998).

Studies of scaling relations were limited to GMC scales in nearby galaxies due to limitations in angular resolution and sensitivity of telescopes. The early studies in nearby galaxies targeted the Local Group: the Large Magellanic Cloud (Fukui et al. 2001), M33 (Wilson & Scoville 1992; Rosolowsky & Blitz 2004). Blitz & Rosolowsky (2006) presented detailed observations of GMCs in five nearby galaxies. Some of the external galaxies GMC studies have found no evidence for some scaling relations like the size - linewidth (Colombo et al. 2014; Maeda et al. 2020).

Recent improvements in instruments are revolutionizing the field as probing of small scale structures of GMCs in external galaxies is now possible. GMCs can now be resolved down to clump scales in the Local Group of galaxies: WLM (Rubio

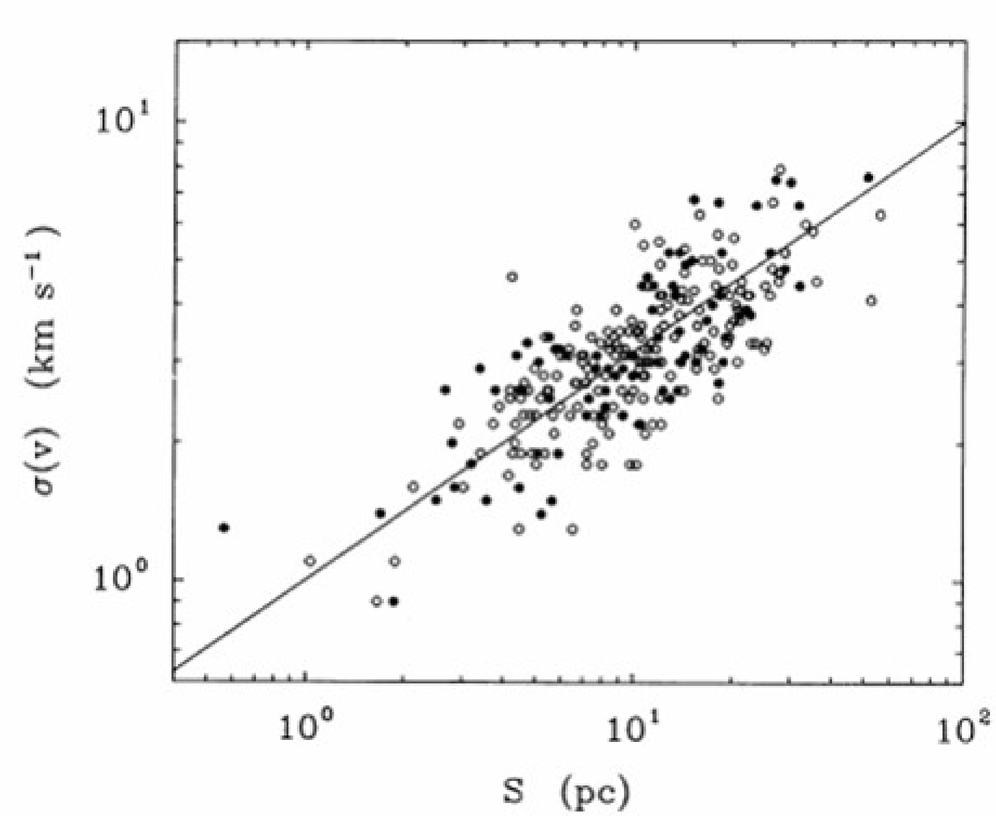

Figure 1.11: Molecular cloud velocity dispersion σ(v) as a function of size S for 273 clouds in the Milky Way Galaxy. The fitted line is $\sigma(\mathrm{v}) = \mathrm{S}^{0.5}$ kms^{-1}. Plot from Solomon et al. (1987)

et al. 2015), LMC (Pineda et al. 2009b; Wong et al. 2017, 2019) and NGC 6822 (Schruba et al. 2017). These studies have probed Larson's scaling relations and found that for large scale structures, the galactic relations hold but at smaller scales they do not as they show some scatter in linewidths. Wong et al. (2017, 2019) conclude that instrumental resolution limitations are causing this scatter at lower scales.

In Figures 1.12 and 1.13, we show plots from the studies of clump scaling relations done by Wong et al. (2019) in the LMC. The figures are based on two tracers, ^{12}CO and ^{13}CO, used to map six GMCs which are resolved down to clump scales enabling investigation of Larson's scaling relations. The sources in these studies are at different evolutionary stages but what is evident is that in both tracers there is a scatter at lower scales as earlier indicated. In most plots of the two figures, sources are comparable to the Galactic relation, though some are below, the Galactic scaling relation of Solomon et al. (1987) with an exception of the sources from 30 Dor which are above.

Faesi et al. (2018) note that determining true physical signatures in extragalactic studies is made difficult due to the wide range of source finding techniques and differing observational characteristics (angular, spectral, and sensitivity) used. This is also because of the nature of the variation on different scales as they are not simple spherical shaped clouds.

1.5 Mass Functions

Stars begin to form when clumps evolve and fragment into prestellar cores with sizes ranging from 0.01—0.1 pc and densities of $10^4 - 10^5$ cm^{-3} (Bergin & Tafalla 2007). Salpeter (1955) showed that the initial mass function (IMF) distribution of stars can be explained by a power-law dN/dM $\propto$ M$^{-\gamma}$ with γ= -1.35 as the power-law index. Other studies have applied this to cores and have confirmed the core mass function (CMF) power-law shape with an index γ falling between -1.1

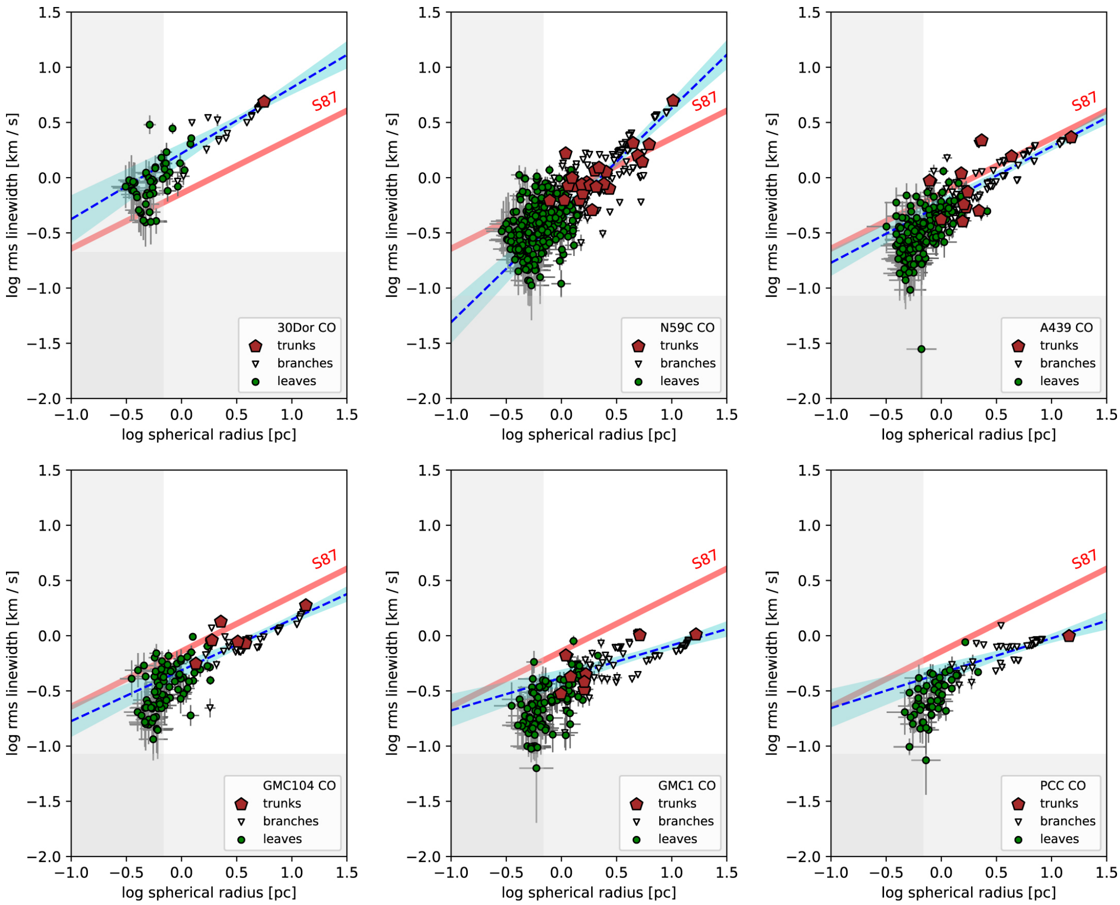

Figure 1.12: Size–line width relations for ^{12}CO structures in six molecular clouds in the LMC. Data for each cloud are shown in a separate panel. Dendrogram structure types (trunks, branches, and leaves) are distinguished by different plot symbols. Dendrogram techniques are discussed in Section 2.5. Power-law fits, with 3σ confidence intervals, are shown as blue dashed lines with associated shading. The Galactic relation of S87 (Solomon et al. 1987) is shown as a pink line. Gray shaded regions at low σ_v and R are poorly resolved and excluded from fitting. Plots from Wong et al. (2019).

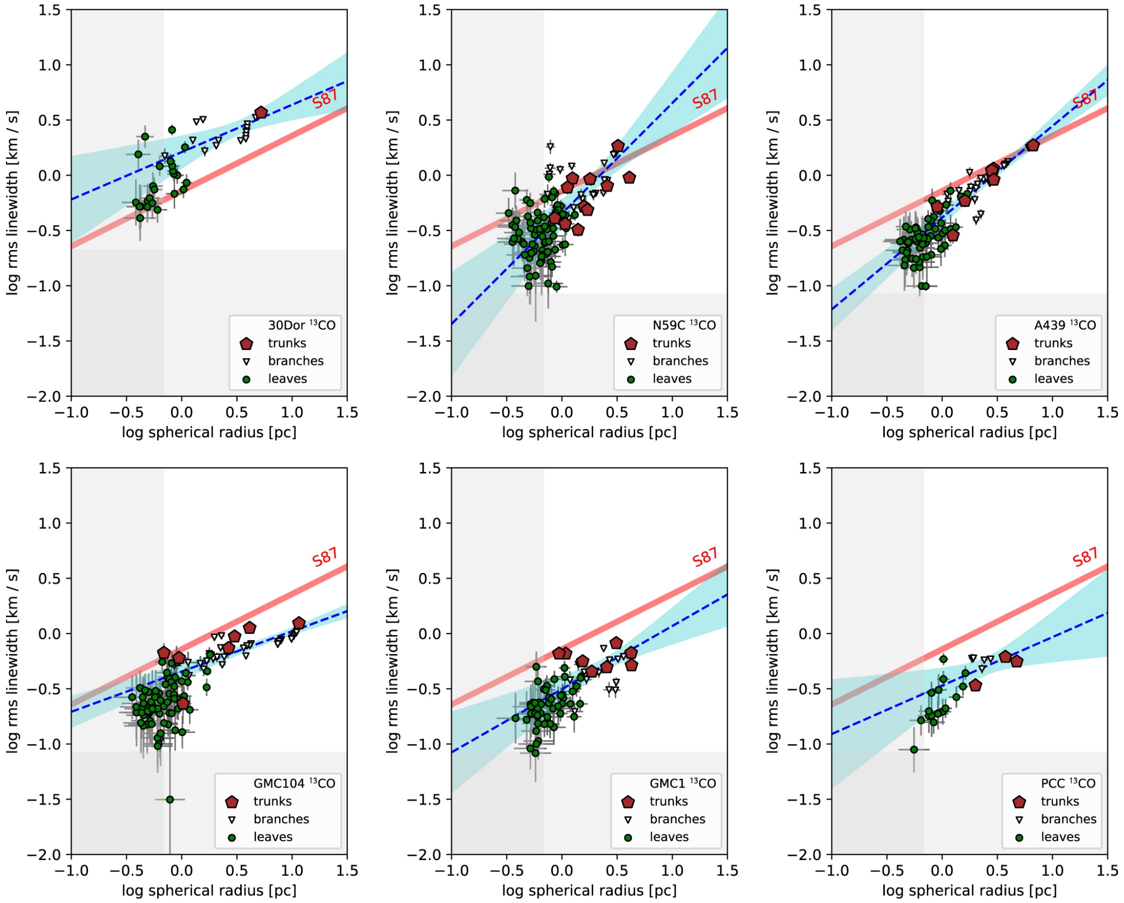

Figure 1.13: Size-linewidth relations for ^{13}CO structures in the six molecular clouds in the LMC. Plot symbols and overlays are the same as in Figure 1.12. Plots from Wong et al. (2019).

and -1.5 while showing a shallower slope and a turn-over for lower masses whose peak is at 0.6 $M_\odot$ (André et al. 2010, and references therein).

The shape of the mass function, mainly any distinct features like the upper or lower cutoffs, provides important information on the physical processes in the formation and evolution of objects (Mok et al. 2019) or they can be due to instrumental/sensitivity limitations.

The distribution by number of clouds of different masses is the cloud mass spectrum. This is related to the mass function of stars and clusters (Kennicutt & Evans 2012). The variation of the mass spectrum in the different regions may indicate differences in the mechanisms that influence cloud formation, evolution and destruction (Colombo et al. 2014). The cloud mass function is often expressed as a power-law, $\frac{\mathrm{dN}}{\mathrm{dM}} \propto \mathrm{M}^{\gamma}$, which after integration over mass, gives a cumulative mass function,

$$\mathrm{N}(\mathrm{M}' > \mathrm{M}) = \left[\left(\frac{\mathrm{M}}{\mathrm{M_o}} \right)^{\gamma+1} \right] \tag{1.27}$$

where γ is an index describing how mass is distributed among clouds (Colombo et al. 2014). The index $\gamma > -2$ means that majority of mass is in the massive large clouds, $\gamma = -2$ means that mass is equally distributed in the clouds and $\gamma < -2$ corresponds to the majority of mass residing in low mass clouds.

If the cloud mass function steepens at the high mass end it becomes a truncated power-law as reported in a number of studies (Williams & McKee 1997; Colombo et al. 2014).

$$\mathrm{N}(\mathrm{M}' > \mathrm{M}) = \mathrm{N_o} \left[\left(\frac{\mathrm{M}}{\mathrm{M_o}} \right)^{\gamma+1} - 1 \right] \tag{1.28}$$

The power-law is truncated due to an upper limit of $\mathrm{M_o}$, above which the mass function drops quickly to zero. This truncated power-law was proposed by Williams & McKee (1997).

Studies of cumulative mass distribution have been done in our Galaxy and others. Mass functions for GMCs in the Milky Way and other local group galaxies were constructed by Rosolowsky (2005) and showed different power-law slope values. In the inner Milky Way they found a truncated power-law slope of $\gamma = -1.5 \pm 0.1$ while for the outer Milky Way $\gamma = -2.1 \pm 0.2$. In the LMC and M33 they found truncated power-law slopes of $\gamma = -1.7 \pm 0.2$ and $\gamma = -2.9 \pm 0.4$ respectively, with a maximum mass of $10^{6.5}$ $M_{\odot}$. In M51 Colombo et al. (2014) used a truncated power-law to fit GMCs and studied variation of their properties in different regions within the galaxy and found a truncated power-law slope of $\gamma = -2.29 \pm 0.09$. Rice et al. (2016) fit both truncated and non-truncated power-law slopes in the studies of GMCs in the Milky Way with values of $\gamma = -1.6 \pm 0.1$ in the inner MW and $\gamma = -2.2 \pm 0.1$ in the outer MW respectively.

For regions distant from us like in external galaxies, observations can only resolve down to clump level currently. Hence, the studies are restricted to the clump mass function (ClMF). The study of ClMF in star forming regions shows that it can also be described by a power-law distribution (Kramer et al. 1998; Wong et al. 2008; Mok et al. 2021) as shown in Figure 1.14, from Mok et al. (2021). In these previous studies, it has been shown consistently that the ClMF slope has an index of $\gamma = -1.4$ to -2.0 which is shallower than the core mass function and the stellar initial mass function.

Molecular cloud structure suggests that ClMF can be used as an indicator of the evolutionary state of a molecular cloud (Ballesteros-Paredes et al. 2011) where a Gaussian distribution in the logarithm of the density (Log-normal distribution) is expected in the molecular clouds where star formation has not yet been triggered. Once star formation begins, gravity dominates denser structures leading to power-law distribution of masses in the upper mass range. Hence, the shape of the observed ClMF is considered as an indicator for the physical status of the molecular cloud (Pekruhl et al. 2013). Figure 1.14 show the clump mass function in the LMC by Mok et al. (2021) who find a ^{12}CO power-law index of $\gamma = -1.8 \pm 0.1$.

GMC mass functions have been studied before in M33 as earlier indicated with a power-law slope of -2.9 ± 0.4 (Rosolowsky 2005) based on the Engargiola et al. (2003) catalog. It is of interest in this thesis to investigate the clump mass function

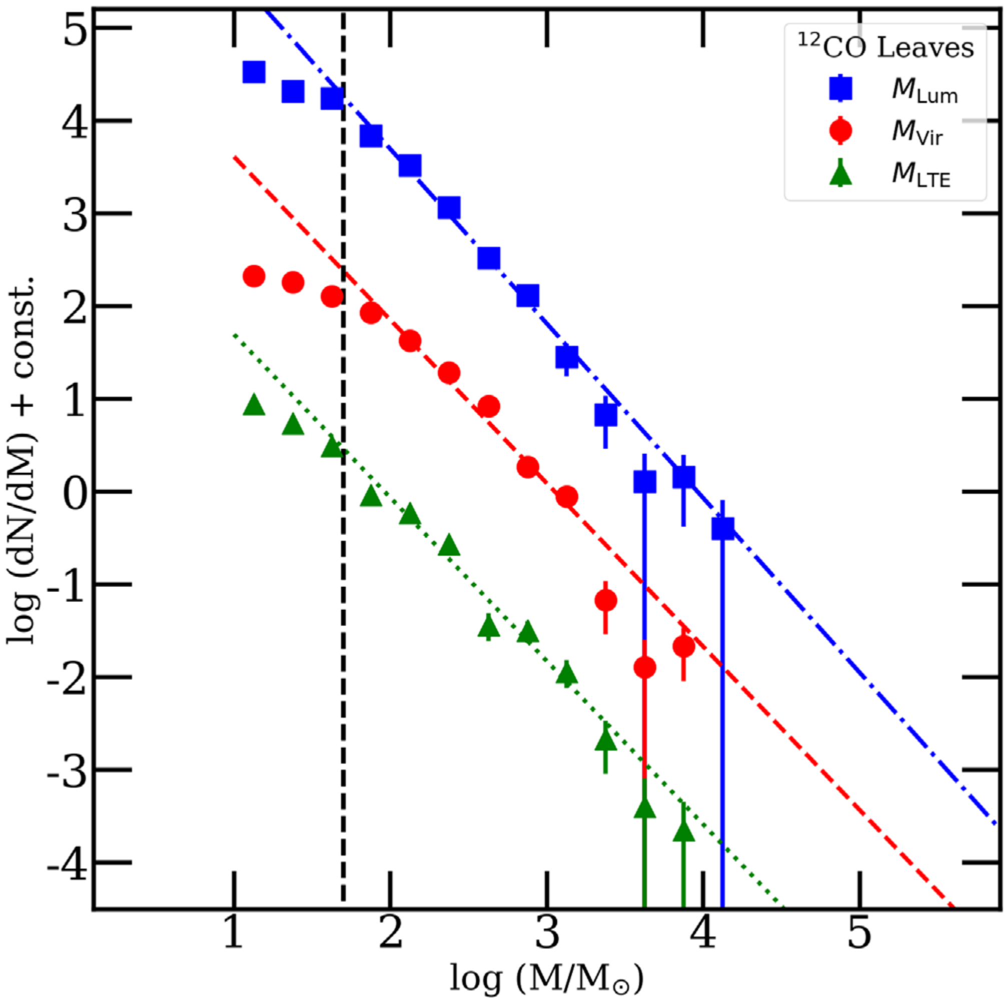

Figure 1.14: Mass functions of dendrogram leaves in the ^{12}CO catalog for the $\mathrm{M_{Lum}}$, $\mathrm{M_{LTE}}$, and $\mathrm{M_{vir}}$ mass estimates in equal logarithmic bins. Vertical normalizations have been shifted for clarity. Diagonal lines are maximum-likelihood fits of power laws to the unbinned masses with best-fit indices γ being 1.88 ± 0.1, 1.76 ± 0.2 and 1.76 ± 0.3 for $\mathrm{M_{Lum}}$, $\mathrm{M_{LTE}}$ and $\mathrm{M_{vir}}$ respectively. The vertical dashed line shows the adopted completeness limit at $\log(\mathrm{M/M_\odot}) = 1.75$ where only sources above this limit are fitted. Plot credit: Mok et al. (2021).

in M33.

1.6 Star Formation in M33

A number of high resolution CO observations have been done in external galaxies, including M33 (Engargiola et al. 2003; Rosolowsky et al. 2003, 2007; Gratier et al. 2012; Druard et al. 2014) and NGC 300 (Faesi et al. 2018). More recently, the Physics at High Angular resolution in Nearby GalaxieS (PHANGS) project has mapped CO(2-1) emission from multiple galaxies, resolving the molecular gas reservoir into individual GMCs across the full disc (Schinnerer et al. 2019; Rosolowsky et al. 2021). In the local group we only have three spiral galaxies excluding our own Milky Way. These three spiral galaxies are M31 (Andromeda), M33 (Triangulum) and the Large Magellanic Cloud (LMC). The most powerful interferometer array in the sub-millimeter is the ALMA array. M31, at 30° declination, is not visible to ALMA. This leaves us with M33 as the only spiral galaxy other than the Milky Way in the Local Group visible to the ALMA telescope.

M33 is a flocculent spiral galaxy. It is metal poor but gas rich and has a metallicity of $12 + \log(\frac{\mathrm{O}}{\mathrm{H}}) = 8.36 \pm 0.04$ (Rosolowsky & Simon 2008). It is at a distance of 840 kpc (Freedman et al. 1991; Kam et al. 2015) and an inclination of 56° (Kam et al. 2015), which allows us to resolve gas components with minimum contamination along the line of sight and to map their inner structure of GMCs. Earlier studies of GMCs in this galaxy include those by Wilson et al. (1997); Rosolowsky et al. (2007); Tosaki et al. (2007); Miura et al. (2010); Gratier et al. (2010, 2012); Tabatabaei et al. (2014); Druard et al. (2014); Williams et al. (2019); Tokuda et al. (2020); Muraoka et al. (2020); Kondo et al. (2021). Figure 1.15, shows a $^{12}\mathrm{CO}(2-1)$ integrated intensity map of M33 galaxy from Druard et al. (2014) with white contours indicating the regions that are HI-poor. The brightest regions in the image are the GMCs, which follow the floculent spiral arms.

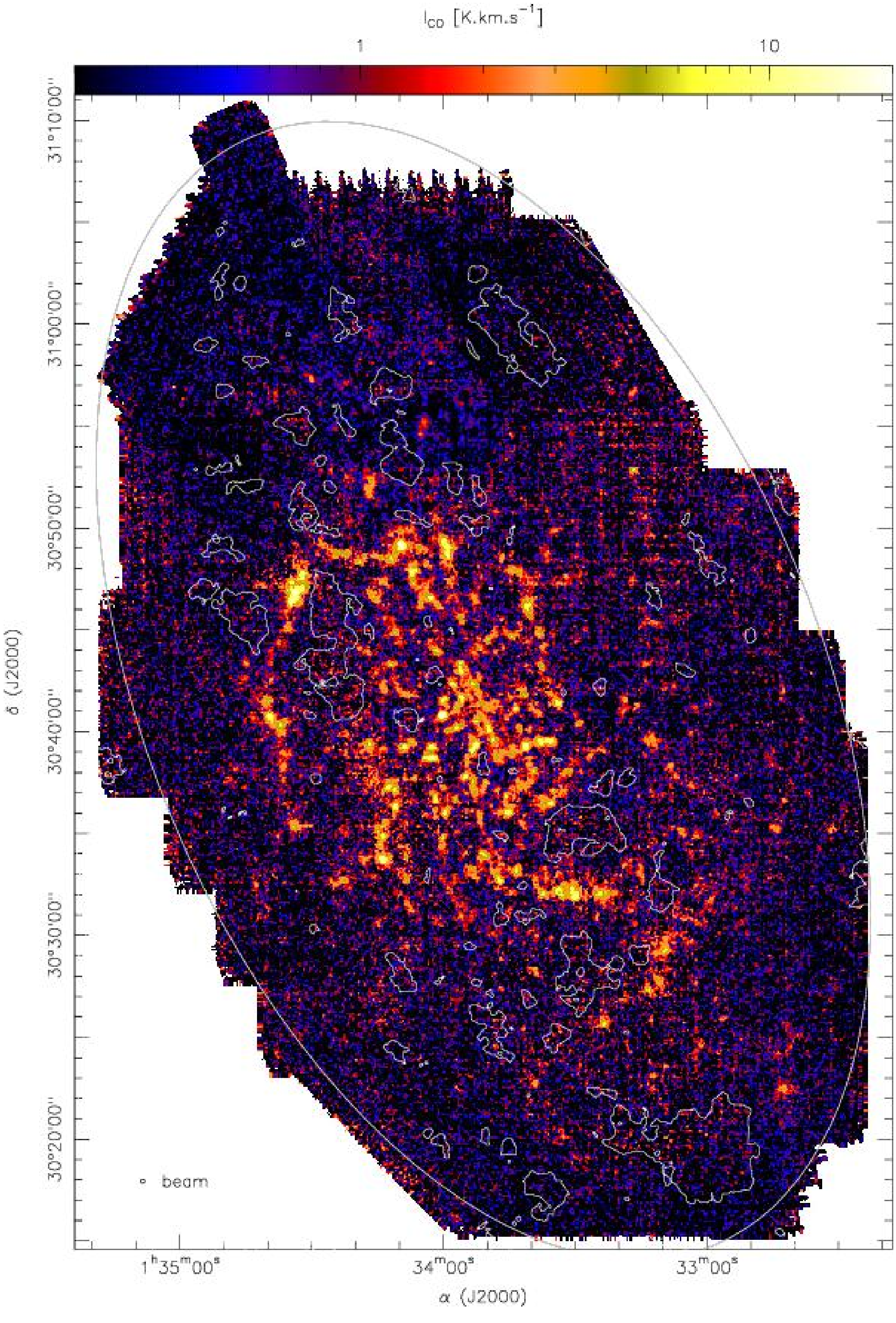

Figure 1.15: The Image of M33 $^{12}CO(2–1)$ integrated intensity map in Kkms^{-1} from Druard et al. (2014). The contours show HI-poor regions where the HI line does not reach 10 K. The beam size is shown in the lower left corner of the figure. The white ellipse represents a 7.2 kpc radius from the center.

1.6.1 Our Science Targets in M33

M33 just like other spiral galaxies harbours a lot of sites for star formation. In this work we focus on GMCs with specific targets being NGC 604, GMC 16 and GMC 8 presented in Figure 1.16 and previously identified by surveys of Rosolowsky et al. (2007), Onodera et al. (2010) and Miura et al. (2012). These targets are selected because of being at different evolutionary stages of star formation based on their associations with H II regions. These clouds harbour massive star formation with developed H II regions (NGC 604), in its intermediate stages with small H II regions (GMC 16), and in its initial stages (quiescent cloud - GMC 8) (Rosolowsky et al. 2007; Miura et al. 2012). Investigating clumpy structures of molecular clouds in an external galaxy is of great importance but also looking at these structures from clouds which are at different stages offers an opportunity to learn about their properties and the process involved on the journey from the cloud formation to the star formation stage. We discuss in brief each target below.

1.6.1.1 NGC 604

The giant H II region (GHR) NGC 604 is located in the northern arm of M33. This region has attracted interest because it has the highest star formation rate in the entire galaxy (Miura et al. 2012). The GHR has been observed in radio emission (Viallefond et al. 1992; Wilson & Scoville 1992; Churchwell & Goss 1999; Tosaki et al. 2007; Miura et al. 2010), optical emission (Drissen et al. 1993) and X-ray emission (Tüllmann et al. 2008). Based on these previous studies, the Hα nebula has a core-halo structure extending out to $200 - 400$ pc. It contains more than 200 O-type stars that are surrounded by photoionized filaments and shells (Relaño & Kennicutt 2009).

1.6.1.2 GMC 16

GMC 16 is located in the northern spiral arm of M33 galaxy. It is associated with several 24 μm sources and H II regions. It was identified previously in several

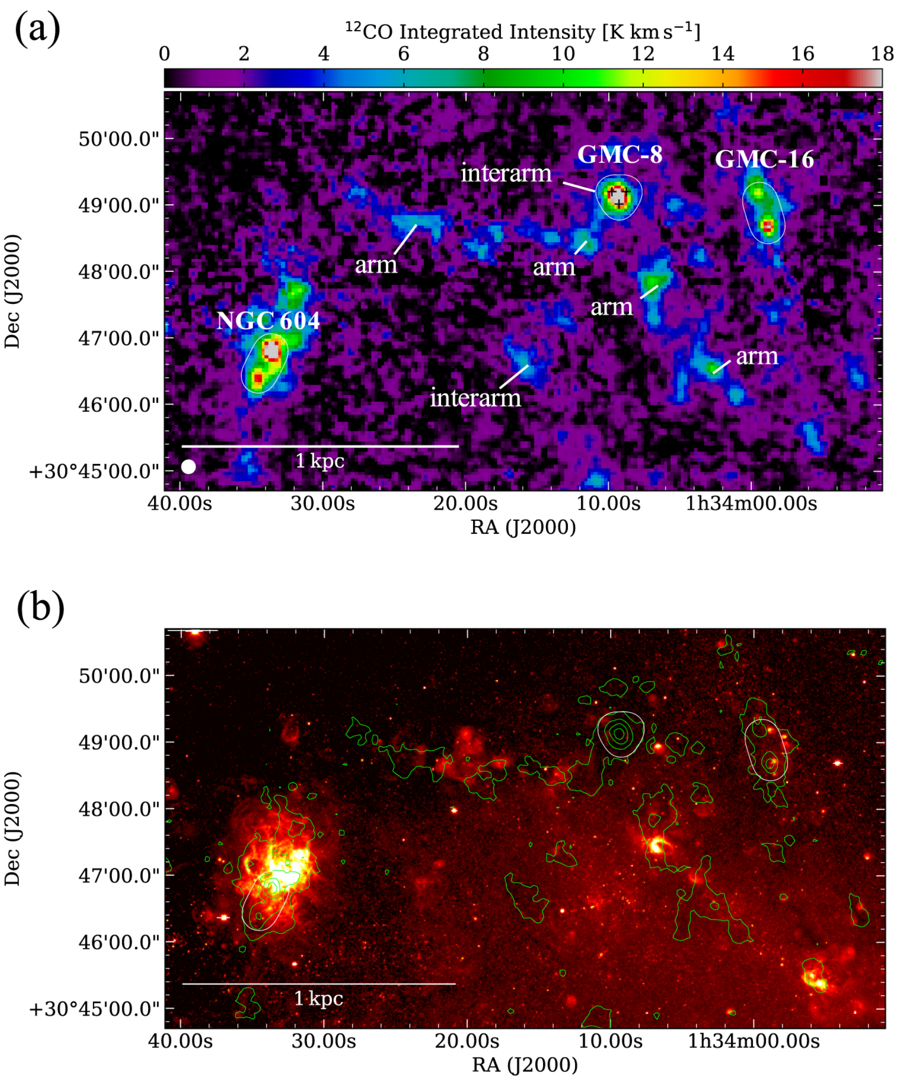

Figure 1.16: Distributions of molecular and ionized gas toward the northern part of M33. (a) The color-scale image shows the integrated intensity image of ^{12}CO$(2-1)$ with the IRAM 30 m telescope (Druard et al. 2014) shown in Figure 1.15. The labels of 'arm' and 'interarm' represent GMC locations with respect to the spiral arm categorized by Rosolowsky et al. (2007). The white lines show the field coverage of our ALMA studies (see Kondo et al. (2021) for GMC 8, Tokuda et al. (2020) for GMC 16 and Muraoka et al. (2020) for NGC 604). The white circle at the lower left corner represents the angular resolution of the CO image, $\sim 1''$. (b) The heat-map shows the H_α emission (Hoopes & Walterbos 2000). The green contours show the CO image, which is the same as panel (a). The lowest contour and subsequent steps are 3 Kkms^{-1} and 6 Kkms^{-1}, respectively. Image credit Kondo et al. (2021).

studies of GMCs done by Rosolowsky et al. (2007), Miura et al. (2012); Gratier et al. (2012). GMC 2 and GMC 16 were treated as one cloud in the work done by Tokuda et al. (2020), and we follow the same in our analysis of GMC 16 in this work. It represents the intermediate stage of molecular cloud evolution.

1.6.1.3 GMC 8

GMC 8 has been catalogued by the ^{12}CO(3-2) survey of Miura et al. (2012) and also identified as GMC number 245 from the studies of Gratier et al. (2012) and other earlier studies. It is located in the inter-arm region of the northern spiral arm in M33. It is one of the most massive GMCs in the galaxy and has little or no star formation activity. This makes it a very good target to study initial stages of star formation.

1.7 Project Aims

Investigating giant molecular clouds (GMCs) in external galaxies presents the opportunity to examine how the distribution, density structure and dynamical state of star forming clouds depends on the galactic environment. It also reveals how galactic-scale processes influence GMC formation and destruction. This research focuses on determining the physical properties and distribution of GMCs and clumps in nearby galaxies. It also looks at how different environments affect GMCs evolution. We use data from ALMA and other telescopes including both continuum and line emission data.

Our main goal is to resolve GMCs in external galaxies down to clump level. The clump properties obtained are compared to those obtained in our own Milky Way like those from the Hi-GAL survey presented in Elia et al. (2017) and shown in Figure 1.10. This will be done in order to understand whether the mechanisms and processes known in our galaxy are at play in external galaxies when we look at smaller scales than previously observed.

Previous cycles of ALMA observations included a number of nearby galaxies (Bolatto et al. 2013; Schruba et al. 2017), but analysis of these data sets is far from complete as some are still unpublished. This project analyzes data sets in the ALMA archive in order to study the physical properties and distribution of GMCs in the M33 by resolving them down to clump level. The mass, radius, linewidths and virial parameter of the GMCs and their clumps will be determined.

Summary of aims:

- Determine the physical properties and distributions of giant molecular clouds in unpublished ALMA observations for nearby galaxies of interest (M33).
- Resolve the GMCs down to clump level in M33 and compare to their equivalents in the Milky Way (e.g. Hi-Gal clumps).
- Compare the physical properties of GMCs and clumps in the nearby galaxies to those measured in M33 from this work.
- Determine whether environmental factors such as metallicity have any influence on these GMC processes and if so to what degree.

1.8 Thesis Structure

We present ALMA observations of ^{13}CO(J=1-0) and 104 GHz continuum emission from NGC 604, ^{12}CO(J=2-1), ^{13}CO(J=2-1), C^{18}O(J=2-1) and 1.3 mm continuum emission from NGC 604, GMC 16 and GMC 8 in M33. We look at whether the CO emission from these M33 GMCs obey Larson's relations in the same way as those in the Milky Way and other external galaxies. Using these new data, we measure the properties of the clouds and examine the state of the star formation in the regions, and we compare to results presented earlier by Wilson & Scoville (1992), Miura et al. (2010), Muraoka et al. (2012, 2020), and Tokuda et al. (2020). We present the interferometry and GMC decomposition algorithm in Chapter 2, the observations and data reduction process in Chapter 3, ALMA Band 3 results in

Chapter 4, ALMA Band 6 results in Chapter 5, and discussion is done in Chapter 6. We summarize our results in Chapter 7.

Chapter 2

Interferometry: Instrumentation and Software.

2.1 Radio Astronomy

Radio Astronomy is a field of astronomy that studies celestial objects at frequencies which range from 10 MHz (30 m) to 1.5 THz (0.2 mm) although these limits are not sharp (Wilson et al. 2013). It is done using large antennas which are called radio telescopes. A radio telescope can be operated as a single antenna or one of multiple antennas linked together using a technique known as interferometry. Using aperture synthesis, interferometry allows us to achieve very high angular resolution enabling astronomers to resolve celestial sources and study their finer details.

The angular resolution of a radio telescope aperture is found by

$$\theta = \mathrm{k}\,\frac{\lambda}{\mathrm{D}} \tag{2.1}$$

where θ is the angular resolution, D is the diameter of the telescope, λ is the wavelength of the radiation and the factor k depends on whether the antenna is uniformly illuminated (k of order unity) or non-uniformly illuminated (k greater than unity). The diameter D needs to be increased in order to improve angular resolution for a fixed wavelength. Materials limit the size of a single telescope that can be made. However, high resolution images can be achieved by combining the signals from separate pairs of telescopes whose separations define an equivalent aperture size D. This is known as aperture synthesis and requires the use of Fourier transforms to combine the measurements into a single image (Wilson et al. 2013).

In order for radiation to be observed or collected by telescopes on Earth, it must pass through the Earth's atmosphere. The ranges of frequencies in which the atmosphere is transparent to space are known as atmospheric windows. These windows or bands spans frequencies from 10 MHz (30 m) to 1.5 THz (0.2 mm). Figure 2.1 shows the atmospheric opacity as a function of wavelength. An opacity of 100% means the atmosphere completely blocks radiation in that wavelength range. When this occurs, telescopes must be stationed in space above the Earth's atmosphere.

The exact location of a telescope determines which part of the radio window it can operate in. Those telescopes operating in the millimeter regime need to be stationed at high and dry altitudes so that they are above the majority of the attenuating water vapour in the atmosphere. Examples include the IRAM 30-m telescope in Sierra Nevada, Spain and James Clerk Maxwell Telescope at the Mauna Kea Observatory in Hawai'i, United States of America. The two indicated are single dish telescopes. The most powerful millimeter telescope that operates as an array of dishes is the Atacama Large Millimeter/sub-millimeter Array (ALMA) in Atacama desert, Chile.

2.2 Interferometers

As earlier defined, interferometers play a crucial role in attaining high angular resolution observations. The most basic interferometer starts with two antennas, which we can call 2-antenna interferometer. Figure 2.2, shows a schematic diagram for a two-antenna interferometer whose antennas are separated by a distance b, called the baseline. Both antennas observe the same target s_o, located at an angle

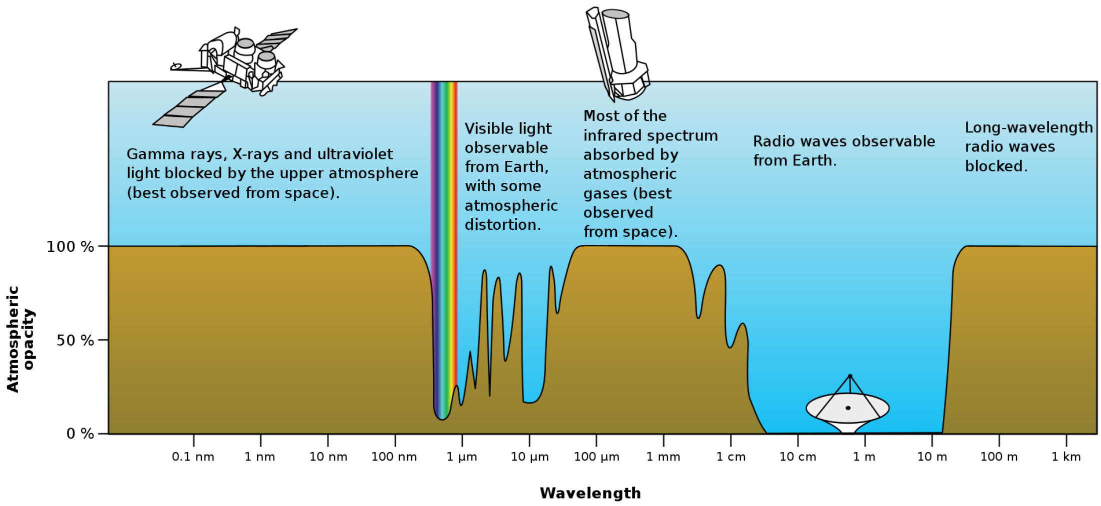

Figure 2.1: Image of the atmospheric opacity at different wavelengths in the electromagnetic spectrum. Picture credit: NASA.

θ from the zenith. The projected separation of the two antennas towards $\mathbf{s}_o$ from the perspective of the source is $\mathbf{u}$=$\mathbf{b}\cos\theta$. In this image, the wave front reaches antenna 2 before antenna 1 and travels an additional path length of $\mathbf{b.s}_o$=$\mathbf{b}$ $\sin\theta$. This simply means emission received by antenna 1 is delayed compared to that received by antenna 2 by a time equal to τ_g=$\mathbf{b.s}_o$/c. Moving slightly off-axis, a small angle from the axis can be described as α, and its 1-D sky position as $\mathrm{l} = \sin\alpha$. At angle α, an off-axis signal reaching antenna 1 will have to travel a slightly longer path than an off-axis signal reaching antenna 2, even with the geometrical delay introduced to compensate for an on-axis signal. This extra path length is $\mathrm{x} = \;\mathrm{u}\sin\alpha\; = \mathrm{ul}$.

Once these signals are received from individual antennas, they are sent to a correlator for processing. A correlator is the virtual focal plane of an interferometer array where all voltage-based signals from all individual antennas are processed. The correlator outputs the derived cross-correlation products from all independent antenna pairs and the auto-correlation functions from each antenna. Figure 2.3, shows the image for part of the ALMA correlators.

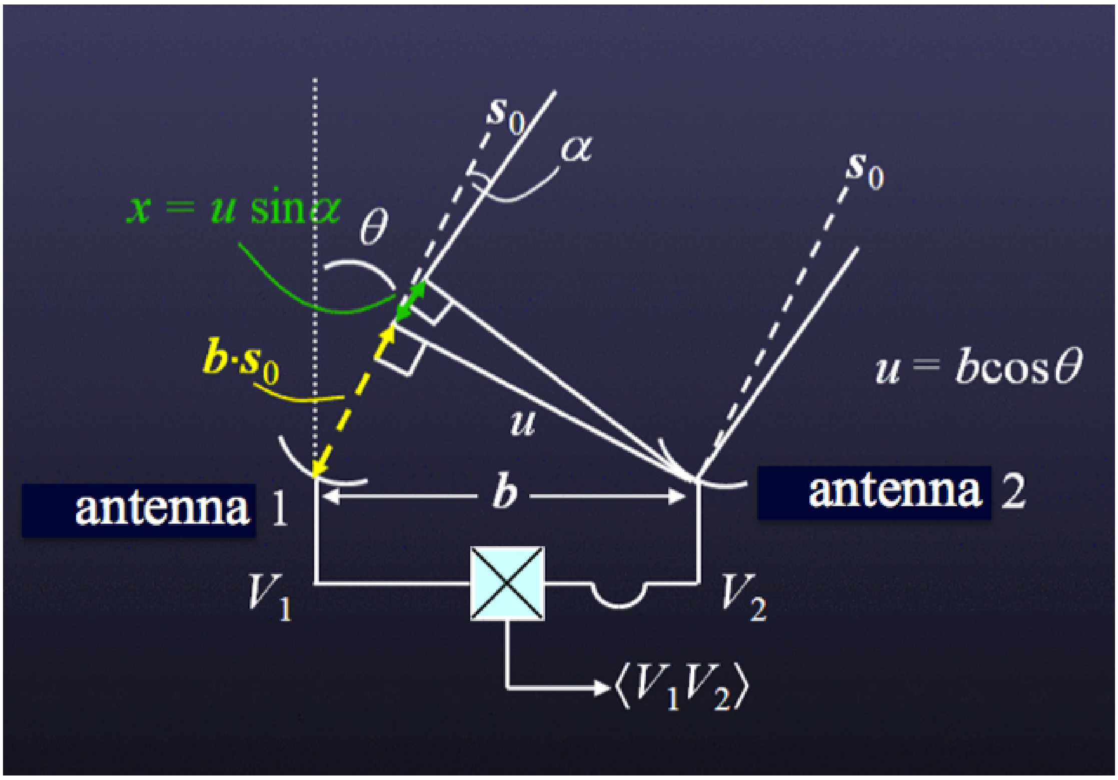

Figure 2.2: An ideal 1-D two-antenna interferometer consisting of two antennas, 1 and 2, separated by physical distance b which is called a baseline. The antennas are both pointed towards a sky location given by s_o, which is at an angle θ from the meridian. The projected distance between the two antennas in that direction is thus u = b $\cos\theta$. Moving slightly off-axis, a small angle from the axis can be described as α, and its 1-D sky position as $l = \sin\alpha$. The two antennas are connected to a correlator where the voltages detected from each are combined. The image is taken from Remijan et al. (2019).

Figure 2.3: The ALMA 64-input Correlator used by the 12–m array. This is housed in the ALMA Array Operations Site Technical Building. Credit: ALMA (ESO/NAOJ/NRAO), S. Argandoña.

2.3 Atacama Large Millimeter/sub-millimeter Array

ALMA is a radio interferometer operating in the millimeter and sub-millimeter regime of the electromagnetic spectrum. ALMA is located at an elevation of 5000 m on the Chajnantor plateau, within Chile's Atacama desert. This site's high elevation and low humidity are necessary to reduce noise as well as signal attenuation from the Earth's atmosphere.

ALMA's high precision antennas operate at wavelengths of 3.6 mm to 0.32 mm (31 - 1000 GHZ). Table 2.1 shows the range of wavelength for each ALMA receiver band. ALMA is designed to operate from Band 1 all the way up to Band 10 but currently only operates from Band 3 - Band 10 (which is around 100 - 1000 GHz) (Remijan et al. 2019). The 66 ALMA antennas are divided into different arrays as shown in Figure 2.4: the 12-m array comprises fifty movable 12-m antennas which can be moved to accommodate the changing array configuration. The Atacama Compact Array (ACA) or Morita array comprises twelve fixed position 7-m dishes (shown by the orange circle in Figure 2.4) and four fixed 12-m dishes provide total power measurements (shown by the blue circles in Figure 2.4). The 12-m dishes can be moved to either a closely packed configuration of about 150 m across or extended out to about 16 km across. Table 2.2 gives a summary of the angular resolution (θ_{res}) and the maximum recoverable scale (θ_{MRS}) based on the chosen antenna configuration and observing band for the 12-m array. The more extended array provides ALMA with high angular resolution to be able to see the finer details of the source.

To understand how the separation of a telescope array elements relates to the spatial scales to which it is sensitive, let us consider a single telescope. The maximum resolution attained by a single radio telescope is inversely proportional to the diameter of its light collecting dish surface. The instrument resolves source sizes that are proportional to the spatial resolution, but nothing smaller than

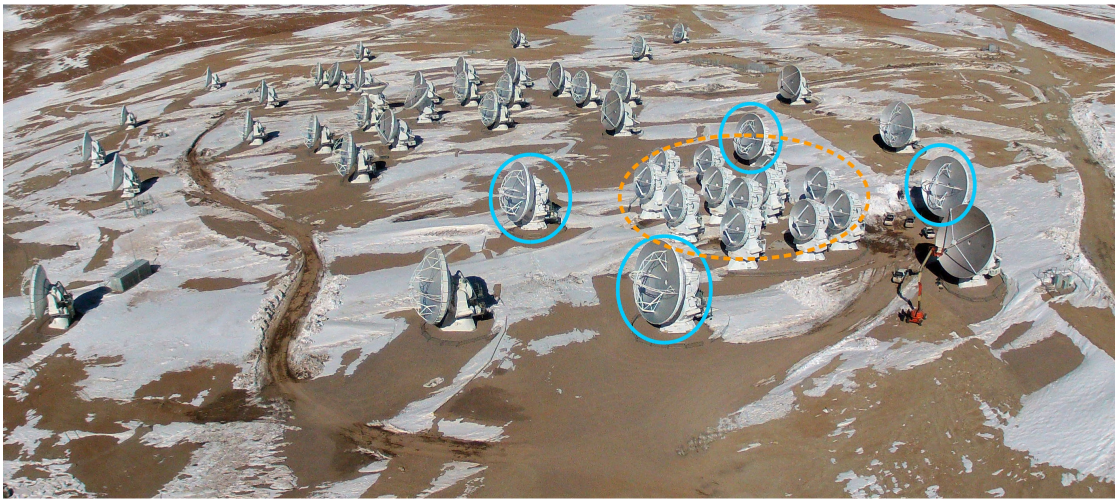

Figure 2.4: Image of ALMA array with the compact array indicated with the orange doted circle while the four 12 m dishes provide total power observations are indicated in blue circles. The rest of them are 12 m dishes through out the array. Image credit to Remijan et al. (2019).

the beam size. If we then connect two telescopes to make an interferometer, the maximum resolution attained is inversely proportional to the separation of the two telescopes. Now we are sensitive to source sizes which are proportional to the interferometer resolution, but not to source sizes which are larger or smaller than that. This is known as the 'missing flux' problem in radio astronomy. The radio interferometer measurement tells you about structure in the source which is equal to the resolution attained with its maximum antenna separation, but nothing about the source structure which would be measured by antenna separations smaller than the shortest antenna separation.

The emission ALMA detects includes thermal (modified blackbody) dust continuum emission, molecular spectral line emission and free-free continuum emission. The main science goals of ALMA are to: study objects in the solar system at millimeter wavelength, image the gas and dust in dense molecular clouds and protostellar discs, observe the formation of dust and molecules around evolved stellar objects, map dust and molecular gas in nearby galaxies and detect dust and spectral line emission from high red-shift galaxies (Blain 2010).

Table 2.1: Frequency and wavelength ranges of ALMA receiver Bands. As of now, only Bands 3-10 are operational (Remijan et al. 2019)

Band	Frequency Range (GHz)	Wavelength range (mm)
1	35 - 50	6.0 - 8.5
2	67 - 91	3.3 - 4.5
3	84 - 116	2.6 - 3.6
4	125 - 163	1.8 - 2.4
5	158 - 211	1.4 - 1.9
6	211 - 275	1.1 - 1.4
7	275 - 373	0.8 - 1.1
8	385 - 500	0.6 - 0.8
9	602 - 720	0.4 - 0.5
10	787 - 950	0.32 - 0.38

2.3.1 Observations with ALMA

ALMA observations are done by site astronomers following the details in the proposal made by the Principal Investigator (PI). ALMA observations are processed through several steps before they can be ready for science use. Observations are scheduled in such a way that measurements alternate between the target (source) and the calibrators. This is done in such a way that the telescope spends a much longer time on the target as compared to the calibrator.

Signals from each ALMA antenna are fed to its front end receiver system. It is designed to detect signals at ten different frequency bands, shown in Table 2.1. Within the front-end system, there is a cryostat which has a cyro-refrigerator that keeps the receivers at extremely low temperatures. Operating at low temperatures permits the use of superconducting materials which greatly improves the sensitivity of the receivers (Remijan et al. 2019). Within the front-end system, there are water vapour radiometers (WVR) which measure the atmospheric opacity that is caused by the presence of water vapour in the Earth's atmosphere.

Once the signals are received by the front-end receivers from each antenna, back-end systems convert them from analog to digital signals and send them to the correlator which is installed in the Array Operation Site technical building. A correlator correlates the signals which are further processed and makes them ready for science use. It acts as a multiplying and time averaging device for the incoming signals from antennas in the array.

The correlator measures a quantity called the complex visibility which is a Fourier transform of the intensity distribution on the sky. The complex visibility is given by,

$$\mathrm{V(u,v)} = \iint \mathrm{I(l,m)e^{2\pi i(ul+vm)}dldm}. \tag{2.2}$$

where V(u,v) is a complex number which is described by an amplitude and a phase, ϕ. The amplitude and phase encode the information about the source brightness and its location relative to the phase center respectively, at spatial frequencies of u and v. After the data is processed, it is sent to the operations support facility for quality checking and subsequently archived (Remijan et al. 2019).

2.3.2 Calibrating and Imaging ALMA Data

ALMA data processing is done in the Common Astronomy Software Application (CASA; McMullin et al. 2007). The final correlated products are output in `ASDM` format, which is the transportation form for ALMA data. The data must then be converted to a `measurement set` (MS) which is the format CASA accepts for processing. The translation is done by using a task in CASA called `import asdm`. Figure 2.5 shows the subsequent routine steps in calibrating and imaging ALMA data in CASA.

Once the data has been converted to MS format, it can now be inspected

Table 2.2: Angular resolutions (θ_{res}) and maximum recoverable scale (θ_{MRS}) for the ALMA 12–m array configurations, in each frequency band. All values are given in arcseconds (Remijan et al. 2019)

Configuration ↓	Band →	3	4	5	6	7	8	9	10
C43-1	θ_{res}	3.83	2.25	1.83	1.47	0.98	0.735	0.52	0.389
	θ_{MRS}	28.5	19.0	15.4	12.4	8.25	6.19	4.38	3.27
C43-2	θ_{res}	2.30	1.53	1.24	0.99	0.66	0.499	0.353	0.264
	θ_{MRS}	22.6	15.0	12.2	9.81	6.54	4.9	3.47	2.59
C43-3	θ_{res}	1.42	0.943	0.765	0.615	0.41	0.308	0.218	0.163
	θ_{MRS}	16.2	10.8	8.73	7.02	4.68	3.51	2.48	1.86
C43-4	θ_{res}	0.918	0.612	0.496	0.399	0.266	0.2	0.141	0.106
	θ_{MRS}	11.2	7.5	6.08	4.89	3.26	2.44	1.73	1.29
C43-5	θ_{res}	0.545	0.363	0.295	0.237	0.158	0.118	0.0838	0.0626
	θ_{MRS}	6.7	4.47	3.62	2.91	1.94	1.46	1.03	0.77
C43-6	θ_{res}	0.306	0.204	0.165	0.133	0.0887	0.0665	0.0471	0.0352
	θ_{MRS}	4.11	2.74	2.22	1.78	1.19	0.892	0.632	0.472
C43-7	θ_{res}	0.211	0.141	0.114	0.0917	0.0612	0.0459	0.0325	0.0243
	θ_{MRS}	2.58	1.72	1.4	1.12	0.749	0.562	0.398	0.297
C43-8	θ_{res}	0.096	0.064	0.0519	0.0417	0.0278	-	-	-
	θ_{MRS}	1.42	0.974	0.768	0.618	0.412	-	-	-
C43-9	θ_{res}	0.057	0.038	0.0308	0.0248	0.0165	-	-	-
	θ_{MRS}	0.814	0.543	0.44	0.354	0.236	-	-	-
C43-10	θ_{res}	0.042	0.028	0.0227	0.0183	0.0122	-	-	
	θ_{MRS}	0.496	0.331	0.268	0.216	0.144	-	-	-

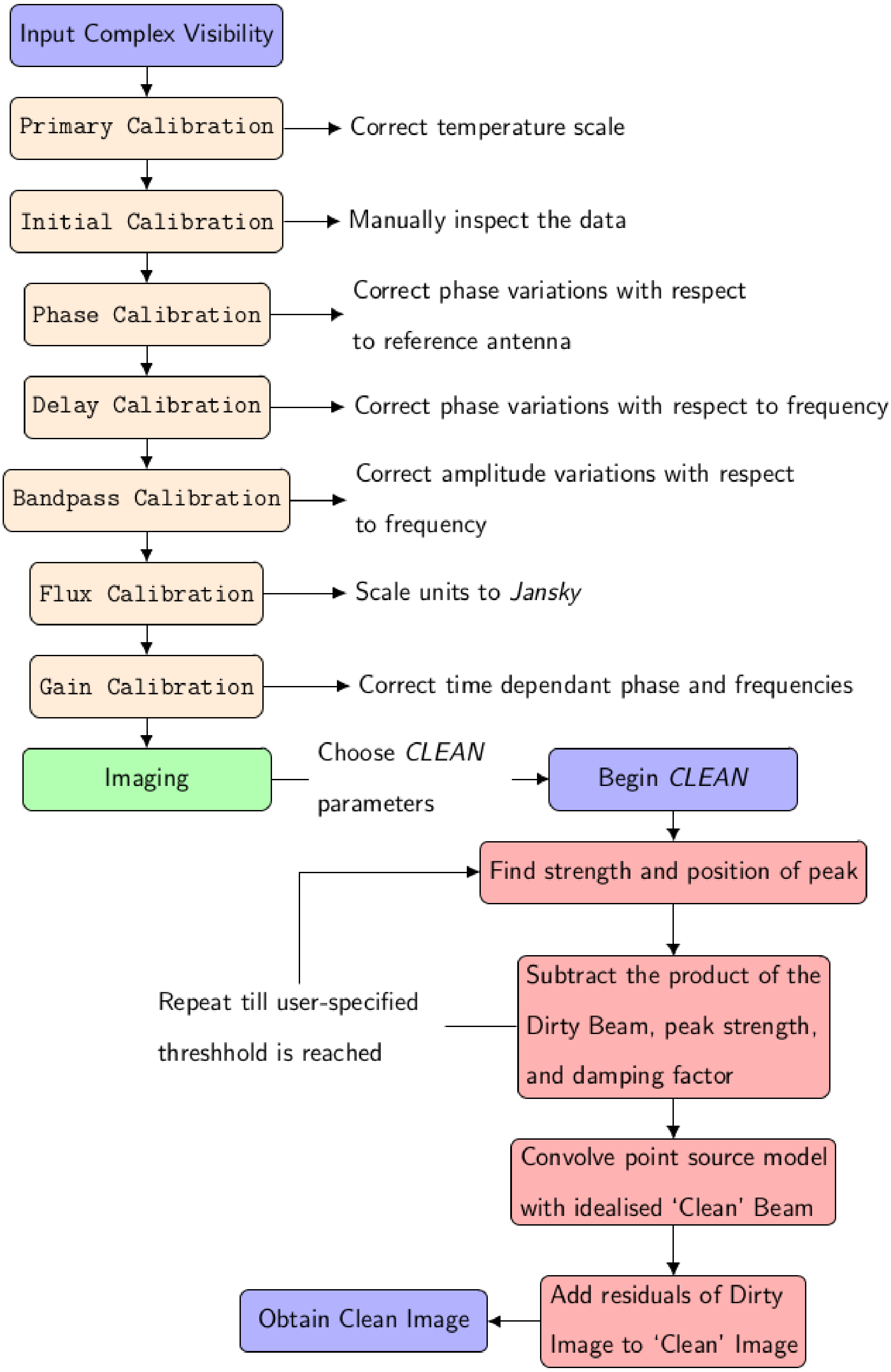

Figure 2.5: Steps required to calibrate and image ALMA data. Image credit to Remijan et al. (2019).

using tasks in CASA like `listobs` and `plotms`. By consulting the observing logs and inspecting diagnostic plots of visibilities, amplitude and phase vs. time or frequency, one identifies areas of data which are not useful because of technical problems or bad weather. Such data can be flagged out, although most of this would have been done at the observatory during the quality assurance procedure.

2.3.2.1 Calibration

Calibrating interferometer data is generally complicated and requires several iterations depending on the quality of the data and the strategy employed for observing calibration sources. For ALMA data, calibration begins with correcting the atmospheric phase measurements from each antenna based upon the water vapour radiometer (WVR) measurents, system temperature (T_{sys}) measurements and some instrumental errors. All this is done at the observatory and the user receives the necessary calibrated measurement set.

Before deconvolution of the Dirty Image can be performed, the data needs to be calibrated. The dirty image is the image reconstructed just from the measured visibilities prior to cleaning (see Section 2.3.2.3). There are several steps that needs to be performed which include:

Primary Calibration : The antennas measure the sky brightness distribution in units of kelvin. Nevertheless, this needs to be converted into units of flux density (Jy where 1 Jy = 10^{-26} Wm^{2}Hz^{-1}). In order to convert the data to an accurate temperature scale, the data first need to be calibrated in the front-end. The amplitude calibration process corrects for any differences in the atmospheric transmission between the target source and the amplitude calibrators (for which the sky brightness distribution is known). The calibrated data will later be scaled to units of Jy during the flux calibration step.

Initial Calibration : The data are then manually inspected and edited. This is done to remove any obvious bad data caused by individual antennas, baselines, or frequencies. The first time-steps from the data are removed to account for some initial pointing delays which is also known as quacking. Time-steps may also be removed if there were malfunctions in the correlator. The radio window is also allocated to services other than radio astronomy; this includes aeroplane communications, satellite downlink, and digital broadcasts. Interference from these sources may also affect the observations, reducing the sensitivity of the image. Therefore, individual antennas, time-steps, frequencies, and baselines may need to be removed. Data from an individual antenna may need to be removed if the antenna itself was faulty. A shadow caused by one antenna may affect the performance of another. Hence, data from the antenna located in a shadow would have to be removed for the time range during which its performance is affected. The removal of an individual antenna will reduce the sensitivity of the observation.

Phase Calibration: A reference antenna is chosen for each observation, for which the phase is set to zero at all times over a set of frequency channels. Phase calibration involves correcting any phase differences between each antenna and the reference antenna.

Delay Calibration: Interferometers operate over large bandwidths. The phase response of an antenna may not always be constant over the frequency range. Therefore, delay calibration needs to be done. As well as this, inaccuracies in the positions of each antenna will cause the phase to vary as a function of frequency. To correct for this, observations of an isolated, point source are needed to determine the phase slope with respect to frequency.

Bandpass Calibration: Each antenna will have a different amplitude and phase response to incoming radio signals. Therefore bandpass calibration is performed to correct any errors that occur in the amplitude with respect to the frequency. A bright point source will need to be observed close to the target on the sky in order to perform bandpass calibrations.

Flux Calibration: Flux calibration is needed to scale the measured amplitudes and convert the signals to conventional units such as Jy. A point source, with a known flux density, will need to be observed. The relative amplitudes from the interferometer can then be converted to absolute amplitudes.

Gain Calibration: The antenna response can be affected by the atmosphere as well as by the instruments themselves. Gain calibration is performed to correct any errors in the time dependent phase and frequencies. Observations of a source close to the target, with a known structure and moderate intensity, need to be made frequently. This will allow the determination of atmospheric phase changes to the line of sight of the target. Gain calibration targets include quasars and planets. The response of an antenna may also be affected by several factors such as opacity of the atmosphere and aperture illumination. Therefore, all of the calibration targets need to be located close to the target source.

Once the data has been calibrated, the deconvolution of the Dirty Beam from the Dirty Image, can be performed. This is done using the CLEAN algorithm in CASA. The routine summary used to calibrate ALMA data is shown in Figure 2.5.

2.3.2.2 Imaging

CASA provides the implementation of most common, new and experimental imaging algorithms for interferometric data as a toolkit which users can use to analyse the quality of their data. Currently the kit is accessed through the algorithm `clean` or `tclean` depending on the version of CASA one may be running. `Clean` was the first algorithm to be implemented in CASA and was superseded by `tclean` in the later versions. The principle of operation is the same but `tclean` has more features that can be used in imaging and visualization of the data as compared to `clean` algorithm. Throughout our studies we make use of `tclean`.

If multiple measurement sets are available for a particular target, it is necessary to concatenate the data together before imaging, which is done using the task `concat`. When it comes to imaging one or more spectral lines, it is useful to use a task `contsub` to subtract the continuum in the visibility data first. A typical approach to doing this is that, at first an image cube of the data without continuum subtraction is created. The cube is used to identify the channels with continuum emission, and those channels are then used to model the final subtraction with `contsub`. This produces a continuum-subtracted image.

2.3.2.3 Tclean

`Tclean` algorithm is an improved version of the `Clean` algorithm used to process radio astronomy observations. `Clean` was first introduced by Hogbom & Brouw (1974), and it is widely used even today. Visibility data is converted into images using a process known as cleaning.

The deconvolution of the dirty image requires interpolation or reconstruction of the missing values in the uv-plane. The algorithm assumes that the sky is made up of point sources, and first finds the brightest pixel in the dirty image and measures its brightness and position. Then, there is subtraction of the product of the dirty beam, peak brightness, and the damping factor γ from the dirty image at the peak position. The damping factor γ is taken to be ≤ 1 which is called *loop gain*. The steps are repeated until the remaining peaks go below what the user has specified to be the last level (level to stop deconvolution).

Visibility weighting must be applied to correct for the local density of sampling in the uv-plane. The imaging weights are calculated on the fly when processing the data. The weighting parameter is very important in the cleaning process of the data. Three standard options of weighting are used in radio interferometry namely Natural, uniform and Briggs weighting.

1. **Natural Weighting:** It uses the statistical weight of each data-point calculated from its inverse noise variance of the visibility. This results in images with more large scale structure.

2. **Uniform Weighting:** Regrids the uv-data so that the weights, as calculated via the natural method are equal. This results in images with small scale structures.

Table 2.3: The data weightings that can be applied when cleaning radio data using the `Clean` or `Tclean` algorithm

	Uniform	Briggs	Natural
Advantages	High resolution	Good resolution and sensitivity	High sensitivity
Limitations	High noise	May end up with unresolved and faint emission	Low resolution
Robust parameter	-2	0	2

3. **Briggs weighting:** this allows for adjusting between two extremes of natural and uniform weightings. The robust parameter can be used to adjust between these extremes, with 2 equivalent to natural and -2 equivalent to uniform. A robust value of 0.5 is commonly used in ALMA imaging as it gives a balance to the two extremes. Throughout this work we use Briggs weighting.

Table 2.3 shows the summary of the three weighting options. Cleaning is an iterative process in which the following is done in each iteration.

- An image is displayed
- Either the user or the program identifies sources and masks them.
- Using the identified sources, the algorithm models and removes them from the image producing a residual image that is used as an input for the next cycle.

Image analysis

The end part of the imaging step that can be done in CASA is statistical and morphological analysis of images. The user can fit geometrical shapes to images and spectral features and calculate common statistical parameters using tasks like `imfit`, `imstat`, `immoments` and `specfit`. CASA has a viewer which produces publication-ready colour plots of images and spectra. These image data can also be further processed or analysed using other programming languages like python.

2.4 ALMA Archive

The ALMA telescope has a science archive which keeps both proprietary and public data of all Principle Investigator (PI) observations. Once observations are made, there is a proprietary period of twelve months after which the data becomes available to the public (Stoehr et al. 2020).

Before the data is archived it passes through three stages of quality assurance. This is done in order to ensure that the products from the data which are put on the archive or sent to the PI are ready for science or will require minimum further processing (Stoehr et al. 2020; Remijan et al. 2019). The three steps of quality assurance (QA) which data passes through are QA0-2. We look at each step below.

2.4.1 The QA0

This is the first stage of quality assurance which is done during observation from the astronomer. The received signal from each antenna is inspected for any outliers along its path from the atmosphere all the way to its input into the correlator. The signals are checked and corrected for atmospheric effects, antenna, front-end, connectivity correlator and observation issues. These calibrations are done during observations by the observer and they are different from the earlier calibrations which are done on the visibility data by everyone who may need to use the data for science.

In terms of atmospheric effects, what are checked are weather parameters, phase fluctuations, and WVR outputs. Antenna delays, shadowing and antenna positions are of interest too. The front-end is monitored to check for the Bandpass stability, receiver temperatures, and phase variations. One other area of interest in QA0 is the connectivity where system temperature, unusual relative phase or amplitude variations between spectral windows and interference are monitored. Correlators are monitored to check for Bandpass shapes and account for delays while the observation data set is checked for calibrator fluxes, incomplete data set and incomplete mapping.

Once QA0 is complete, the data is classified as; pass, semi-pass, or fail. This is also done at QA1 and QA2 as well. A data set classified as fail cannot be used, is deemed to be of no scientific value, and is not made available to the PIs. Semi-pass data may have some scientific value but contains issues. Such data is made available to the PIs but the ALMA team do not create the final products for the archive. Those classified as pass do not have issues and advance to the next step of QA checks.

2.4.2 The QA1

The second QA step considers the actual performance of the array as a whole. Individual antenna performance in the array is tracked during observations. The performance of these elements can vary slowly (mostly longer than a week) which can affect the quality of the data. In such cases the specific antennas may be set to a non-integrated state which means that they are no longer used for science observations (Remijan et al. 2019). Once this is done, calibrations of both antenna and array are performed which involve the following;

- Array calibrations including baseline and antenna positions movements.
- Antenna calibrations including pointing models, beam patterns, and front-end delay measurements.
- Source calibrations including the monitoring of standard flux targets.

2.4.3 The QA2

This is the third stage of quality assurance for ALMA data. After this point, the data is ready to be calibrated and imaged. Various issues as well as parameters are checked to make sure they meet the standard and are fit to be sent to the PIs.

The flux scale quality is checked to ensure that the flux accuracy is above 5% for Bands 3,4 and 5, 10% for Bands 6,7 and 8, then 20% for Bands 9 and 10 (Stoehr et al. 2020).

Bandpass quality is checked as well as the noise root mean square (RMS) of the target to ensure they are comparable to those requested by the PI. A number of parameters are checked to ensure they meet the science goals of the project and assess the quality of the data. Such parameters are: spatial resolution, uv-coverage, time on target, and contamination of the target by bright sources within and outside the field of view.

After these steps, the data is archived and made available to the PIs. Once the proprietary period is over it becomes available to the public.

2.4.4 Archive Search

Data that has passed QA2 is deposited within the ALMA data archive [1]. Sources can be queried either by name, position on the sky specified in Right Ascension and Declination or Galactic coordinates. It can also be done by the PI's name and source names which are entered by the PI in the Observing Tool (OT). Figure 2.6 shows the interface of the ALMA archive query. One can use a number of constraints such as angular resolution, ALMA receiver band number, observation date and many more in order to search for specific projects on the archive.

Once the project(s) has been selected, the files are downloaded through a download script or direct download per file.

We have used archival data in these studies which is fully described in Chapter 3. The process of archival search was conducted in which the data we use in this research was acquired. The steps described here for calibration and imaging have been used to process data that is presented in Chapter 3.

[1] https://almascience.nrao.edu/aq

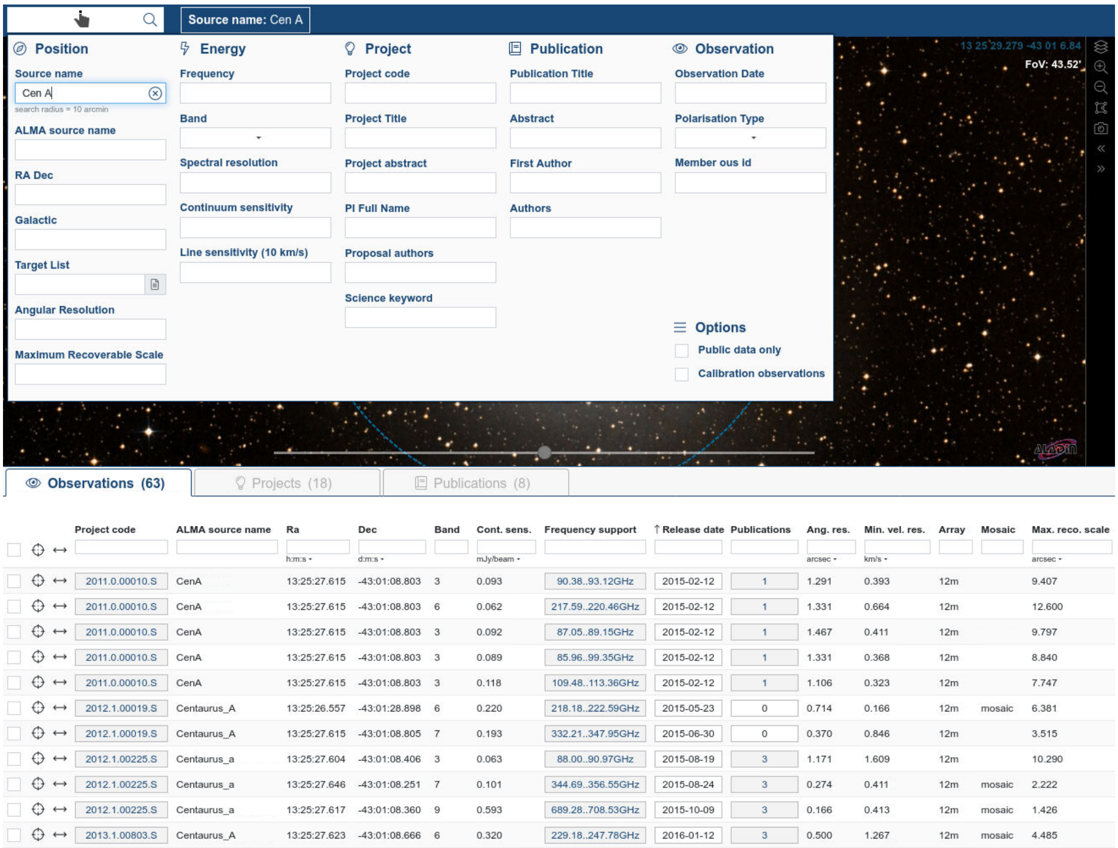

Figure 2.6: The archive query interface.

2.5 GMCs and Clumps Identification

GMCs have a hierarchy of nested structures which consist of GMC complexes, GMCs, filaments, clumps and and finally cores which are sites of star formation. Due to limitations of angular resolution extra-galactic studies have been limited to GMC complexes, GMCs and some giant filaments. Now current improvements in observational capabilities such as ALMA, are resolving them down to clump scales. This is a new frontier in extragalactic GMC studies. In this work, we identify clumps and measure their properties. We are unable to study cores due to limited resolution of ALMA to resolve the interior structures of the clumps.

Different techniques are applied to identify and analyze GMCs and clumps. They are generally identified by contouring images above a certain column density or flux levels. Clouds are defined as sets of connected pixels (either 2D or 3D) above a certain threshold level. These operations were done by eye in the earlier studies (Dame et al. 1986). However, the use of position-position velocity (PPV) data cubes complicated the recognition of GMCs by eye so automated algorithms have been developed. These are able to handle the third dimension, as well as large data sets with different levels of blending between structures. These algorithms are based either on iteratively fitting and subtracting a model to the molecular emission or on the "friends-of-friends" paradigm that connects pixels according to their nearest neighbours and values, without assuming a particular shape for the objects to decompose. Example of the first method include `GAUSSCLUMPS` (Stutzki & Guesten 1990) or `Getsources` (Men'shchikov et al. 2012). Examples of the second method include `ClumpFind` (Williams et al. 1994) or `CPROPS` (Rosolowsky & Leroy 2006; Rosolowsky et al. 2021). Gravity-based alternatives have also been proposed like `astrodendro` (Rosolowsky et al. 2008) and `G-Virial` (Li et al. 2015). These later approaches all assign individual pixels in a data cube to belong to single objects and GMC identification is thus a segmentation problem.

2.5.1 Dendrograms

Depending on the complexity of the molecular environment, an algorithm provides different results (Hughes et al. 2013) in such a way that low resolution causes the blending of emission from unrelated clouds (Colombo et al. 2014) and high resolution makes segmentation algorithms identify cloud sub-structures as individual clouds. As we have noted before that molecular clouds are hierarchical in structure, it is important to have analytical techniques which can characterize the hierarchical structures in molecular clouds and relate it to the processes of star formation. Dendrograms have been used to graphically represent hierarchical structure of nested isosurface contours in 2D maps and cubes. Dendrograms are like a tree in nature with trunks, branches and leaves. The structure tree or dendrogram in astronomy represents the hierarchy of structures of molecular gas and dust. Several implementations of dendrograms are available which includes: `astrodendro` (Rosolowsky et al. 2008), Conservative Source Algorithm `CSAR` (Kirk et al. 2013) and `SCIMES` (Colombo et al. 2015). These try to address the segmentation problem on high resolution data.

As part of this project, we use `astrodendro` [2] algorithm which is open source to identify GMCs and clumps in our data. The reason this algorithm was chosen is because of its capability to identify clouds without over dividing the molecular emission that would lead to invalid identification. This dendrogram implementation package requires setting three input parameters: the signal S_{min} below which any value is not considered in the dendrogram construction, the interval Δ_S indicating how significant a leaf must be to be considered independent and A_{min}, the minimum number of pixels needed for a leaf to be independent structure. The final clouds are branches that contain leaves.

`Astrodendro` operates for both 2D and 3D maps (data). Beginning with the brightest pixel in the data, the first structure is created from the pixel. Then it moves to the pixel with the next largest value, and each time a decision of whether

[2] http://www.dendrograms.org/

to join the pixel to the already existing structure or start making a new one is made. Only if the value of the pixel is greater than the immediate neighbours and there is a local maximum will a new structure be created (Rosolowsky et al. 2008; Colombo et al. 2015). Shown in Figure 2.7 is a schematic of a 1-dimensional dendrogram tree construction.

Data sets contain some level of noise and it is imperative to make sure that this is not part of the tree construction. This is achieved by setting up a parameter called $S_{\rm min}$. By default this parameter is set to negative infinity in the algorithm which allows all pixels to be part of the tree construction. Setting the minimum value to 3 times noise level allows the tree to have true physical structures only. The minimum value is represented with a horizontal purple line in the Figure 2.7. Another parameter that is of great importance in dendrogram tree construction is the $\Delta_{\rm S}$ which gives the minimum value for the structure to separate or merge with another and in this first example the minimum value is set at $\Delta_{\rm S} = 0.01$ Jy. Moving down, the flux the tree structure looks red to signify that the tree is not part of the structure yet, but once the value exceeds the $\Delta_{\rm S}$, the structure turns green to show that it is now part of the tree.

In Figure 2.8 the experiment is repeated, but this time with a larger minimum value for structures to be retained ($\Delta_{\rm S} = 0.025$). Once it reaches the point where the second peak would have been merged in the top-left panel, we can see that it is not high enough above the merging point to be considered an independent structure, which is indicated in red. In this case the pixels are then simply added to the first structure, rather than creating a branch as shown in top-right panel. We see that the final tree looks a little different to the original one in the bottom panel, because the second largest peak was deemed insignificant.

Figure 2.9 below shows a PPV data cube for the Orion Monoceros complex in ^{12}CO(1-0) by (Wilson et al. 2005) obtained using Harvard-Smithsonian 1.2-m millimetre-wave telescope. The PPV data cube in Figure 2.9, is used in their `astrodendro` algorithm which identifies the clouds as shown in red colour

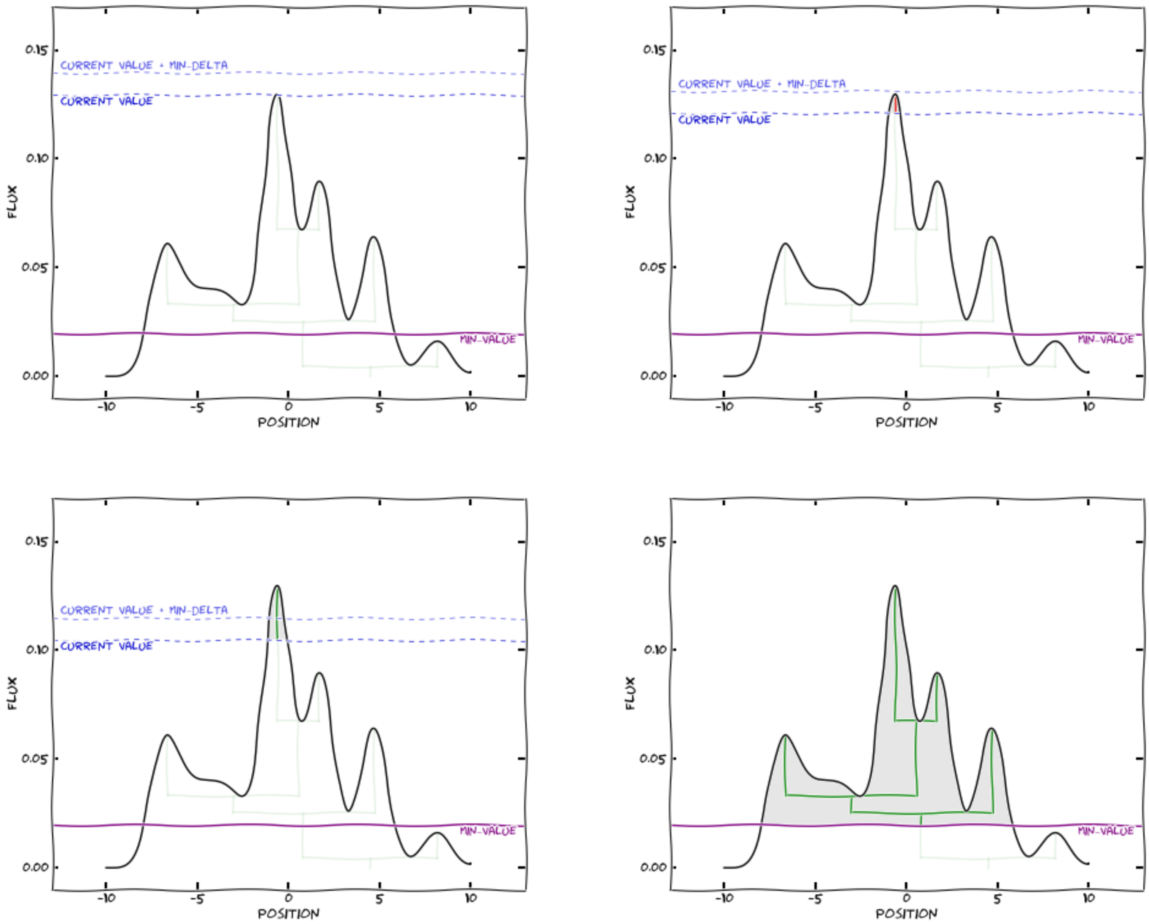

Figure 2.7: A schematic of 1-Dimensional dendrogram tree construction. The purple horizontal line demarcates the minimum value below which the tree cannot be constructed. The blue lines shows the minimum significance for the structure to remain independent. The images are taken from `astrodendro`

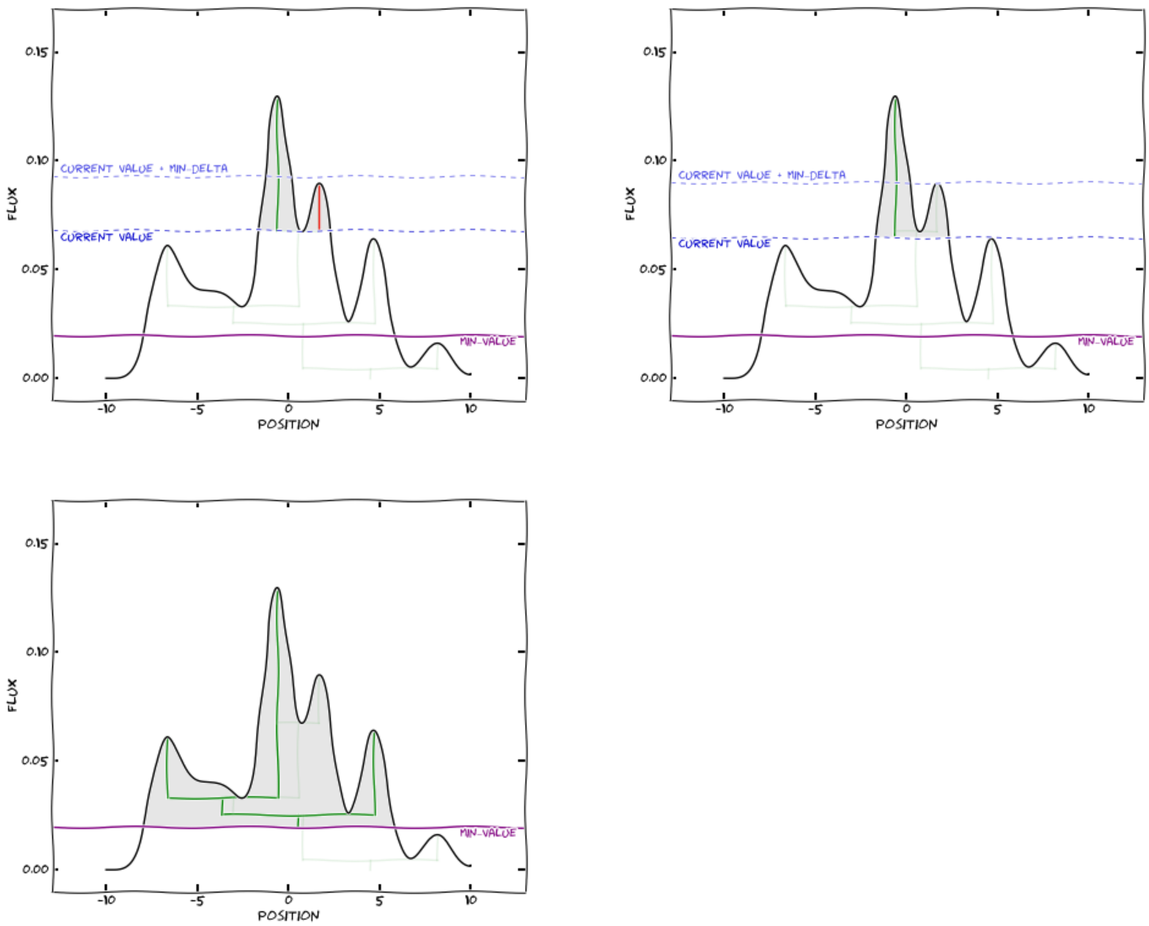

Figure 2.8: Continuation of a schematic for 1-Dimensional dendrogram tree construction from Figure 2.7. The experiment is repeated, but this time, with a larger minimum height for structures to be retained ($\Delta_S = 0.025$ Jy). Once we reach the point where the second peak would have been merged in top-left panel, we see that it is not high enough above the merging point to be considered as independent structure and the pixels are then simply added to the first structure, rather than creating a branch in the top-right panel. The bottom panel shows the final tree which looks a little different to the original one, because the second largest peak was deemed insignificant. The images are taken from astrodendro website.

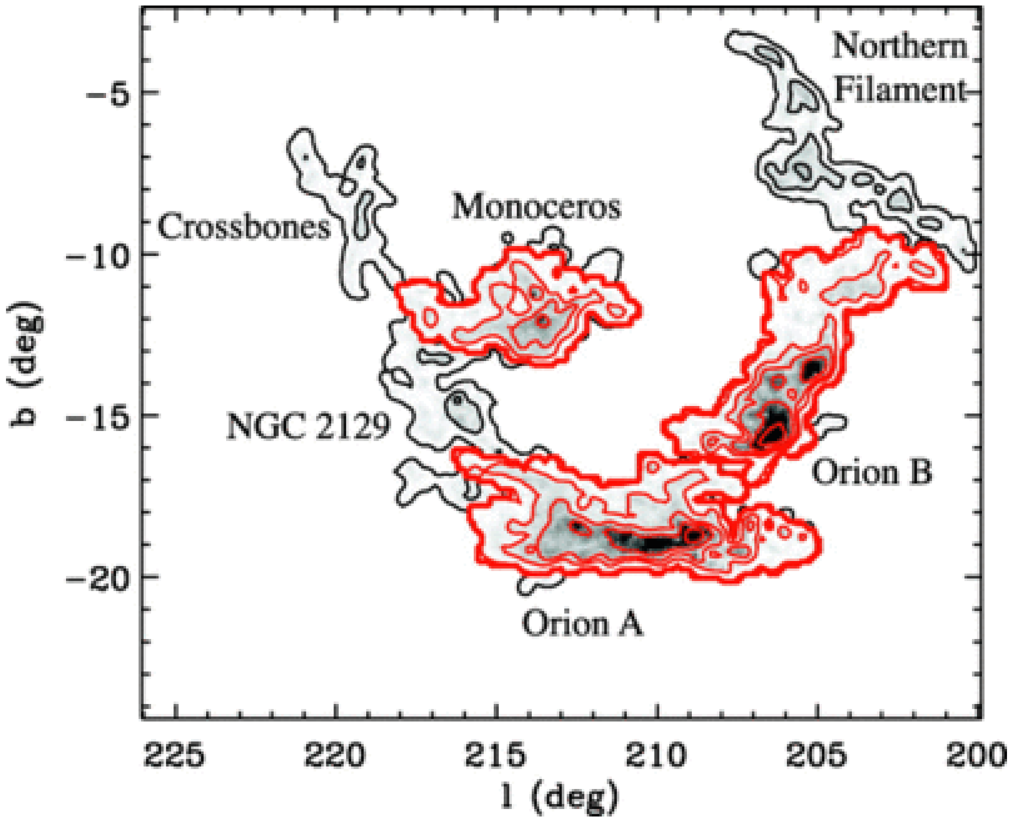

Figure 2.9: Map of emission for the Orion-Monoceros region contained within a T_{mb}=0.4 K contour. The three constituent GMCs in the complex have been identified using the dendrogram analysis, and their boundaries are indicated in red. The regions are labeled according to their designations in Wilson et al. (2005). Image taken from Rosolowsky et al. (2008)

(Rosolowsky et al. 2008).

2.5.2 Dendrogram statistics

Dendrogram statistics once computed can be accessed in two different ways which are on a structure-by-structure basis or as a flat catalog. For both 2-dimensional (2-D) position-position (PP) and 3-dimension (3-D) position-position-velocity (PPV) observational data, `astrodendro` can produce a catalogue of basic properties for all structures identified. Metadata must be specified, as it is needed by the statistical routines, which depends on what statistics are required and on the units of the data (Rosolowsky & Leroy 2006; Rosolowsky et al. 2008) and the `astrodendro` website.

The basic properties of the identified structures are also determined by `astrodendro` using the bijection approach. Bijection maps PPV space to physical space in a one-to-one where one pixel in a data cube corresponds to single volume element in a cloud (Rosolowsky et al. 2008). In the bijection paradigm, the total flux of a structure is nothing but the sum of the fluxes of all pixels within that structure with no constant background flux being removed. These properties include spatial and velocity centroids $(\bar{\mathrm{x}}, \bar{\mathrm{y}}, \bar{\mathrm{v}})$, the integrated flux F, the rms line-width $\Delta\mathrm{v}$ (defined as the intensity-weighted second moment of the structure along the velocity axis), the position angle of the major axis ϕ, and the scaling terms along the major and minor axes, σ_{maj} and σ_{min}.

Dendrograms have been extensively used in both galactic (Rice et al. 2016; Mazumdar et al. 2021, and references therein) and extragalactic (Kirk et al. 2015; Williams et al. 2019; Wong et al. 2017, 2019) studies for identification of GMCs, filaments, clumps up to cores.

In conclusion, we use `astrodendro` to identify molecular clouds and clumps throughout this work. In Chapter 4 and Chapter 5 we present the computed dendrograms and the identified molecular clouds and clumps respectively.

Chapter 3

Observations and Data Reduction

3.1 Introduction

ALMA observations of giant molecular clouds have hierarchical internal structures both in our own Galaxy and in external galaxies (Schruba et al. 2017; Wong et al. 2017, 2019; Schinnerer et al. 2019; Tokuda et al. 2020; Maeda et al. 2020; Muraoka et al. 2020, and the references therein). Resolving these structures, gives us an opportunity to understand the properties of star forming clumps. Studies that have resolved GMCs to clump level have been done extensively in our galaxy (Elia et al. 2017, and references therein) and in nearby galaxies (Schruba et al. 2017; Wong et al. 2017, 2019). Not much has been done at the distance of M33, 840 kpc, in resolving GMCs down to clump level. We have an opportunity to investigate these sites of star formation by using ALMA's high angular resolution.

Our target from the outset was the Local Group of galaxies where ALMA can resolve clumps on scales similar to those done in the Milky Way. The M33 galaxy, due to the fact that it is almost face-on to our line of sight, was picked as a preferred candidate for the studies. It is also the third spiral galaxy in the Local Group after Andromeda (which is not observable with ALMA) and our own Milky Way. It has low metallicities compared to the Milky Way as shown in Chapter 1, which provides a different environment for GMC structures.

A search was conducted on the ALMA archive for GMC observations towards M33 that had been carried out since its coming online in Cycle 0. High angular resolution was of great importance during our search. A number of projects were found, some surveys and some individual programs. We chose the two programs, Cycle 2 (project code 2013.1.00639.S; PI: T. Tosaki) and Cycle 5 (project code 2017.1.00461.S; PI: K. Muraoka) which looked at the spatial distribution of the physical and chemical properties of dense clumps at different evolutionary stages in super giant HII region NGC604 revealing the roles of filamentary clouds in this GMC. These became the best projects for our study as we are interested in looking at GMCs internal structures and their properties in different environments and also at different evolutionary stages. The two projects traced three GMCs in M33 at three different evolutionary stages, namely, NGC 604, GMC 16 and GMC 8.

Figure 3.1, shows BVH_α image false-colour (top left) and the CO image (top-right) of M33 presented by Tosaki et al. (2011). The bottom image is a zoom-in (indicated by the yellow box on the top images) from IRAM ^{12}CO(2-1) image Gratier et al. (2012); Druard et al. (2014). The white boxes indicate the positions of our three target GMCs. Inside the boxes are black circles indicating the actual field of view of ALMA observations. Some cloud properties of masses, velocity and star formation rates (SFR) based on IRAM 30 m ^{12}CO(2-1) observations are indicated on the zoomed integrated map.

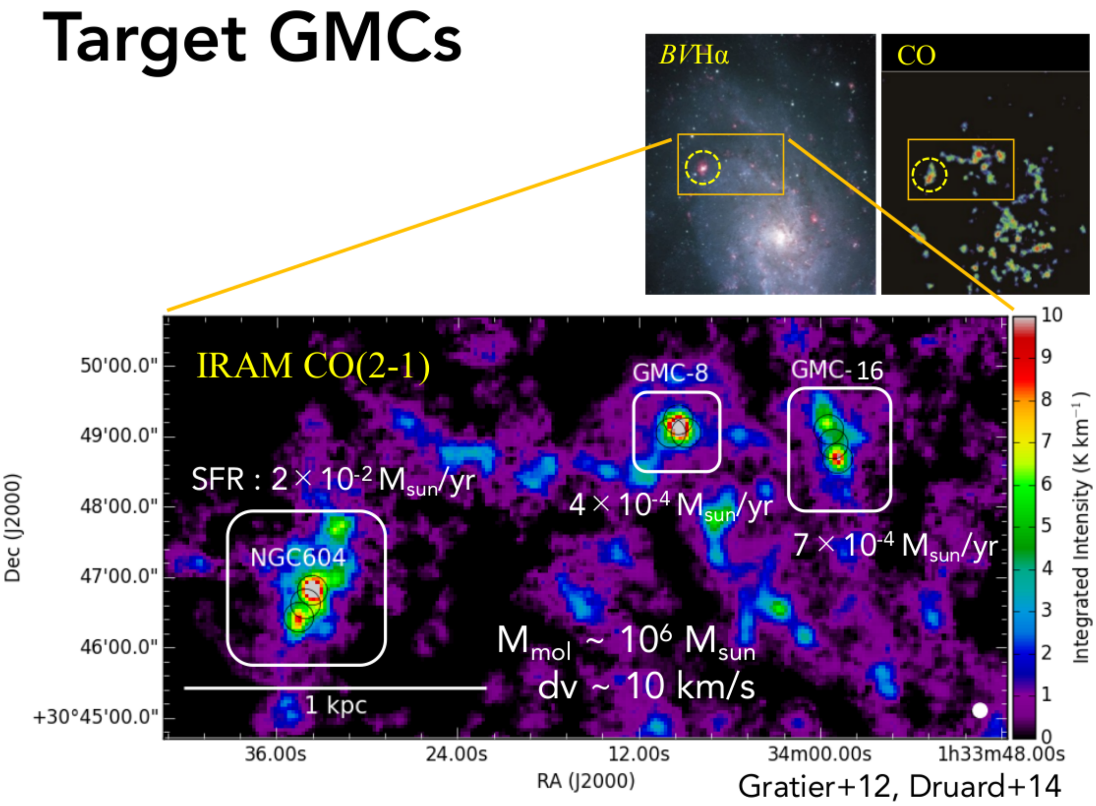

Figure 3.1: The top left panel: the BVH$_\alpha$ image and top right panel: CO image presented by Tosaki et al. (2011). The bottom image is a zoomed in image indicated by the yellow box from top images, which is a map from IRAM ^{12}CO(2-1) image presented both by Gratier et al. (2012) and Druard et al. (2014). The white boxes indicate the positions of our three target GMCs. Image Credit: Atsushi NISHIMURA from Osaka Prefecture University.

3.2 Data

We will consider the lower resolution Band 3 data of NGC 604 separately from the higher resolution data of NGC 604, GMC 16 and GMC 8 from Band 6.

3.2.1 ALMA Band 3 Data

We use archival ALMA Band 3 observations of the ^{13}CO(J=1-0) (110.27 GHz) line emission from NGC 604 obtained during Cycle 2 (project code 2013.1.00639.S; PI: T. Tosaki). The target was observed with the ALMA 12-m array on 18 January 2015 for a total of 60 minutes on-source. Figure 3.2 shows the ALMA configuration that was used. This is the C34-2/1 configuration with 34 antennas (although two are flagged as unusable) arranged with baselines ranging from 15 m to 349 m, which yields a minimum beam angular resolution of 2.2 arcsec and a maximum recoverable scale of 29 arcsec (at 110.27 GHz). This corresponds to physical scales of 9 to 116 pc at the distance of 840 kpc to M33. The observed field of view is 43 arcsec. Quasar J2258-2758 was used as a bandpass calibrator, Mars as a flux calibrator and Quasar J0237+2848 as a phase calibrator. Four spectral windows were used in the observations. Three of the spectral windows cover ^{13}CO (J=1-0) at 110.2 GHz, C^{18}O(J=1-0) at 109.8 GHz and CH_3OH at 96.7 GHz lines; each of these spectral windows contained 180 channels with widths of 244.14 kHz, covering a bandwidth of 117.2 MHz. The fourth spectral window covered continuum emission from 98.56 - 99.50 GHz using 3840 channels with widths of 244.14 kHz (~ 0.664 kms^{-1}). Only the ^{13}CO (J=1-0) and continuum emission are detected in this data.

The Common Astronomy Software Application package (CASA; McMullin et al. 2007) version 5.6.1 was used to process the data. We first performed the standard pipeline calibration on the visibility data without changing any parameters in the script for pipeline calibration and then produced line cubes and continuum images using `tclean`. The plot in Figure 3.3, from CASA pipeline reduction

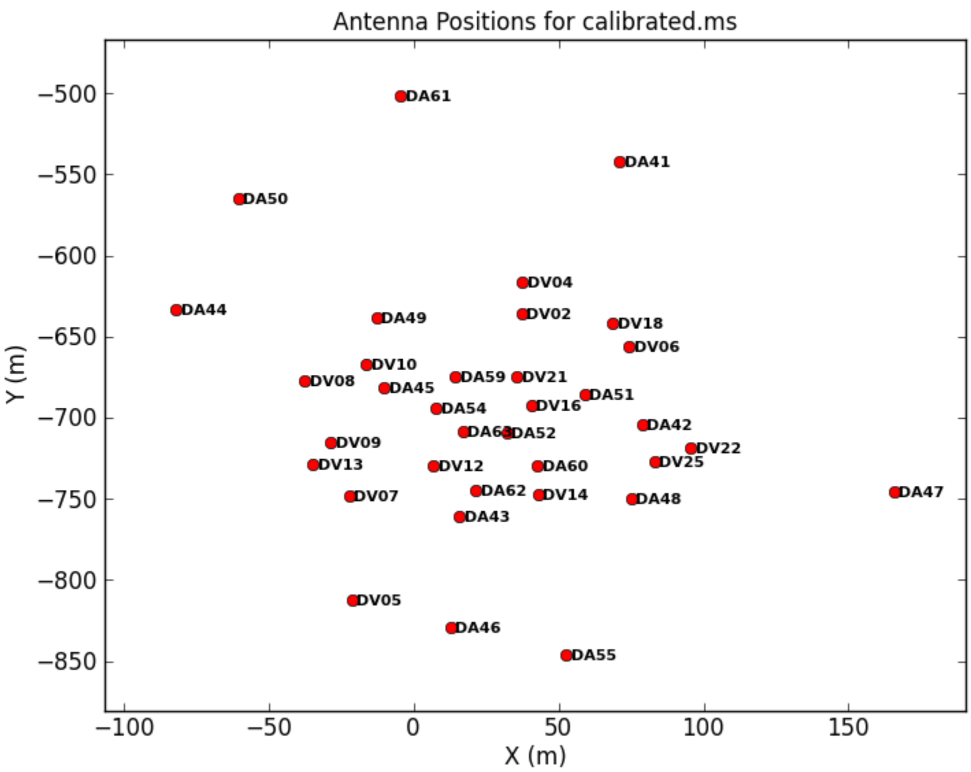

Figure 3.2: Antenna configuration for ALMA ^{13}CO (J=1-0) observation.

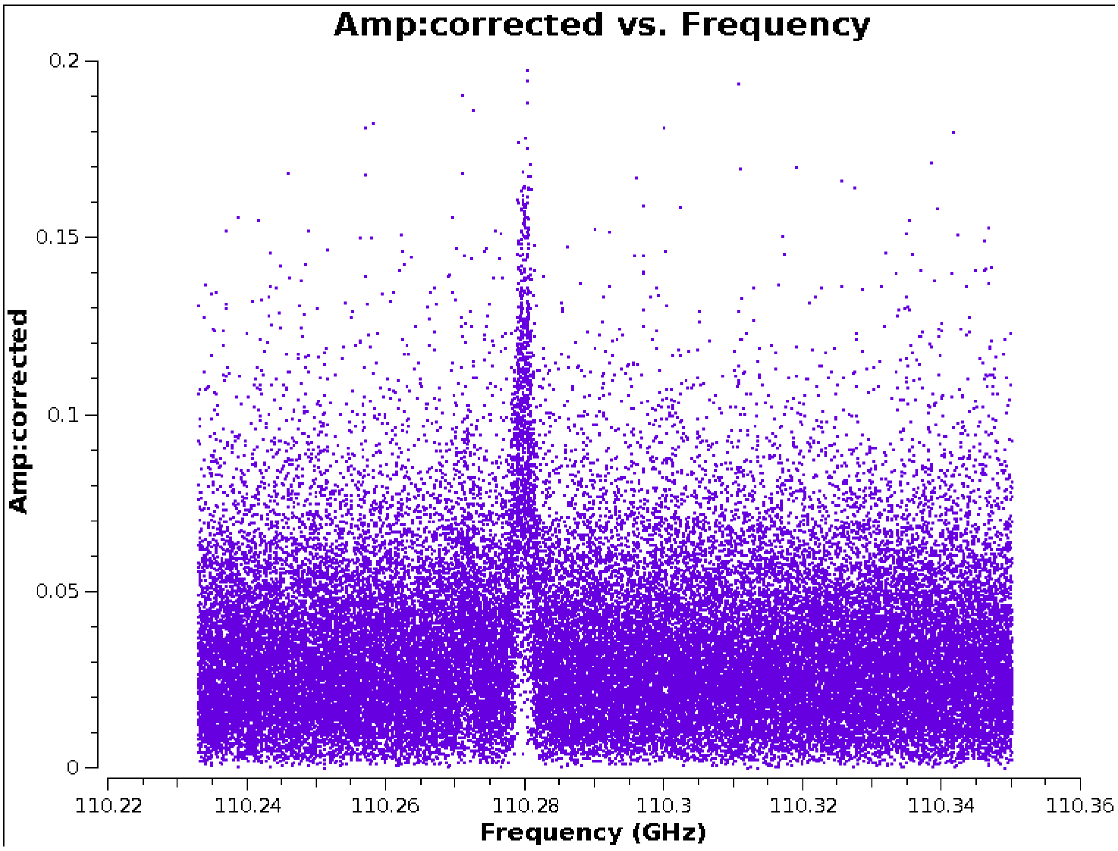

Figure 3.3: Plot from CASA showing amplitude plotted against frequency for ALMA Band 3 data. The detection is clear for the ^{13}CO (J=1-0) line at around 110.28 GHz.

Table 3.1: ^{13}CO(J=1-0) ALMA Observational Properties for NGC 604 in M33.

Parameter	^{13}CO(J=1-0)	Continuum
Frequency (GHz)	110.2	104
Observing Period	18 Jan. 2015	18 Jan. 2015
Array Configurations	C34-2/1	C34-2/1
FWHM of FOV (arcsecs)	42.6	42.6
Beam size (arcsecs)	3.2 × 2.4	3.9 × 2.8
Velocity resolution (km/s)	0.664	—

shows amplitude plotted against frequency for ALMA Band 3 data with a clear detection of ^{13}CO (J=1-0) line emission at around 110.28 GHz. We set the pixel scale for both the continuum and line images to 0.36 arcsec. The channel width for the ^{13}CO image was set to 0.664 km s^{-1}. We used Briggs weighting with the robust parameter set to 0.5 to improve the angular resolution of the final images without severely compromising the image sensitivity. The synthesized beam sizes are 3.2 $\times$ 2.4 arcsec ($\sim 13 \times 10$ pc) for the line data and 3.9 $\times$ 2.8 arcsec ($\sim 16 \times 11$ pc) for the continuum data. The achieved rms sensitivity in the line data is 2.6 mJy beam^{-1} and for the continuum data it is 0.04 mJy beam^{-1}. The calibration uncertainty is expected to be 5% (Braatz et al. 2020). A summary of observational properties is presented in Table 3.1.

The Herschel SPIRE 250 μm map, ALMA ^{13}CO(J=1-0) integrated intensity map and the 104 GHz continuum map are shown in Figure 3.4. The left panel shows the SPIRE 250 μm image of M33 tracing cold interstellar dust emission reduced and imaged by George Bendo from the ALMA UK node and used here with his permission. The brightest spot in the north-east of the image is NGC 604 which is the brightest and biggest H II region in M33. Our ALMA Band 3 data was taken from the region shown in a red box and is clearly presented in the right hand side both in line and continuum emission. The top right panel shows ^{13}CO(J=1-0) line emission from NGC 604. The red cross represents the centre of the H II region.

Most of our line emission is to the south-east of the centre. The gray contours show the 250 μm emission which appears as a bright spot in the red box of the left hand side SPIRE map. The bottom-right panel shows the 104 GHz continuum emission from NGC 604, which has been resolved into three sources which are referred to as millimeter sources (MMS) (Miura et al. 2010; Muraoka et al. 2020) and we adopt that nomenclature throughout our work . The gray contours are the same as in the top-right panel. The MMS resolved are named MMS1, MMS2 and MMS4 and we do not have MMS3 in our data because MMS1 in the work done by Muraoka et al. (2020) was resolved and given the names of MMS1 and MMS2, hence we preserve the nomenclature of these sources in this work. The 104 GHz continuum emission detected in NGC 604 (as shown in the bottom right panel of Figure 3.4) is believed to be dominated by free-free emission (as indicated by the spectral energy distribution analyses of other galaxies by Peel et al. 2011, Bendo et al. 2015, and Bendo et al. 2016) that originates from OB stars within NGC 604.

As an additional visualization aid, the ^{13}CO(J=1-0) emission is overlaid as contours on the continuum image in Figure 3.5. We find spatial offsets between ^{13}CO line and 104 GHz continuum emission. The peaks of line emission are consistently offset with those of continuum emission. One other feature that is clear from the overlay of these images is that continuum emission is detected only near the centre of the GHR. The ^{13}CO emission is detected beyond the edges of the continuum emission.

3.2.2 ALMA Band 6 Data

We use archival ALMA Band 6 observations of the ^{12}CO(J=2-1) (230.54 GHz), ^{13}CO(J=2-1) (220.40 GHz), C^{18}O(J=2-1) (219.56 GHz) line emission towards NGC 604, GMC 16 and GMC 8 obtained during Cycle 5 (project code 2017.1.00461.S; PI: K. Muraoka). The target was observed with the ALMA 12-m array in configuration C43-5 as well as 7-m array in 2017 and 2018 October. Three spectral

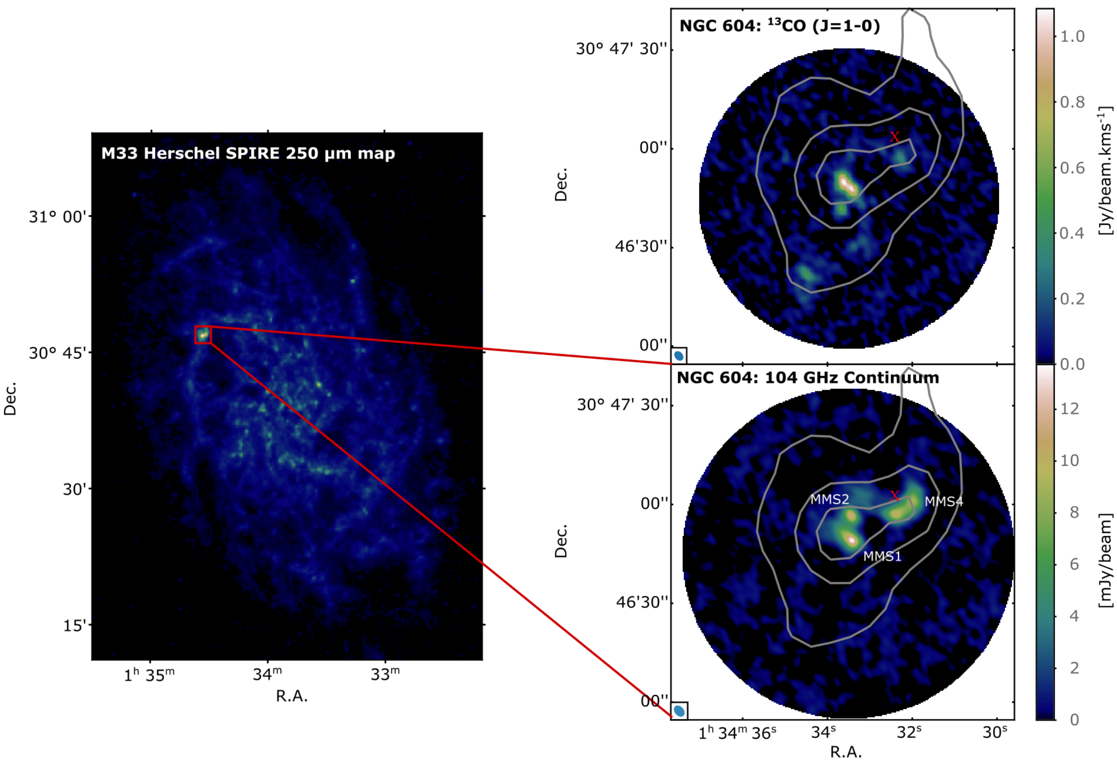

Figure 3.4: *Left panel:* A 250 μm image of M33 tracing cold interstellar dust emission. *Right top panel:* The ^{13}CO(J=1-0) emission in NGC 604 as observed by ALMA. *Right bottom panel:* The ALMA 104 GHz continuum emission in NGC 604 resolved into three sources, which we call millimeter sources (MMS). The gray contours in both right panels show the 250 μm emission, and the red cross symbol shows the centre of the giant HII region (GHR).

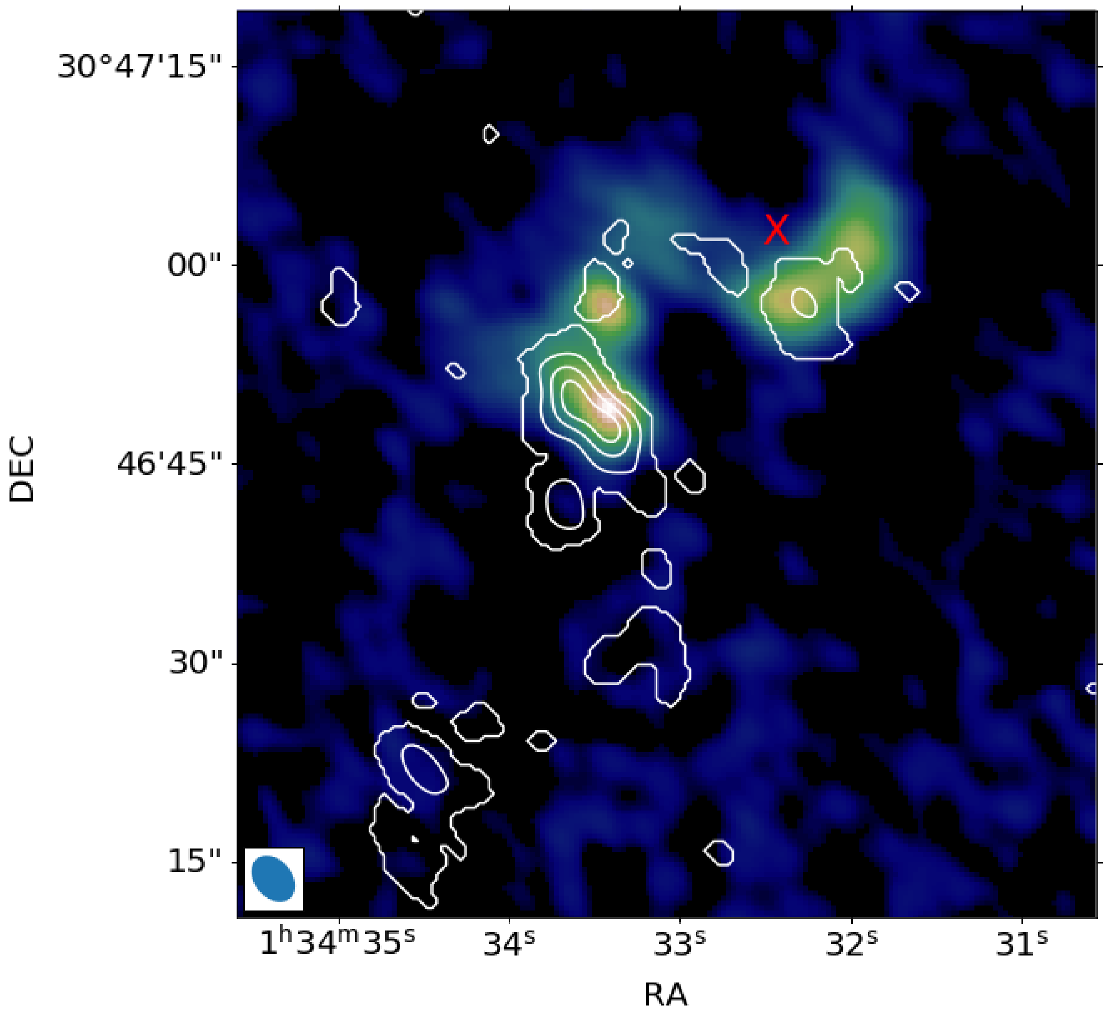

Figure 3.5: The ALMA 104 GHz continuum image of NGC 604 in colour with the integrated $^{13}CO(J=1\text{-}0)$ emission overlaid as white contours. The contour levels represent 20, 40, 60, and 80% of the peak emission. The angular resolution is 3.9 arcsec $\times$ 2.8 arcsec for ALMA 104 GHz continuum. The continuum emission is seen only near the centre of the GHR, and some regions with $^{13}CO(J=1\text{-}0)$ emission do not have continuum emission. The color bar is the same as the bottom right panel of Fig 3.4.

windows were used in the observations targeting $^{12}CO(J=2\text{-}1)$, $^{13}CO(J=2\text{-}1)$ and $C^{18}O(J=2\text{-}1)$. The correlator settings for the bandwidths were 117.19 MHz with 1920 channels for ^{12}CO and 960 channels for ^{13}CO and $C^{18}O$. Two spectral windows were used for continuum observations with bandwidth of 3750 MHz and channel width of 0.98 MHz.

CASA version 5.6.1 was used to process Band 6 data. We first performed the standard pipeline calibration on the visibility data using standard scripts provided on the archive without changing any parameter. The calibrated data were imaged using the `tclean` task in CASA with a multiscale deconvolver. The Briggs weighting with a robust parameter of 2 was used in order to trade towards higher sensitivity. An algorithm which masks regions during the cleaning process thereby mimicking what an experienced user would do when masking images manually, called automasking, is implemented in `tclean` (Kepley et al. 2020). Auto-masking was applied during imaging and finished with cleaning manually. During automasking we set usemask parameter to 'auto-multithresh', sidelobethreshold to 1.25, noisethreshold to 5.0, meanbeamfrac to 0.1, growiterations to 100, and negativethreshold to zero (0). All these automasking parameters are implemented following the ALMA guides on automasking. The final image cubes have the following properties; the average beam size for the ^{12}CO data 0.53 arcsec $\times$ 0.33 arcsec (corresponding to $\sim$ 2 pc $\times$ 1 pc) and the rms noise level is 4.1 mJy beam^{-1} at a velocity resolution of 0.2 kms^{-1}. The average beam size for ^{13}CO data 0.55 arcsec $\times$ 0.35 arcsec corresponding to $\sim$ 2 pc $\times$ 1 pc and the rms noise level is 4.1 mJy beam^{-1} at a velocity resolution of 0.2 kms^{-1}. The average beam size for $C^{18}O$ data 0.55 arcsec $\times$ 0.35 arcsec corresponding to $\sim$ 2 pc $\times$ 1 pc and the rms noise level is 4.1 mJy beam^{-1} at a velocity resolution of 0.2 kms^{-1}. The beam size and the sensitivity of 1.3-mm continuum are 0.53 arcsec $\times$ 0.35 arcsec corresponding to $\sim$ 2 pc $\times$ 1 pc and 0.07 mJy beam^{-1}. The summary of the observation properties have been presented in Table 3.2.

Table 3.2: ALMA Band 6 Observational Properties for NGC 604, GMC 16 and GMC 8 in M33.

Parameter	^{12}CO(J=1-0)	^{13}CO(J=1-0)	C^{18}O(J=1-0)	Continuum
NGC 604				
Frequency (GHz)	230.538	220.399	219.560	1.3mm
Observing Period	Oct. 2017 - Oct. 2018	Oct. 2017 - Oct. 2018	Oct. 2017 - Oct. 2018	Oct. 2017 - Oct. 2018
Array Configurations	C43-5	C43-5	C43-5	C43-5
Beam size (arcsecs)	0.53 × 0.33	0.55 × 0.35	0.55 × 0.35	0.53 × 0.35
Velocity resolution (km/s)	0.2	0.2	0.2	—
GMC 16				
Frequency (GHz)	230.538	220.399	219.560	1.3mm
Observing Period	Oct. 2017 - Oct. 2018	Oct. 2017 - Oct. 2018	Oct. 2017 - Oct. 2018	Oct. 2017 - Oct. 2018
Array Configurations	C43-5	C43-5	C43-5	C43-5
Beam size (arcsecs)	0.53 × 0.33	0.55 × 0.35	0.55 × 0.35	0.53 × 0.35
Velocity resolution (km/s)	0.2	0.2	0.2	—
GMC 8				
Frequency (GHz)	230.538	220.399	219.560	1.3mm
Observing Period	Oct. 2017 - Oct. 2018	Oct. 2017 - Oct. 2018	Oct. 2017 - Oct. 2018	Oct. 2017 - Oct. 2018
Array Configurations	C43-5	C43-5	C43-5	C43-5
Beam size (arcsecs)	0.53 × 0.33	0.55 × 0.35	—	—
Velocity resolution (km/s)	0.2	0.2	0.2	—

3.2.2.1 NGC 604 Band 6 Data

The top-left panel of Figure 3.6, shows ALMA ^{12}CO(J=2-1) line emission integrated intensity map covering the two major GMCs in NGC 604 namely, NMA 8 and NMA 9 (Miura et al. 2010). From this map, we see that these two GMCs have been resolved into both filamentary and clumpy structures. A focus on the upper side of the image, shows two separate bright filaments which are resolved into individual clumpy structures. In the bottom part of the same image, there is enough sensitivity to detect structures but they are fainter than the ones detected in the upper part of the image.

The top-right Figure 3.6, shows the ALMA ^{13}CO(J=2-1) integrated intensity map for NGC 604 covering the same region as the ^{12}CO image. The emission is detected with bright filamentary and clumpy structures in the upper side of the image which is associated with NMA 8, the largest GMC in NGC 604, are clearly visible. In the bottom part of the image, we hardly detect any ^{13}CO emission as we did for ^{12}CO in the same region. Generally, this kind of distribution of emission is expected between the two tracers of ^{12}CO and ^{13}CO as the first traces both the dense and diffuse gas while the later traces only the denser gas.

The bottom-left of Figure 3.6, shows C^{18}O(J=2-1) emission from NGC 604. The emission is only detected in three main bright sources associated with NMA 8. These detected regions represents the densest parts of the GMC which gives signs that these are areas where star formation might start.

Figure 3.6 bottom-right, shows the 1.3 mm continuum emission map for NGC 604. The synthesized beam size for this image is 0.53 arcsec $\times$ 0.35 arcsec which translates to 2.12 pc $\times$ 1.4 pc to the M33 distance. The continuum emission is detected in the same region where C^{18}O is detected in NGC 604. This confirms that these regions which have both C^{18}O and 1.3 mm continuum emission have high densities which usually correlates with star formation. There are three millimeter sources detected namely MMS1, MMS2 and MMS3 which are all associated with NMA 8 GMC.

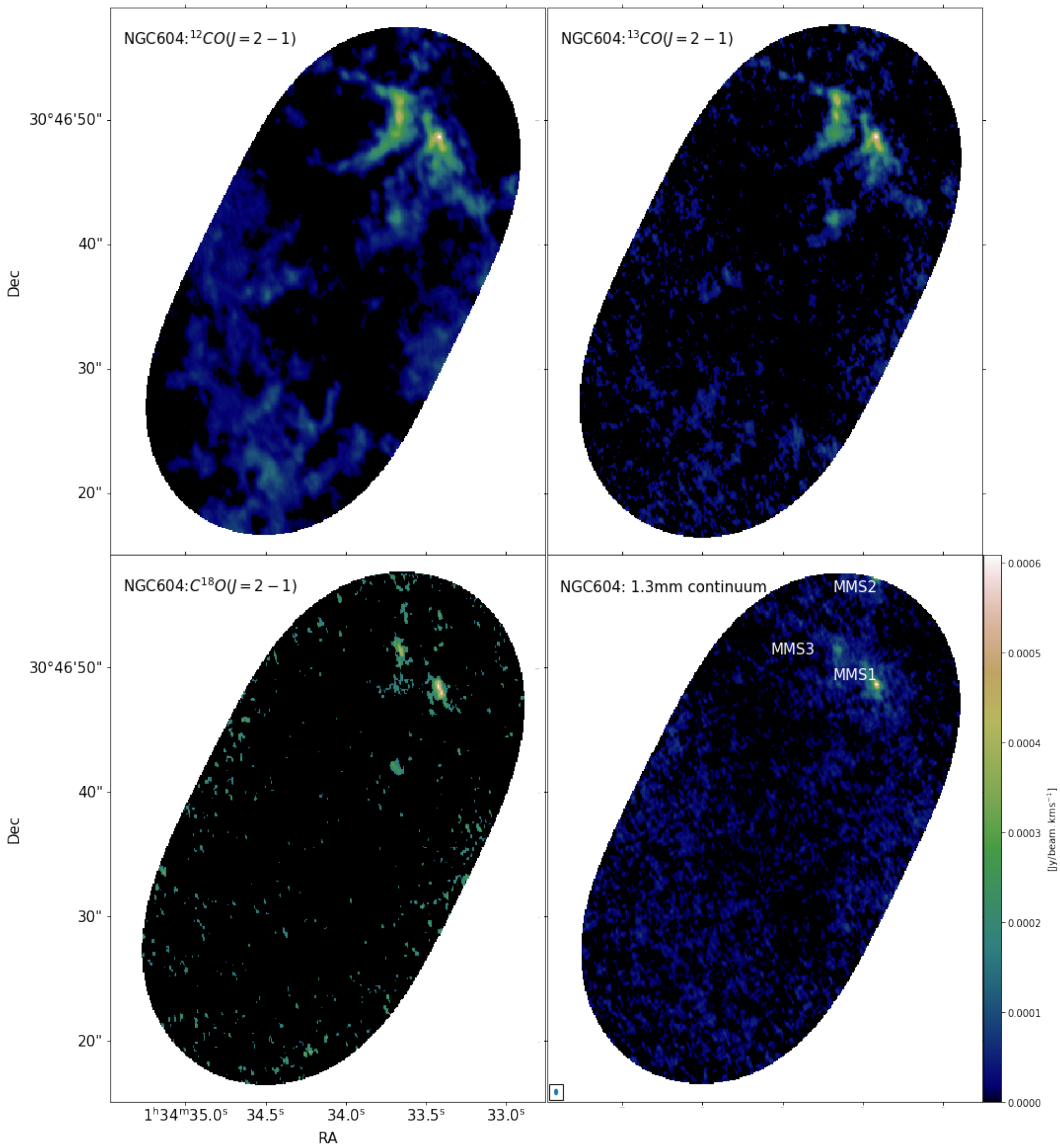

Figure 3.6: (Top-left) ^{12}CO(J=2-1) integrated intensity map of NGC 604 with a lot of filamentary and clumpy structures. (Top-right) ^{13}CO(J=2-1) integrated map of NGC 604. The detection of ^{13}CO(J=2-1) shows the most denser areas. (Bottom-left) C^{18}O(J=2-1) integrated map of NGC 604 which traces the densest parts of the molecular clouds. (Bottom-right) 1.3 mm continuum emission from NGC 604 which is detected in the same region as C^{18}O($J = 2-1$).

We compare the Band 3 lower resolution ^{13}CO(J=1-0) to the Band 6 higher resolution ^{13}CO(J=2-1) data by convolving and smoothing the ^{13}CO(J=2-1) to the same resolution as the ^{13}CO(J=1-0) using the J=1-0 synthesized beam and the imstat task in CASA (McMullin et al. 2007). The smoothed J=2-1 image is overlayed with the J=1-0 data shown in white contours in Figure 3.7. There is good agreement in the distribution of both lines at the same resolution. This implies that the J=2-1 observations are not resolving away significant emission as compared with J=1-0 observation. We recover most of our J=1-0 emission in the higher resolution maps for the sources within the field of view.

3.2.2.2 GMC 16 Band 6 Data

Figure 3.8 top-left, is an image showing ALMA ^{12}CO(J=2-1) integrated emission from GMC 16. The emission shows filamentary structures with clumpy features within them. At the bottom of the image on one of the filament, there is a very bright source. We investigate this source in the other maps of ^{13}CO, C^{18}O and 1.3 mm continuum to ascertain if it is prominent in them too. The top-right panel shows ALMA ^{13}CO(J=2-1) integrated emission map. In this map there are three main filaments which are prominent and the bright spot seen in ^{12}CO(J=2-1) is also very prominent here in ^{13}CO(J=2-1). These filaments run the full length of the mapped area. They appear to follow the northern spiral arm of M33 (Miura et al. 2012; Tokuda et al. 2020). The bright source could be a candidate for emerging star formation.

The bottom-left panel of Figure 3.8 shows an image of C^{18}O(J=2-1) from GMC 16 which only has emission in one place which is specifically on the bright spot seen in ^{12}CO and ^{13}CO emission. This is the only region we detect C^{18}O emission in the whole of GMC 16.

Figure 3.8 bottom-right, shows 1.3 mm continuum detected from GMC 16 which is indicated as MMS for conformity with nomenclature of continuum sources adopted in this work. The continuum emission is only detected in one source which

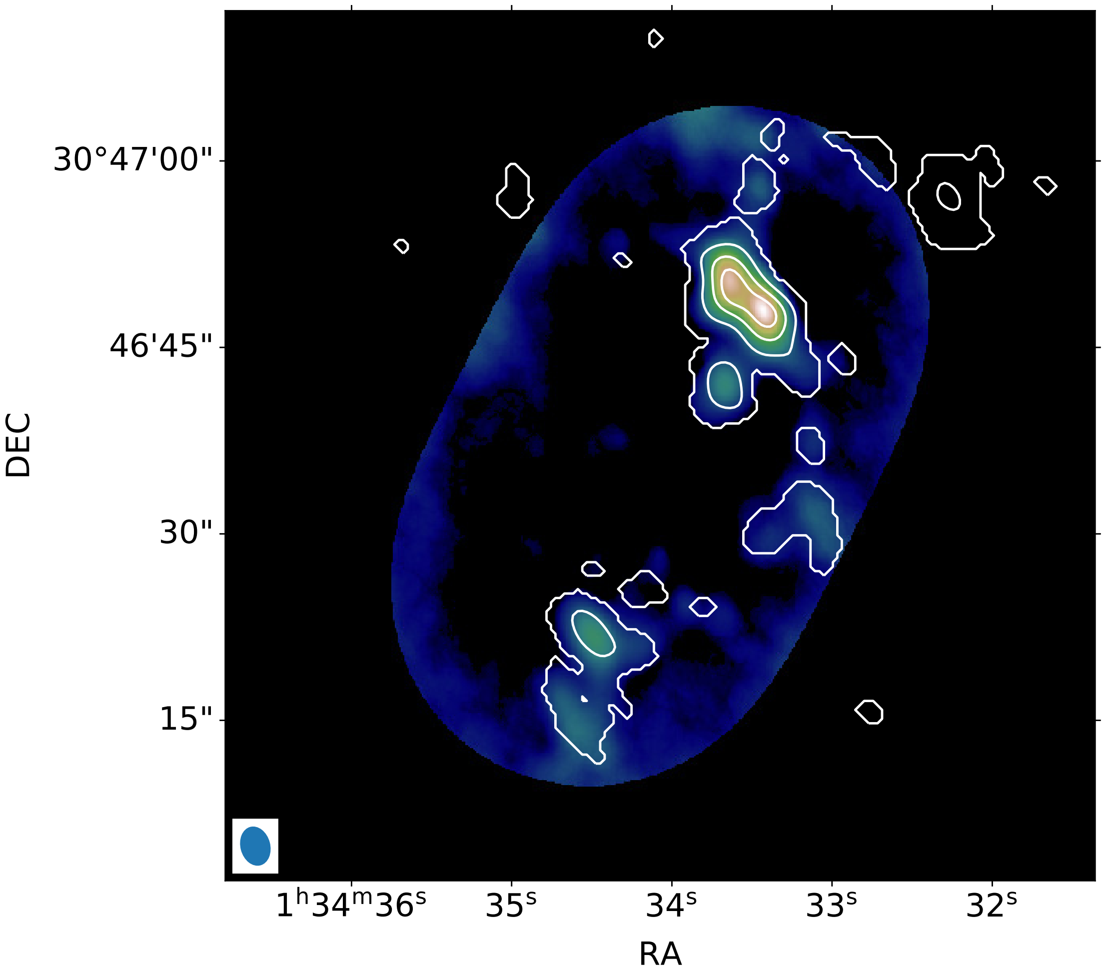

Figure 3.7: ^{13}CO(J=2-1) data convolved and smoothed to a lower resolution using the J=1-0 synthesized beam. The smoothed higher resolution image is overlayed with the lower resolution ^{13}CO(J=1-0) data shown in white contours. From the map it shows that we recover most of the lower resolution emission.

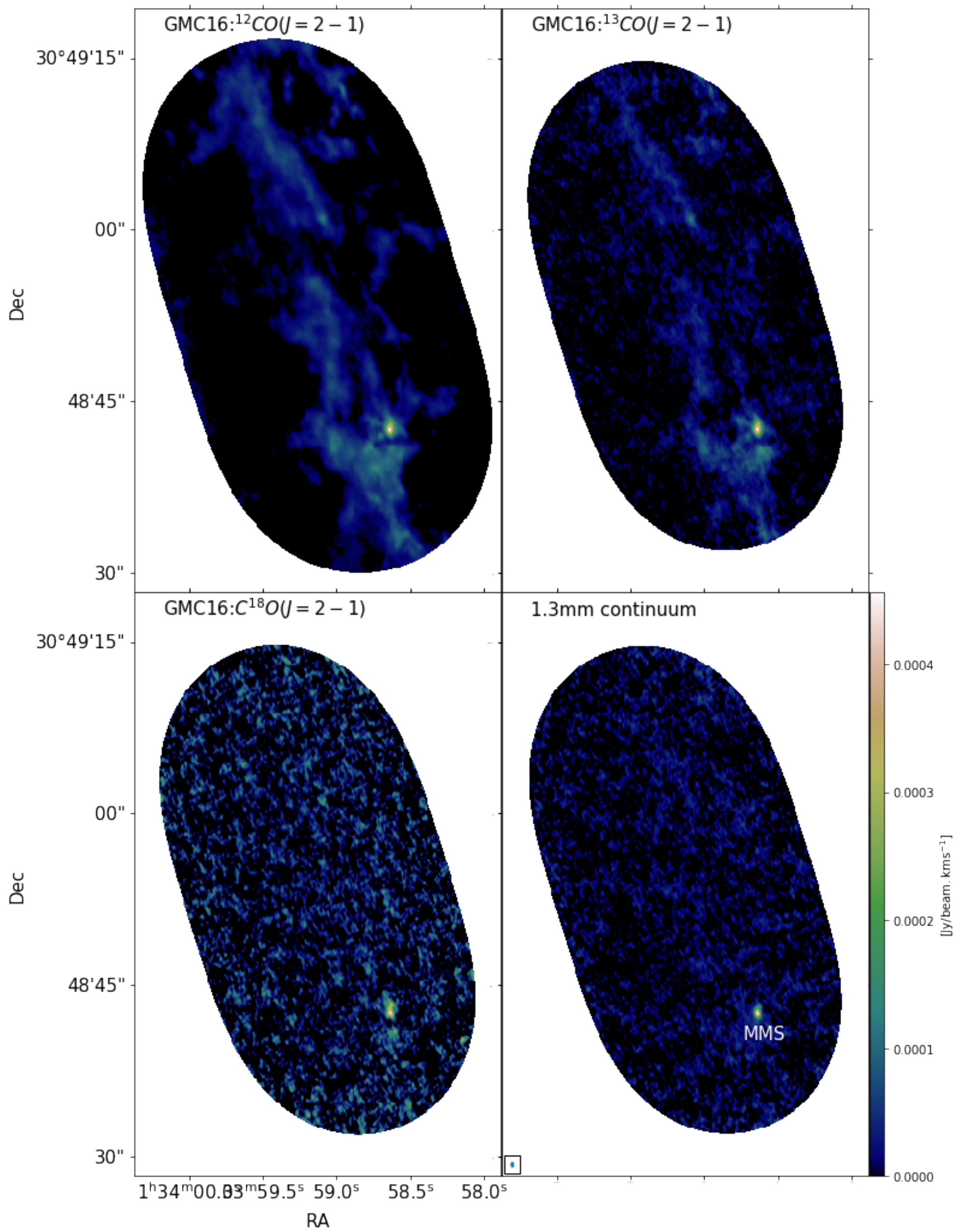

Figure 3.8: (Top-left) ^{12}CO(J=2-1) integrated map of GMC 16. The image shows filaments which align with the northern spiral arm of M33. There is a single bright spot in the bottom filament which we think its a protostar(s). (Top-right) ^{13}CO(J=2-1) integrated map which shows filaments like in ^{12}CO image. The single bright spot in the bottom filament is also visible in all panels. (Bottom-left) C^{18}O emission detected at the only brightest spot in ^{12}CO and ^{13}CO emission. (Bottom-right) 1.3 mm continuum emission from detected at the brightest spot in ^{12}CO and ^{13}CO emission.

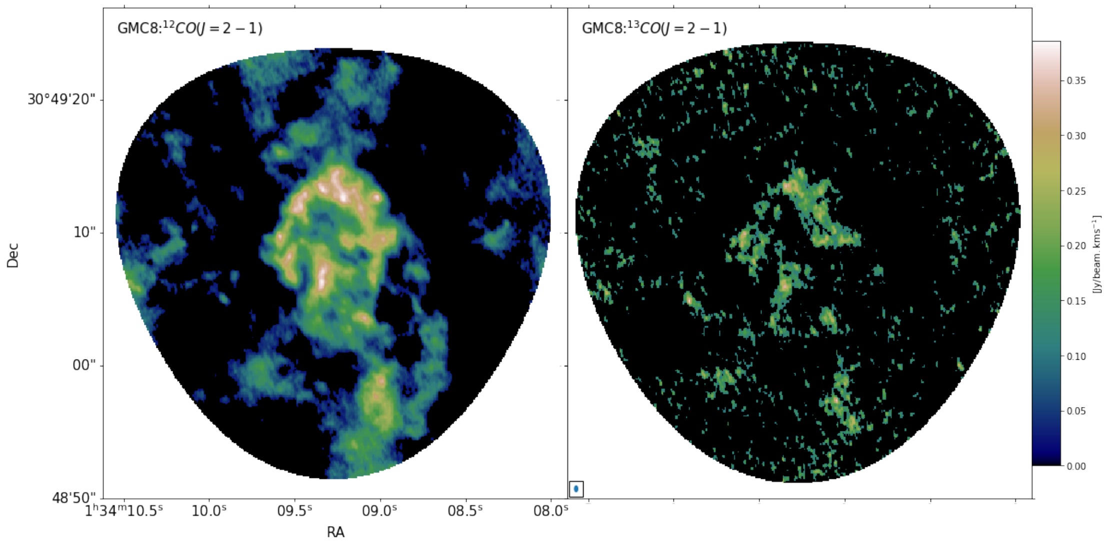

Figure 3.9: (Left) ^{12}CO(J=2-1) integrated map of GMC 8. The image shows a loop or arc with clumpy bright features concentrated at the centre of the GMC and image. Away from the centre is more spurious emission. (Right) ^{13}CO(J=2-1) integrated map of GMC 8 clumpy structures which are concentrated at the center.

is very bright in ^{12}CO and ^{13}CO. It is the region where we also detect C^{18}O, which traces the densest gas. The 1.3 mm continuum emission being the tracer of high densities which correlates with star formation, does signify that this bright source could be attributed to the formation of a protostar or a cluster of protostars. We shall investigate in more details in Chapter 5 as we deal with the detailed analysis of all band 6 data.

3.2.2.3 GMC 8 Band 6 Data

The left panel of Figure 3.9, is an image showing the ALMA ^{12}CO(J=2-1) integrated intensity map of GMC 8. The emission shows a loop or arc at the centre with more diffuse emission away from the centre. The synthesized beam size for ^{13}CO is 0.53 arcsec × 0.33 arcsec which translates to 2.22 pc × 1.32 pc to the M33 distance. Figure 3.9 right-panel, is the integrated ^{13}CO(J=2-1) line emission. The emission shows more clumpy structures at the centre and a bit at the bottom of the image. Most of the diffuse emission detected in ^{12}CO has been resolved in

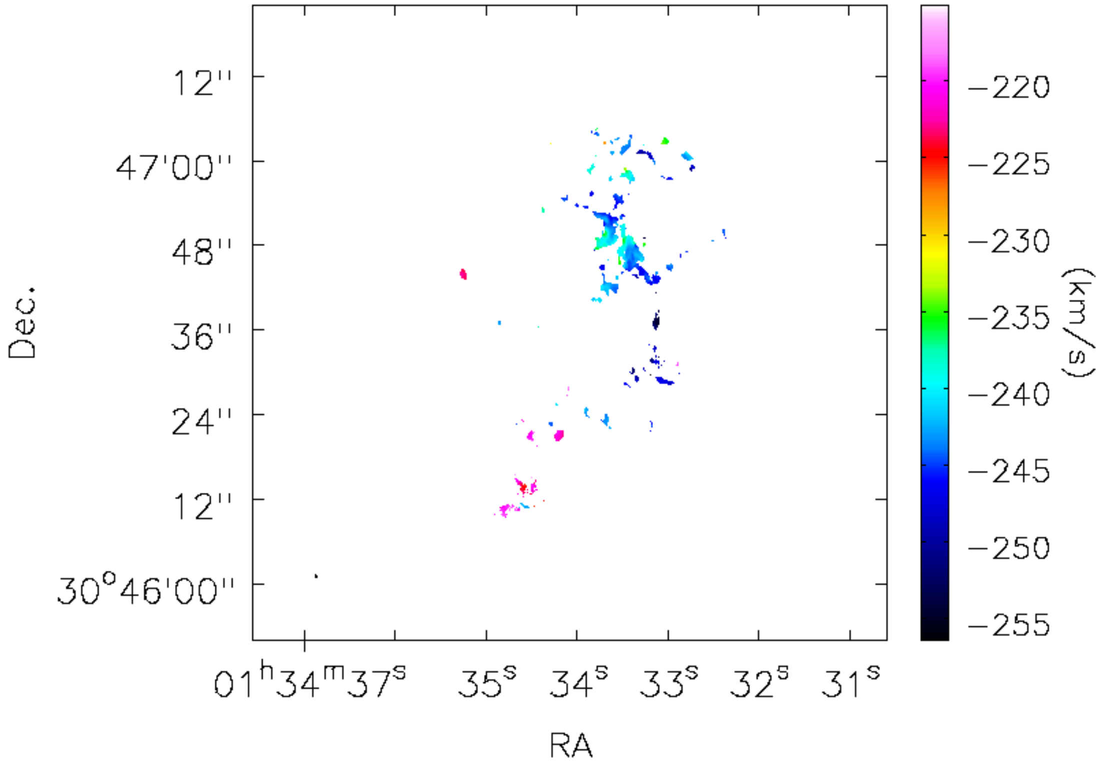

Figure 3.10: NGC 604 ^{12}CO(J=2-1) first order moment (velocity) map. This shows the velocity distribution of the ^{12}CO(J=2-1) gas in NGC 604 where the north side the gas is blue-shifting and the south part it is red-shifting.

^{13}CO, which traces the denser gas.

We do not detect C^{18}O(2-1) as well as 1.3 mm continuum emission in GMC 8. This indicates that in this region there are no dense clumps or clouds.

3.2.2.4 Velocity map for ^{12}CO from our data

Figure 3.10 shows the velocity map for NGC 604 ^{12}CO(J=2-1). The velocity distribution in NGC 604 gas indicates that the gas in the south-east is red-shifted while that in the north-west is blue shifted. Focusing on the north-west gas distribution, we see that some of the clouds are slightly red shifted on one side while blue shifted on the other side. This tells us that the gas is rotating.

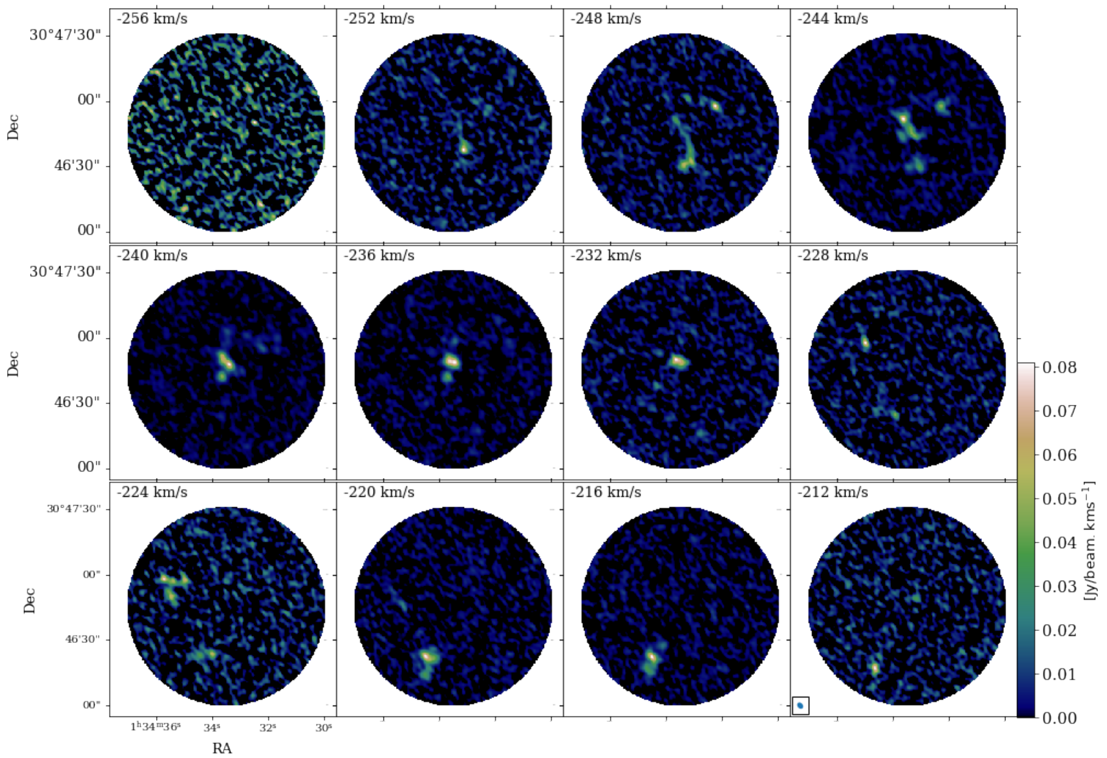

Figure 3.11: NGC 604 ^{13}CO(J=1-0) channel maps binned at 4.0 kms^{-1}. The highest velocity is shown in the upper left corner in each panel. The angular resolution is given by the blue ellipse in a box in the lower left corner of the lower right panel.

3.2.2.5 Channel maps for ^{12}CO and ^{13}CO for our data

Figure 3.11 shows channel maps for the ^{13}CO(J=1-0) cube from NGC 604. The 0.664 kms^{-1} channels in our cube are binned to 4.0 kms^{-1} and we create 12 channel maps from it. The distribution of structure across the cube shows that there is a systematic motion of gas as it is more centrally and the last four bottom panels they are south of the major part of the field of view.

Figure 3.12 shows the channel map for the ^{12}CO(J=2-1) cube from NGC 604. The 0.2 kms^{-1} channels in our cube are binned to 3.2 kms^{-1} and we create 16 channel maps from it. The distribution of structure across the cube running from the top-left panel to the bottom-right panel indicates that the structure starts from the top side of the field of view running all the way to the bottom as the velocity increases.

Figure 3.13 shows the channel map for the ^{13}CO(J=2-1) cube from NGC 604. The 0.2 kms^{-1} channels in our cube are binned to 3.2 kms^{-1} and we create 16 channel maps from it same as what was done in Figure 3.12. The distribution of structure across the cube running from the top-left panel to the bottom-right panel indicates that the structure starts from top side of the field of view running all the way to the bottom as the velocity increases. But we get a lot of panels which are without structure or with very little structure in ^{13}CO as compared to ^{12}CO.

Figure 3.14 shows the channel map for the ^{12}CO(J=2-1) cube from GMC 16. The 0.2 kms^{-1} channels are binned to 2.4 kms^{-1} and we create 12 channel maps from it. We see a similar trend as observed from the NGC 604 channel maps where the structure emanates from the top side of the field and moves across to the bottom of the field across the velocity range. These similarities could be explained with attaching these to their location in the galaxy which we discuss later in Chapter 5.

Figure 3.15 shows the channel map for the ^{13}CO(J=2-1) cube from GMC 16. The binning and number of channel maps is as in Figure 3.14. The distribution is similar and the conclusion made in the case of the ^{12}CO channel maps is applicable here. There is less structure in ^{13}CO as compared to ^{12}CO which is expected as ^{13}CO traces the denser gas and resolves out less dense gas which is seen in ^{12}CO.

Figure 3.16 shows the channel map for the ^{12}CO(J=2-1) cube from GMC 8. The 0.2 kms^{-1} channels in the GMC 8 cube are binned to 2.4 kms^{-1} and we create 12 channel maps from it. The structures are detected mostly at the center of the field.

Figure 3.17 shows the channel map for the ^{13}CO(J=2-1) cube from GMC 8. The binning and number of channel maps is the same as in Figure 3.16. We detect very little structure from ^{13}CO in here.

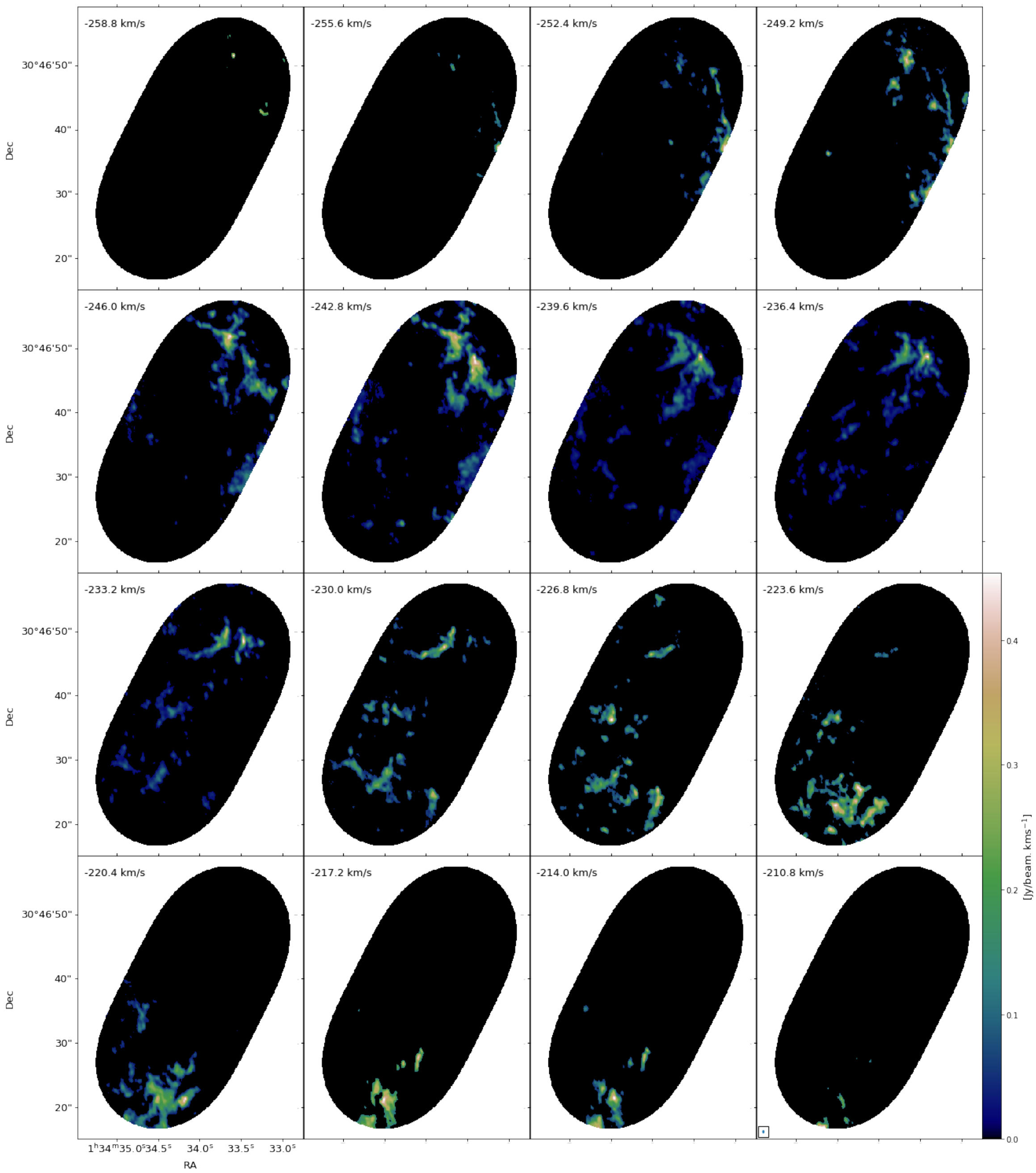

Figure 3.12: NGC 604 ^{12}CO(J=2-1) channel maps binned at 3.2 kms^{-1}. The highest velocity is shown in the upper left corner in each panel. The angular resolution is given by the blue ellipse in a box in the lower left corner of the lower right panel.

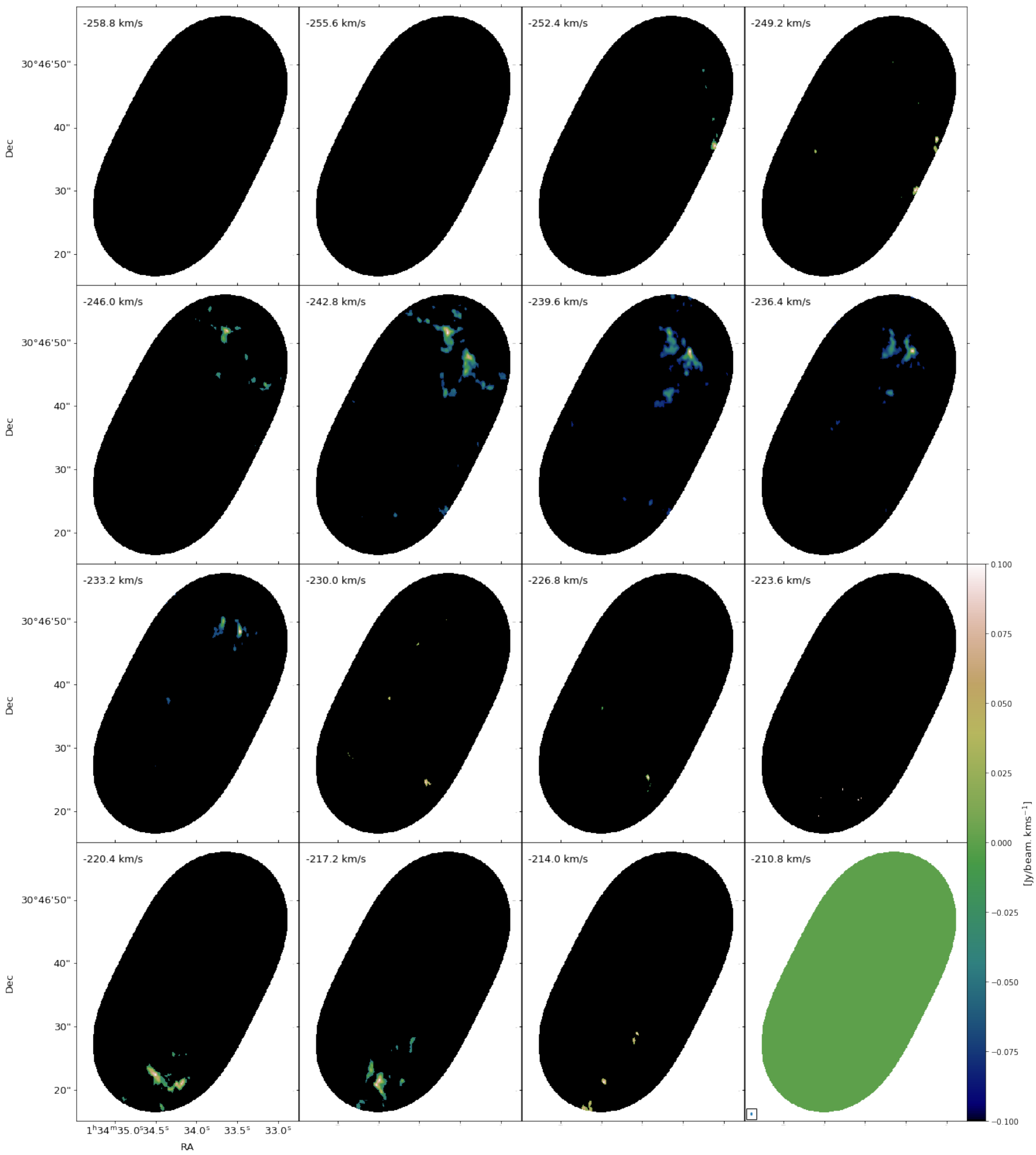

Figure 3.13: NGC 604 ^{13}CO(J=2-1) channel maps binned at 3.2 kms^{-1}. The highest velocity is shown in the upper left corner in each panel. The angular resolution is given by the blue ellipse in a box in the lower left corner of the lower right panel which is the same as in Figure 3.12.

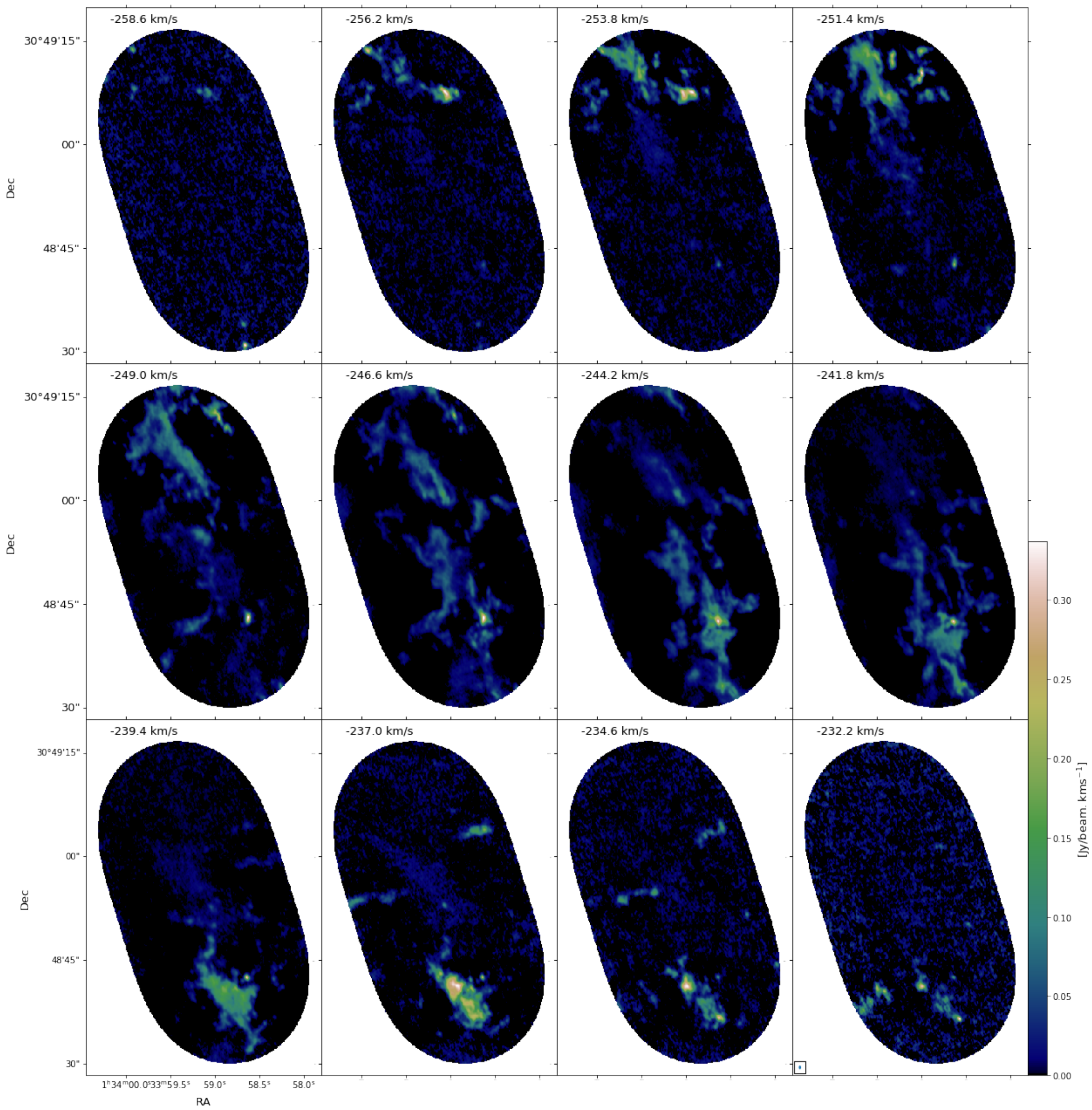

Figure 3.14: GMC 16 ^{12}CO(J=2-1) channel maps binned at 2.4 kms^{-1}. The highest velocity is shown in the upper left corner in each panel. The angular resolution is given by the blue ellipse in a box in the lower left corner of the lower right panel.

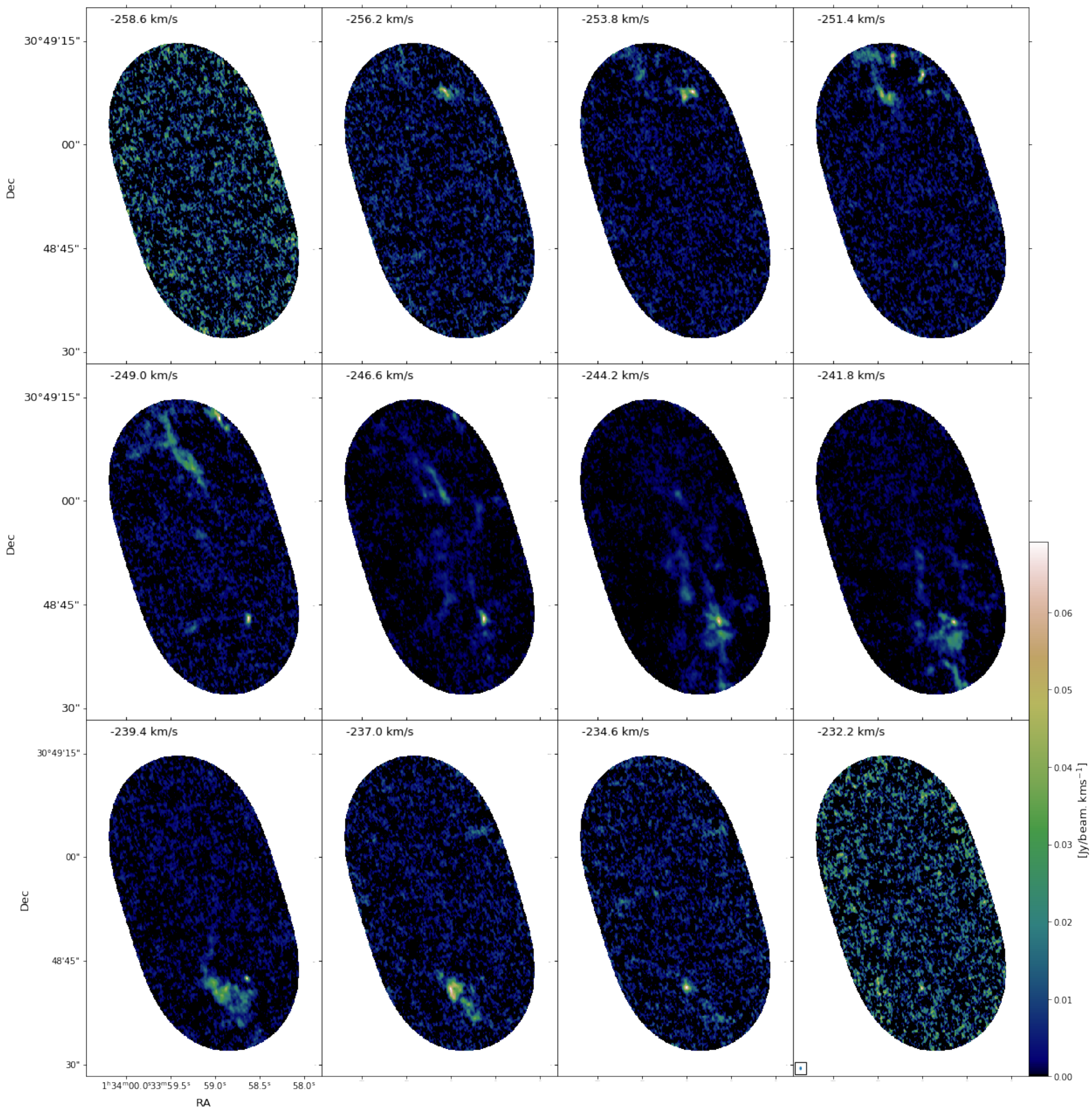

Figure 3.15: GMC 16 ^{13}CO(J=2-1) channel maps binned at 2.4 kms^{-1}. The highest velocity is shown in the upper left corner in each panel. The angular resolution is given by the blue ellipse in a box in the lower left corner of the lower right panel which is the same as in Figure 3.14.

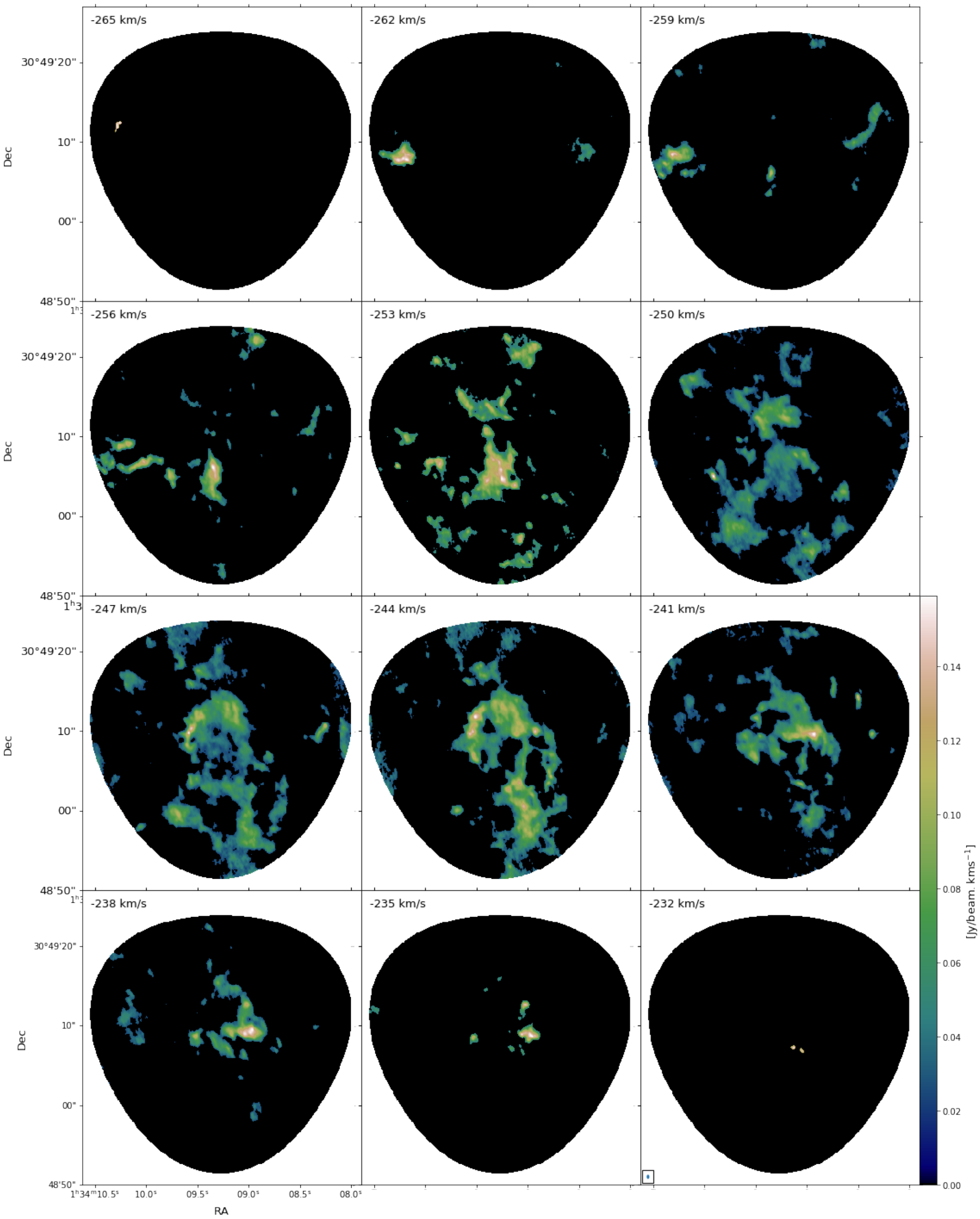

Figure 3.16: GMC 8 ^{12}CO(J=2-1) channel maps binned at 3.0 kms^{-1}. The highest velocity is shown in the upper left corner in each panel. The angular resolution is given by the blue ellipse in a box in the lower left corner of the lower right panel.

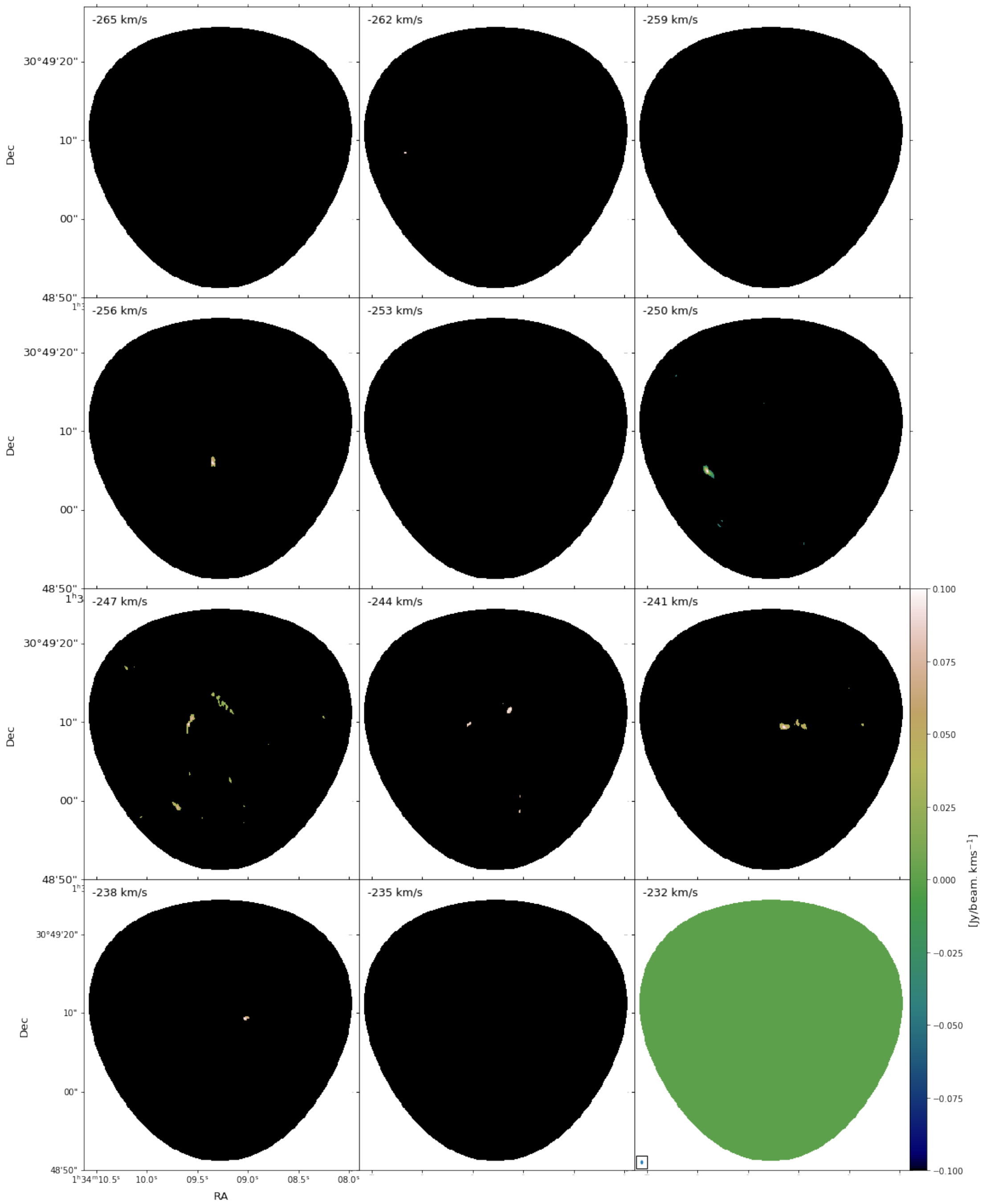

Figure 3.17: GMC 8 ^{13}CO(J=2-1) channel maps binned at 3.0 kms^{-1}. The highest velocity is shown in the upper left corner in each panel. The angular resolution is given by the blue ellipse in a box in the lower left corner of the lower right panel which is the same as in Figure 3.16.

3.2.3 Herschel PACS and SPIRE Data

In this work, we also make use of continuum data in the far-infrared (FIR)/submillimeter from the Herschel space observatory archive. The observations were taken as part of the Herschel M33 extended survey (HerM33es, Kramer et al. 2010), which mapped a 70 arcmin^2 region around M33. Observations at 100 μm and 160 μm were taken by the Photo-conductor Array Camera and Spectrometer (PACS, Poglitsch et al. 2010), with beam sizes of 7.7 arcsecs and 12 arcsecs respectively. Her33es simultaneously used the Spectral and Photo-metric Imaging Receiver (SPIRE Griffin et al. 2010) which mapped M33 at 250 μm, 350 μm and 500 μm, with a resolution of 17.6 arcsecs, 23.9 arcsecs and 35.2 arcsecs, respectively. Details of the data reductions for both PACS and SPIRE are given in Boquien et al. (2011, 2015). The left panel of Figure 3.4 shows the SPIRE 250 μm map of M33 galaxy.

Chapter 4

ALMA Band 3 Results

In this section, we focus on the results for the ^{13}CO($J = 1 - 0$) transition observations of NGC 604, based on the data presented in Chapter 3. These results have been published as Phiri et al. (2021) and the paper is in Appendix D.

4.1 ALMA Band 3 Dendrogram Analysis

To identify structures within the ^{13}CO(J=1-0) image cube, we used the ASTRODENDRO package, which decomposes emission into a hierarchy of nested structures (Rosolowsky et al. 2008; Colombo et al. 2015) as discussed in Chapter 2. This dendrogram technique provides a precise representation of the topology of star forming complexes. Parameters were chosen so that the algorithm could identify local maxima in the cube above the $S_{\rm min} = 4\sigma_{\rm rms}$ level that were also $\Delta_{\rm S} = 3\sigma_{\rm rms}$ above the merge level with adjacent structures. Isorsurfaces surrounding the local maxima were categorized as branches or leaves based on whether they were the largest contiguous structures (branches) or had no resolved substructure (leaves). The resulting dendrogram for ^{13}CO(J=1-0) in NGC 604 is shown in Figure 4.1. We identified 20 structures in the entire dendrogram, consisting of 15 leaves and 4 branches, using the above parameters. The position of each leaf and of its bounding contour is shown in Figure 4.2 left panel. Spectra for the peak brightness

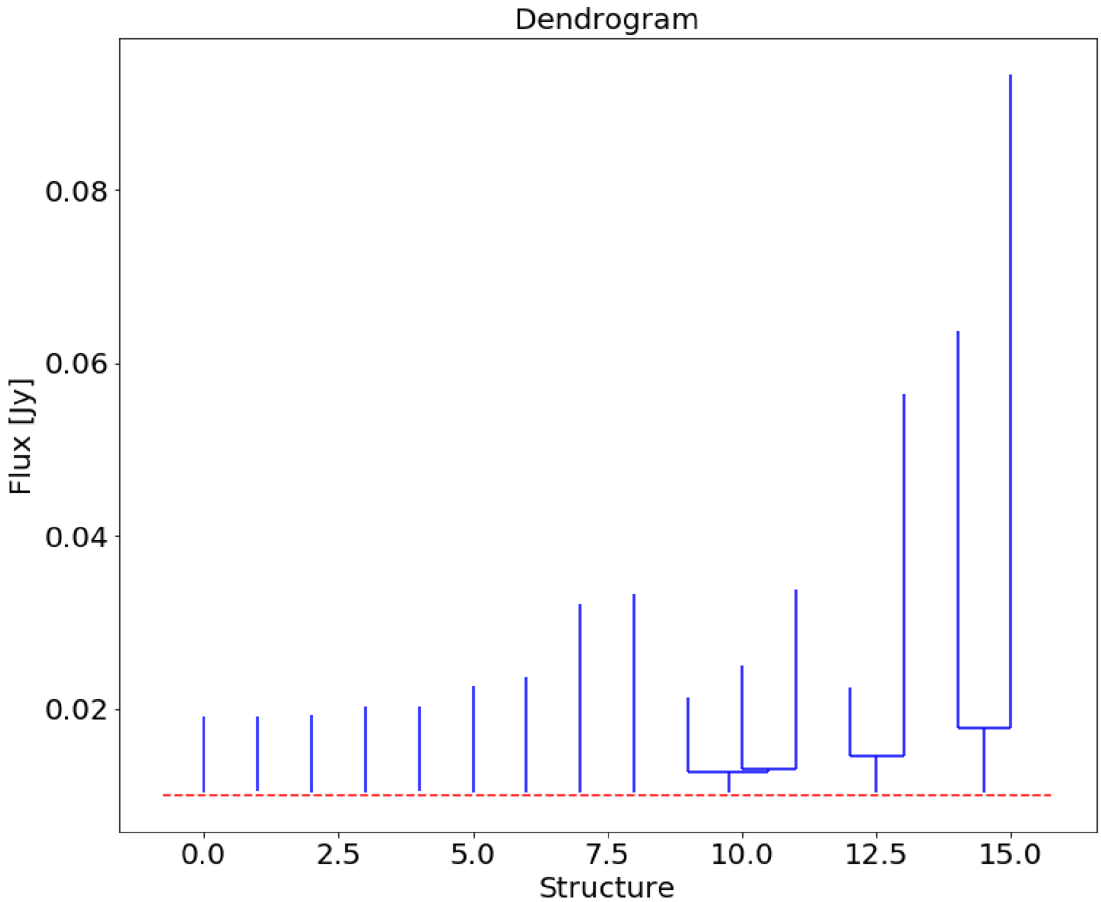

Figure 4.1: The dendrogram of the ALMA ^{13}CO(J=1-0) structures in NGC 604. The top of each vertical line indicates a leaf node, which we assume to be a molecular cloud. The horizontal red dotted line represents the minimum value of the tree, which is at 4σ noise level where 1σ is 0.003 Jy.

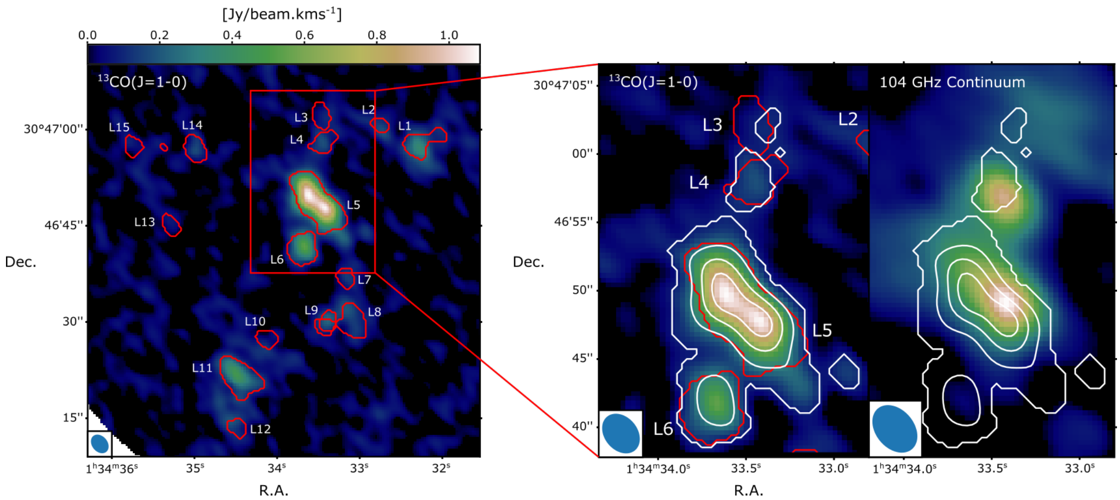

Figure 4.2: The left panel shows the ^{13}CO(J=1-0) emission from NGC604 with the red contours demarcating the clouds identified by ASTRODENDRO. The red box shows the NMA-8 region, which is shown in detail in the two right-hand zoomed panels. The left-hand zoomed panel shows the ^{13}CO(J=1-0) emission from the four resolved molecular clouds, while the right-hand zoomed panel shows the 104 GHz continuum emission. White contours showing the ^{13}CO(J=1-0) line emission are overlaid on both zoomed panels. The contour levels represent 20, 40, 60, and 80% of the peak emission.

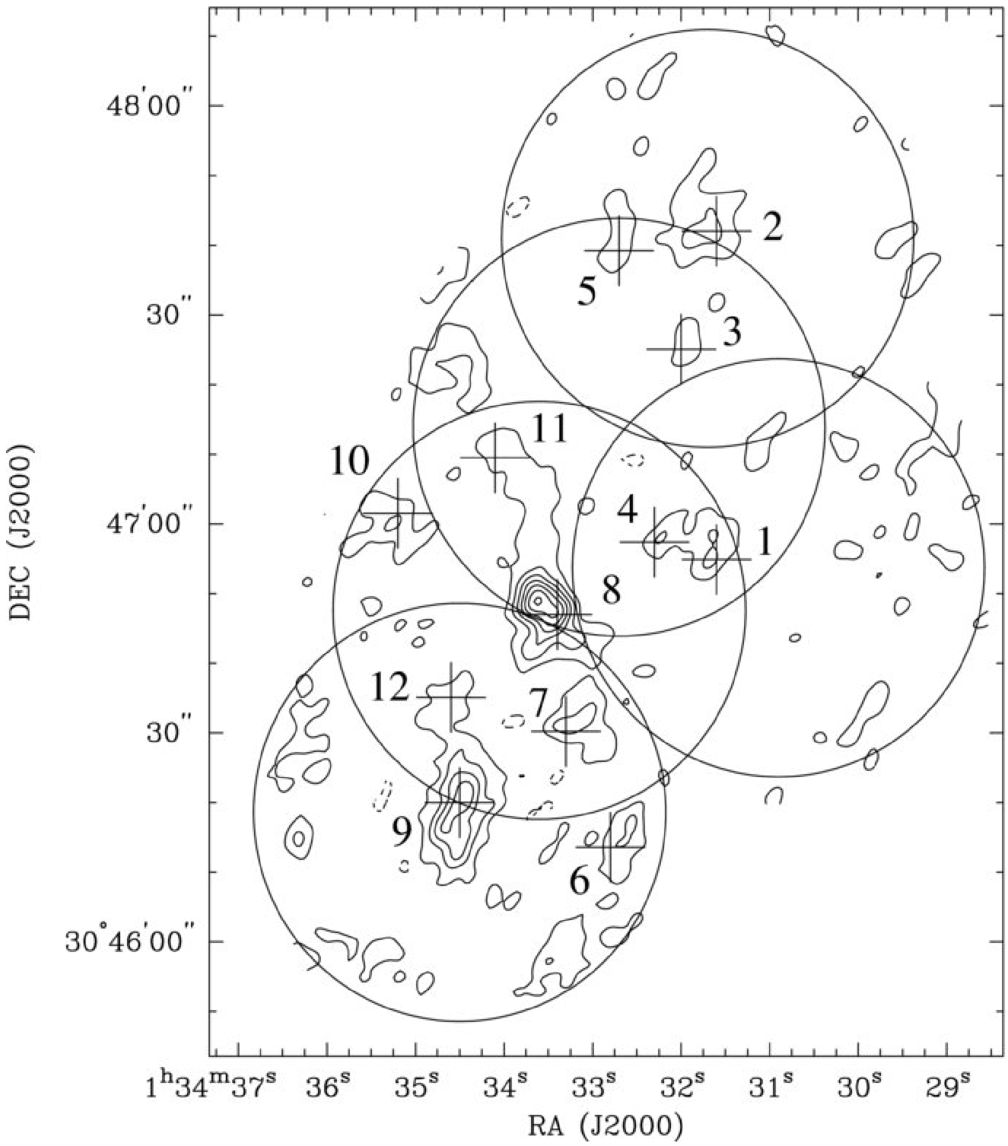

Figure 4.3: Total integrated-intensity map of ^{12}CO over five field of views (FoVs) from the Nobeyama millimeter array (NMA). The crosses represent the positions of the 12 NMA identified clouds with their names labeled by a number. The circles represent the five FoVs that were observed in CO line emission. The parts of the emission outside the FoVs are masked out. Figure is taken from Miura et al. (2010).

pixels, for each leaf, are presented in Appendix A.1. We use letter **L** to represent the leaf number in our labels for the structures. From now on, we shall refer to these leaves as molecular clouds.

Studies of physical properties of GMCs in NGC 604 have been done previously both by single dish (Wilson & Scoville 1992; Viallefond et al. 1992; Tosaki et al. 2007; Muraoka et al. 2012) and interferometry (Wilson & Scoville 1990, 1992; Viallefond et al. 1992; Miura et al. 2010; Muraoka et al. 2020, and references therein) observations. We compared our results with the results from Miura et al. (2010) as they are both interferometry with comparable resolutions, who show observations of ^{12}CO(J=1-0) line emission from NGC 604 as observed by the Nobeyama Millimeter Array as shown in Figure 4.3. We detected and resolved the clouds that they labelled NMA 4, 7, 8, 9, 10. We, however, are not able to detect NMA 1, 3, 6, 11 and 12 above our $4\sigma_{rms}$ noise level. This is because Miura et al. (2012) used a lower detection threshold. If we lower our detection threshold to 3σ, we can detect these sources, but we also detect additional spurious noise in the maps. Given this situation, we chose to use only sources detected at the higher threshold. NMA 2 and 5 are outside of our five fields of view.

We proceeded to determine the basic properties of the identified structures at this point following the steps presented in Chapter 2. From these basic quantities, we calculated additional cloud properties which are listed in Table 4.1. The effective rms spatial size σ_r is given by the geometric mean of σ_{maj} and σ_{min} ($\sigma_{\rm r} = \sqrt{\sigma_{\rm maj}\sigma_{\rm min}}$). The deconvoled spherical radius R is set to 1.91 σ_r following Solomon et al. (1987) and Rosolowsky & Leroy (2006). The luminosity-based mass for ^{13}CO(J=1-0) is computed using

$$\frac{\rm M_{lum}}{\rm M_\odot} = \frac{\rm X_{^{13}CO}}{2\times 10^{20}[\rm cm^{-2}/(K\ km\ s^{-1})]} \times 4.4 \frac{\rm L_{^{13}CO}}{\rm K\ km\ s^{-1}\ pc^2} = 4.4 \rm X_2 L_{^{13}CO} \qquad (4.1)$$

from Rosolowsky et al. (2008), where $\rm X_{^{13}CO}$ is the assumed $^{13}\rm CO(1-0)-to-H_2$ conversion factor. This calculation includes a factor of 1.36 to account for the mass of helium. Changes to the first term or conversion factor are represented with the parameter X_2. We have adopted $X_2 = 5$ based on the average $^{13}CO(1-0) - to - H_2$ conversion factor of $1.0 \times 10^{21} cm^{-2}/(K\ km\ s^{-1})$ for nearby disc spiral galaxies found by Cormier et al. (2018). This average is equivalent to what would be expected for the conversion factor for a galaxy with $12 + \log(O/H) = 8.4$. This is close to the abundance of $12 + \log(O/H) = 8.45 \pm 0.04$ measured for NGC 604 (Esteban et al. 2009). The scatter in $X_{^{13}CO}$ value is 0.3 dex (Cormier et al. 2018). This uncertainty means that masses will have a systematic error of about a factor of 2.

The virial mass of molecular clouds is computed using Equation 1.15 which is

$$M_{vir} = \frac{5R\sigma_v^2}{G} \tag{4.2}$$

Linewidth Δv and velocity dispersion σ_v relate with the following relation at FWHM,

$$\Delta v = \sqrt{8\ln(2)}\sigma_v \tag{4.3}$$

Replacing velocity dispersion by linewidth in equation 4.3 we get,

$$M_{vir} = \frac{5R}{G}\left(\frac{\Delta v^2}{8\ln 2}\right) \tag{4.4}$$

Taking G to be $1/232\ \ pc\,km^{-2}\,s^2$ (Solomon et al. 1987) we get,

$$M_{vir} = 210\Delta v^2 R \qquad [M_\odot] \tag{4.5}$$

where Δv is the linewidth in km s^{-1} and R is the spherical radius in pc. This formulation assumes a spherical density distribution of $\rho \propto R^{-\beta}$ with $\beta = 2$ and that magnetic fields and external pressure are negligible (Solomon et al. 1987). In this equation, M_{vir} is only defined for finite clouds with resolved radii.

The average molecular gas surface density Σ_{lum} is defined as

$$\Sigma_{lum} = \frac{M_{lum}}{\pi R^2} \qquad [M_\odot/pc^2] \tag{4.6}$$

where M_{lum} is the luminosity-based mass and R is the radius of the cloud.

The dynamic state of a cloud is described by the virial parameter, α_{vir}, which is given by

$$\alpha_{\rm vir} = \frac{\rm M_{vir}}{\rm M_{lum}} = \frac{210\Delta v^2 R}{\rm M_{lum}} \tag{4.7}$$

where $\mathrm{M_{lum}}$ is the mass derived from luminosity with the chosen CO-conversion factor while $\mathrm{M_{vir}}$ is the mass derived from the virial theorem assuming clouds are spherical with radius R and linewidth Δv. Allowing for uncertainties in measured parameters, a virtual ratio of ≤ 2 is generally taken to mean that a cloud is gravitational bound. However, a cloud with an α_{vir} ratio significantly lower than this would need additional internal support (e.g. magnetic fields) to survive for longer than the usual dynamical timescale (Faesi et al. 2018).

The uncertainties in the molecular clouds properties R, Δv, $\mathrm{L_{^{13}CO}}$ and $\mathrm{M_{lum}}$ are computed using a bootstrap method with 50 iterations. The bootstrapping determines errors by generating several trials from the original cloud data through sampling with replacement. The properties are measured for each trial cloud, and the uncertainties are estimated from the variance of properties derived from these resampled and remeasured datasets. The final uncertainty in each property is the standard deviation of the bootstrapped values scaled by the square root of the oversampling rate (Rosolowsky & Leroy 2006; Rosolowsky et al. 2008). Other uncertainties in derived properties presented in this work are calculated using the standard propagation of errors.

The properties of the fifteen molecular clouds (leaves) identified by our dendrogram analysis are presented in Table 4.1, and the left panel of Figure 4.2 shows the locations of these clouds. The two right panels in Figure 4.2 show magnified versions of the NMA-8 region. Miura et al. (2010) only detected a single object in this region, but we detected four separate sources and resolved the structure in the brightest source. We discuss this more in Section 4.3.

Table 4.1: Cloud properties derived from ^{13}CO(J=1-0) in NGC 604 using dendrogram analysis. See Chapter 4.1 text for the details on how the properties were derived.

MC ID	RA J2000	DEC J2000	V_{LSR} (km s^{-1})	Δv (km s^{-1})	$L_{^{13}CO}$ K km s^{-1} pc^2	R (pc)	M_{mol} (10^3 $M_\odot$)	M_{vir} 10^3 $M_\odot$)	α_{vir}	Σ_{lum} $M_\odot$ pc^{-2}
L1	$01^h34^m32^s.28$	+30:46:57.07	-245.7	2.4 ± 0.3	498 ± 60	9.8 ± 0.9	11.0 ± 1.0	10.5 ± 2.8	1.0 ± 0.25	36 ± 7
L2	$01^h34^m32^s.73$	+30:46:59.84	-249.1	0.3 ± 0.01	20 ± 3	4.2 ± 0.6	0.4 ± 0.06	0.1 ± 0.0	0.22 ± 0.04	6 ± 2
L3	$01^h34^m33^s.39$	+30:47:01.85	-243.8	0.7 ± 0.1	60 ± 7	5.7 ± 0.5	1.3 ± 0.2	0.6 ± 0.2	0.42 ± 0.12	13 ± 2
L4	$01^h34^m33^s.46$	+30:46:57.98	-244.4	1.3 ± 0.1	78 ± 13	6.9 ± 0.5	1.7 ± 0.2	2.1 ± 0.4	1.2 ± 0.24	11 ± 2
L5	$01^h34^m33^s.54$	+30:46:48.88	-243.1	2.9 ± 0.3	3660 ± 520	13.4 ± 1.2	80.5 ± 11.1	21.3 ± 4.8	0.3 ± 0.06	143 ± 26
L6	$01^h34^m33^s.67$	+30:46:41.92	-241.1	1.9 ± 0.2	672 ± 97	8.1 ± 0.6	14.8 ± 2.0	5.7 ± 1.3	0.4 ± 0.1	72 ± 11
L7	$01^h34^m33^s.13$	+30:46:37.09	-252.0	1.4 ± 0.1	122 ± 17	8.5 ± 0.7	2.7 ± 0.3	3.0 ± 0.5	1.1 ± 0.2	12 ± 2
L8	$01^h34^m33^s.16$	+30:46:31.80	-247.1	1.7 ± 0.2	412 ± 51	13.5 ± 1.2	9.1 ± 0.9	7.1 ± 1.8	0.8 ± 0.2	16 ± 3
L9	$01^h34^m33^s.37$	+30:46:30.44	-252.4	0.8 ± 0.1	47 ± 5	5.3 ± 0.5	1.0 ± 0.1	0.7 ± 0.2	0.7 ± 0.17	12 ± 2
L10	$01^h34^m34^s.18$	+30:46:25.48	-219.2	0.3 ± 0.03	21 ± 3	5.1 ± 0.5	0.5 ± 0.06	0.1 ± 0.02	0.2 ± 0.04	6 ± 1.1
L11	$01^h34^m34^s.49$	+30:46:21.91	-220.5	2.2 ± 0.3	1076 ± 158	15.5 ± 1.8	23.7 ± 4.0	13.6 ± 3.6	0.6 ± 0.17	31 ± 7
L12	$01^h34^m34^s.57$	+30:46:14.66	-217.9	0.5 ± 0.06	32 ± 4	5.0 ± 0.4	0.7 ± 0.1	0.2 ± 0.1	0.3 ± 0.09	9 ± 1.4
L13	$01^h34^m35^s.30$	+30:46:46.12	-223.2	0.4 ± 0.07	40 ± 6	6.3 ± 0.6	0.9 ± 0.1	0.2 ± 0.1	0.25 ± 0.08	7 ± 1.4
L14	$01^h34^m34^s.98$	+30:46:57.35	-229.8	0.8 ± 0.1	114 ± 17	6.6 ± 0.5	2.5 ± 0.3	0.8 ± 0.2	0.31 ± 0.08	18 ± 3
L15	$01^h34^m35^s.80$	+30:46:58.45	-226.5	0.6 ± 0.08	42 ± 6	8.3 ± 0.7	0.9 ± 0.1	0.6 ± 0.2	0.7 ± 0.19	4 ± 1

4.2 Scaling Relations

Figure 4.4 shows the size-linewidth relation for our sources. The clouds in blue are the fifteen clouds identified as resolved substructure (leaves) by our analysis technique, and those in red are the branches which harbor resolved multiple substructures. To investigate whether our molecular clouds are in virial equilibrium, we plot molecular mass versus virial mass in Figure 4.5. In the absence of other forces, the virial parameter, which is the ratio of kinetic to gravitational potential energies, indicates the level of boundedness. The *unbound* ones are those with $\alpha_{vir} > 2$, while the *bound* are those with α_{vir} below 2.

4.2.1 Size - Line width Relation

Figure 4.4 shows the size-linewidth relation for our GMCs. There is a clear trend, with larger clouds having larger linewidths, as is found in Milky Way clouds. The blue solid line is the power-law slope for NGC 604 clouds. The Spearman

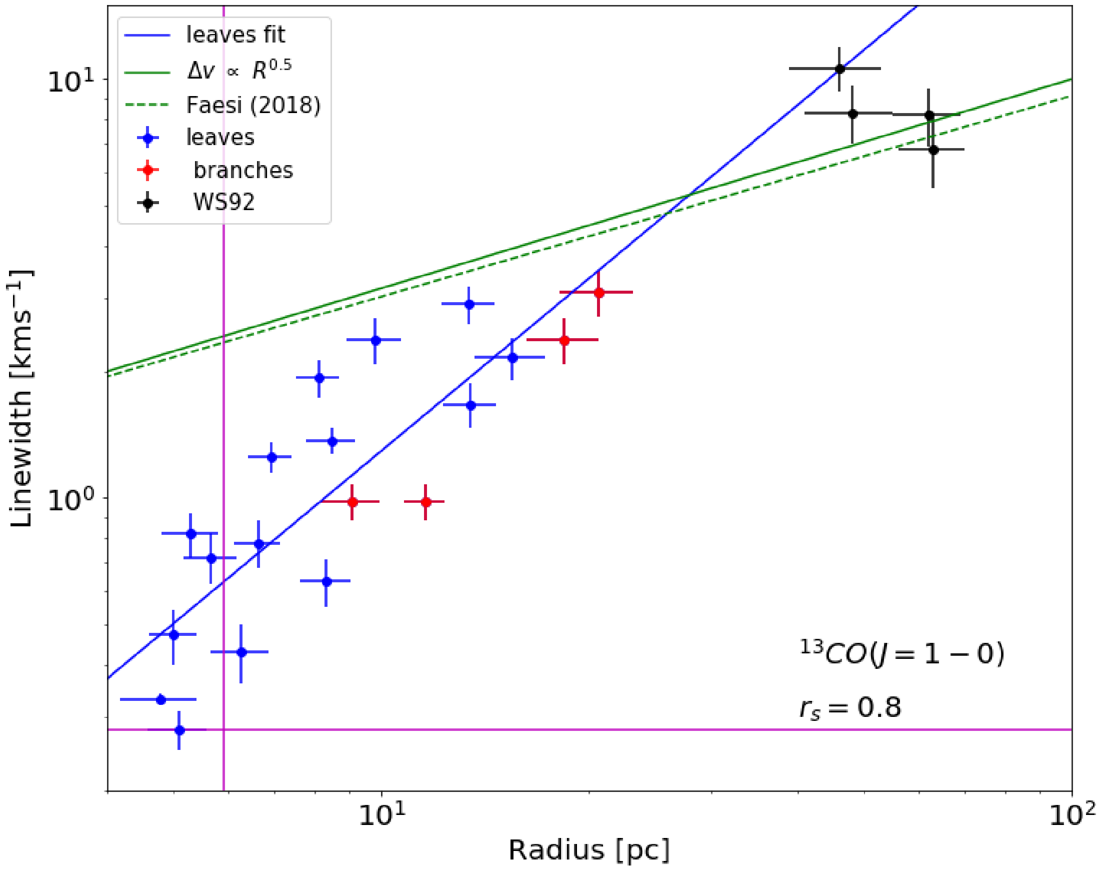

Figure 4.4: Size-linewidth relation of resolved molecular clouds in NGC 604. The blue solid line is the power-law slope for NGC 604 clouds. The green solid and dashed lines are the power-law slopes of Milky Way (Solomon et al. 1987) and extragalactic (Faesi et al. 2018) giant molecular clouds, respectively. The blue and red points represent the molecular clouds identified as leaves and branches in the dendrogram tree, respectively. The black points are the molecular clouds from Wilson & Scoville (1992) in NGC 604. There is a correlation with spearman rank of, $r_s = 0.8$. The purple lines indicate the regions where, based on instrumental resolution (left) and sensitivity (bottom), we do not trust the results.

correlation coefficient for these data has the value of $r_s = 0.8$, which indicates that there is a correlation between size and linewidths of GMCs in NGC 604. We also show in Figure 4.4 the Milky Way power-law slope (green solid line) from Solomon et al. (1987) and the extragalactic slope (green dashed line) from Faesi et al. (2018) for NGC 300. The relation for the NGC 604 clouds does not match the Milky Way and NGC 300 slopes; the linewidths at small radii for the NGC 604 data fall below the Milky Way and NGC 300 relations. In the figure, we plot results from Owens Valley Millimeter-Wave Interferometer done by Wilson & Scoville (1992) (black points). Despite their results having considerable poorer resolution ($8'' \times 7''$ compared to our ALMA $3.2'' \times 2.4''$), there is consistency between the two results on large sizes having large linewidths (Wilson & Scoville 1992, results) and smaller sizes having smaller linewidths (our clouds). The features are a typical characteristics of a turbulent spectrum which has a range of scales with increasing kinetic energy at large scales (McKee & Ostriker 2007). We find their results to be in agreement with both the Milky Way and NGC 300 relations. The purple lines indicate the cut based on the instrumental resolution where below it we do not trust the results. This resolution limit in size is defined as the FWHM of the synthesized beam divided by $\sqrt{8\ln 2}$ and multiplied by 1.91. This gives an instrumental resolution of 5.92 pc in size. Sources below this limit are considered unresolved. How the factor $\sqrt{8\ln 2}$ comes about can be shown easily as below.

When smoothing images and functions using Gaussian kernels, often we convert a given value for full-width at half maximum (FWHM) to the starndard deviation of the filter (sigma σ). The conversion is done as shown below.

The probability density function (pdf) for the Gaussian distribution with mean μ and the standard deviation σ is:

$$\mathrm{f(x)} = \frac{1}{\sigma\sqrt{2\pi}} \mathrm{e}^{-\dfrac{(\mathrm{x}-\mu)^2}{2\sigma}} \tag{4.8}$$

If the filter is centered at the origin, the mean is zero and the FWHM is the distance between $-\mathrm{x_w}$ and $+\mathrm{x_w}$ that produces the half of the peak. For the normal distribution, the mean is the same as the mode (peak) and we have then to find the $\mathrm{x_w}$ that will produce $\mathrm{f(x_w)} = \mathrm{f}(\mu)/2$:

$$\frac{1}{\sigma\sqrt{2\pi}}\mathrm{e}^{-\frac{\mathrm{x_w^2}}{2\sigma^2}} = \frac{1}{2\sigma\sqrt{2\pi}} \tag{4.9}$$

For $\sigma \neq 0$ and solving for $\mathrm{x_w}$:

$$\mathrm{x_w} = \pm\sqrt{2\sigma^2 \mathrm{ln2}} \tag{4.10}$$

The FWHM is $+\mathrm{x_w} - (\mathrm{x_w}) = 2\mathrm{x_w}$:

$$\mathrm{FWHM} = 2\sqrt{2\sigma^2\mathrm{ln2}} = \sigma\sqrt{8\mathrm{ln2}} \tag{4.11}$$

Which gives the common conversion factor of 2.355 and it is the same conversion factor we apply in converting linewith to velocity dispersion when computing virial masses throughout this thesis.

In terms of the linewidth resolution it is determined by channel width divided by $\sqrt{8\ln 2}$ which in our case it is 0.28 $\mathrm{kms^{-1}}$.

4.2.2 Molecular Mass - Virial Mass Relations

The Milky Way observations have shown that the majority of GMCs are in self-gravitational equilibrium (e.g., Larson 1981; Solomon et al. 1987; Heyer et al. 2009; Heyer & Dame 2015). This leads to a direct correlation between M_{vir} and the mass measured through other independent method (in our case the ^{13}CO luminosity). We show in Figure 4.5 that the clouds in NGC 604 are in near virial equilibrium and that the data are strongly correlated, with a Spearman coefficient of $r_s = 0.98$. This agree with recent extragalactic studies of NGC 300 by Faesi et al. (2018) and NGC 1300 by Maeda et al. (2020) have found a strong correlation between M_{vir} and M_{lum} and a low scatter in α_{vir} near unity. Most of the clouds are lying below a one-to-one relation, illustrating that the masses estimated from the luminosities are slightly higher than the virial masses, which is a direct consequence of underestimating linewidths as discussed in the previous Section 4.2.1. These clouds have virial parameters ranging from 0.2—1.1, indicating that some clouds are in virial equilibrium while others could be in a state of forming stars as shown in Figure 4.6. The two green horizontal lines show the region where clouds are expected to be in equilibrium. Most of our sources are below unity. The Wilson & Scoville (1992) data, which are also shown in Figure 4.5, largely seem consistent with the results from NGC 604.

4.3 Discussion

As seen in Figure 3.5, both continuum and ^{13}CO(J=1-0) emission are detected near the centre of the H II region, although at locations further from the centre of the H II region we found only a few locations with ^{13}CO(J=1-0) emission. The regions which are associated with continuum emission are actively forming stars. Muraoka et al. (2020) identified three sources in this region, and following their convention we have labelled the three continuum sources with the abbreviation MMS (millimetre source), with MMS1 corresponding to L5, MMS2 corresponding to L4, and MMS4 corresponding to L1 as seen in the bottom right panel of Figure 3.4. Our MMS2 corresponds to their MMS2, but they were able to resolve the brighter source, which we labelled as MMS1, into two sources labelled MMS1 and MMS3 (which is why we labelled our third source as MMS4).

Regions only detected in ^{13}CO(J=1-0) emission are far out from the center. In these regions, atomic hydrogen (HI) could be forming H_2, and these clouds may form stars as the H II expands. Previous studies in this region have found similar results and suggested that GMCs in NGC 604 are at different evolutionary stages, which would lead to sequential star formation induced by the expansion of the H II region (Tosaki et al. 2007; Miura et al. 2010). To make comparison to the work done previously by Miura et al. (2010), we use the nomenclature for their clouds and identify how many clouds we have resolved in each major GMC. To further ascertain whether the location from the center of the H II has any information, we

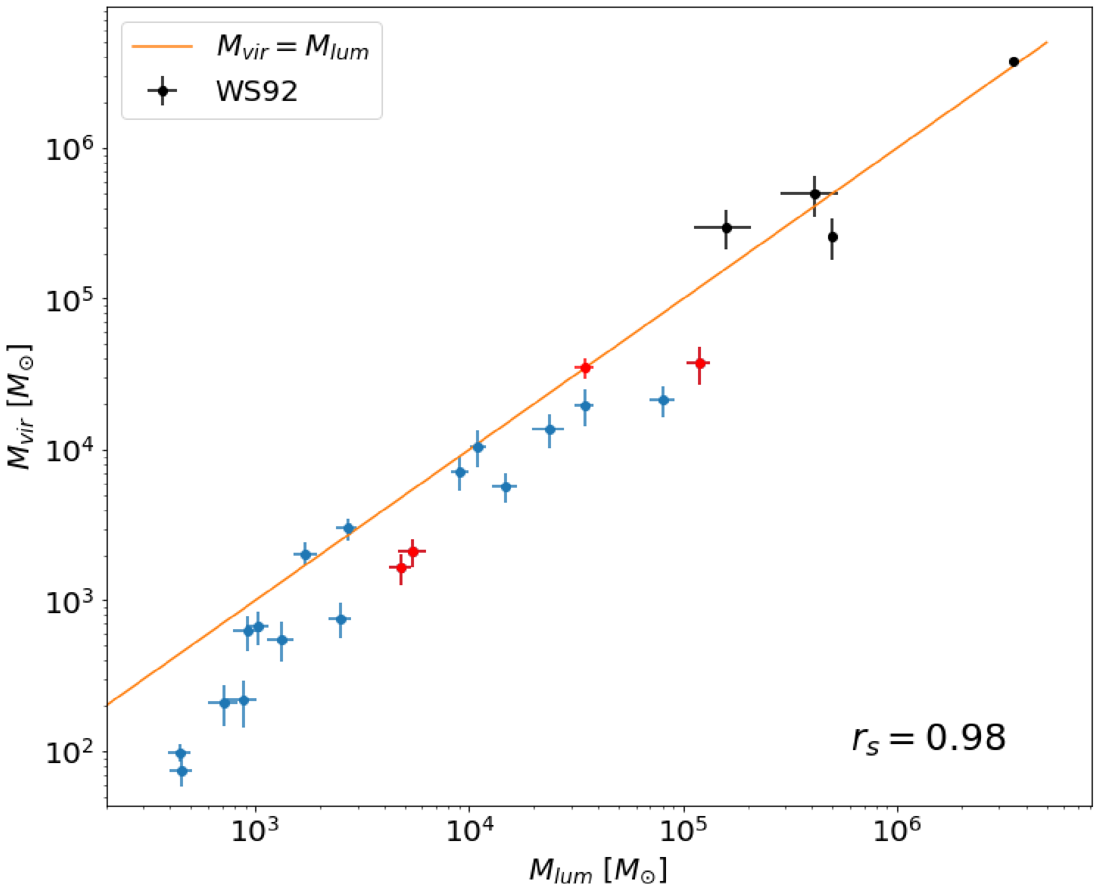

Figure 4.5: Luminosity mass plotted against virial mass. We see a strong correlation between these two parameters with a spearman coefficient of $r_s = 0.98$ indicated in the bottom right corner. The yellow line indicate a one-to-one relation. Despite being correlated most clouds fall below the one-to-one relation. The red, blue and black points are the same as in Figure 4.4.

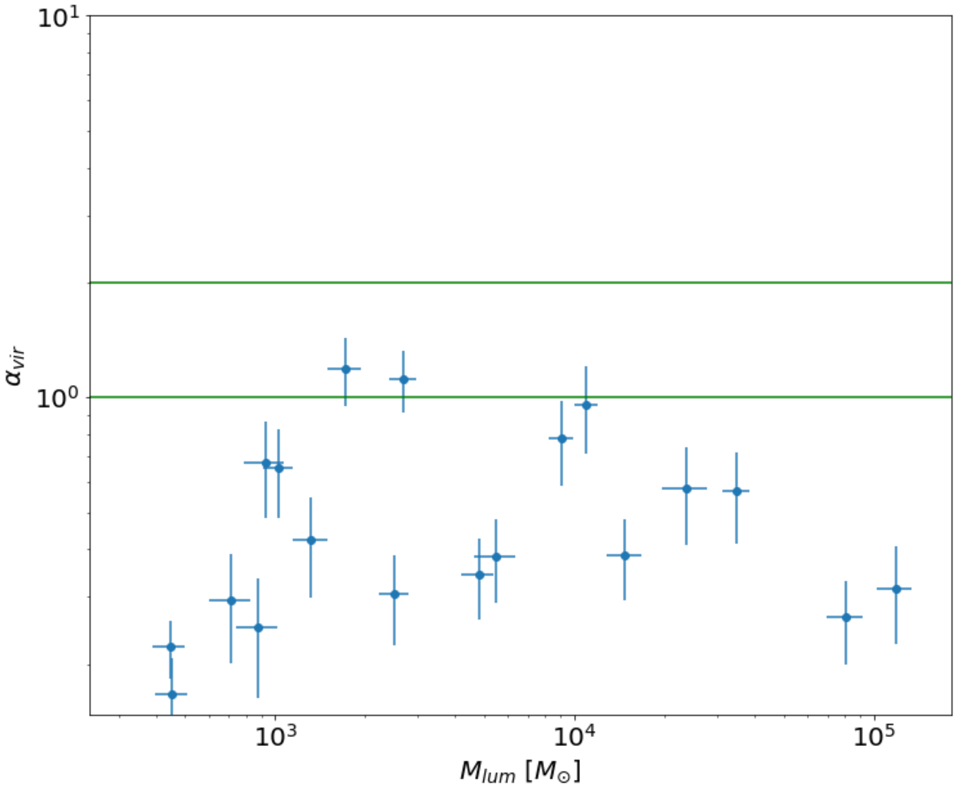

Figure 4.6: Virial parameter plotted against luminosity derived mass. The two green horizontal lines show the region where clouds are expected to be in equilibrium. Most of our sources are below unity, hence, they are likely to be bound too.

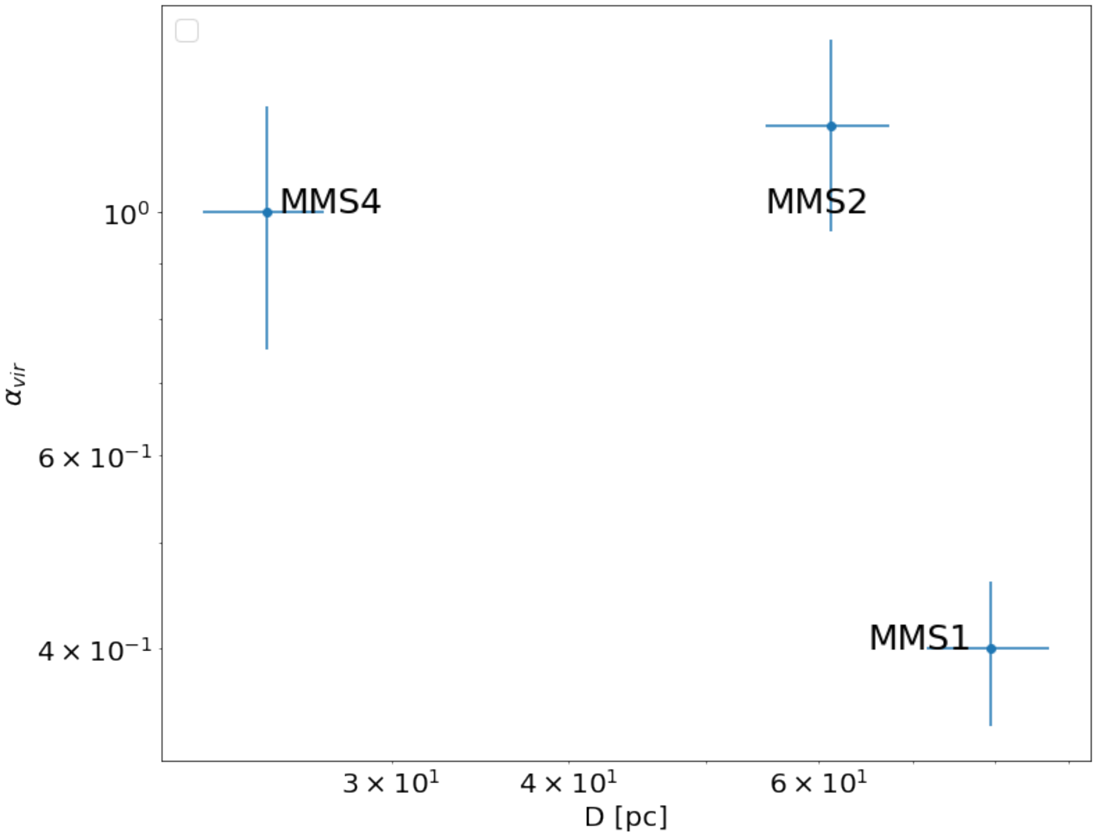

Figure 4.7: Virial parameter plotted against distance of the three continuum sources from the centre of the H II region. We see no trend.

see no trend at all to help understand whether their proximity to the centre has any effect as shown in Figure 4.7.

4.3.1 NMA-8

We have resolved NMA-8, the largest GMC in NGC 604 found by Miura et al. (2010), into four individual molecular clouds that we labelled L3, L4, L5 and L6. It is possible that L5 contains two or more smaller clouds, but we could not separate them into smaller clouds when applying ASTRODENDRO to the ^{13}CO data. Based on the ^{12}CO(J=1-0) observations, NMA-8 is known to be the most massive ($7.4 \pm 2.8 \times 10^5$ M$_\odot$) GMC in the giant H II region (Miura et al. 2010, and references therein). Using ^{13}CO(J=1-0), we estimate a virial mass of $0.8 \pm 0.3 \times 10^5$ M$_\odot$

and a luminosity derived mass of $1.2 \pm 0.2 \times 10^5$ $M_\odot$ in NMA-8, which is a factor of 5 less than the ^{12}CO(J=1-0) molecular mass presented by Miura et al. (2010). This is attributed to ^{13}CO(J=1-0) only tracing the dense gas, hence, resolving away diffuse gas which makes up large scale structure and also to the underestimation of linewidths. Our computed ^{13}CO molecular mass for NMA-8 is comparable to the Orion A GMC, which has an estimated ^{12}CO luminosity mass of 1.1×10^5 $M_\odot$ (Wilson et al. 2005). The NMA-8 molecular mass estimate from ^{13}CO is higher than the virial mass estimated from the linewidths and the spherical radius but in agreement within the errors. The estimated luminosity derived mass of $0.8 \pm 0.1 \times 10^5$ $M_\odot$ in L5 is comparable to Orion B in the Milky Way, which has a mass of 0.82×10^5 $M_\odot$ (Wilson et al. 2005).

The association of L4 and L5 with 104 GHz continuum sources, which is expected to be dominated by free-free emission (e.g. Peel et al. 2011; Bendo et al. 2015, 2016), clearly indicates that they are undergoing star formation. However, the peaks in the ^{13}CO emission from these sources do not coincide exactly with the continuum peaks, as seen in the right zoomed panel of Figure 4.2. The continuum peaks lie closer to the centre of the H II region than the ^{13}CO peaks. This misalignment in this region has been reported previously by Miura et al. (2010). The spatial offset between these peaks is an indication that these two tracers do trace different regions. The continuum appears to trace warm dust associated with the photoionization region. The ^{13}CO(1-0) line, being the lowest J-transition with a very low excitation temperature, preferentially traces cold dense molecular gas away from the centre. It is thus insensitive to the warm gas traced by the continuum emission. Earlier studies in NGC 604 by Muraoka et al. (2012) also found a temperature gradient in the NGC 604 clouds.

4.3.2 NMA-9

We have for the first time resolved NMA-9 into three sources (L7, L8, and L9). NMA-9 is the second massive and second largest complex in the imaged area, with a molecular mass of about $0.6 \pm 0.1 \times 10^5$ $M_\odot$. As we indicated before, the clouds without continuum emission could be places where the atomic gas is currently forming molecular gas, but when the GHR expands, these clouds may form stars.

4.3.3 Other GMCs in NGC 604

We have for the first time resolved NMA-7 into three sources (L10, L11, and L12). Other than L1 associated with NMA 4, these other GMCs are not associated with continuum sources. The properties of these other molecular clouds are listed on Table 4.1.

Generally, the NGC 604 molecular clouds appear to be at different evolutionary stages within the H II region, with some being associated with both continuum and line emission while others only line emission. Additional dendrogram analyses with higher resolution data is necessary to explore these phenomena in more detail. The next Chapter explores the higher resolution data from the same source and two other sources within M33.

Chapter 5

ALMA Band 6 Results

The main area of interest in this Chapter is to investigate the physical properties of molecular clumps in M33 as measured from the higher resolution Band 6 ALMA data in Chapter 3. The investigation of these properties will range from histogram plots, scaling relation plots and cumulative mass distribution plots of the properties.

5.1 Introduction

In this Chapter we explore ALMA Band 6 data for ^{12}CO, ^{13}CO, C^{18}O and 1.3 mm continuum emission. The integrated maps and channel maps for these three giant molecular clouds are shown in Chapter 3. Here we present the source catalogue created following the procedure presented in Chapter 2, and compare the properties of the extracted GMCs and clumps with those in LMC, NGC 6822, and the Milky Way.

5.2 Distribution of Emission in NGC 604, GMC 16 and GMC 8

Intensity integrated maps of ^{12}CO, ^{13}CO, C^{18}O and 1.3 mm continuum emission across NGC 604, GMC 16 and GMC 8 clouds where presented in chapter 3 and are respectively shown in Figures 3.6, 3.8 and 3.9.

The zoomed map in Figure 5.1 shows that the brightest regions in ^{12}CO in NGC 604 are associated with 1.3 mm continuum and C^{18}O. The colour is ^{12}CO, white contours are 1.3 mm continuum and red contours are C^{18}O. What is notable in the image is that C^{18}O is associated with MMS1 and MMS3 but not with MMS2. Since both of these tracers trace the densest gas regions it implies that these regions are likely to form stars or they may actually harbour newly born stars. We find that the MMS2, which does not have C^{18}O, is near the centre of the HII region with more than 200 OB stars (Relaño & Kennicutt 2009) as compared to MMS1 and MMS3 which are further from the centre. The absence of C^{18}O detection of MMS2 has been described before as due to the selective photodissociation of C^{18}O molecules due to the far-UV radiation as it sits between the two strong overlapping shells of H$_\alpha$ emission (Muraoka et al. 2020) as in similar cases with Galactic molecular clouds (Buckle et al. 2012; Shimajiri et al. 2014). The continuum emission absence in other regions where we detect line emission could be due to limited sensitivity of the instrument.

In Figure 5.2, we show a zoomed in image of GMC 16's brightest source. All the colours and contours are the same as those in Figure 5.1. The labelling is the same. In GMC 16 we detect C^{18}O and 1.3 mm continuum at the brightest spot in ^{12}CO emission only. It is high likely that this region star formation has been or is about to be triggered.

The emission detected in NGC 604 in ALMA Band 6 data have shows most structures from Band 3 data presented in Chapter 4 have been resolved out. The ^{13}CO(1-0) presented in chapter 4 for ALMA Band 3 emission associated with

Table 5.1: 1.3 mm continuum emission

Source ID	Wavelength	Size	Flux density	M_d	M_{total}^{MMS}	Cloud
	(mm)	pc	mJy	$M_\odot$	$M_\odot$	
MMS1	1.3	11.7 × 5.4	10.50 ± 0.04	128.50 ± 0.49	3.9×10^4	NGC 604
MMS2	1.3	5.9 × 2.7	3.91 ± 0.05	47.85 ± 0.61	1.4×10^4	NGC 604
MMS3	1.3	7.6 × 2.6	2.03 ± 0.08	24.84 ± 0.98	0.7×10^4	NGC 604
MMS	1.3	4.59 × 2.41	2.90 ± 0.16	35.49 ± 1.96	1.1×10^4	GMC 16

NMA 9 is completely resolved out with Band 6 data of the same region and same tracer leaving just little spots of emission. Higher transition (Band 6) CO resolves out most extended structures and only retains the denser ones. We see such distribution of structures (emission) in $^{13}CO(2-1)$ which are associated with NMA 8 and less in NMA 9. This indicates that much of the dense gas is associated with NMA 8 (L3, L4, L5, and L6 from Chapter 4) and not NMA 9.

From the three MMSs in NGC 604 and one MMS in GMC 16, we computed their sizes and dust mass. We assume a temperature of 22 K from Tabatabaei et al. (2014). We use Equation 1.25 to compute the dust mass:

$$M_d = \frac{k_{1.3mm} F_\nu D^2}{B(\nu, T_d)}. \tag{5.1}$$

where M_d is the dust mass, F_ν is the flux density at frequency ν, $B(\nu, T_d)$ is the Planck function at 1.3 mm wavelength, and dust temperature T_d, D is the distance to the source and $k_{1.3mm} = 1\ cm^2 g^{-1}$ (Ossenkopf & Henning 1994) is the dust absorption coefficient at frequency ν. The results of the size, dust mass and total mass of the MMS (M_{total}^{MMS}) taking the gas-to-dust ratio of 300 (Relaño et al. 2018) are tabulated in Table 5.1. These masses are similar (despite assuming different k_ν) to those from Hi-Gal clumps in the Milky Way presented earlier in Figure 1.10 (Elia et al. 2017).

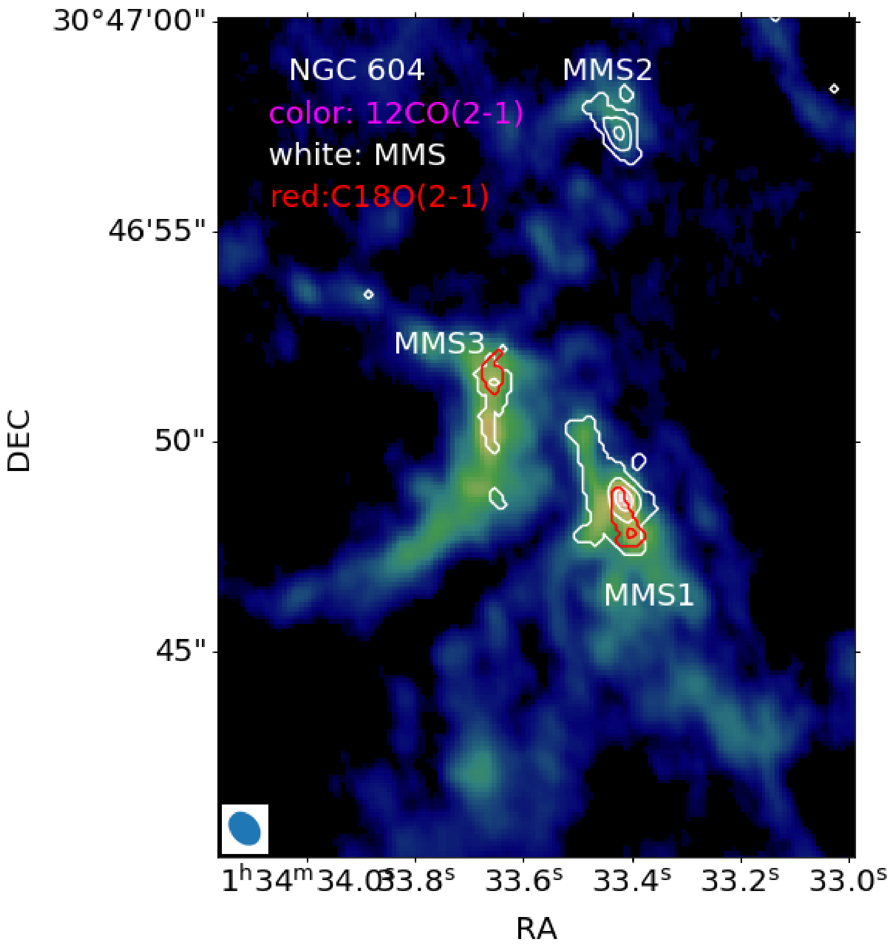

Figure 5.1: NGC 604 ^{12}CO in colour overlaid with C^{18}O (red contours) and 1.3 mm continuum (white contours) emission. The MMS1 and MMS2 are associated with C^{18}O while in MMS2 we do not detect C^{18}O.

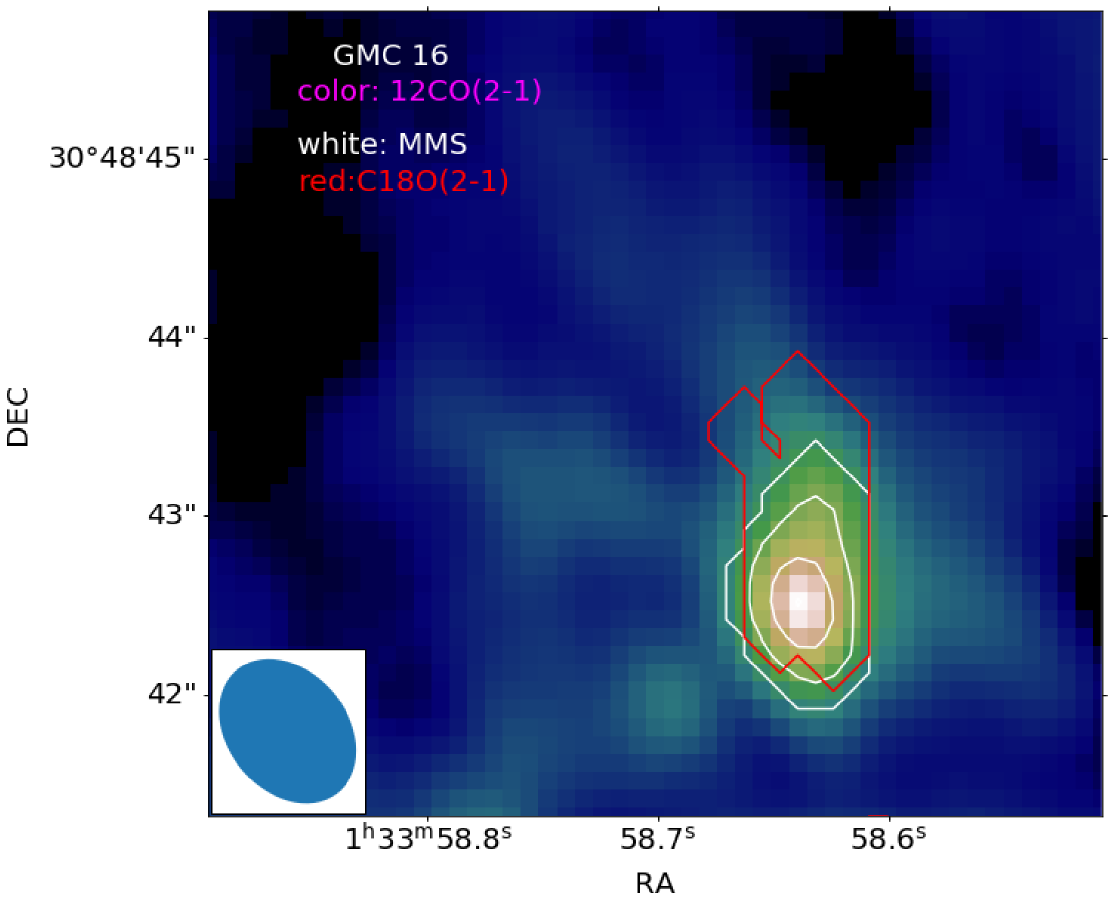

Figure 5.2: GMC 16 ^{12}CO in colour overlaid with C^{18}O (red contours) and 1.3 mm continuum (white contours) emission. The C^{18}O and 1.3 mm continuum is only detected on the brightest source in ^{12}CO.

5.3 Clumps Identification

The process of clump identification is the same as that of GMCs discussed in Chapter 2. Parameters were chosen so that the algorithm could identify local maxima in the cube above the $S_{min} = 3\sigma_{rms}$ level that were also $\Delta_S = 2.5\sigma_{rms}$ above the merge level with adjacent structures. Isorsurfaces surrounding the local maxima were categorized as branches or leaves based on whether they were the largest contiguous structures, intermediate in scale (branches) or had no resolved substructure (leaves). These parameters were used for all ^{12}CO and ^{13}CO data cubes from NGC 604, GMC 16 and GMC 8.

The resulting dendrogram tree for the ^{12}CO(J=2-1) and ^{13}CO(J=2-1) in NGC 604 is shown in Figure 5.3 left and right respectively. We identified 522 structures (branches and leaves) in the entire dendrogram tree, consisting of 301 leaves, using the above parameters for ^{12}CO. We further identify 337 structures were 216 are leaves from the ^{13}CO dendrogram tree. There is a reduction of 85 in the number of leaves which represent clumps in our sources. This represents 28% of the sources not detected with the ^{13}CO tracer. The ellipses obtained from the dendrogram tree leaves are plotted on the integrated maps of both ^{12}CO(J=2-1) and ^{13}CO(J=2-1) maps as shown in Figure 5.4 and 5.5 respectively.

For GMC 16, the resulting dendrogram tree for the ^{12}CO(J=2-1) and ^{13}CO(J=2-1) is shown in Figure 5.6 left and right respectively. We identified 345 structures (branches and leaves) in the entire dendrogram, consisting of 197 leaves, using the above parameters for ^{12}CO. We further identify 239 structures where 153 are leaves from the ^{13}CO dendrogram tree. There is a reduction of 44 in the number of leaves which represent clumps in our sources. This represents 22% of the sources not detected with the ^{13}CO tracer. The ellipses obtained from the dendrogram trees are plotted on the integrated maps of both ^{12}CO(J=2-1) and ^{13}CO(J=2-1) maps as shown in Figure 5.7 and 5.8 respectively.

In terms of GMC 8, the resulting dendrogram tree for the ^{12}CO(J=2-1) and ^{13}CO(J=2-1) is shown in Figure 5.9 right column. We identified 212 structures

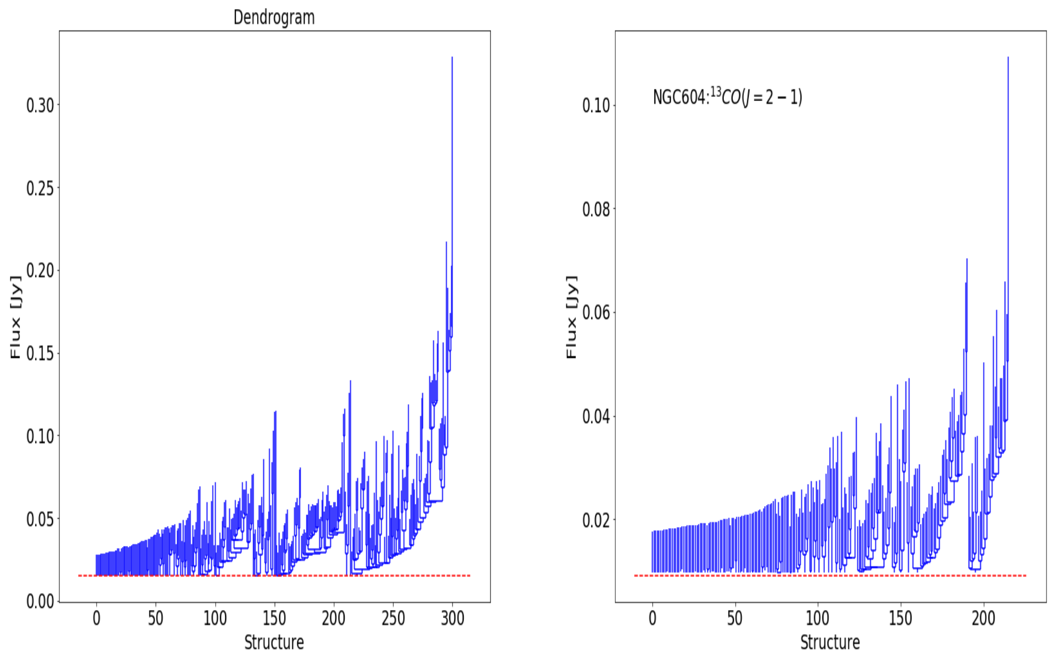

Figure 5.3: NGC 604 dendrogram trees where left is for ^{12}CO(J=2-1) and the right is for ^{13}CO(J=2-1). The horizontal red line represents a 3 σ cut, below this line dendrogram stops identifying structures.

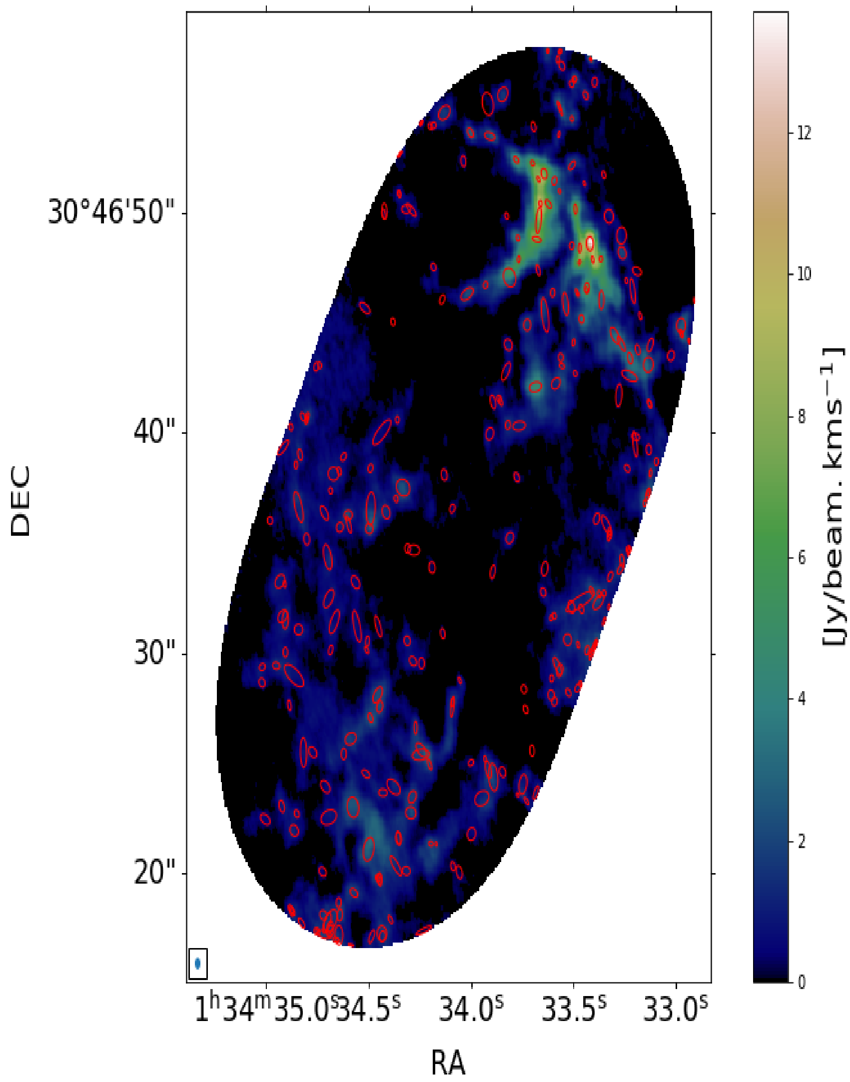

Figure 5.4: NGC 604 ^{12}CO(J=2-1) dendrogram trees ellipses from leaves are plotted on the integrated map.

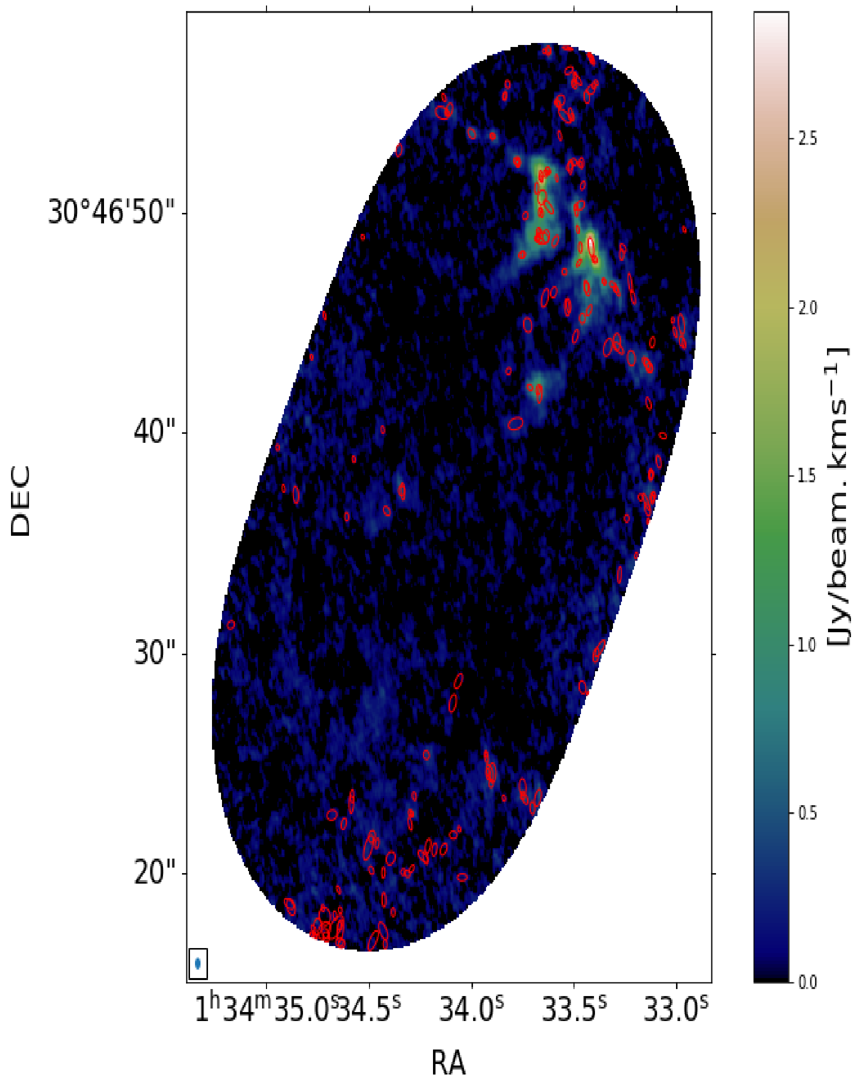

Figure 5.5: NGC 604 ^{13}CO(J=2-1) dendrogram trees ellipses from leaves are plotted on the integrated map.

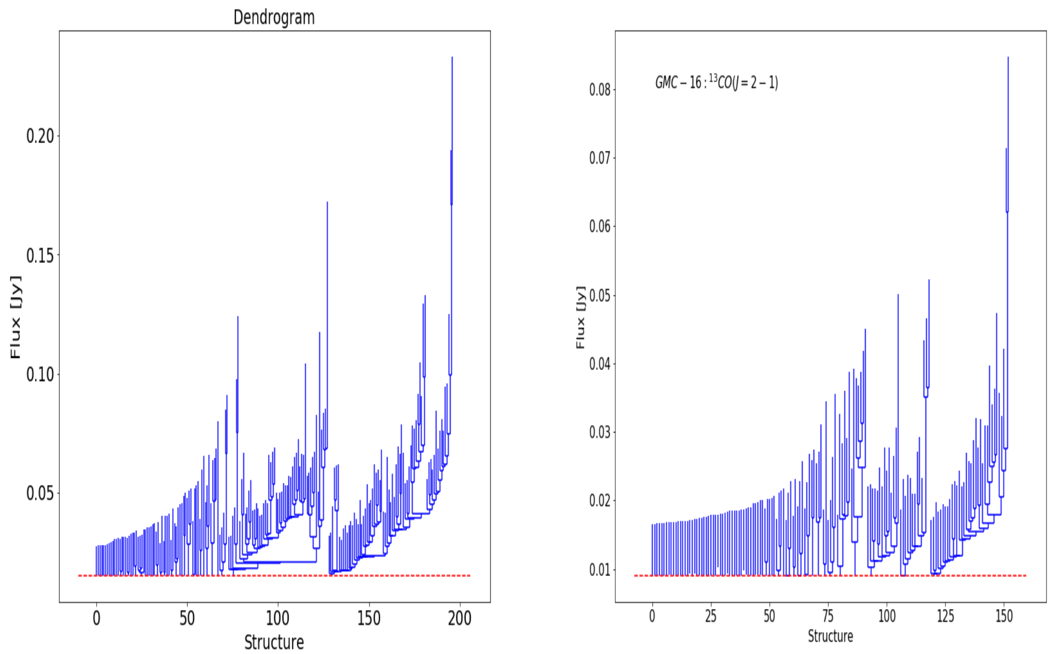

Figure 5.6: GMC 16 dendrogram trees where left is for ^{12}CO(J=2-1) and the right is for ^{13}CO(J=2-1). The horizontal red line represents a 3 σ cut, below this line dendrogram stops identifying structures.

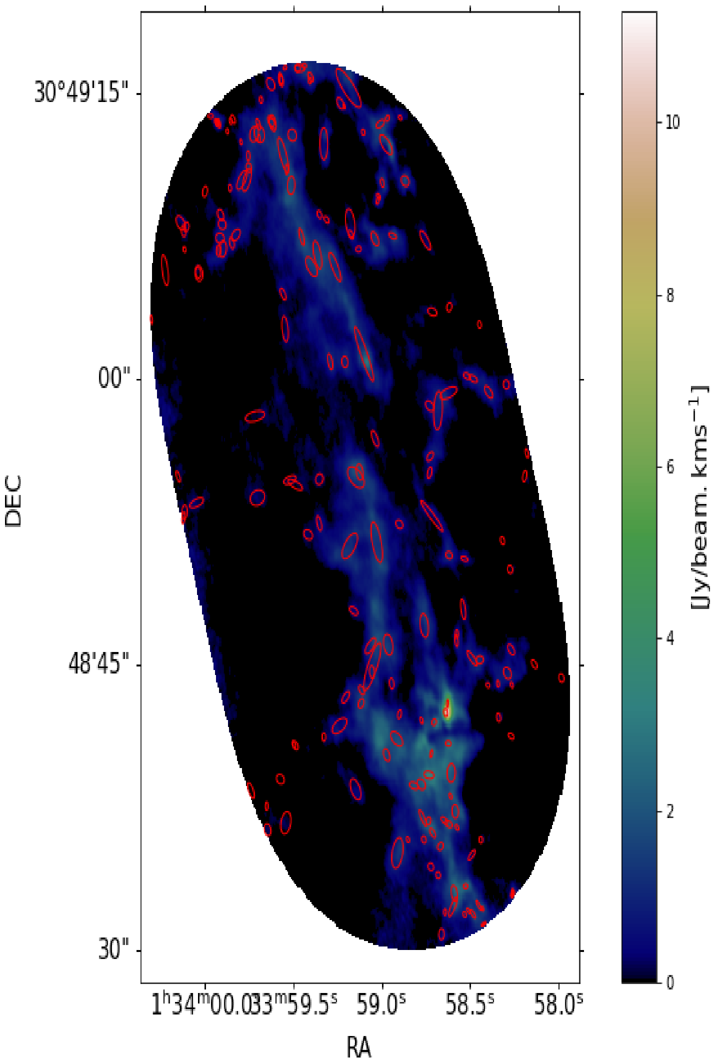

Figure 5.7: GMC 16 ^{12}CO(J=2-1) dendrogram trees ellipses from leaves are plotted on the integrated map.

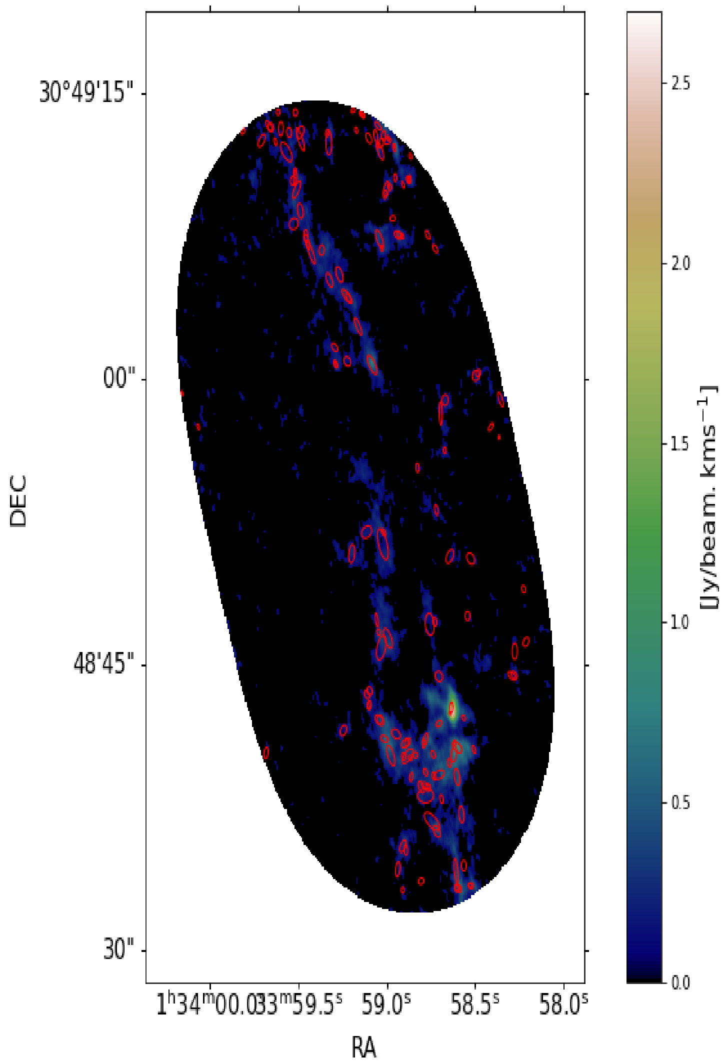

Figure 5.8: GMC 16 $^{13}CO(J=2\text{-}1)$ dendrogram trees ellipses from leaves are plotted on the integrated map.

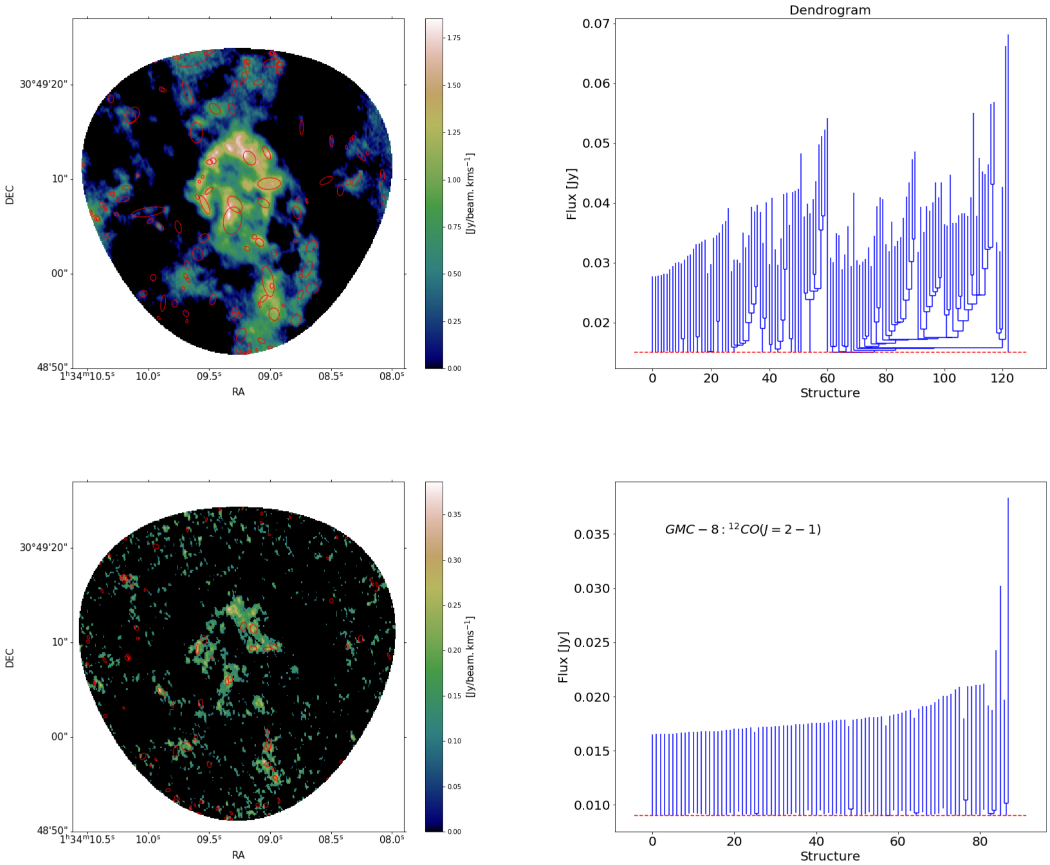

Figure 5.9: GMC 8 dendrogram trees are shown to the right side and their ellipses from leaves are plotted on the integrated maps to the left. The top row is for ^{12}CO(J=2-1) and the bottom row is for ^{13}CO(J=2-1). The horizontal red line represents a 3 σ cut, below this line dendrogram stops identifying structures.

(branches and leaves) in the entire dendrogram, consisting of 123 leaves, using the above parameters for ^{12}CO. We further identified 96 structures where 88 are leaves from ^{13}CO dendrogram tree. There is a reduction of 35 in the number of leaves which represent clumps in our sources. This represents 28% of the sources not detected with the ^{13}CO tracer. Generally, there is continuous reduction on the difference between ^{12}CO clumps and ^{13}CO clumps in all the three GMCs. This reduction is systematic from clumps associated with massive star formation GMC (NGC 604) to clumps associated with quiescent cloud (GMC 8). Whether these differences arise from physical properties of these different types of clouds would need a further investigation in future. Dendrogram leaves derived from both ^{12}CO$(2-1)$ and ^{13}CO$(2-1)$ are shown on top of integrated maps in Appendix B and their catalogues (clumps) are shown in Appendix C.

5.4 Histograms of Clumps Properties in M33

The physical properties of clumps are computed using the same methods as those used in Chapter 4 for molecular clouds in NGC 604. The luminosity derived mass computation takes into consideration the scaling factor from the CO lower transition of J=1-0 to the higher transition of J=2-1, which is 0.8 for M33 (Druard et al. 2014).

5.4.1 Size

Figure 5.10 top row, shows the histograms of the distributions of their deconvolved radii for ^{12}CO clumps (left panel) and ^{13}CO clumps (right panel).

The histograms show that the ^{12}CO clumps are all smaller than 10 pc in size with an average beam size for the images of 2 pc $\times$ 1 pc. The colour codes in the plots represent the clumps from three GMCs, with blue representing the clumps in NGC 604, black for GMC 16 and green for GMC 8. These colour codes have been kept this way throughout this chapter. There are more clumps with size below 4 pc which is comparable to those studied in our galaxy (Pineda et al. 2009a; Elia et al. 2017; Mazumdar et al. 2021, and the references therein), NGC6822 (Schruba et al. 2017) and the LMC (Pineda et al. 2009b; Wong et al. 2017, 2019). ^{13}CO clumps in NGC 604 have sizes that go up to slightly above 3 pc. ^{13}CO traces denser clumps which are not associated with diffuse gas. The red vertical lines show the median value of the three GMC clumps distribution in all the histograms in this work. We find the median value of 1.26 pc for ^{12}CO clumps and 1.13 pc for ^{13}CO clumps.

5.4.2 Mass

The bottom row of Figure 5.10, shows the ^{12}CO luminosity derived mass histogram in NGC 604 (left panel) and the ^{13}CO luminosity derived mass histogram (right panel). The colour coding on the histograms is the same as those indicated in the histograms for the size distribution. The ^{12}CO mass distribution ranges from 10 $M_{\odot}$ up to 10^4 $M_{\odot}$ while that for ^{13}CO ranges from 10 $M_{\odot}$ to slightly below 10^4 $M_{\odot}$. We find median values of 216 $M_{\odot}$ for ^{12}CO clumps and 73 $M_{\odot}$ for ^{13}CO clumps in luminosity mass.

Figure 5.11 top row, shows ^{12}CO virial mass histograms (left panel) and ^{13}CO virial mass histograms (right panel). The ^{12}CO virial mass distribution ranges from 10 $M_{\odot}$ up to 10^4 $M_{\odot}$ while that for ^{13}CO ranges from 10 $M_{\odot}$ to slightly below 10^4 $M_{\odot}$. We find a median value of 73 $M_{\odot}$ for ^{12}CO clumps and 26 $M_{\odot}$ for ^{13}CO clumps in virial mass.

5.4.3 Surface Density

Surface density distributions are shown in the bottom row of Figure 5.11. We compute the surface density using Equation 4.6. In both plots we find that the surface density goes roughly up to 10^3 $M_{\odot}/pc^2$. We find median values of 57 $M_{\odot}/pc^2$ for ^{12}CO clumps and 18 $M_{\odot}/pc^2$ for ^{13}CO clumps in virial mass.

5.4.4 Virial Parameter

Figure 5.12 shows the virial parameter distributions for both ^{12}CO and ^{13}CO. The vertical red line indicates the average median value for the three clouds. We find a median value of 0.17 for ^{12}CO clumps and 0.07 for ^{13}CO clumps. The virial parameters in both plots show that majority are below unity. We explore this more in Section 5.5.3.

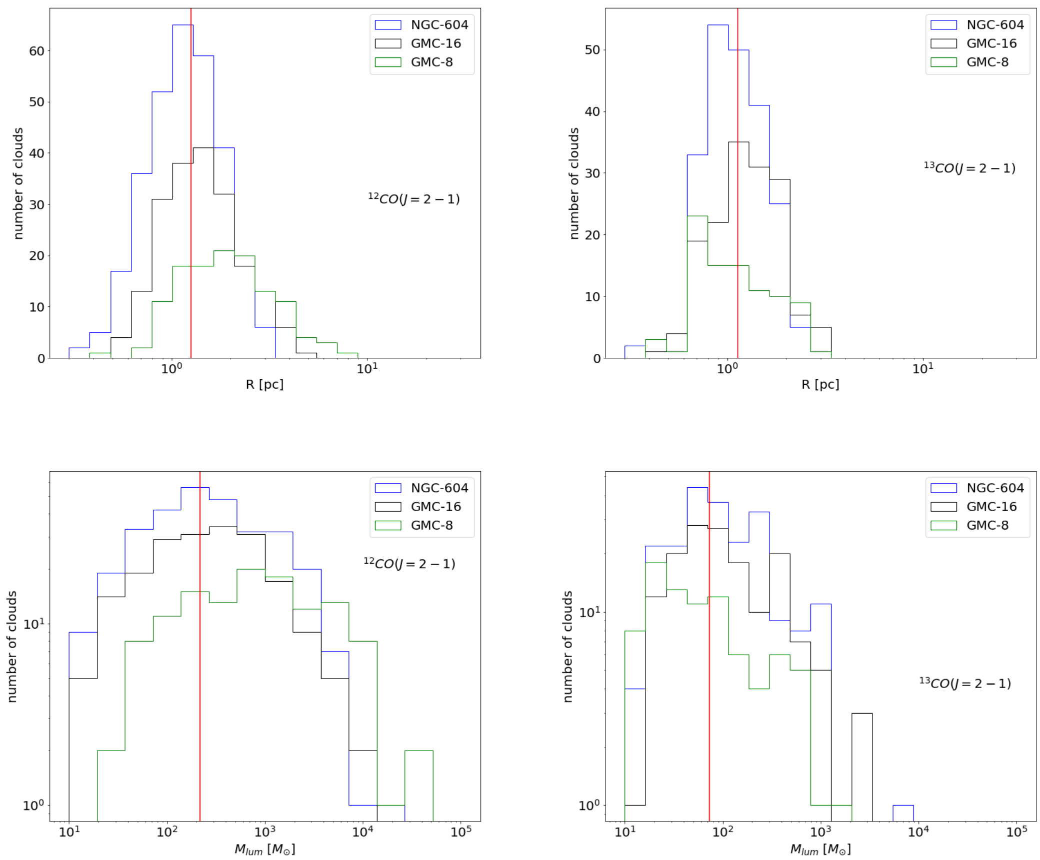

Figure 5.10: (top-left) ^{12}CO clump size distribution with size below 10 pc and ^{13}CO clump size distribution (top-right) with size below 4 pc. The red vertical lines show the average median value of the three GMC clump size distributions. (Bottom-left) ^{12}CO luminosity derived mass histograms and (bottom-right) ^{13}CO luminosity derived mass histograms for all three GMCs. Their clump masses all go up to 10^4 $M_\odot$.

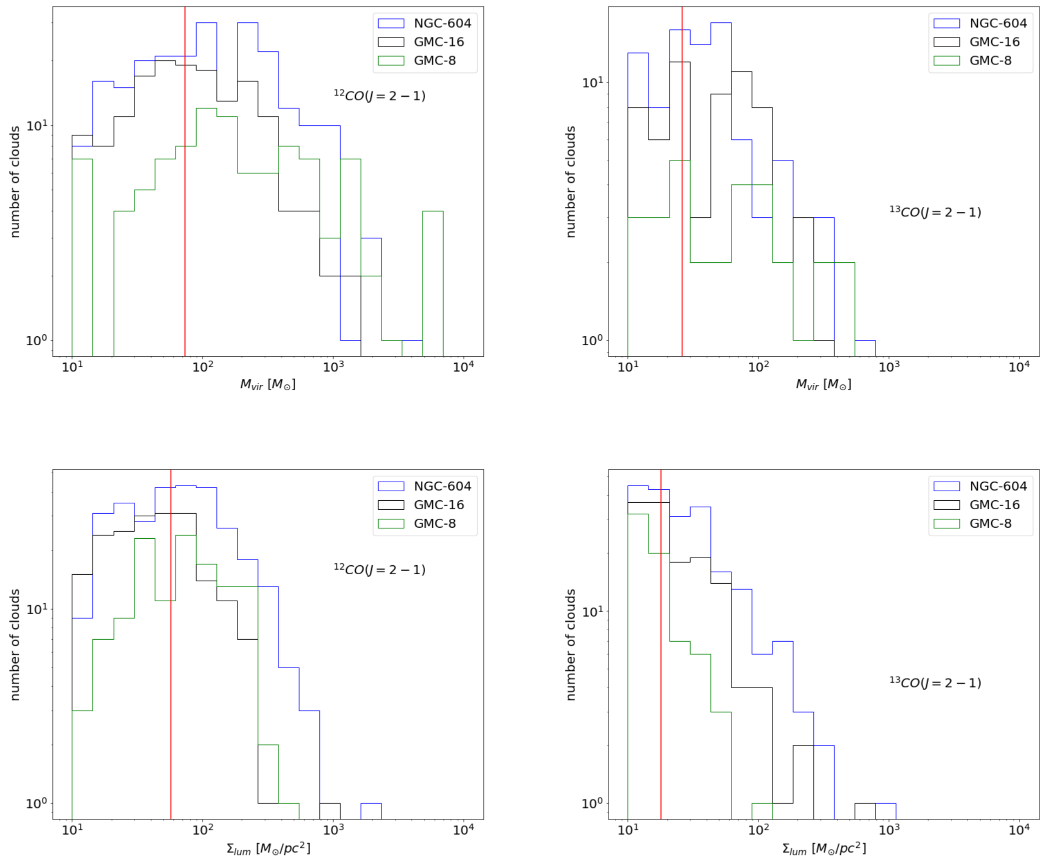

Figure 5.11: Top row: histogram distribution of virial masses in both ^{12}CO (left) and ^{13}CO (right). Most ^{12}CO clumps have masses less than 10^3 $M_\odot$ and ^{13}CO clumps are below $10^{2.5}$ $M_\odot$. The bottom row shows the surface density distribution for ^{12}CO (left) and ^{13}CO (right) with most of the ^{12}CO clumps having surface densities between 10^1 and $10^{2.8}$ $M_\odot/pc^2$ while ^{13}CO ranges from $10^1 - 10^{2.5}$ $M_\odot/pc^2$. The red vertical lines show the average median value of the three GMC clump virial mass and surface density distributions.

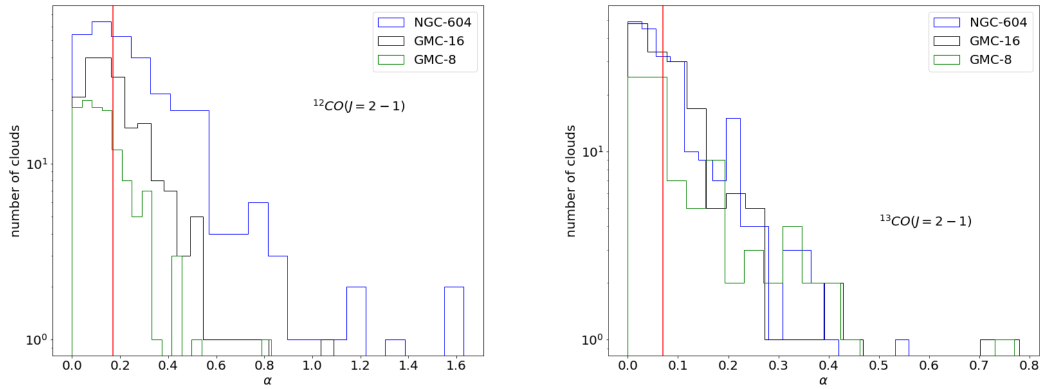

Figure 5.12: The distribution of virial parameters which shows whether the clumps are in virial equilibrium or not. The left panel is for the ^{12}CO clumps virial parameter distribution and the right panel for ^{13}CO clumps. In both nearly all the clumps' virial parameters are below unity indicating they are not in virial equilibrium. The red vertical lines show the average median value of the three GMC clump virial parameter distribution.

5.5 Clumps Scaling Relation

Studies of the properties of clumps have shown them to have correlations between different properties both in our own Galaxy (Rice et al. 2016; Elia et al. 2017) and in external galaxies (Schruba et al. 2017; Wong et al. 2017, 2019). Some Galactic studies of clumps follow the GMC scaling relations, as discussed in Section 1.4. On the other hand, other studies done in external galaxies have shown no correlation between size and linewidth (Colombo et al. 2014; Maeda et al. 2020).

To characterise the relations between cloud properties, we fit linear relations between the logarithmic properties. We utilize the KMPFIT module of the Python package kapteyn (Terlouw & Vogelaar 2016). This provides nonlinear least-squares fitting of user specified functions. In order to take into account the estimated errors for the slopes and intercepts, we follow the procedure by Wong et al. (2017). This is done in such a way that an initial estimate of the slope and intercept is obtained using an unweighted least-square fit code in `scipy.stats.linregress` which optimizes these parameters in KMPFIT after weighting each sample by the inverse of its effective variance. This effective variance method does assume that an error δx_i in x_i changes the value of y_i by an amount $f'(x_i)\delta x_i$, which can be added in quadrature to the error δy_i in y_i. The KMPFIT code provides the standard error.

In the subsections below, we investigate the scaling relations based on the physical properties that we have given above ranging from size, linewidths, masses, surface density and virial parameter.

5.5.1 Size - Linewidth Relations

Figure 5.13 shows plots for the size-linewidth relation for ^{12}CO (left) and ^{13}CO (right). The open shapes are hierarchical structures within the GMC identified by trunks of the dendrogram tree. The filled shapes represents the leaves of the dendrogram and sources without resolved substructure, which we refer to as clumps. The sources in blue are from NGC 604, those in black are from GMC 16 and the ones in green are from GMC 8. The colour code is maintained for the other plots made based on this data. The yellow solid line is the Milky Way slope for GMC studies (Solomon et al. 1987). The clumps in M33 match this Galactic relation, especially at larger scales. At smaller scales there is a spread in linewidth which could be due to limited resolution.

The sources in Figure 5.13 were fitted using KMPFIT with a power-law of the form,

$$\mathrm{logV} = \beta \mathrm{logR} + \mathrm{C} \tag{5.2}$$

where β is the slope and C the intercept of the fitted line; equivalent to $\mathrm{V} \propto \mathrm{R}^{\beta}$. The solid lines (blue, black, and green) show the individual R-Δv relations for the three clouds in ^{12}CO and ^{13}CO respectively. If β is $\dfrac{1}{3}$ it is interpreted as evidence of incompressible Kolmogorov turbulence (Larson 1981) while if β is $\dfrac{1}{2}$ it suggests that the relationship arises from clouds virial equilibrium (Solomon et al. 1987). This has been explored in detail in Section 1.4.

Table 5.2: Power-law slopes fitted for size - linewidth relation in the form of $\log V = \beta \log R + C$ where β is the slope and C is the intercept.

	^{12}CO		^{13}CO		
Cloud	β	C	β	C	references
30 Dor	0.61± 0.03	0.23 ± 0.01	0.58± 0.06	0.16± 0.02	Wong et al. (2017)
PCC	0.51± 0.02	-0.47± 0.01	0.91± 0.14	-0.53± 0.04	Wong et al. (2017)
Milky Way	0.5	0.72	-	-	Solomon et al. (1987)
NGC 604	0.86± 0.03	-0.34± 0.01	1.39± 0.06	-0.72± 0.02	this work
GMC 16	0.75± 0.02	-0.50± 0.02	1.24± 0.05	-0.84± 0.02	this work
GMC 8	0.95 ± 0.04	-0.59± 0.03	1.52± 0.11	-0.90± 0.03	this work

The results of fitting power-law exponents to the ^{12}CO and ^{13}CO data are listed in Table 5.2 alongside several literature values for comparison. The exponents for ^{12}CO are in the range 0.75 - 0.95 while those for ^{13}CO are in the range 1.24 to 1.52. The slopes from the fits are higher than the Galactic value of 0.5 (Solomon et al. 1987) which is labelled in the plot of Figure 5.13. There is a significant scatter in linewidth at lower scales (sizes) in our size - linewidth relation. It is possible that the slopes are higher than the Galactic value due to the sharp tail at lower scales which pulls the fits down compared to the Galactic slope. The other important information in Figure 5.13 is that the linewidths of the leaves range up to 3 kms^{-1} and sizes ranging up to 10 pc.

5.5.2 Molecular Mass - Virial Mass Relations

The two CO-based mass estimators, the luminous mass ($M_\odot$) based on the integrated CO flux assuming a constant X_{CO} factor, and the virial mass M_{vir} based on the radius and linewidths are compared in this section.

Figure 5.14, shows a plot of luminosity against virial mass. It can be seen that ^{12}CO luminosity scales linearly with virial mass as well as ^{13}CO luminosity. The power-law exponents from fitting the luminosity against virial mass is labelled on

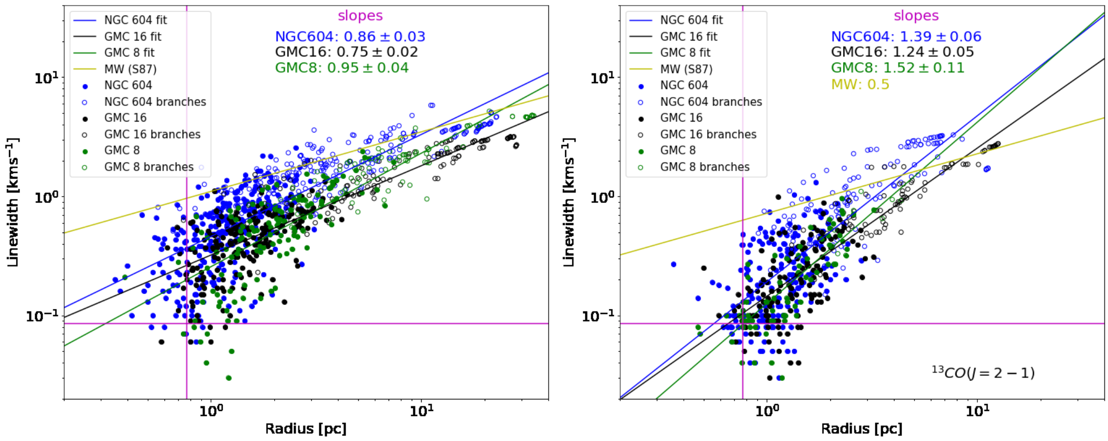

Figure 5.13: Size-linewidth plot for ^{12}CO (left) and ^{13}CO (right). The purple cross lines are instrumental resolution limit in both size (vertical) and linewidth (horizontal). The sources in blue are from NGC 604, those in black in GMC 16 and green from GMC 8. The filled circles are leaves (clumps) and open circles are branches (clouds). Slopes are fitted to the sources from each GMC and the lines are presented in the colours of their sources. Power-law exponents are indicated at the top of each plot. The yellow solid line is the power-law slope for Galactic GMC studies from Solomon et al. (1987).

the plot. The fits appear to have a constant ratio of integrated luminosity to virial mass, which might be expected if there is a constant alpha ratio ($\alpha_{\rm CO}$). Such results in GMC studies have been reported where virial mass scales very well with luminosity (Solomon et al. 1987; Wong et al. 2017).

Figure 5.15 top panels show their correlation for ^{12}CO (left panel) and ^{13}CO (right panel). Both mass estimates appear below the one-to-one relation with luminosity mass generally being larger than the virial mass in both ^{12}CO and ^{13}CO.

In Figure 5.15 bottom panels we show the luminosity derived mass against virial mass with the luminosity derived mass derived assuming the Galactic CO conversion factor of 2×10^{20} Kkms^{-1}pc^2 (Bolatto et al. 2013). Most sources in ^{12}CO are in virial equilibrium and those from ^{13}CO are below the one-to-one relation but near the equilibrium. The power-law exponents of the properties are labelled in all the plots of Figure 5.15.

Taking from the power-law exponents values of ^{12}CO sources whose masses have been computed using the $X_{\rm CO}$ conversion factor of 4×10^{20} cm^{-1}(Kkms^{-1})$^{-1}$ (Gratier et al. 2010; Druard et al. 2014), we conclude that the sources are in near virial equilibrium. This is the similar case for ^{13}CO which are in near virial equilibrium too.

5.5.3 Virial Parameter - Luminosity mass relations

The virial parameter, α, which is a ratio of virial mass against luminosity mass is plotted in Figure 5.16 top panels. Both ^{12}CO (left) and ^{13}CO (right) clumps fall below the $\alpha = 1$ line. The clumps (clouds) that have a virial parameter of 1 are in virial equilibrium while those above 2 are not gravitationally bound and will disperse without forming stars. The ones below 1 are said to have been triggered and in the process of star formation and if not they are being supported by magnetic fields (Faesi et al. 2018).

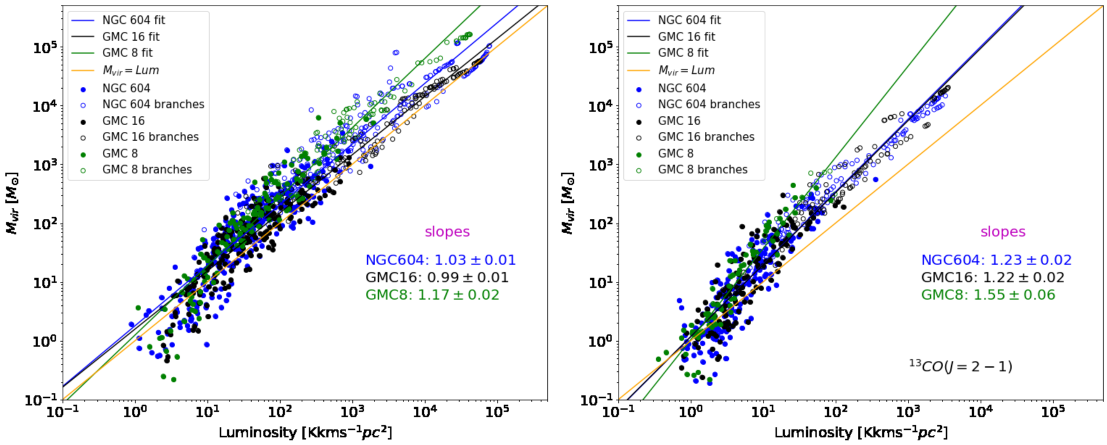

Figure 5.14: The relationship between luminosity and virial mass is presented for ^{12}CO (left) and ^{13}CO (right). The yellow line is a one-to-one relation. We see that there is a one-to-one relation at clump scales (leaves) but not at cloud (branches) scales as the sources are above the one-to-one relation.

Several studies have found clumps that have α below unity (sub-virial) especially the most massive of them (Roman-Duval et al. 2010; Kauffmann et al. 2013; Tan et al. 2013; Urquhart et al. 2014; Traficante et al. 2018, 2020). A recent study of Galactic clumps in the Gould Belt by Singh et al. (2021) did not find clumps to be subvirial. They argue that several types of systematic errors can enhance the appearance of low kinetic-to-gravitational energy ratios. The suggested systematic errors are: insufficient removal of foreground and background material, ignoring kinetic energy associated with velocity differences across a resolved cloud and over-correcting for stratification when evaluating the gravitational energy. Having adopted a method which avoids such errors, they found that clumps had virial motions and were not subvirial. Our results here conform to what many studies have found which is that most clumps have $\alpha < 1$, an indication that they are subvirial. In future, it would be good to try using their method on our data and see if we may arrive at their conclusion or not.

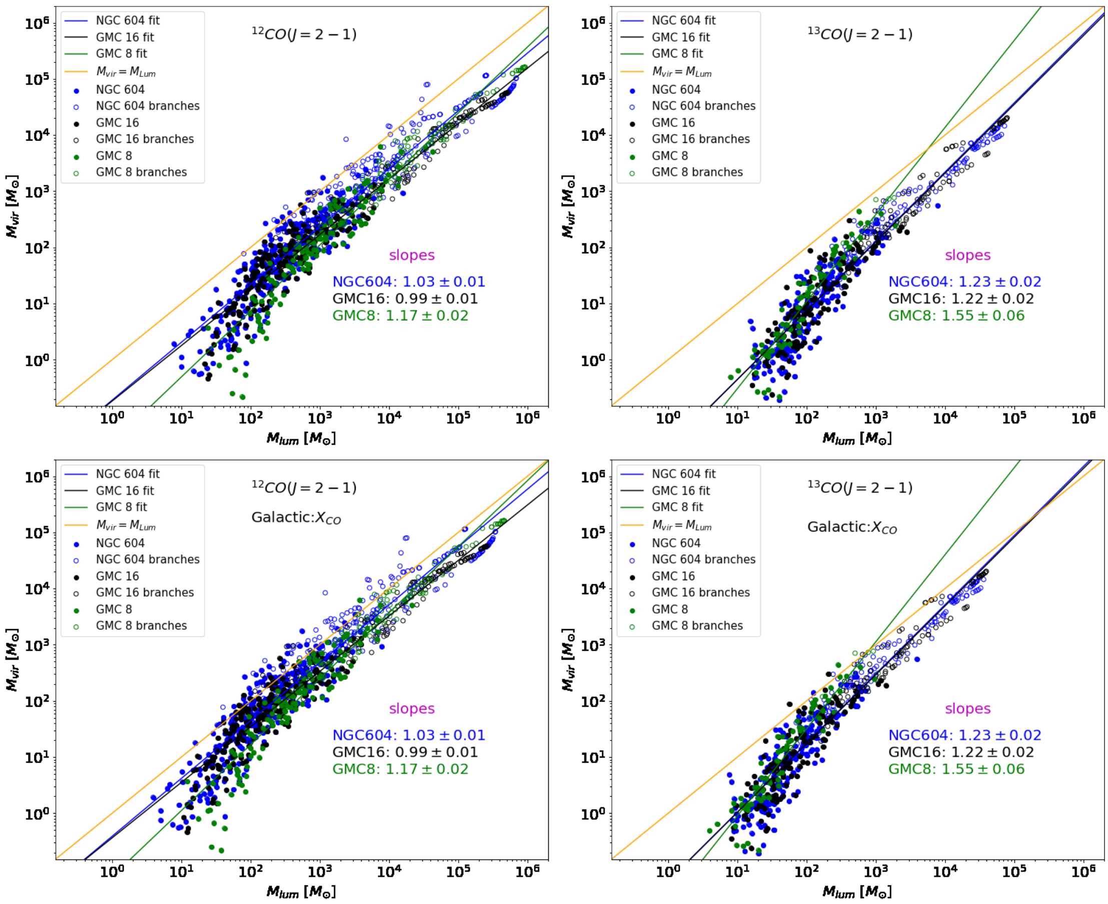

Figure 5.15: Top row: relationship between luminosity and virial mass. In both ^{12}CO and ^{13}CO the relations are below the one-to-one relation. Luminosity mass is higher than virial mass, which could be as a consequence of the choice of our CO conversion factor. Bottom panel: the same data plotted using the Galactic CO conversion factor with sources now in near virial equilibrium.

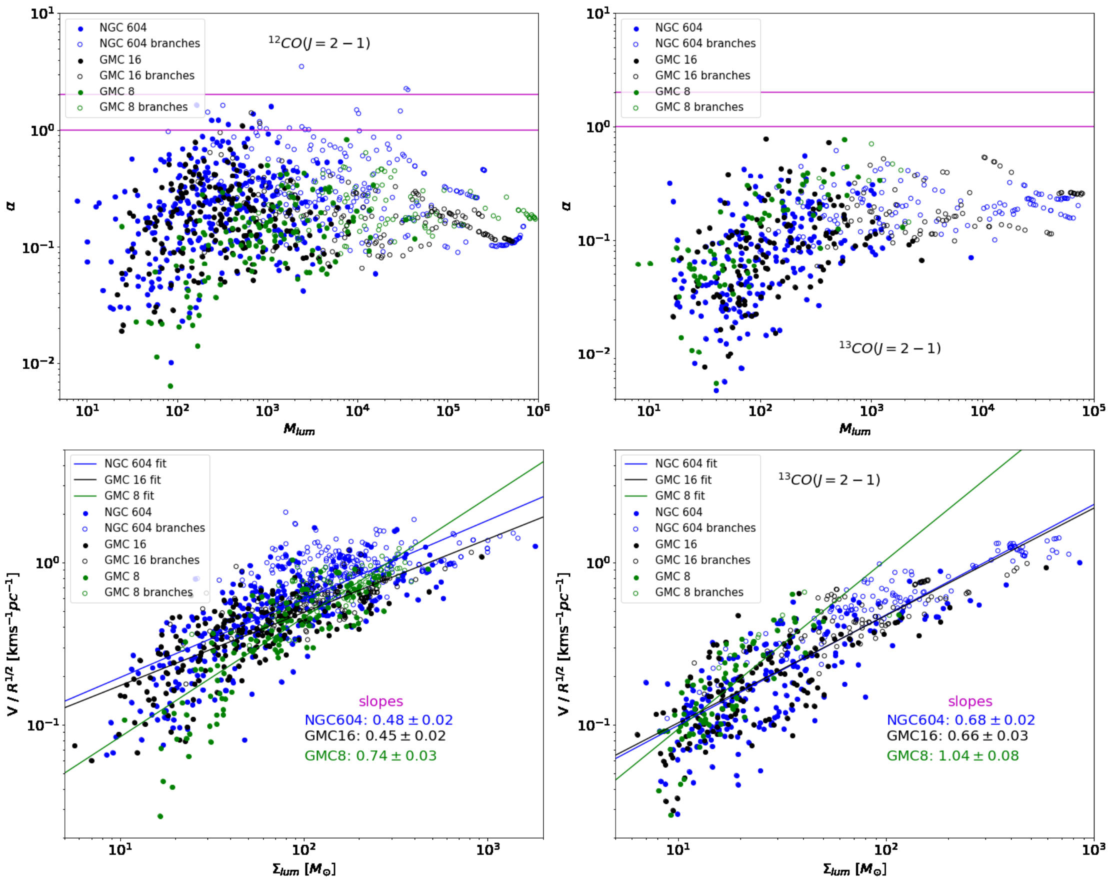

Figure 5.16: Top panels: virial parameter plotted against luminosity derived mass for ^{12}CO (left) and ^{13}CO (right). The horizontal lines (magenta) indicate virial parameters of $\alpha = 1$ and 2. In the top-left panel most of the sources are below the equilibrium line and in the right panel all the sources are below the equilibrium line. The bottom panels show the scaling coefficient with surface density relation. The surface densities of our sources mainly fall within $10^1 - 10^3$ $M_\odot/pc^2$. This surface density range is common within luminosity mass $M_{lum} = 10^1 - 10^4$ $M_\odot$ for both CO tracers.

5.5.4 Molecular Mass - Size Relations

The Milky Way GMC studies by Larson (1981) discovered the ‘mass-size’ relation which was later confirmed by other Galactic studies (Solomon et al. 1987; Heyer et al. 2009) and extragalactic studies (Rosolowsky et al. 2003; Bolatto et al. 2008; Hughes et al. 2010; Faesi et al. 2018). The relation $M_{cl} \propto R_{cl}^2$, can be interpreted as molecular clouds having constant surface density.

The relationship between virial mass and size is presented in the top panels of Figure 5.17 with ^{12}CO to the left and ^{13}CO to the right. The markers and colours follow those established in Figure 5.13, best-fit power-laws are plotted for each cloud, and the exponents are listed on the figure. Also plotted are the equivalent relationships for the LMC (Wong et al. 2017). It can be seen that most of our sources sit above the slope of those studied in LMC. The bottom panels show plots of the luminosity derived mass against radius where sources in ^{12}CO sit above LMC slopes. We do not have slopes for ^{13}CO studies from the LMC. Fitting our data with KMPFIT as described in the previous sections, we find power-law slopes shown in the labels of the plots in Figure 5.17.

In all four plots shown in Figure 5.17, we see that properties of our sources (mass-size) have a high degree of correlation despite them not having similar slopes with those from LMC. We explore the aspect of surface density in the next subsection.

5.5.5 Scaling Coefficient - Surface Density Relations

Following the re-examination of the Milky Way GMCs cataloged by Solomon et al. (1987), Heyer et al. (2009) noted that the scatter in GMC surface density looked to be systematic. They found that surface density scaled with the coefficient of the velocity structure function as $c_{R\Delta v} \propto \Sigma^{0.5}$ when the size-linewidth assumes a 0.5 exponent. We find a similar correlation in Figure 5.16 bottom panels especially for ^{12}CO (left) in NGC 604, GMC 16 and GMC 8. ^{13}CO (bottom-right panel) slopes

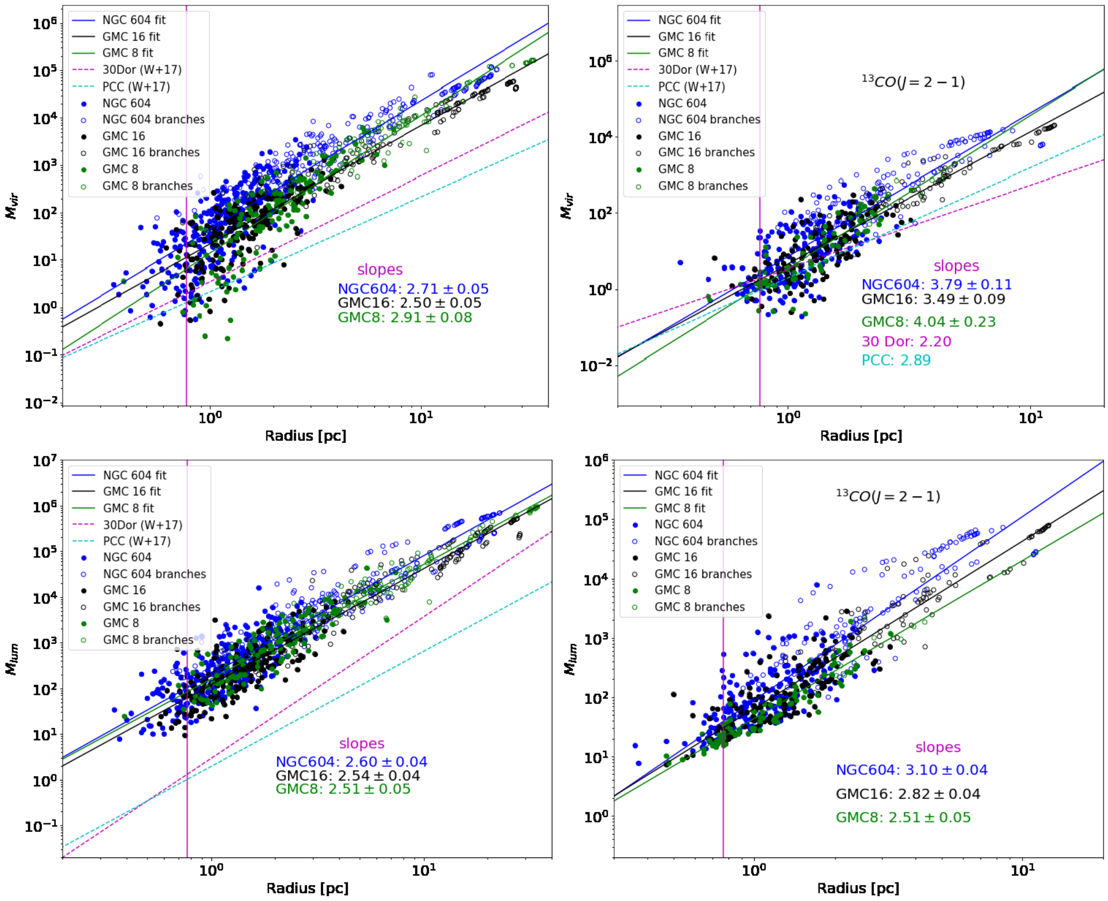

Figure 5.17: The relationship between virial mass and size is presented in the top panels with both ^{12}CO to the left and ^{13}CO to the right. Our sources sit above the slope of those studied in LMC while those in lower sizes are spread out reaching below the LMC slopes. ^{13}CO sources also mainly branches sit above the slopes while the leaves (clumps) are comparable. Bottom panels show plots of the luminosity derived mass against radius where sources in ^{12}CO sit above LMC slopes. We do not have slopes for ^{13}CO studies from LMC. In all the four plots shown in Figure 5.17, we see that properties of our sources (mass-size) are tightly correlated despite them not having similar slopes with those from LMC. Vertical lines are resolution limit in size.

are to the higher side when compared to the expected vale of 0.5. The scaling nearly matches the prediction for clouds in virial equilibrium in a comprehensively turbulent medium (Larson 1981; Solomon et al. 1987; Heyer et al. 2009) especially for ^{12}CO samples.

When one makes an assumption that $\mathrm{M_{lum}} = \mathrm{M_{vir}}$ or $\alpha = 1$ and that $\mathrm{v} \propto \mathrm{R}^{0.5}$ and they hold, the relation $\mathrm{c_{R\Delta v}} = \sqrt{\pi \mathrm{G}/5}\Sigma^{0.5}$ comes out naturally. Following the process described in section 5.5, we fit the data here. The results are labelled on the plots in Figure 5.16. The slopes from ^{12}CO sample are close to the expected result of 0.5 for clouds in gravitational equilibrium with a turbulent medium as opposed to those from ^{13}CO which are quite high.

5.6 Cumulative Mass Distribution in NGC 604, GMC 16 and GMC 8

We compute the cumulative mass distributions of M33 clumps from leaves of our dendrograms from both ^{12}CO and ^{13}CO in the three GMCs. Figure 5.18 shows the cumulative mass distribution of clumps from NGC 604, GMC 16 and GMC 8. We use `KMPFIT` to perform the truncated power-law fits to the cumulative mass distributions. For ^{12}CO clump mass we fit the clumps with mass above $\mathrm{M_o} = 10^{3.0}\ \mathrm{M_\odot}$ while for ^{13}CO we fit those above $\mathrm{M_o} = 10^{2.5}\ \mathrm{M_\odot}$. The fits are shown in Figure 5.18 for each cumulative mass distribution. The truncated power-law values for our clump studies are: For ^{12}CO, we have $\gamma = -1.97 \pm 0.40$ (NGC 604), $\gamma = -1.60 \pm 0.22$ (GMC 16) and $\gamma = -1.26 \pm 0.08$ (GMC 8). For ^{13}CO we get $\gamma = -1.35 \pm 0.30$ (NGC 604), $\gamma = -1.46 \pm 0.23$ (GMC 16) and $\gamma = -1.56 \pm 0.27$ (GMC 8) respectively.

The results in ^{12}CO$(2-1)$ show a marginally steeper slope in NGC 604 (-1.97 ± 0.40) as compared to GMC 16 (-1.60 ± 0.22) and (-1.26 ± 0.08). This may indicate the dependency on environment for this mass spectrum. Generally, the results show nearly equal to or below -2. This suggests that in NGC 604 mass is equally

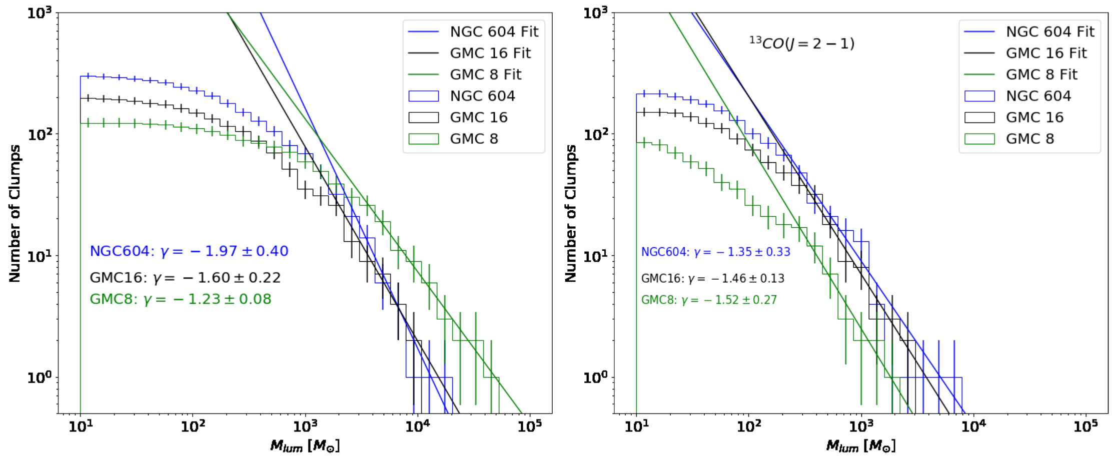

Figure 5.18: M33 cumulative mass distribution for ^{12}CO (left) and ^{13}CO (right) clump mass. The ^{12}CO cumulative mass distribution is fit with truncated power law with the fit only performed on masses above $10^{2.8}$M$_\odot$ while ^{13}CO is above $10^{2.5}$M$_\odot$. The slopes to the fit are labelled under the cumulative distribution graphs. These slopes show that they are below -2 which means most mass is in clumps and not clouds.

distributed in molecular clumps while in GMC 16 and GMC 8 a lot of mass is distributed in small clumps.

The ^{13}CO clump mass distribution in NGC 604, has a marginally shallower slope of -1.35 ± 0.30 as compared to GMC 16 with -1.46 ± 0.13 and GMC 8 with -1.52 ± 0.27. All these results indicate that more mass is concentrated in smaller clumps. What is interesting in interpreting these results is that the slope behaviour in Figure 6.5 is vice versa when you look at the ^{12}CO results where the steepness was from the clumps associated with well developed H II region to the quiescent cloud. It is different with ^{13}CO clumps as their slope steepness is higher beginning with the clumps associated with quiescent cloud to those clumps associated with well developed H II region.

Chapter 6

Discussion

In this Chapter we discuss the major findings of our work and what it means regarding the current knowledge in the field of star formation. We first discuss the work done in Chapter 4 which looks at physical properties of molecular clouds in NGC 604. We then discuss the clump analysis and their physical properties presented in chapter 5. These clumps are from M33 GMCs of NGC 604, GMC 16 and GMC 8 based on observations from ALMA Band 6.

6.1 Introduction

A lot of studies of molecular clouds have been done in external galaxies and most of them have shown similar trends in physical properties to those studied in our Galaxy. The identification of molecular clouds using dendrogram techniques has been extensively done in both Galactic (Rice et al. 2016) and extra-galactic environments: M31 (Kirk et al. 2015), NGC300 (Faesi et al. 2018) and M33 (Williams et al. 2018)).

The identification of internal structures of molecular clouds known as clumps using the same technique has been done in our Galaxy (Mazumdar et al. 2021) and in external galaxies limited to the LMC (Wong et al. 2017, 2019) and NGC 6822 (Schruba et al. 2017). All these studies are for clouds just within 600 kpc from the

Milky Way. This work on the other hand has applied this technique to identify molecular clouds (ALMA Band 3 data) and clumps (ALMA Band 6 data) from M33 galaxy at a distance of 840 kpc (Kam et al. 2015) for the first time.

We discuss the results beginning with ALMA Band 3 data where GMCs in NGC 604 have been resolved to smaller molecular clouds for the first time (Phiri et al. 2021). This gave way to think of applying the technique to the higher resolution data (ALMA Band 6) in order to resolve them further down to clump scales and ascertain Band 6 results.

6.2 ALMA Band 3

The first data to be investigated in this work was the ^{13}CO$(1-0)$ maps of NGC 604 taken with ALMA Band 3. I identified 15 small molecular clouds which cannot be classified as clumps because they have sizes larger than typical clump sizes. The position and properties of these clouds relative to the center of the H II region was analysed. 104 GHz continuum emission was detected in NGC 604 which is near the center of the H II region but we do not attempt to compute the dust mass. This is because emission around 100 GHz is believed to be dominated by free-free emission (Bendo et al. 2015).

There is a discrepancy between 104 GHz continuum emission and ^{13}CO$(1-0)$ emission peaks with the continuum peaks being closer to the center of the H II region while the peaks for ^{13}CO$(1-0)$ are away from the center. The spatial offset of peaks from different tracers within this region is also apparent in higher resolution data for Band 6 as it can be seen in Figure 6.1. This shows that these two tracers are tracing different regions within star forming sites. The continuum emission traces the densest regions while ^{13}CO$(1-0)$ only traces the dense gas. The evidence of a temperature gradient within NGC 604 clouds has been reported before by Muraoka et al. (2012).

This dense gas detected by line emission covers a wider area from the center of

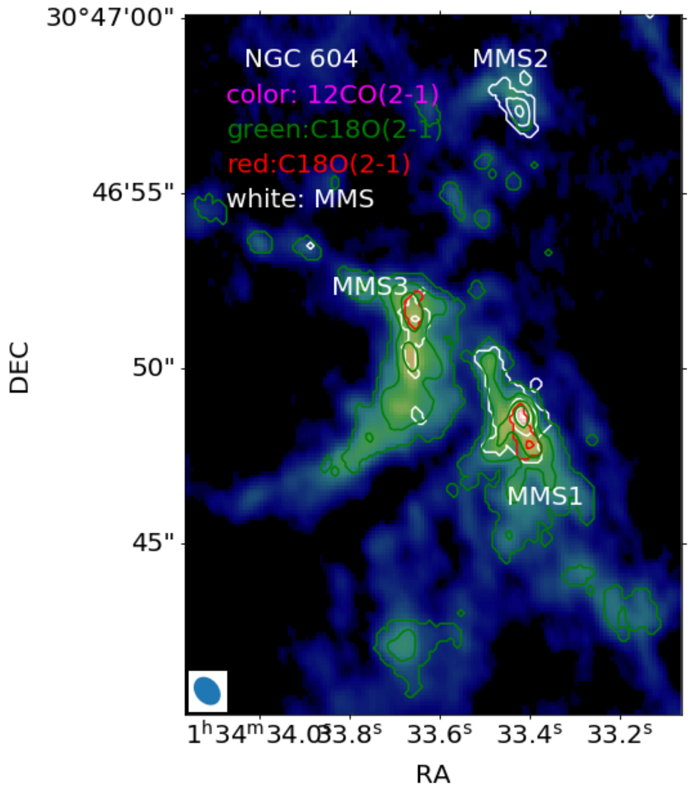

Figure 6.1: NGC 604 ^{12}CO in colour overlaid with C^{13}CO (green contours) C^{18}O (red contours) and 1.3 mm continuum (white contours) emission. The peak emission of continuum and line emission is not coinciding.

the H II region as compared to the dense gas detected by continuum emission which is traced just near the center. The center harbours more than 200 OB stars (Relaño & Kennicutt 2009) and now we see the continuum emission around the center and detect the dense gas in the outer regions creating a sequence of events for star formation. This is similar to what Tosaki et al. (2007) proposed to be happening in this region and depicted in a schematic diagram shown in Figure 6.2. The central cluster of stars is the one referred to as the 1st generation star formation and it is the center of the H II region. The stellar winds and supernovae from these central stars compress the ISM around creating the dense gas and triggering the 2nd generation of star formation observed with the H_α shell and continuum emission (Tosaki et al. 2007). The 3rd generation of star formation is possible from the regions where we detect dense gas but we do not detect continuum emission. The observation of $^{13}CO(1-0)$ and 104 GHz continuum emission from this region have been published by Phiri et al. (2021). Similar interpretation has been noted by Miura et al. (2010) using Nobeyama millimeter array.

From the studies of ALMA $^{13}CO(1-0)$ data we have noted that the size-linewidth relation for sources is below the Galactic slope with smaller scale structures (clouds) having a huge scatter in linewidths. Similar results have been reported by Wong et al. (2017, 2019) who found off-sets in the size-linewidth relationship between Milky Way and LMC clouds observed with ALMA. In Figure 4.5, a one-to-one relation between luminosity derived mass and the virial derived mass show that our sources are in near virial equilibrium assuming the X_{CO} conversion factor for M33 adopted in this work in Chapter 4 and Chapter 5. A comparison to the sources studied by Wilson & Scoville (1992) from the same region, shows that they sit well on a one-to-one relation. The observations of the sources from Wilson & Scoville (1992) have a poor resolution as compared to ours hence they depict only GMC size scales and show they are in virial equilibrium.

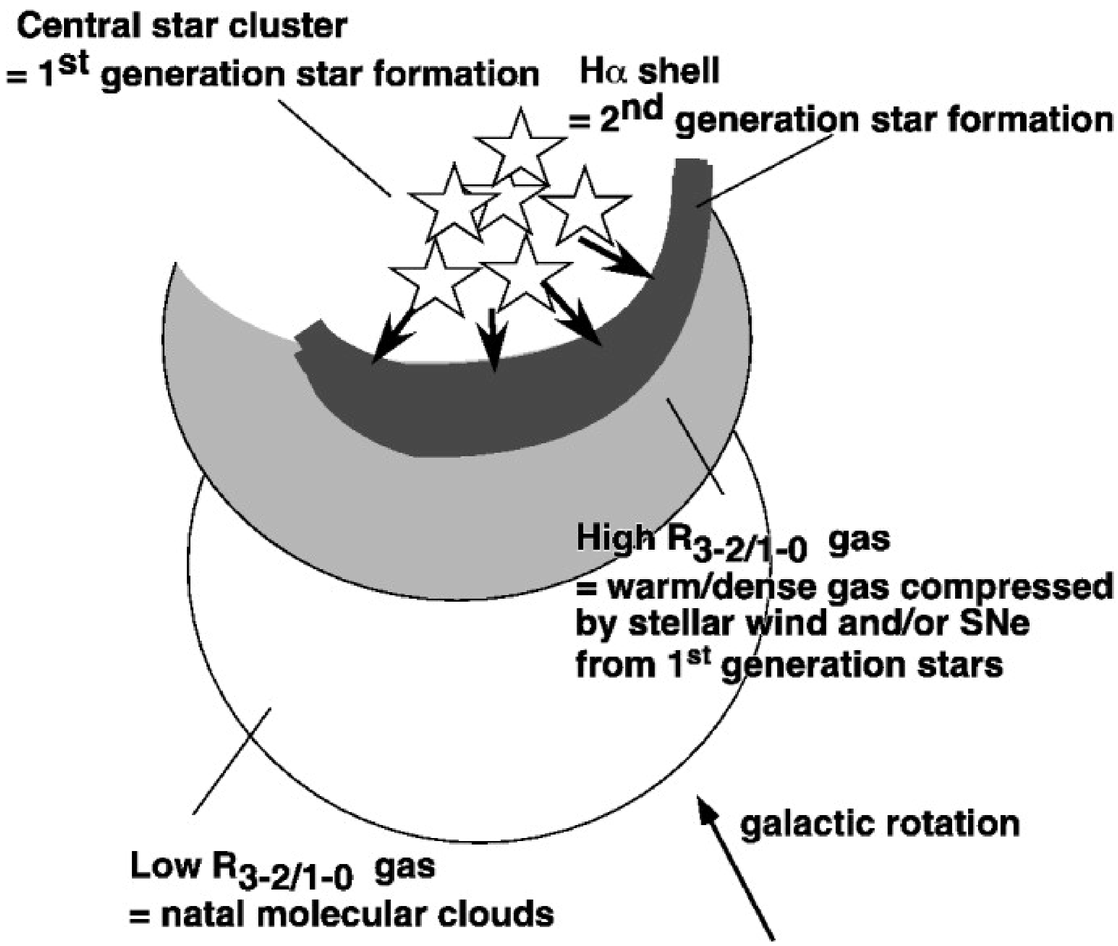

Figure 6.2: Sequential star formation schematic diagram in NGC 604. Schematic diagram taken from Tosaki et al. (2007).

6.3 ALMA Band 6

The observations of GMCs at higher angular resolution allows for the resolving of internal structures and the investigation of physics at the clump level. ALMA Band 6 data has high angular resolution which enabled us to resolve GMCs down to clump scales. We have observed clumps on a scale comparable to those mapped in our own Galaxy (e.g. Elia et al. 2017).

We have detected MMSs in NGC 604 and GMC 16 in 1.3-mm continuum emission and these sources are associated with regions with densest gas just like those from Band 3. In previous studies by Muraoka et al. (2020) and Tokuda et al. (2020), the MMSs were found to be associated with H_α the tracer of ionized gas from young stellar objects. These MMSs are detected within the shell for 2nd generation of star formation as proposed by Tosaki et al. (2007). Figure 6.3 shows the schematic diagram for their proposed star formation process of cloud - cloud collision due to the colliding gas flow. MMS1 is associated with a hub-filament which has three filamentary structures emanating from the MMS itself. We do not detect any MMS or $C^{18}O(2-1)$ in GMC 8 indicating that it is a quiescent cloud with low star-forming activity.

6.4 Observational properties

Physical properties like size, linewidth, mass and surface density were measured for all our molecular clouds (ALMA Band 3 data) and clumps (ALMA Band 6 data). The measured results shown in the catalogs in Appendix C have been plotted on scaling relations to ascertain if their physical conditions are the same to those of our Galaxy and the other nearby galaxies studied so far like the Large and Small Magellanic Clouds, WLM and NGC6822 in Section 6.4.2.

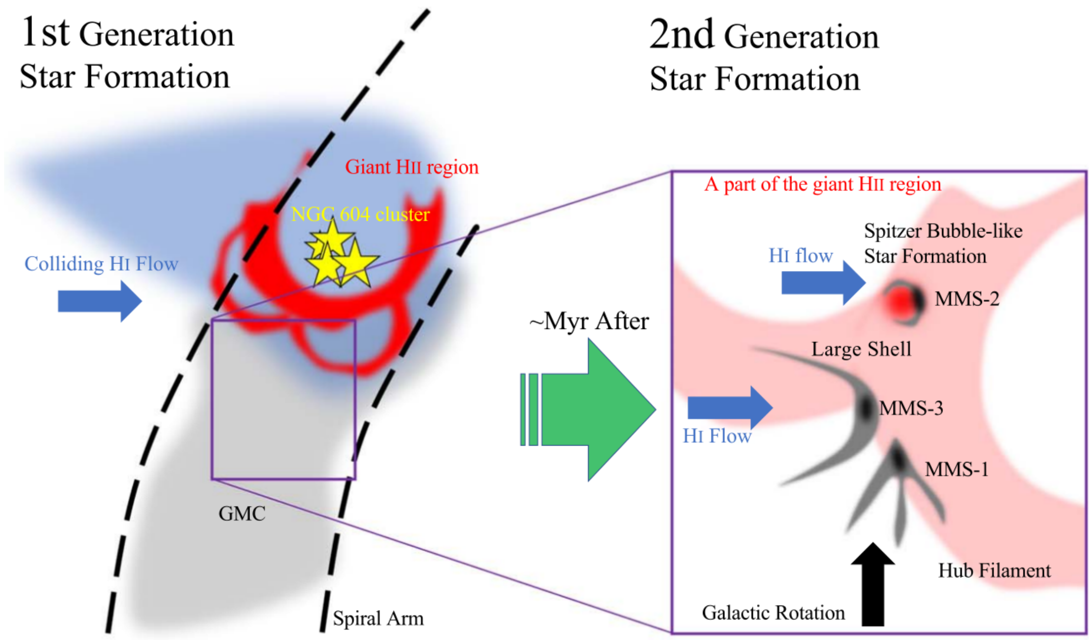

Figure 6.3: Schematic diagram proposing cloud - cloud star formation in NGC 604. Picture taken from Muraoka et al. (2020). The HI gas flow is taken from Tachihara et al. (2018).

6.4.1 Mass estimates and the CO conversion factors.

Mass is an important physical property of stellar and pre-stellar objects. Its measurement is not trivial as it needs a number of assumptions to be made. There are theoretical ways of measuring masses like the virial mass, observational mass measured based on the CO conversion factor, thermodynamic equilibrium and dust mass. Here we focus on the masses computed using the CO conversion factor and compared to those computed using the virial theorem.

The CO conversion factor X_{CO}, as discussed in Chapter 1, is used to convert the integrated CO intensity measured towards a source into mass. Thus, the choice of X_{CO} will have a systematic effect on all of the luminosity based masses. Here we discuss the reasons and choice of the conversion factor that we used in our mass estimates presented in Chapter 4 and Chapter 5.

The X_{CO} factor depends on the metallicity of the galaxy. M33 has a central metallicity of $12 + \log(\frac{O}{H}) = 8.36 \pm 0.04$ (Rosolowsky & Simon 2008) which is half of the Milky Way. The Galactic value of X_{CO} factor is 2×10^{20} cm^{-2}(Kkms^{-1})$^{-1}$ which is extrapolated to suit the M33 metallicity value for the half-solar. The value for ^{12}CO$(1-0)$ X_{CO} conversion factor in M33 is 4×10^{20}cm^{-2}(Kkms^{-1})$^{-1}$ (Druard et al. 2014) which we adopted throughout our work while making extrapolations depending on the tracer and ALMA Band (i.e., from lower transition of ^{12}CO$(1-0)$ to higher transition of ^{12}CO$(2-1)$). An assumption of this nature (galaxy value for X_{CO}) may have an impact on the results for individual clouds. Utilizing the data from the M33 metallicity project, Rosolowsky & Simon (2008) found an exponential abundance profile with a gradient of -0.027 ± 0.012 dexkpc^{-1}. This indicates that there is a change in metallicity as you move from the center of M33. Our GMCs under study are approximately just above 3 kpc from the center which means the metallicity value at the center may not be the best value to be used to derive the X_{CO} conversion factor. In this case, going forward, it would be imperative that for such studies the X_{CO} factor should be calculated for the individual GMCs which will give more reliable GMC masses.

For ^{13}CO$(1-0)$ we used the value, derived from a similar type of nearby spiral galaxy and with similar metallicities, of 1×10^{21} cm^{-2} (Kkms^{-1})$^{-1}$ (Cormier et al. 2018). This value was used to derive masses from luminosity measured from all ^{13}CO intensity maps while changing the ratio depending on the lines involved (ALMA Band 3 or 6). The similar reasons in ^{12}CO are applicable here.

On the theoretical mass (virial mass) estimate, we note that it depends on linewidths and radius of the source. There is an assumption that the source is spherical, but many of our clouds are clearly not spherical. Another aspect we note from our sources is that smaller structures have smaller linewidths values and these dominate the clump samples. The two dictate the value of mass estimated which in this case will not be that high as evidenced in the values we have gotten in their computed virial mass.

With the low values in virial mass and high values in CO estimated mass shown in Figure 5.15, we can safely say is the reason we see the one-to-one relation for both M33 and Galactic based conversion factors shear towards the X_{CO} estimated mass as it is higher than the virial mass. This can be corrected with the suggested ways above of correcting the X_{CO} values for each GMC to ascertain the true values of it which would lead to estimating actual masses of the sources.

6.4.2 Comparisons of M33 GMCs and Clumps to other Catalogues

We have presented and analysed our molecular clouds and clumps from M33 in Chapter 3, Chapter 4 and Chapter 5, respectively. The physical properties computed must be compared thoroughly with other sources studied in our Galaxy and other galaxies in order to understand whether they have similar conditions. In this regard, we make comparisons with studies done at similar scales to ours. We achieve these comparisons by looking at sizes, linewidths, mass, surface density, virial parameter, Larson's scaling relations power-law exponents from the fits that we get from our sources and what was found in other galaxies. We also investigate the cumulative mass distribution of our sources and those from other galaxies including our Galaxy.

6.4.2.1 Size, Line-width, Mass, Surface density and Virial parameter

Using ALMA Band 3 data, I have found molecular clouds with sizes ranging from 5 pc to 21 pc, linewidths of 0.3 to 3.0 kms^{-1}, luminosity derived mass ranging from 4×10^2 to 8.1×10^4 M$_\odot$ and surface density ranging from $4 - 143$ M$_\odot$/pc^2. These sizes, limewidths, masses and surface densities are comparable to the Milky Way molecular clouds (Wilson et al. 2005; Heyer et al. 2009).

From ALMA Band 6 data, I have found clumps with sizes ranging from 0.3 pc to 9 pc, linewidths of 0.1 to 2.8 kms^{-1}, luminosity derived mass ranging from 1.0×10^1 to $10^{4.4}$ M$_\odot$, virial mass ranging from 1.0×10^1 to $10^{3.4}$ M$_\odot$, surface density ranging from $10 - 1000$ M$_\odot$/pc^2 and the virial parameter ranging from 0.1 to 1.6. These values of different physical properties are comparable to clump studies

Table 6.1: The power-law exponents for size - linewidth relation from our studies and those from other studies where β is the power-law exponent. Our slopes are generally higher compared to the rest. This may be due to the fact that the other studies they fit ellipses to the identified sources and used the size of the fitted ellpises to compute their slopes while we have used the actual size of the source as identified by `astrodendro`.

Cloud	^{12}CO β	^{13}CO β	Other Tracers	category	references
30 Dor	0.61± 0.03	0.58± 0.06		clumps	Wong et al. (2017)
PCC	0.51± 0.02	0.91± 0.14		clumps	Wong et al. (2017)
MW	0.5	-		GMCs	Solomon et al. (1987)
NGC 604	0.86± 0.03	1.39 ± 0.06		clumps	this work
GMC 16	0.75± 0.02	1.24± 0.05		clumps	this work
GMC 8	0.95 ± 0.04	1.52± 0.11		clumps	this work
MW		0.21± 0.03		cores	Caselli & Myers (1995)
MW			0.3	clumps	Shirley et al. (2003)
MW		0.09± 0.04	0.09± 0.04	clumps	Traficante et al. (2018)
LMC	0.65± 0.03			clumps	Wong et al. (2019)

conducted in other external galaxies such as WLM (Rubio et al. 2015), NGC6822 (Schruba et al. 2017), LMC (Wong et al. 2017, 2019) and in our Galaxy (Elia et al. 2017; Traficante et al. 2018, and references therein).

6.4.2.2 Larson's Scaling Relations

Below we discuss the scaling relations for our clumps in M33 and how they compare to clumps from other galaxies:

Size - linewidth relation

Larson's first scaling relation of size and linewidth will be the first to look at in this case. Figure 6.4 shows the the size - linewidth relation for our sources (NGC 604, GMC 16 and GMC 8) and those from other galaxies like NGC 6822 (red-dotted line Schruba et al. 2017), 30 Doradus (cyan dotted line Wong et al. 2017) and MW (yellow solid line Solomon et al. 1987). Sources from NGC 6822 and M33 sit in the same space of the size-linewidth relation. The power-law exponent values for our sources are higher as compared to the similar studies of 30 Dor in LMC and NGC 6822, which can be explained by the fact that our results at lower scales create a large scatter in linewidth and we do not remove the sources below resolution limit when fitting the slope. Removing the sources gives no significant difference as the sources below resolutions are few with significantly scattered sources still being above the resolution limit.

Traficante et al. (2018) tested the three Larson relations in 213 massive clumps in our Galaxy using the Herschel Infrared Galactic Plane (Hi-GAL) survey and millimeter Astronomy Legacy Team 90GHz (MALT90) survey of 3 mm emission lines. They divided clumps into five evolutionary stages to help them understand the Larson relations as a function of evolution. They found that the clumps do not follow the three Larson relations regardless of clumps evolutionary phase. This breakdown indicates that the dependence of virial parameter on mass and radius is only a function of potential energy while independent of the kinetic energy of the system, hence, making the virial parameter not good at describing clump dynamics (Traficante et al. 2018). They found the power-law exponent of 0.09 which indicates a very low correlation between velocity dispersion and radius. Such results have been found before: Caselli & Myers (1995) found a power-law exponent of 0.21, and Shirley et al. (2003) found a power-law exponent of 0.3 in clumps and cores in molecular clouds. In external galaxies at GMC level other studies have also found no correlation between size and linewidth, including M51 (Colombo et al. 2014) and NGC 1300 (Maeda et al. 2020).

Dobbs et al. (2019) carried out simulations of GMCs in M33, computed their properties and compared to the real observations of GMCs in M33. They found a good agreement between both the number of clouds and the maximum mass of the clouds. They also found that simulated and observed scaling relations were in

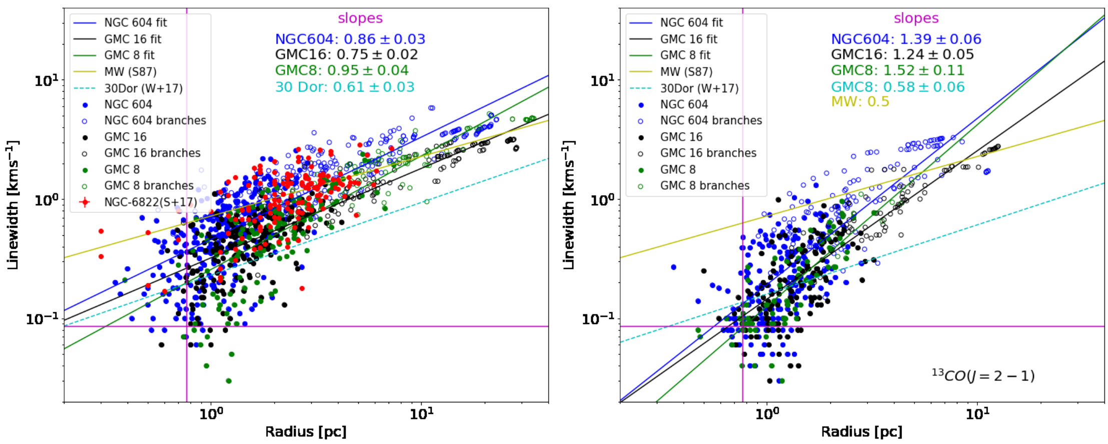

Figure 6.4: Size-linewidth plot for ^{12}CO (left) and ^{13}CO (right). The purple cross lines are instrumental resolution limit in both size (vertical) and linewidth (horizontal). The caption is same as in Figure 5.13 we have just added sources and slopes from similar studies in other galaxies. The red dots are from NGC 6822 clumps done by Schruba et al. (2017) and they sit in the same space with our sources indicating that they have similar sizes.

agreement such as size-linewidth relation and virial relation.

This shows that our results, having values away from the 0.5 power-law slope as shown in Table 6.1, are not unique but are part of results telling us about different galactic environments. We find power-law exponents in our sources to be inclined to virialised clumps entailing that they follow Larson's relations. We note that the power-law exponents from clump and core studies of the Milky Way reviewed so far show very low correlations between size and linewidth compared to those done in the LMC and ours from M33. We also see that our power-law exponents are very comparable to those of the LMC. This would indicate that these clumps are from GMCs with similar environments or metallicities. Studies have shown that in both LMC and M33 the metallicities are half-solar (Rosolowsky & Simon 2008). The idea of different environments may be at play on their physical properties being different and affecting the scaling relations differently.

Luminosity mass - virial mass relation

One other area of discussion is based on the one-to-one relation of observationally derived mass (from CO luminosity) and theoretically derived mass (virial mass). These scale one-to-one indicating that molecular clouds or clumps do not change their virial ratio with mass. This is not the case as evidenced in the luminosity mass against virial mass relation in Figure 5.15. The molecular clouds and clumps show a higher value in luminosity derived masses as compared to the virial derived masses. We do not see an $\alpha = 1$ relationship. Figure 5.14 and Figure 5.15 show the luminosity - virial mass and luminous mass - virial mass relations. These relations are suppose to give a slope of 1 for the sources if they are in virial equilibrium. What we have found are slopes ranging from 0.99 - 1.23 and one with 1.55 for GMC 8 from ^{13}CO.

The luminosity - mass plot for ^{12}CO shows the slope in NGC 604 is 1.03 ± 0.01, GMC 16 is 0.99 ± 0.01 and GMC 8 is 1.17 ± 0.02. In other similar studies of clumps in the LMC, Wong et al. (2017) finds slopes of 0.86 ± 0.01 from ^{12}CO$(2-1)$ and 0.8 ± 0.02 from ^{13}CO$(2-1)$. Clearly, this shows for the clumps and clouds in these GMCs, the luminosity is correlated with the mass.

The conversion of luminosity into luminosity derived mass using the X_{CO}-factor does not change the value of the slope, rather, it just changes the intercept. This is so in both ^{12}CO and ^{13}CO graphs. When we use the Galactic X_{CO} conversion factor the slopes do not change as well but the intercept with majority within the Galactic slope (of 1). In this case, the mass derived from the Galactic conversion factor sits in between the two on the graph with the majority of sources falling within the equilibrium region.

Mass - size relation

One of Larson's scaling relations is the mass - size relation which suggests that molecular clouds have constant surface density as proposed by Larson (1981) when he compiled MW data and noted an inverse correlation between density and size. This has been verified by other GMC Galactic studies (Solomon et al. 1987; Heyer et al. 2009) and extragalactic studies (Rosolowsky et al. 2003; Hughes et al. 2010). However, other studies have found a range in surface densities mainly associated with different environments in galaxies (Bolatto et al. 2008; Utomo et al. 2015).

In Figure 5.17, we show the mass - size relation of M33 clumps and find power-law slopes for ^{12}CO ranging from 2.5 - 2.9 and ^{13}CO ranging from 3.49 - 4.05. These slopes are from CO-luminosity derived masses (from X_{CO} in M33 and that from our Galaxy) and virial mass plotted against the radius. The plots show a high correlation between the two parameters. Our slopes are comparable to those from LMC studies by Wong et al. (2017) who found slopes ranging from 2 - 3.1 for virial mass and radius of the clumps. This also supports the view that the clumps in M33 have similar environments and physical properties to those in the LMC.

Cumulative mass distribution

Here in Figure 6.5, we show cumulative mass distribution for ^{12}CO clumps in M33 and those from ^{12}CO studies of NGC 6822 by Schruba et al. (2017). The power-law exponent fitted to our M33 clump mass is below -2 which indicates that most masses are distributed in clumps (which are smaller clouds) and not large clouds. If the power-law exponent were above -2 it would mean most mass is distributed in large clouds and if equal to -2 it would mean they are equally distributed across a range of cloud sizes. These clumps show that masses go up to 10^4 $M_{\odot}$, in both ^{12}CO and ^{13}CO derived masses as presented in chapter 5. What is interesting about the cumulative mass distribution results from Schruba et al. (2017) is that they fall within the similar distributions of M33 and their masses go up to $10^{3.3}$ $M_{\odot}$. Their cumulative mass distribution is similar to ours (M33), showing that we are looking at sources with similar physical properties and that the conditions of clumps in M33 are similar to those in NGC 6822 regarding their masses.

Blitz (1993) studied the mass function of clumps and found a power-law slope of -1.6 ± 0.2. Similar studies have been done in our Galaxy and external galaxies which found the slopes ranging from -1.2 to -2.5 (Blitz 1993; Pineda et al. 2009a; Mok et al. 2019, 2021, and references therein). The slopes found in M33 for our studies fall within this range which indicates that the mass range and distribution

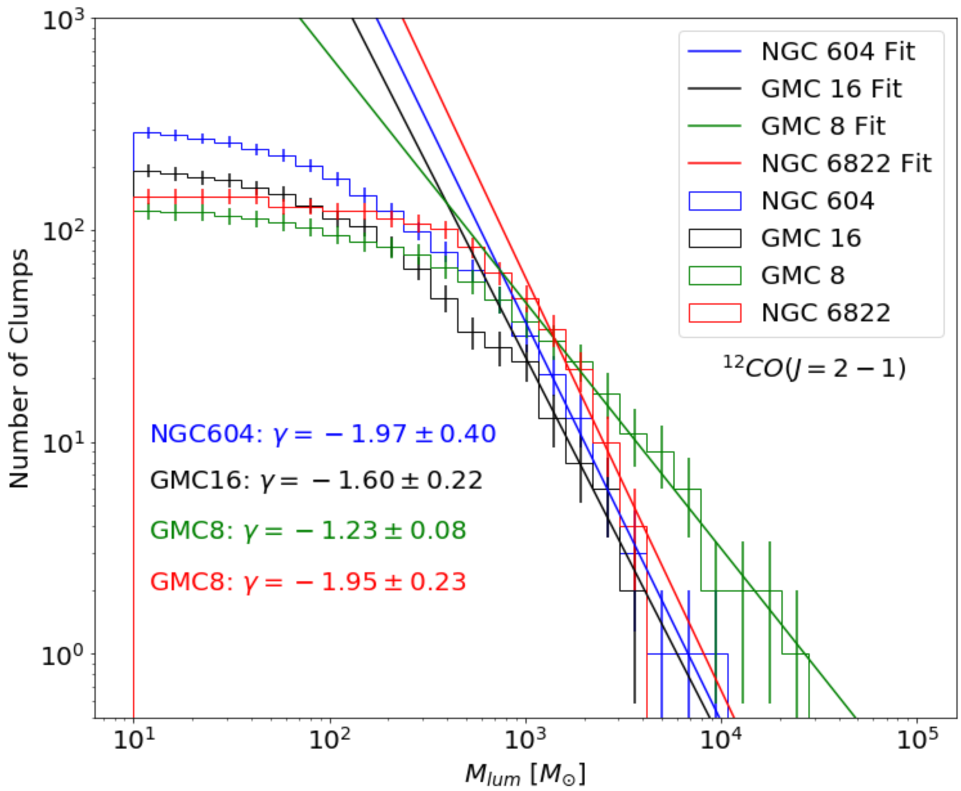

Figure 6.5: M33 and NGC 6822 (red) cumulative mass distribution for ^{12}CO clump mass. The ^{12}CO cumulative mass distribution is fit with truncated power-law labelled under the cumulative distribution graphs. The NGC 6822 cumulative distribution graph falls in similar distribution as those from M33.

in clumps of M33 are similar to those in LMC, NGC 6822 and the Milky Way.

6.5 Conclusion

The properties of molecular clouds and their clumps in M33 are similar to those in LMC, NGC 6822 and the Milky Way. We find similar sizes, linewidths, masses, surface densities, virial parameters and power-law slopes be it when we look at Larson's relations or cumulative mass distribution for our clumps.

Chapter 7

Conclusions

In this thesis I have studied the physical properties of molecular clouds and clumps. This was done in a quest to understand if the physical conditions of internal structures of molecular clouds in external galaxies with different metallicities are the same as those found in the Milky Way.

This study has uncovered properties of molecular clouds at clump level for the first time in M33 at a distance of 840 kpc. We began with the identification of substructures of GMCs classified as molecular clouds and clumps. This was followed by computing of their basic properties and analysis of the Larson's scaling relations. A catalog of their properties has been created and presented in Appendix C.

We conclude our work in three parts one being for Band 3 data main results and the second one for Band 6 data main results. The third one is to give the outlook of the study as this area is in constant evolution with new discoveries as technology keep getting better.

7.1 ALMA Band 3

We have presented ALMA ^{13}CO(1-0) and 104 GHz continuum observations of NGC 604. Using the ASTRODENDRO algorithm, we identified 15 molecular clouds.

The main results are given as follows:

1. The identified molecular clouds have sizes R ranging from 5-21 pc, linewidths Δv, of 0.3-3.0 km s^{-1} and luminosity-derived masses M_{lum}, of $(0.4 - 80.5) \times 10^3$ M$_\odot$. These sizes, linewidths and masses are comparable to typical Milky Way molecular clouds.

2. For the first time, this work has resolved NMA-8, the most massive GMC, into four molecular clouds named L3, L4, L5 and L6, with L5 showing two clear peaks. We detect 104 GHz continuum emission from L5, although it is offset from the ^{13}CO emission.

3. We only detect 104 GHz continuum emission near the centre of GHR. Further out from the centre, only ^{13}CO line emission is detected. This indicates that the GMCs in NGC 604 are in different evolutionary stages as previously suggested by Tosaki et al. (2007) and Miura et al. (2010). Additionally, we find a spatial misalignment between ^{13}CO and 104 GHz continuum in NGC 604. The center has photoionizing stars which photoionize the gas surrounding which we trace by continuum in turn while the ^{13}CO(1-0) line, being the lowest J-transition with a very low excitation temperature, preferentially traces cold dense molecular gas away from the centre. It is thus insensitive to the warm gas traced by the continuum emission. This is a confirmation of what previous studies found in the same region.

4. We have found that the sizes and linewidths are correlated for the NGC 604 GMCs but that the relationship is offset from the Milky Way scaling relation. This may be a consequence of the limited resolution of our data or artefact of the dendrogram analysis as applied to bright sources. The relation for the clouds in NGC 604 is consistent with the idea of compressible hierarchical turbulence in the ISM within this region as discussed in Section 1.4.

5. We find a clear one-to-one relationship between virial mass and luminous

mass indicating that the clouds in NGC 604 are in near virial equilibrium. This relation is consistent with the earlier relation published by Wilson & Scoville (1992).

6. The virial parameter ranges from 0.2-1.1. This result entails that some of the molecular clouds are below $\alpha_{\rm vir} = 1$ which means that not only are they in a state of forming stars but photoionizing stars have been formed. Other clouds have α_{vir} values near unity, which means that they are in virial equilibrium.

7.2 ALMA Band 6

We have presented ALMA ^{12}CO$(2-1)$, ^{13}CO$(2-1)$, C^{18}O$(2-1)$ and 1.3 mm continuum observations of NGC 604, GMC 16 and GMC 8. Using the ASTRODENDRO algorithm, we identified 714 clumps from ^{12}CO in the three GMCs. We have detected 301 clumps in NGC 604, 197 clumps in GMC 16 and and 123 clumps in GMC 8. Doing the same analysis on ^{13}CO$(2-1)$ data, we detected a total of 457 clumps with 216 from NGC 604, 153 from GMC 16 and 88 from GMC 8.

The detected emission and clumps have given us insights in molecular clouds and clumps state. We present the main results below:

1. 1.3 mm continuum has been detected in three regions in NGC 604 along the 2nd generation shell of star formation proposed by Tosaki et al. (2007). These three millimeter sources named MMS1, MMS2 and MMS3, two of them (MMS1 and MMS3) have C^{18}O$(2-1)$ detected on them but not on MMS2. There size and dust mass is comparable to those in our Galaxy.

2. Another MMS has been detected and coincides with C^{18}O emission in GMC 16 at only one region in the entire GMC. The region where the MMS is detected is the brightest in the entire maps for ^{12}CO and C^{18}O.

3. We have resolved the three GMCs namely NGC 604, GMC 16 and GMC 8

and found clumps of sizes ranging from 10 pc, linewidths Δv, of 0.1 - 2.6 km s^{-1} with masses going up to slightly above 10^4 M$_\odot$ which is are typical characteristics of clumps in the Milky Way, WLM, SMC, NGC 6822 and the LMC.

4. The size - linewidth relation slopes are comparable to those found in the MW, SMC and LMC with our results having higher values. We deduce that this is due to the scatter in linewidths at the lower scale which in turn we never removed when fitting the data. This does not remove the fact that clumps follow the relation that the linewidth in molecular clouds increases as there is an increase in size. We have found generally average slope of 0.85 for ^{12}CO clumps and 1.38 for ^{13}CO clumps in M33.

5. The luminosity - virial mass relation in M33 shows that there is a one-to-one relation. This clearly indicates that sources have a constant alpha ratio ($\alpha_{\rm CO}$). Their slopes are all near unity and below two. The story is not different when we look at luminous mass vs virial mass. This suggests that the sample of the sources is near virial equilibrium.

6. The mass - size relation is investigated for our clumps in M33 and we get slopes ranging from 2.5 - 4.0. This is the range of slopes found in the LMC and shows that M33 clumps have constant surface density as proposed by Larson (1981) and several other studies done thereafter in our Galaxy and other galaxies.

7. We find cumulative mass distribution truncated power-law slopes of M33 clumps ranging from -1.23 down to -1.97 for both ^{12}CO and ^{13}CO. The average slope value from these studies is -1.52 which is slightly lower as compared to -1.8 for the LMC. This implies that most of our masses are in smaller sources. This is a similar case (conclusion) for the truncated power-law slopes found in LMC and the MW clumps.

8. We have found that NGC 604 and GMC 16 are often close to galactic properties, but the GMC 8 is often an outlier. This may indicate that physical conditions in this quiescent cloud are different compared to those in NGC 604, GMC 16 and other clouds from nearby galaxies. It would be great to investigate further these results with other further studies.

7.3 Summary.

In general, this study has confirmed that the physical properties of molecular clouds and their internal structures (e.g., clumps) are similar to those in our Galaxy and other nearby galaxies such as LMC, SMC, WLM and NGC 6822. Despite the differences in metallicities, the physical properties of their molecular clouds and clumps are similar.

7.4 Outlook.

The area of star formation being an active area of research, it is important to note that techniques continue to evolve relating to how these properties of molecular clouds are dealt with or estimated.

Going forward, the assumption of the global galaxy value for the X_{CO} conversion factor must be addressed so that it is computed for each GMC in order to deal with overestimating or underestimating the molecular mass. Each GMC metallicity value should be determined and use it to calculate the X_{CO} conversion factor. The calculated X_{CO} conversion factor for each GMC should be used to estimate the luminosity derived mass of the clumps or the entire GMC.

Analysis of these data should not just end here but continue to estimate the star formation rate in each GMC and look at other previous studies with H_α emission. This would be used to deal with whether these regions or which specific clumps are associated with Young Stellar Objects.

It would be also interesting to do an investigation on the clumps from ^{12}CO which are also identified in ^{13}CO. A source-to-source comparison will be important.

Bibliography

André, P., Men'shchikov, A., Bontemps, S., et al. 2010, *Astron. Astrophys.*, 518, L102

Arimoto, N., Sofue, Y., & Tsujimoto, T. 1996, *Pub. Astron. Soc. Japan*, 48, 275

Ballesteros-Paredes, J., Vázquez-Semadeni, E., Gazol, A., et al. 2011, *Mon. Not. Roy. Astron. Soc.*, 416, 1436

Bania, T. M. & Lyon, J. G. 1980, *Astrophys. J.*, 239, 173

Barnard, E. E. 1919, *Astrophys. J.*, 49, 1

Bendo, G. J., Beswick, R. J., D'Cruze, M. J., et al. 2015, *Mon. Not. Roy. Astron. Soc.*, 450, L80

Bendo, G. J., Henkel, C., D'Cruze, M. J., et al. 2016, *Mon. Not. Roy. Astron. Soc.*, 463, 252

Bergin, E. A. & Tafalla, M. 2007, *Ann. Rev. Astron, Astrophys.*, 45, 339

Beuther, H., Klessen, R., Dullemond, C., & Henning, T. 2014, Protostars and Planets VI (University of Arizona Press, Tucson)

Binney J., M. M. 2014, Galactic Astronomy (Princeton University Press, Princeton)

Blain, A. 2010, in 38th COSPAR Scientific Assembly, Vol. 38, 2

Blitz, L. 1993, in Protostars and Planets III, ed. E. H. Levy & J. I. Lunine, 125

Blitz, L. & Rosolowsky, E. 2006, *Astrophys. J.*, 650, 933

Blitz, L. & Thaddeus, P. 1980, *Astrophys. J.*, 241, 676

Bloemen, H. 1996, in Unsolved Problems of the Milky Way, ed. L. Blitz & P. J. Teuben, Vol. 169, 437

Bolatto, A. D., Leroy, A., Israel, F. P., & Jackson, J. M. 2003, *Astrophys. J.*, 595, 167

Bolatto, A. D., Leroy, A. K., Rosolowsky, E., Walter, F., & Blitz, L. 2008, *Astrophys. J.*, 686, 948

Bolatto, A. D., Warren, S. R., Leroy, A. K., et al. 2013, *Nature*, 499, 450

Booth, C. M., Theuns, T., & Okamoto, T. 2007, *Mon. Not. Roy. Astron. Soc.*, 376, 1588

Boquien, M., Calzetti, D., Aalto, S., et al. 2015, *Astron. Astrophys.*, 578, A8

Boquien, M., Calzetti, D., Combes, F., et al. 2011, *Astron. J.*, 142, 111

Braatz, J., Impellizzeri, V., Biggs, A., & P., S. 2020, ALMA Cycle 8 Proposer's Guide, version 1.0 (Joint ALMA Observatory, Santiago)

Buckle, J. V., Davis, C. J., di Francesco, J., et al. 2012, *Mon. Not. Roy. Astron. Soc.*, 422, 521

Caselli, P. & Myers, P. C. 1995, *Astrophys. J.*, 446, 665

Chevance, M., Kruijssen, J. M. D., Vazquez-Semadeni, E., et al. 2020, *Space Sci. Rev.*, 216, 50

Churchwell, E. & Goss, W. M. 1999, *Astrophys. J.*, 514, 188

Colombo, D., Hughes, A., Schinnerer, E., et al. 2014, *Astrophys. J.*, 784, 3

Colombo, D., Rosolowsky, E., Ginsburg, A., Duarte-Cabral, A., & Hughes, A. 2015, *Mon. Not. Roy. Astron. Soc.*, 454, 2067

Corbelli, E., Braine, J., & Giovanardi, C. 2019, *Astron. Astrophys.*, 622, A171

Cormier, D., Bigiel, F., Jiménez-Donaire, M. J., et al. 2018, *Mon. Not. Roy. Astron. Soc.*, 475, 3909

Costa, A. H., Johnson, K. E., Indebetouw, R., et al. 2021, *Astrophys. J.*, 918, 76

Dame, T. M., Elmegreen, B. G., Cohen, R. S., & Thaddeus, P. 1986, *Astrophys. J.*, 305, 892

Dobbs, C. L., Rosolowsky, E., Pettitt, A. R., et al. 2019, *Mon. Not. Roy. Astron. Soc.*, 485, 4997

Draine, B. T. 1978, *Astrophys. J. Supple.*, 36, 595

Draine, B. T. 2003, *Ann. Rev. Astron, Astrophys.*, 41, 241

Drissen, L., Moffat, A. F. J., & Shara, M. M. 1993, in Astronomical Society of the Pacific Conference Series, Vol. 35, Massive Stars: Their Lives in the Interstellar Medium, ed. J. P. Cassinelli & E. B. Churchwell, 528

Druard, C., Braine, J., Schuster, K. F., et al. 2014, *Astron. Astrophys.*, 567, A118

Elia, D., Molinari, S., Schisano, E., et al. 2017, *Mon. Not. Roy. Astron. Soc.*, 471, 100

Elmegreen, B. G. & Elmegreen, D. M. 1983, *Mon. Not. Roy. Astron. Soc.*, 203, 31

Engargiola, G., Plambeck, R. L., Rosolowsky, E., & Blitz, L. 2003, *Astrophys. J. Supple.*, 149, 343

Esteban, C., Bresolin, F., Peimbert, M., et al. 2009, *Astrophys. J.*, 700, 654

Faesi, C. M., Lada, C. J., & Forbrich, J. 2018, *Astrophys. J.*, 857, 19

Fan, X., Carilli, C. L., & Keating, B. 2006, *Ann. Rev. Astron, Astrophys.*, 44, 415

Freedman, W. L., Wilson, C. D., & Madore, B. F. 1991, *Astrophys. J.*, 372, 455

Fukui, Y., Mizuno, N., Yamaguchi, R., Mizuno, A., & Onishi, T. 2001, *Pub. Astron. Soc. Japan*, 53, L41

Galliano, F., Hony, S., Bernard, J. P., et al. 2011, *Astron. Astrophys.*, 536, A88

Goldsmith, P. F., Heyer, M., Narayanan, G., et al. 2008, *Astrophys. J.*, 680, 428

Goodman, A. A., Barranco, J. A., Wilner, D. J., & Heyer, M. H. 1998, *Astrophys. J.*, 504, 223

Gould, R. J. & Salpeter, E. E. 1963, *Astrophys. J.*, 138, 393

Gratier, P., Braine, J., Rodriguez-Fernandez, N. J., et al. 2012, *Astron. Astrophys.*, 542, A108

Gratier, P., Braine, J., Rodriguez-Fernandez, N. J., et al. 2010, *Astron. Astrophys.*, 522, A3

Griffin, M. J., Abergel, A., Abreu, A., et al. 2010, *Astron. Astrophys.*, 518, L3

Hennemann, M., Motte, F., Schneider, N., et al. 2012, *Astron. Astrophys.*, 543, L3

Heyer, M. & Dame, T. M. 2015, *Ann. Rev. Astron, Astrophys.*, 53, 583

Heyer, M., Krawczyk, C., Duval, J., & Jackson, J. M. 2009, *Astrophys. J.*, 699, 1092

Heyer, M. H., Carpenter, J. M., & Snell, R. L. 2001, *Astrophys. J.*, 551, 852

Hogbom, J. A. & Brouw, W. N. 1974, *Astron. Astrophys.*, 33, 289

Hoopes, C. G. & Walterbos, R. A. M. 2000, in Proceedings 232. WE-Heraeus Seminar, ed. E. M. Berkhuijsen, R. Beck, & R. A. M. Walterbos, 111–114

Hughes, A., Meidt, S., Colombo, D., et al. 2016, in IAU Symposium, Vol. 315, From Interstellar Clouds to Star-Forming Galaxies: Universal Processes?, ed. P. Jablonka, P. André, & F. van der Tak, 30–37

Hughes, A., Meidt, S. E., Colombo, D., et al. 2013, *Astrophys. J.*, 779, 46

Hughes, A., Wong, T., Ott, J., et al. 2010, *Mon. Not. Roy. Astron. Soc.*, 406, 2065

Indebetouw, R., Brogan, C., Chen, C. H. R., et al. 2013, *Astrophys. J.*, 774, 73

Jackson, J. M., Finn, S. C., Chambers, E. T., Rathborne, J. M., & Simon, R. 2010, *Astrophys. J. Letters*, 719, L185

Joung, M. R., Mac Low, M.-M., & Bryan, G. L. 2009, *Astrophys. J.*, 704, 137

Kam, Z. S., Carignan, C., Chemin, L., Amram, P., & Epinat, B. 2015, *Mon. Not. Roy. Astron. Soc.*, 449, 4048

Kauffmann, J., Pillai, T., & Goldsmith, P. F. 2013, *Astrophys. J.*, 779, 185

Kennicutt, R. C. & Evans, N. J. 2012, *Ann. Rev. Astron, Astrophys.*, 50, 531

Kepley, A. A., Tsutsumi, T., Brogan, C. L., et al. 2020, *Pub. Astron. Soc. Pac.*, 132, 024505

Kirk, J. M., Gear, W. K., Fritz, J., et al. 2015, *Astrophys. J.*, 798, 58

Kirk, J. M., Ward-Thompson, D., Palmeirim, P., et al. 2013, *Mon. Not. Roy. Astron. Soc.*, 432, 1424

Kondo, H., Tokuda, K., Muraoka, K., et al. 2021, *Astrophys. J.*, 912, 66

Kramer, C., Buchbender, C., Xilouris, E. M., et al. 2010, *Astron. Astrophys.*, 518, L67

Kramer, C., Stutzki, J., Rohrig, R., & Corneliussen, U. 1998, *Astron. Astrophys.*, 329, 249

Krumholz, M. R. & McKee, C. F. 2005, *Astrophys. J.*, 630, 250

Kuno, N., Nakai, N., Handa, T., & Sofue, Y. 1995, *Pub. Astron. Soc. Japan*, 47, 745

La Vigne, M. A., Vogel, S. N., & Ostriker, E. C. 2006, *Astrophys. J.*, 650, 818

Lada, C. J. & Lada, E. A. 2003, *Ann. Rev. Astron, Astrophys.*, 41, 57

Larson, R. B. 1981, *Mon. Not. Roy. Astron. Soc.*, 194, 809

Leroy, A. K., Bolatto, A. D., Ostriker, E. C., et al. 2015, *Astrophys. J.*, 801, 25

Li, G.-X., Wyrowski, F., Menten, K., Megeath, T., & Shi, X. 2015, *Astron. Astrophys.*, 578, A97

Lynds, B. T. 1962, *Astrophys. J. Supple.*, 7, 1

Maeda, F., Ohta, K., Fujimoto, Y., & Habe, A. 2020, *Mon. Not. Roy. Astron. Soc.*

Mazumdar, P., Wyrowski, F., Urquhart, J. S., et al. 2021, arXiv e-prints, arXiv:2109.09615

McKee, C. F. & Ostriker, E. C. 2007, *Ann. Rev. Astron, Astrophys.*, 45, 565

McKee, C. F. & Ostriker, J. P. 1977, *Astrophys. J.*, 218, 148

McMullin, J. P., Waters, B., Schiebel, D., Young, W., & Golap, K. 2007, in Astronomical Society of the Pacific Conference Series, Vol. 376, Astronomical Data Analysis Software and Systems XVI, ed. R. A. Shaw, F. Hill, & D. J. Bell, 127

Men'shchikov, A., André, P., Didelon, P., et al. 2012, *Astron. Astrophys.*, 542, A81

Miura, R., Okumura, S. K., Tosaki, T., et al. 2010, *Astrophys. J.*, 724, 1120

Miura, R. E., Kohno, K., Tosaki, T., et al. 2012, *Astrophys. J.*, 761, 37

Mizuno, N., Rubio, M., Mizuno, A., et al. 2001, *Pub. Astron. Soc. Japan*, 53, L45

Mok, A., Chandar, R., & Fall, S. M. 2019, *Astrophys. J.*, 872, 93

Mok, A., Chandar, R., & Fall, S. M. 2021, *Astrophys. J.*, 911, 8

Muraoka, K., Kondo, H., Tokuda, K., et al. 2020, arXiv e-prints, arXiv:2009.05804

Muraoka, K., Tosaki, T., Miura, R., et al. 2012, *Pub. Astron. Soc. Japan*, 64, 3

Nishimura, A., Tokuda, K., Kimura, K., et al. 2015, *Astrophys. J. Supple.*, 216, 18

Onodera, S., Kuno, N., Tosaki, T., et al. 2010, *Astrophys. J. Letters*, 722, L127

Ossenkopf, V. & Henning, T. 1994, *Astron. Astrophys.*, 291, 943

Padoan, P., Nordlund, Å., Rögnvaldsson, Ö. E., & Goodman, A. 2001, in Astronomical Society of the Pacific Conference Series, Vol. 243, From Darkness to Light: Origin and Evolution of Young Stellar Clusters, ed. T. Montmerle & P. André, 279

Palmeirim, P., André, P., Kirk, J., et al. 2013, *Astron. Astrophys.*, 550, A38

Passot, T., Vazquez-Semadeni, E., & Pouquet, A. 1995, *Astrophys. J.*, 455, 536

Peel, M. W., Dickinson, C., Davies, R. D., Clements, D. L., & Beswick, R. J. 2011, *Mon. Not. Roy. Astron. Soc.*, 416, L99

Pekruhl, S., Preibisch, T., Schuller, F., & Menten, K. 2013, *Astron. Astrophys.*, 550, A29

Phiri, S. P., Kirk, J. M., Ward-Thompson, D., Sansom, A. E., & Bendo, G. J. 2021, *Mon. Not. Roy. Astron. Soc.*, 504, 4511

Pineda, J. E., Rosolowsky, E. W., & Goodman, A. A. 2009a, *Astrophys. J. Letters*, 699, L134

Pineda, J. L., Ott, J., Klein, U., et al. 2009b, *Astrophys. J.*, 703, 736

Poglitsch, A., Waelkens, C., Geis, N., et al. 2010, *Astron. Astrophys.*, 518, L2

Prialnik, D. 2010, in Icy Bodies of the Solar System, ed. J. A. Fernandez, D. Lazzaro, D. Prialnik, & R. Schulz, Vol. 263, 121–125

Relaño, M., De Looze, I., Kennicutt, R. C., et al. 2018, *Astron. Astrophys.*, 613, A43

Relaño, M. & Kennicutt, Robert C., J. 2009, *Astrophys. J.*, 699, 1125

Remijan, A., Biggs, A., Cortes, P. A., et al. 2019, ALMA Doc 7.3,1

Rhee, J., Zwaan, M. A., Briggs, F. H., et al. 2013, *Mon. Not. Roy. Astron. Soc.*, 435, 2693

Rice, T. S., Goodman, A. A., Bergin, E. A., Beaumont, C., & Dame, T. M. 2016, *Astrophys. J.*, 822, 52

Roman-Duval, J., Jackson, J. M., Heyer, M., Rathborne, J., & Simon, R. 2010, *Astrophys. J.*, 723, 492

Rosolowsky, E. 2005, *Pub. Astron. Soc. Pac.*, 117, 1403

Rosolowsky, E. & Blitz, L. 2004, *Astrophys. Space Sci.*, 289, 265

Rosolowsky, E., Engargiola, G., Plambeck, R., & Blitz, L. 2003, *Astrophys. J.*, 599, 258

Rosolowsky, E., Hughes, A., Leroy, A. K., et al. 2021, *Mon. Not. Roy. Astron. Soc.*, 502, 1218

Rosolowsky, E., Keto, E., Matsushita, S., & Willner, S. P. 2007, *Astrophys. J.*, 661, 830

Rosolowsky, E. & Leroy, A. 2006, *Pub. Astron. Soc. Pac.*, 118, 590

Rosolowsky, E. & Simon, J. D. 2008, *Astrophys. J.*, 675, 1213

Rosolowsky, E. W., Pineda, J. E., Kauffmann, J., & Goodman, A. A. 2008, *Astrophys. J.*, 679, 1338

Rubio, M., Elmegreen, B. G., Hunter, D. A., et al. 2015, *Nature*, 525, 218

Salpeter, E. E. 1955, *Astrophys. J.*, 121, 161

Sano, H., Tsuge, K., Tokuda, K., et al. 2021, *Pub. Astron. Soc. Japan*, 73, S62

Schinnerer, E., Hughes, A., Leroy, A., et al. 2019, *Astrophys. J.*, 887, 49

Schneider, D. P., Darland, J. J., & Leung, K. C. 1979, *Astron. J.*, 84, 236

Schruba, A., Leroy, A. K., Kruijssen, J. M. D., et al. 2017, *Astrophys. J.*, 835, 278

Seo, Y. M., Majumdar, L., Goldsmith, P. F., et al. 2019, *Astrophys. J.*, 871, 134

Seo, Y. M., Shirley, Y. L., Goldsmith, P., et al. 2015, *Astrophys. J.*, 805, 185

Shimajiri, Y., Kitamura, Y., Saito, M., et al. 2014, *Astron. Astrophys.*, 564, A68

Shirley, Y. L., Evans, Neal J., I., Young, K. E., Knez, C., & Jaffe, D. T. 2003, *Astrophys. J. Supple.*, 149, 375

Singh, A., Matzner, C. D., Friesen, R. K., et al. 2021, *Astrophys. J.*, 922, 87

Smith, M. W. L., Eales, S. A., Gomez, H. L., et al. 2012, *Astrophys. J.*, 756, 40

Solomon, P. M., Rivolo, A. R., Barrett, J., & Yahil, A. 1987, *Astrophys. J.*, 319, 730

Solomon, P. M., Sanders, D. B., & Scoville, N. Z. 1979, in The Large-Scale Characteristics of the Galaxy, ed. W. B. Burton, Vol. 84, 35

Stoehr, F., Murphy, E., Lacy, M., & et al. 2020, ALMA Doc 8.15, 1

Stutzki, J. & Guesten, R. 1990, *Astrophys. J.*, 356, 513

Tabatabaei, F. S., Braine, J., Xilouris, E. M., et al. 2014, *Astron. Astrophys.*, 561, A95

Tachihara, K., Gratier, P., Sano, H., et al. 2018, *Pub. Astron. Soc. Japan*, 70, S52

Tan, J. C., Kong, S., Butler, M. J., Caselli, P., & Fontani, F. 2013, *Astrophys. J.*, 779, 96

Terlouw, J. P. & Vogelaar, M. G. R. 2016, Kapteyn Package: Tools for developing astronomical applications

Thirlwall, J. J., Popescu, C. C., Tuffs, R. J., et al. 2020, *Mon. Not. Roy. Astron. Soc.*, 495, 835

Tokuda, K., Muraoka, K., Kondo, H., et al. 2020, *Astrophys. J.*, 896, 36

Tosaki, T., Kuno, N., Onodera, Sachiko Miura, R., et al. 2011, *Pub. Astron. Soc. Japan*, 63, 1171

Tosaki, T., Miura, R., Sawada, T., et al. 2007, *Astrophys. J. Letters*, 664, L27

Traficante, A., Duarte-Cabral, A., Elia, D., et al. 2018, *Mon. Not. Roy. Astron. Soc.*, 477, 2220

Traficante, A., Fuller, G. A., Duarte-Cabral, A., et al. 2020, *Mon. Not. Roy. Astron. Soc.*, 491, 4310

Tüllmann, R., Gaetz, T. J., Plucinsky, P. P., et al. 2008, *Astrophys. J.*, 685, 919

Urquhart, J. S., Moore, T. J. T., Csengeri, T., et al. 2014, *Mon. Not. Roy. Astron. Soc.*, 443, 1555

Utomo, D., Blitz, L., Davis, T., et al. 2015, *Astrophys. J.*, 803, 16 van Dishoeck, E. F. & Black, J. H. 1988, The Photodissociation of Interstellar Co/, ed. R. L. Dickman, R. L. Snell, & J. S. Young, Vol. 315, 168

Vázquez-Semadeni, E., Ryu, D., Passot, T., González, R. F., & Gazol, A. 2006, *Astrophys. J.*, 643, 245

Viallefond, F., Boulanger, F., Cox, P., et al. 1992, *Astron. Astrophys.*, 265, 437

Walch, S., Girichidis, P., Naab, T., et al. 2015, *Mon. Not. Roy. Astron. Soc.*, 454, 238

Ward-Thompson, D. & Whitworth, A. P. 2011, An Introduction to Star Formation

Weinreb, S., Barrett, A. H., Meeks, M. L., & Henry, J. C. 1963, *Nature*, 200, 829

Williams, J. P., de Geus, E. J., & Blitz, L. 1994, *Astrophys. J.*, 428, 693

Williams, J. P. & McKee, C. F. 1997, *Astrophys. J.*, 476, 166

Williams, T. G., Gear, W. K., & Smith, M. W. L. 2018, *Mon. Not. Roy. Astron. Soc.*, 479, 297

Williams, T. G., Gear, W. K., & Smith, M. W. L. 2019, *Mon. Not. Roy. Astron. Soc.*, 483, 5135

Wilson, B. A., Dame, T. M., Masheder, M. R. W., & Thaddeus, P. 2005, *Astron. Astrophys.*, 430, 523

Wilson, C. D. & Scoville, N. 1990, *Astrophys. J.*, 363, 435

Wilson, C. D. & Scoville, N. 1992, *Astrophys. J.*, 385, 512

Wilson, C. D., Walker, C. E., & Thornley, M. D. 1997, *Astrophys. J.*, 483, 210

Wilson, R. W., Jefferts, K. B., & Penzias, A. A. 1970, *Astrophys. J. Letters*, 161, L43

Wilson, T. L., Rohlfs, K., & Hüttemeister, S. 2013, Tools of Radio Astronomy

Wolfire, M. G., Hollenbach, D., & McKee, C. F. 2010, *Astrophys. J.*, 716, 1191

Wong, T., Hughes, A., Ott, J., et al. 2011, *Astrophys. J. Supple.*, 197, 16

Wong, T., Hughes, A., Tokuda, K., et al. 2017, *Astrophys. J.*, 850, 139

Wong, T., Hughes, A., Tokuda, K., et al. 2019, *Astrophys. J.*, 885, 50

Wong, T., Ladd, E. F., Brisbin, D., et al. 2008, *Mon. Not. Roy. Astron. Soc.*, 386, 1069

Young, J. S. & Scoville, N. Z. 1991, *Ann. Rev. Astron, Astrophys.*, 29, 581

Appendix A

Peak Spectra for the sources

Presented here in Figure A.1 are the spectra (as measured at the peak of the emission) for

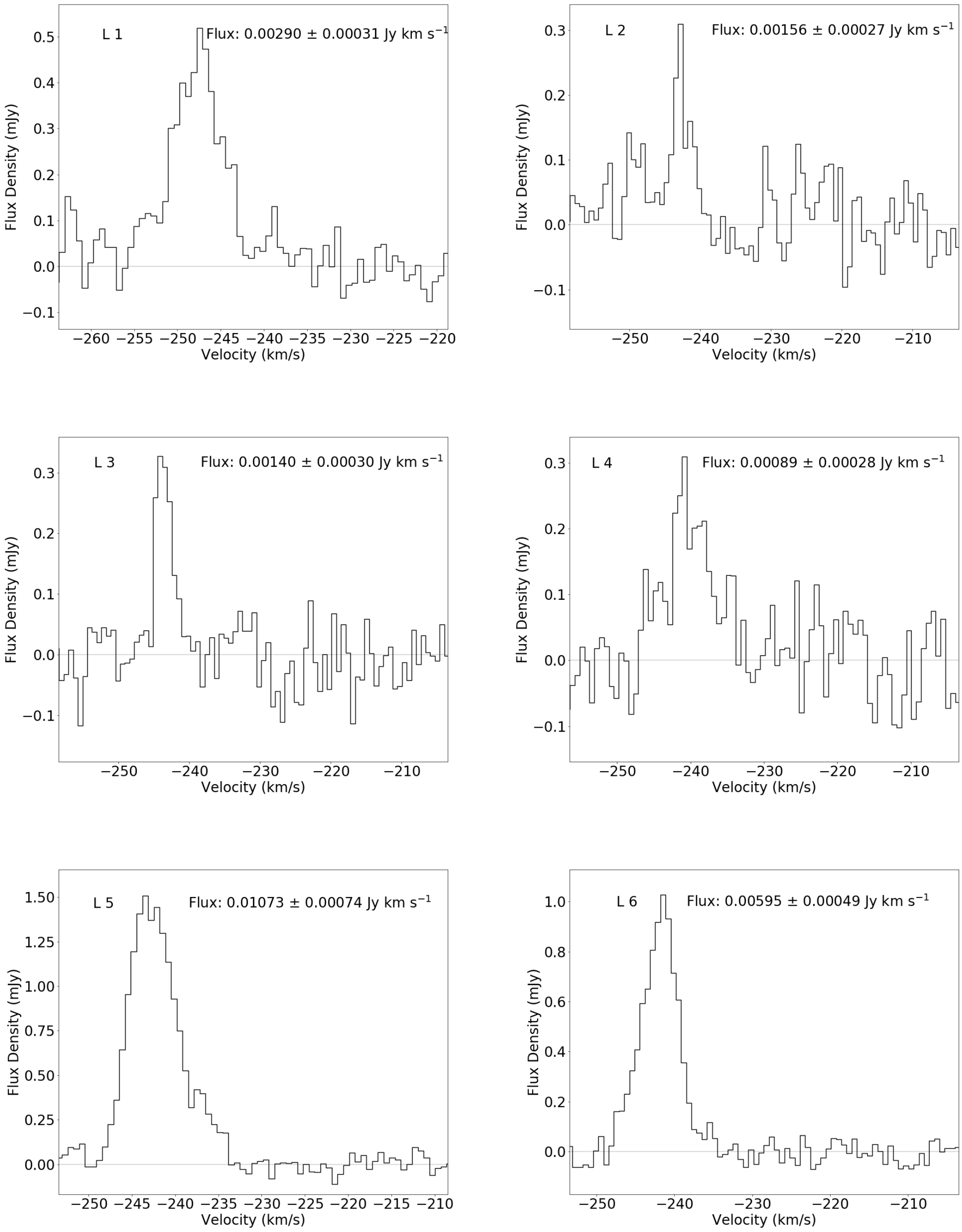

Figure A.1: NGC 604 GMC spectra as measured at the peak of the emission from each source.

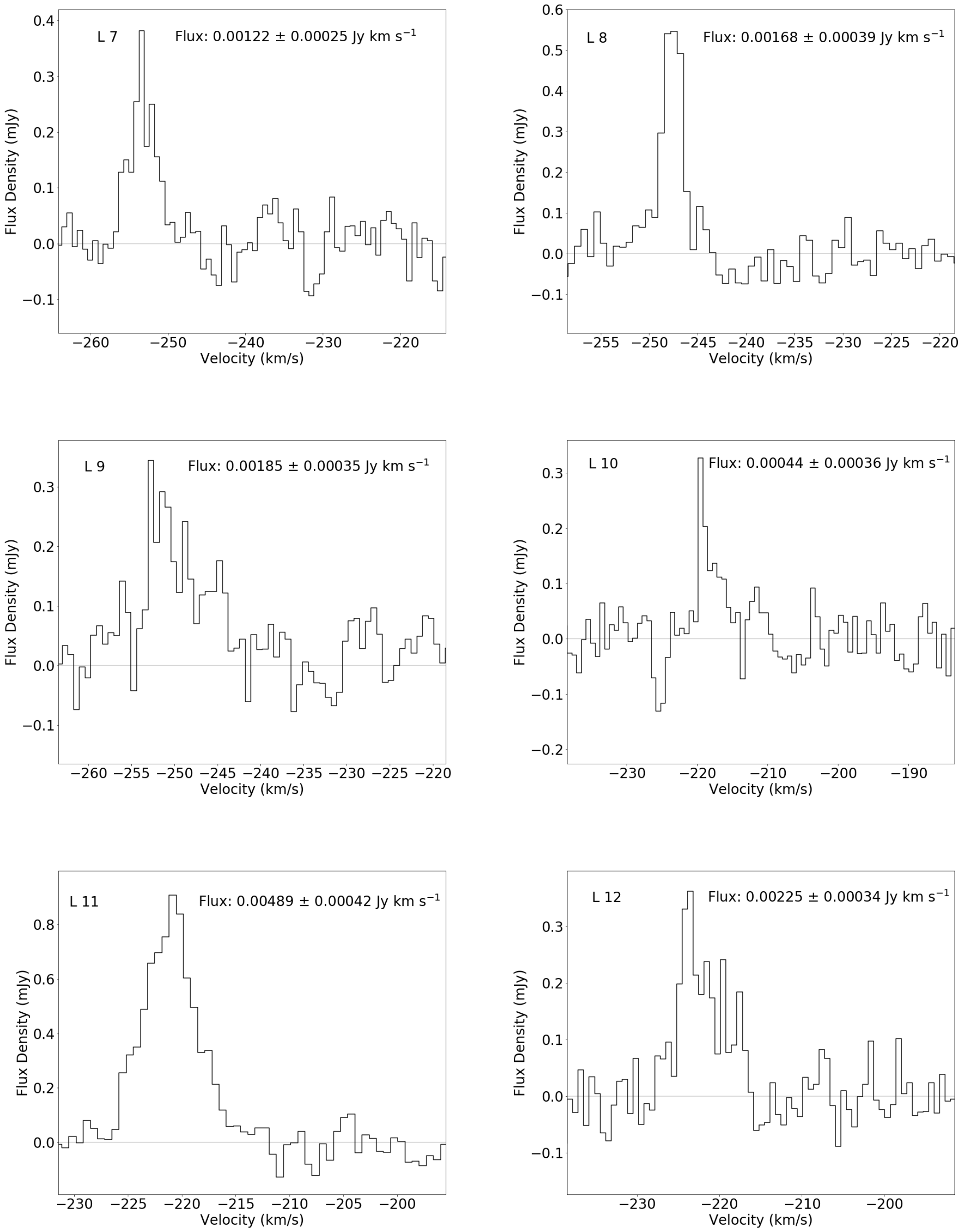

Figure A.1: continued.

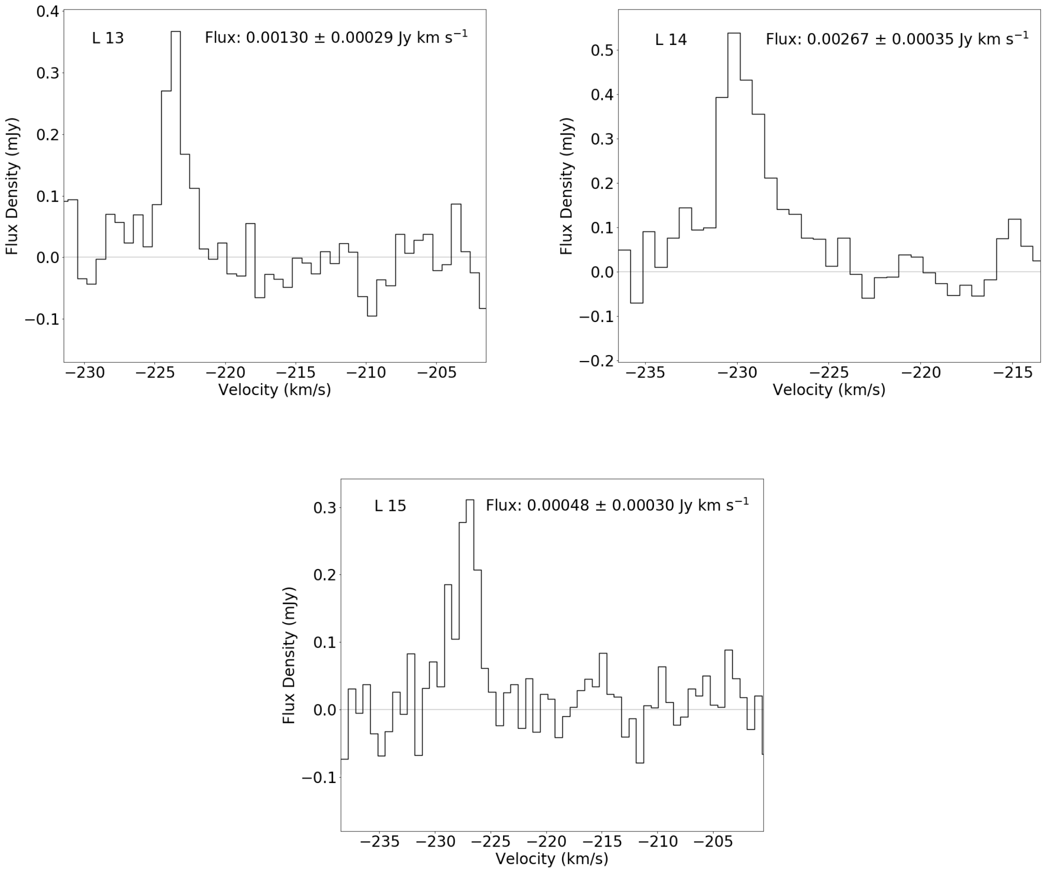

Figure A.1: continued.

Appendix B

Dendrogram Actual Leaves (clumps)

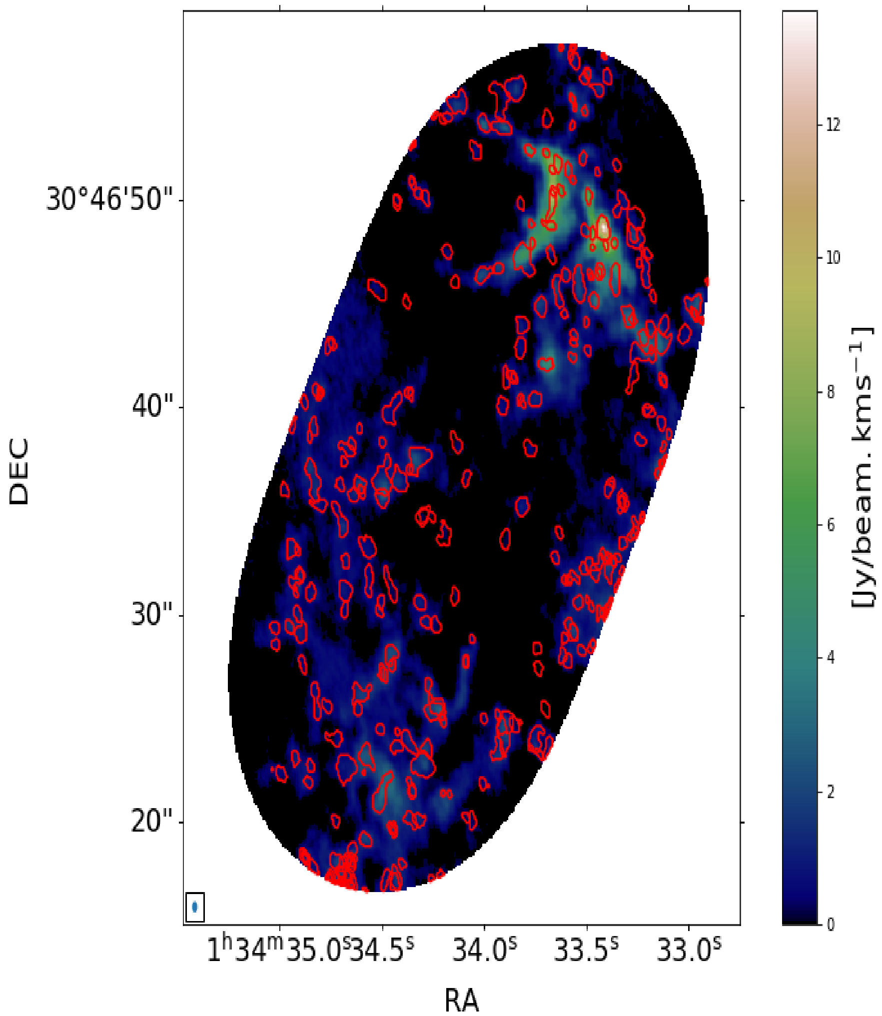

Figure B.1: NGC 604 ^{12}CO(J=2-1) dendrogram tree leaves are plotted on the integrated map.

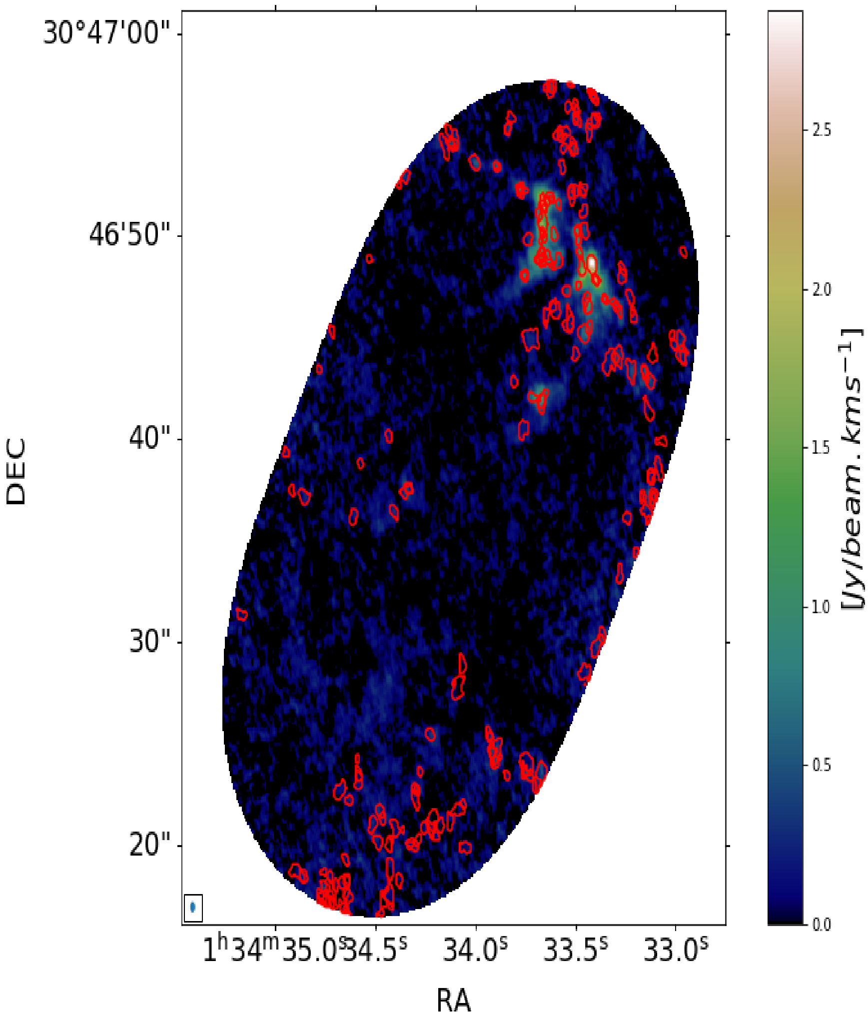

Figure B.2: NGC 604 ^{13}CO(J=2-1) dendrogram tree leaves are plotted on the integrated map.

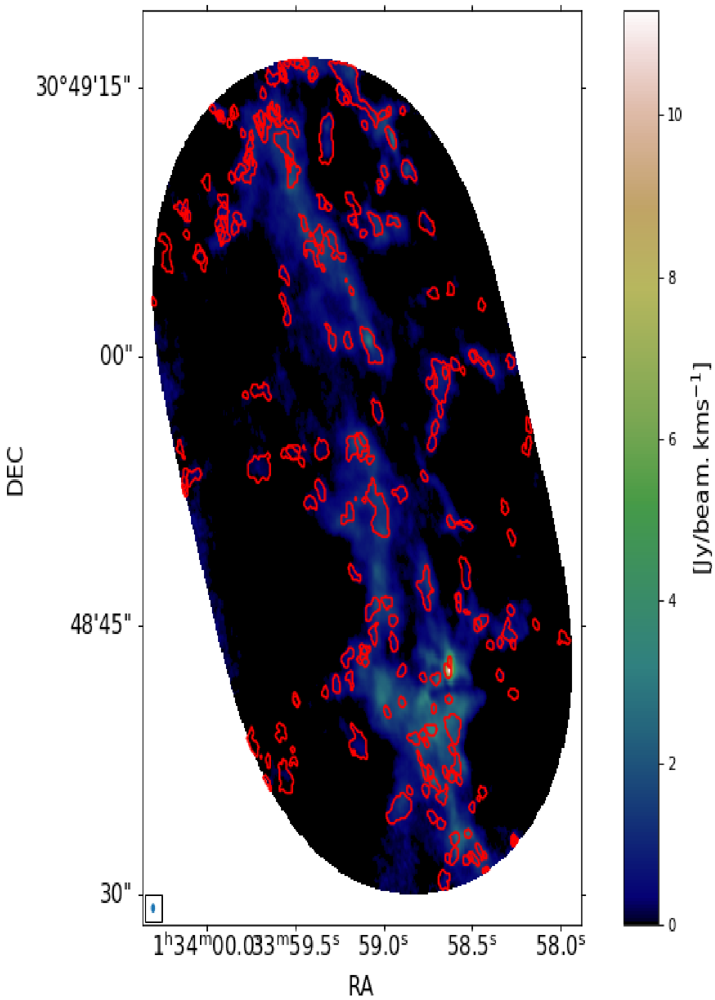

Figure B.3: GMC 16 ^{12}CO(J=2-1) dendrogram tree leaves are plotted on the integrated map.

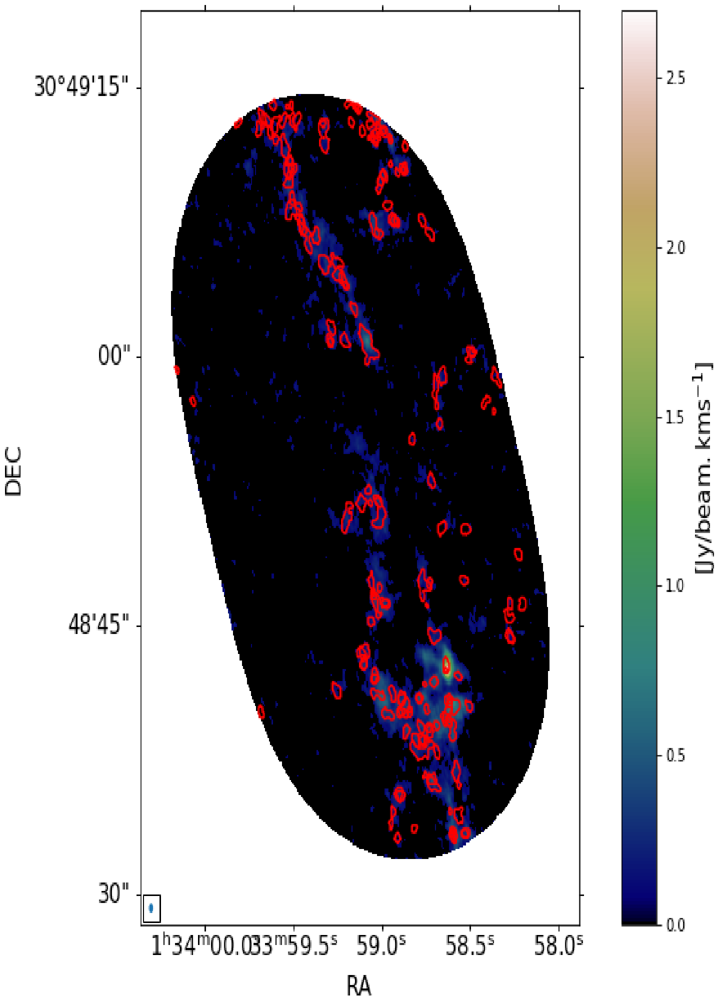

Figure B.4: GMC 16 $^{13}CO(J=2\text{-}1)$ dendrogram tree leaves are plotted on the integrated map.

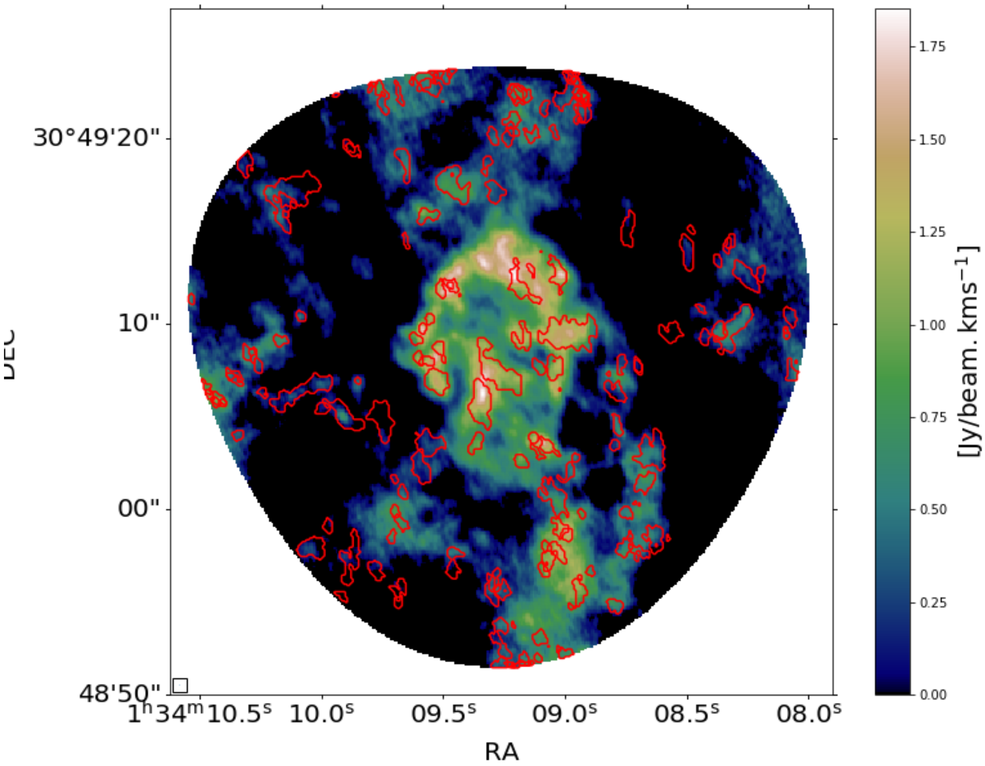

Figure B.5: GMC 8 ^{12}CO(J=2-1) dendrogram tree leaves are plotted on the integrated map.

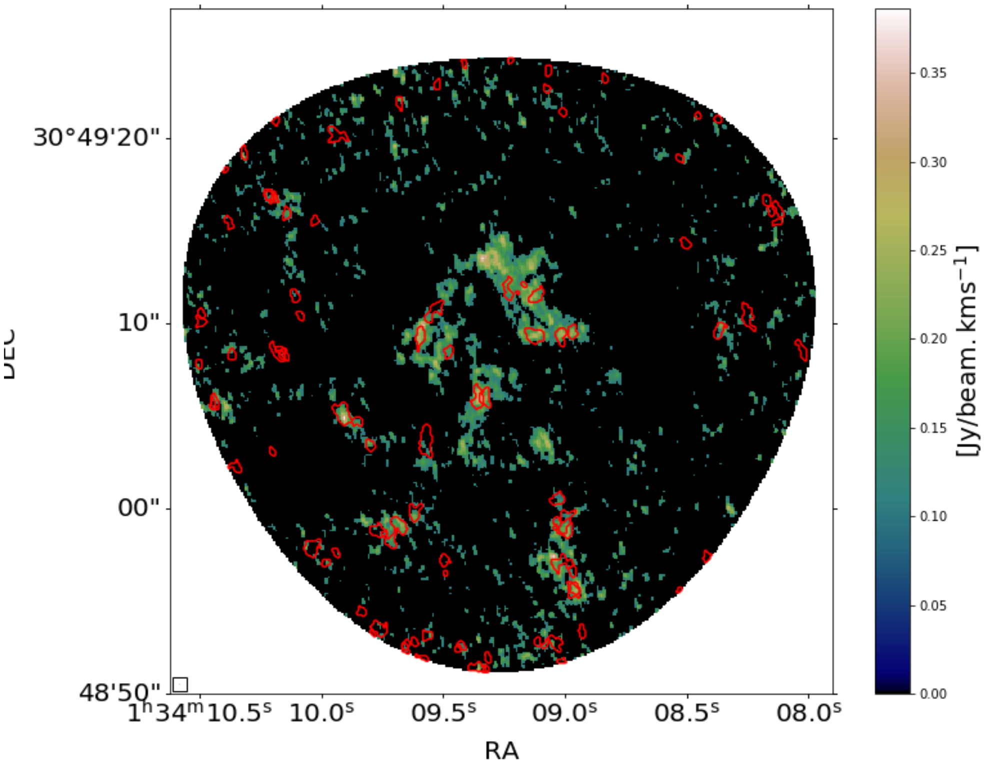

Figure B.6: GMC 8 $^{13}CO(J=2-1)$ dendrogram tree leaves are plotted on the integrated map.

Appendix C

^{12}CO Clumps Catalogs in M33 from NGC 604, GMC 16 and GMC 8

Table C.1: ^{12}CO catalogs for clumps in NGC 604

No.	MC ID	RA	DEC	Δv	R	$L_{^{12}CO(2-1)}$	M_{lum}	M_{vir}	Σ_{lum}	α_{vir}	c
		J2000	J2000	(km s^{-1})	(pc)	K km s^{-1} pc^2	($M_\odot$)	$M_\odot$)	$M_\odot$ pc^{-2}		
1	0	+01:34:33.59	+23:38:23.88	1.13±0.05	1.08±0.06	27±4	240±11	290.8±1.3	66±2	1.21±0.02	0.422±0.012
2	1	+01:34:33.23	+23:38:18.38	0.362±0.015	2.02±0.12	40±3	350±9	55±3	27±4	0.158±0.003	0.272±0.008
3	2	+01:34:33.18	+23:38:17.77	0.51±0.02	1.13±0.07	23±4	198±12	61±3	49±3	0.306±0.006	0.37±0.01
4	6	+01:34:33.13	+23:38:16.99	0.099±0.004	0.68±0.04	2±13	20±40	1±19	13±5	0.0750±0.0015	0.186±0.005
5	22	+01:34:33.14	+23:38:17.04	0.87±0.04	1.18±0.07	85±2	748±6	185.5±1.6	172.3±1.5	0.248±0.005	0.683±0.019
6	30	+01:34:33.35	+23:38:20.25	0.100±0.004	0.81±0.05	4±10	40±30	2±17	18±5	0.0458±0.0009	0.221±0.006
7	33	+01:34:33.78	+23:38:26.65	0.81±0.03	1.14±0.07	52±3	455±8	156.7±1.8	111.7±1.8	0.344±0.007	0.550±0.015
8	35	+01:34:33.39	+23:38:20.79	0.81±0.03	1.35±0.08	38±3	336±9	184.8±1.6	58±3	0.550±0.011	0.397±0.011
9	37	+01:34:33.26	+23:38:18.97	0.73±0.03	2.12±0.12	209.3±1.4	1842±4	234.3±1.5	130.7±1.7	0.127±0.003	0.594±0.017
10	40	+01:34:33.38	+23:38:20.65	0.77±0.03	1.89±0.11	100±2	877±6	238.1±1.4	78±2	0.271±0.005	0.460±0.013
11	42	+01:34:33.13	+23:38:16.91	0.321±0.013	0.88±0.05	22±4	198±12	19±5	81±2	0.0963±0.0019	0.468±0.013
12	46	+01:34:33.33	+23:38:19.90	0.477±0.019	0.96±0.06	9±6	82±19	46±3	28±4	0.561±0.011	0.277±0.008
13	47	+01:34:33.09	+23:38:16.40	0.282±0.012	0.93±0.05	16±5	141±14	16±6	52±3	0.110±0.002	0.38±0.01
14	48	+01:34:33.21	+23:38:18.14	0.68±0.03	1.7±0.1	137.4±1.7	1209±5	167.1±1.7	128.0±1.7	0.138±0.003	0.588±0.016
15	50	+01:34:33.24	+23:38:18.55	0.56±0.02	1.05±0.06	30±4	263±11	68±3	76±2	0.260±0.005	0.452±0.013

Table C.1: **Table C.1 Continued:**

No.	MC ID	RA J2000	DEC J2000	Δv (km s^{-1})	R (pc)	$L_{^{12}CO(2-1)}$ K km s^{-1} pc^2	M_{lum} ($M_\odot$)	M_{vir} $M_\odot$)	Σ_{lum} $M_\odot$ pc^{-2}	α_{vir}	c
16	51	+01:34:33.36	+23:38:20.44	0.55±0.02	1.63±0.09	53±3	464±8	102±2	56±3	0.220±0.004	0.388±0.011
17	52	+01:34:33.51	+23:38:22.61	0.390±0.016	0.98±0.06	13±5	112±16	31±4	37±3	0.280±0.006	0.318±0.009
18	56	+01:34:33.19	+23:38:17.91	0.392±0.016	1.20±0.07	28±4	247±11	39±4	55±3	0.157±0.003	0.384±0.011
19	60	+01:34:33.65	+23:38:24.70	0.97±0.04	1.11±0.06	34±3	299±10	220.0±1.5	77±2	0.736±0.015	0.458±0.013
20	61	+01:34:33.13	+23:38:16.89	0.171±0.007	0.88±0.05	12±6	101±17	5±10	41±3	0.0536±0.0011	0.335±0.009
21	63	+01:34:33.81	+23:38:27.16	1.39±0.06	2.54±0.15	464.1±0.9	4084±3	1028.8±0.7	202.2±1.4	0.252±0.005	0.74±0.02
22	65	+01:34:33.39	+23:38:20.87	0.223±0.009	0.71±0.04	10±6	84±19	7±8	53±3	0.0885±0.0018	0.38±0.01
23	67	+01:34:33.32	+23:38:19.84	0.25±0.01	1.09±0.06	8±7	70±20	15±6	19±4	0.208±0.004	0.225±0.006
24	68	+01:34:33.12	+23:38:16.84	0.52±0.02	0.72±0.04	20±4	177±13	41±3	109.6±1.9	0.229±0.005	0.544±0.015
25	71	+01:34:33.35	+23:38:20.25	0.183±0.007	0.69±0.04	4±10	40±30	0±10	25±4	0.130±0.003	0.260±0.007
26	72	+01:34:34.60	+23:38:39.00	1.25±0.05	1.46±0.08	134.4±1.7	1182±5	482±1	176.6±1.5	0.408±0.008	0.691±0.019
27	76	+01:34:33.15	+23:38:17.27	0.360±0.015	0.72±0.04	19±4	171±13	20±5	106.6±1.9	0.114±0.002	0.537±0.015
28	78	+01:34:33.20	+23:38:17.97	0.351±0.014	1.70±0.10	12±6	107±17	44±3	12±6	0.410±0.008	0.179±0.005
29	79	+01:34:33.58	+23:38:23.65	0.90±0.04	1.68±0.10	147.8±1.6	1300±5	289.1±1.3	145.9±1.6	0.222±0.004	0.628±0.017
30	80	+01:34:33.34	+23:38:20.06	0.397±0.016	1.92±0.11	21±4	186±13	64±3	16±5	0.341±0.007	0.208±0.006

Table C.1: **Table C.1 Continued:**

No.	MC ID	RA	DEC	Δv	R	$L_{^{12}CO(2-1)}$	M_{lum}	M_{vir}	Σ_{lum}	α_{vir}	c
		J2000	J2000	(km s^{-1})	(pc)	K km s^{-1} pc^2	(M$_\odot$)	M$_\odot$)	M$_\odot$ pc^{-2}		
31	82	+01:34:33.40	+23:38:20.93	0.387±0.016	1.07±0.06	27±4	235±11	34±4	65±2	0.144±0.003	0.419±0.012
32	87	+01:34:33.69	+23:38:25.41	0.79±0.03	1.08±0.06	31±4	270±10	140.8±1.9	74±2	0.522±0.011	0.446±0.012
33	91	+01:34:33.17	+23:38:17.60	0.412±0.017	0.75±0.04	12±6	108±17	27±4	61±2	0.247±0.005	0.407±0.011
34	99	+01:34:33.77	+23:38:26.49	0.232±0.009	0.69±0.04	3±11	30±30	8±8	18±5	0.296±0.006	0.219±0.006
35	101	+01:34:33.41	+23:38:21.11	0.393±0.016	1.26±0.07	26±4	226±11	41±3	46±3	0.180±0.004	0.351±0.010
36	102	+01:34:33.82	+23:38:27.26	1.04±0.04	1.56±0.09	123.6±1.8	1088±5	354.8±1.2	141.7±1.6	0.326±0.007	0.619±0.017
37	103	+01:34:33.70	+23:38:25.52	0.57±0.02	1.19±0.07	23±4	205±12	82±2	46±3	0.400±0.008	0.353±0.010
38	107	+01:34:33.64	+23:38:24.59	0.82±0.03	1.56±0.09	31±3	280±10	217.9±1.5	36±3	0.788±0.016	0.312±0.009
39	108	+01:34:33.13	+23:38:16.97	0.77±0.03	1.21±0.07	60±3	526±8	149.5±1.8	114.0±1.8	0.284±0.006	0.555±0.015
40	110	+01:34:33.84	+23:38:27.66	1.19±0.05	2.00±0.12	388.2±1.0	3417±3	592.0±0.9	271.0±1.2	0.173±0.003	0.86±0.02
41	111	+01:34:33.23	+23:38:18.44	0.233±0.009	0.98±0.06	6±8	50±20	11±7	16±5	0.224±0.005	0.211±0.006
42	112	+01:34:33.51	+23:38:22.63	0.083±0.003	0.91±0.05	3±12	20±30	1±19	9±6	0.0524±0.0011	0.160±0.004
43	113	+01:34:33.46	+23:38:21.91	0.197±0.008	1.09±0.06	6±8	60±20	9±7	15±5	0.157±0.003	0.203±0.006
44	115	+01:34:33.48	+23:38:22.14	···	0.69±0.04	2±13	20±40	···	13±5	···	0.190±0.005
45	119	+01:34:33.42	+23:38:21.27	0.117±0.005	0.82±0.05	6±8	50±20	2±14	25±4	0.0448±0.0009	0.259±0.007

Table C.1: **Table C.1 Continued:**

No.	MC ID	RA J2000	DEC J2000	Δv (km s^{-1})	R (pc)	$L_{^{12}CO(2-1)}$ K km s^{-1} pc^2	M_{lum} ($M_\odot$)	M_{vir} $M_\odot$)	Σ_{lum} $M_\odot$ pc^{-2}	α_{vir}	c
46	128	+01:34:33.72	+23:38:25.87	0.91±0.04	1.48±0.09	246.2±1.2	2166±4	257.1±1.4	316.3±1.1	0.119±0.002	0.92±0.03
47	129	+01:34:33.61	+23:38:24.12	0.431±0.018	1.35±0.08	43±3	381±9	53±3	66±2	0.138±0.003	0.424±0.012
48	131	+01:34:33.52	+23:38:22.86	0.420±0.017	1.00±0.06	23±4	205±12	37±4	66±2	0.180±0.004	0.421±0.012
49	133	+01:34:32.97	+23:38:14.55	0.182±0.007	0.66±0.04	7±8	60±20	0±10	42±3	0.0792±0.0016	0.338±0.009
50	137	+01:34:33.73	+23:38:25.99	0.384±0.016	1.02±0.06	12±6	106±17	31±4	33±3	0.297±0.006	0.296±0.008
51	141	+01:34:33.19	+23:38:17.84	0.51±0.02	1.43±0.08	13±5	115±16	79±2	18±5	0.690±0.014	0.220±0.006
52	143	+01:34:33.91	+23:38:28.62	1.36±0.06	1.45±0.08	272.5±1.2	2398±4	568.7±0.9	361±1	0.237±0.005	0.99±0.03
53	144	+01:34:33.41	+23:38:21.13	0.68±0.03	0.97±0.06	34±3	302±10	95±2	101.3±1.9	0.315±0.006	0.523±0.015
54	145	+01:34:34.00	+23:38:30.04	1.36±0.06	1.19±0.07	231.0±1.3	2033±4	462±1	459.7±0.9	0.227±0.005	1.11±0.03
55	146	+01:34:33.27	+23:38:19.04	0.62±0.03	1.19±0.07	46±3	404±9	96±2	91±2	0.237±0.005	0.497±0.014
56	148	+01:34:33.13	+23:38:17.00	0.73±0.03	2.02±0.12	362±1	3187±3	225.4±1.5	248.8±1.2	0.0707±0.0014	0.82±0.02
57	150	+01:34:32.97	+23:38:14.58	0.55±0.02	0.85±0.05	26±4	230±11	54±3	100.8±1.9	0.234±0.005	0.522±0.015
58	155	+01:34:33.30	+23:38:19.45	0.73±0.03	1.83±0.11	242.7±1.3	2136±4	205.6±1.6	203.0±1.4	0.0963±0.0019	0.74±0.02
59	156	+01:34:33.67	+23:38:25.07	0.477±0.019	1.05±0.06	18±5	154±14	50±3	44±3	0.326±0.007	0.347±0.010
60	158	+01:34:33.43	+23:38:21.48	0.295±0.012	1.03±0.06	14±5	124±15	19±5	37±3	0.152±0.003	0.316±0.009

Table C.1: **Table C.1 Continued:**

No.	MC ID	RA	DEC	Δv	R	$L_{^{12}CO(2-1)}$	M_{lum}	M_{vir}	Σ_{lum}	α_{vir}	c
		J2000	J2000	(km s^{-1})	(pc)	K km s^{-1} pc^2	($M_\odot$)	$M_\odot$)	$M_\odot$ pc^{-2}		
61	160	+01:34:33.51	+23:38:22.59	1.19±0.05	1.15±0.07	102.1±1.9	898±6	343.2±1.2	214.6±1.3	0.382±0.008	0.76±0.02
62	163	+01:34:33.57	+23:38:23.48	0.162±0.007	0.63±0.04	0±10	30±30	3±12	26±4	0.106±0.002	0.267±0.007
63	164	+01:34:33.74	+23:38:26.12	0.76±0.03	1.11±0.06	23±4	200±12	136.5±1.9	52±3	0.681±0.014	0.37±0.01
64	165	+01:34:33.23	+23:38:18.44	0.067±0.003	0.75±0.04	3±12	20±40	0±30	13±5	0.0303±0.0006	0.188±0.005
65	170	+01:34:33.64	+23:38:24.63	0.67±0.03	1.29±0.07	246.9±1.2	2173±4	120±2	417.5±1.0	0.0552±0.0011	1.06±0.03
66	172	+01:34:33.44	+23:38:21.59	0.74±0.03	1.03±0.06	67±2	592±7	120±2	175.9±1.5	0.203±0.004	0.690±0.019
67	174	+01:34:33.48	+23:38:22.16	0.466±0.019	1.12±0.06	51±3	450±8	51±3	114.1±1.8	0.113±0.002	0.556±0.015
68	176	+01:34:34.13	+23:38:31.95	1.31±0.05	2.09±0.12	389.0±1.0	3423±3	755.0±0.8	249.0±1.2	0.221±0.004	0.82±0.02
69	177	+01:34:34.29	+23:38:34.41	0.86±0.04	1.86±0.11	275.5±1.2	2424±3	289.8±1.3	224.2±1.3	0.120±0.002	0.78±0.02
70	178	+01:34:33.23	+23:38:18.42	0.144±0.006	0.61±0.04	3±11	30±30	3±14	25±4	0.0927±0.0019	0.258±0.007
71	179	+01:34:34.60	+23:38:38.95	0.52±0.02	1.34±0.08	19±5	163±13	76±3	29±4	0.468±0.009	0.280±0.008
72	180	+01:34:34.83	+23:38:42.51	0.64±0.03	1.20±0.07	56±3	491±8	103±2	107.9±1.9	0.209±0.004	0.540±0.015
73	182	+01:34:34.74	+23:38:41.09	0.202±0.008	0.87±0.05	6±8	60±20	7±8	24±4	0.132±0.003	0.254±0.007
74	183	+01:34:33.33	+23:38:19.89	1.56±0.06	1.86±0.11	116.1±1.8	1022±5	942.5±0.7	94±2	0.922±0.019	0.505±0.014
75	185	+01:34:34.37	+23:38:35.49	0.50±0.02	1.87±0.11	33±3	290±10	97±2	26±4	0.334±0.007	0.267±0.007

Table C.1: **Table C.1 Continued:**

No.	MC ID	RA J2000	DEC J2000	Δv (km s^{-1})	R (pc)	$L_{^{12}CO(2-1)}$ K km s^{-1} pc^2	M_{lum} ($M_\odot$)	M_{vir} $M_\odot$)	Σ_{lum} $M_\odot$ pc^{-2}	α_{vir}	c
76	186	+01:34:34.69	+23:38:40.42	0.54±0.02	2.51±0.15	159.1±1.6	1400±5	153.5±1.8	71±2	0.110±0.002	0.437±0.012
77	189	+01:34:33.53	+23:38:22.92	0.76±0.03	1.57±0.09	119.0±1.8	1047±5	191.0±1.6	135.1±1.7	0.182±0.004	0.605±0.017
78	190	+01:34:32.91	+23:38:13.64	0.157±0.006	0.37±0.02	0±20	10±60	2±16	18±5	0.246±0.005	0.222±0.006
79	193	+01:34:33.56	+23:38:23.44	0.382±0.016	0.90±0.05	53±3	466±8	28±4	181.9±1.4	0.0594±0.0012	0.70±0.02
80	195	+01:34:33.56	+23:38:23.43	0.401±0.016	0.59±0.03	12±6	102±17	20±5	93±2	0.195±0.004	0.502±0.014
81	196	+01:34:34.50	+23:38:37.45	1.51±0.06	1.46±0.08	175.5±1.5	1545±4	693.5±0.8	232.3±1.3	0.449±0.009	0.79±0.02
82	197	+01:34:33.78	+23:38:26.68	0.97±0.04	0.90±0.05	160.2±1.5	1410±5	178.2±1.7	555.9±0.8	0.126±0.003	1.23±0.03
83	198	+01:34:33.57	+23:38:23.55	0.226±0.009	0.59±0.03	8±7	70±20	6±9	62±2	0.0930±0.0019	0.409±0.011
84	200	+01:34:33.22	+23:38:18.34	0.87±0.04	1.22±0.07	174.3±1.5	1534±4	192.6±1.6	325.7±1.1	0.126±0.003	0.94±0.03
85	201	+01:34:33.24	+23:38:18.62	0.53±0.02	0.66±0.04	8±7	70±20	39±4	52±3	0.535±0.011	0.38±0.01
86	203	+01:34:34.62	+23:38:39.32	0.191±0.008	1.27±0.07	12±6	103±17	10±7	20±4	0.0948±0.0019	0.235±0.007
87	204	+01:34:33.40	+23:38:21.07	0.361±0.015	0.68±0.04	36±3	314±10	19±5	217.3±1.3	0.0592±0.0012	0.77±0.02
88	205	+01:34:33.70	+23:38:25.48	0.67±0.03	0.74±0.04	68±2	597±7	69±3	348±1	0.115±0.002	0.97±0.03
89	206	+01:34:33.51	+23:38:22.61	0.48±0.02	0.69±0.04	40±3	355±9	34±4	235.7±1.3	0.0958±0.0019	0.80±0.02
90	209	+01:34:33.61	+23:38:24.08	0.056±0.002	0.85±0.05	2±13	20±40	0±30	8±7	0.0293±0.0006	0.151±0.004

Table C.1: **Table C.1 Continued:**

No.	MC ID	RA	DEC	Δv	R	$L_{^{12}CO(2-1)}$	M_{lum}	M_{vir}	Σ_{lum}	α_{vir}	c
		J2000	J2000	(km s^{-1})	(pc)	K km s^{-1} pc^2	($M_\odot$)	$M_\odot$)	$M_\odot$ pc^{-2}		
91	211	+01:34:34.80	+23:38:41.98	0.355±0.015	0.82±0.05	13±5	112±16	22±5	53±3	0.195±0.004	0.378±0.011
92	212	+01:34:34.76	+23:38:41.33	0.178±0.007	1.03±0.06	8±7	70±20	7±8	21±4	0.098±0.002	0.238±0.007
93	213	+01:34:33.50	+23:38:22.48	0.362±0.015	0.77±0.04	24±4	209±12	21±5	111.2±1.8	0.102±0.002	0.548±0.015
94	214	+01:34:32.97	+23:38:14.60	0.84±0.03	1.91±0.11	292.9±1.1	2577±3	282.6±1.3	223.9±1.3	0.110±0.002	0.78±0.02
95	216	+01:34:33.64	+23:38:24.56	1.35±0.06	2.48±0.14	242.8±1.3	2137±4	948.5±0.7	110.3±1.8	0.444±0.009	0.546±0.015
96	217	+01:34:34.18	+23:38:32.74	0.66±0.03	1.02±0.06	38±3	335±9	93±2	102.2±1.9	0.277±0.006	0.526±0.015
97	218	+01:34:33.73	+23:38:25.93	0.359±0.015	0.77±0.04	20±4	176±13	21±5	94±2	0.119±0.002	0.503±0.014
98	219	+01:34:33.26	+23:38:18.93	0.49±0.02	1.18±0.07	27±4	241±11	60±3	55±3	0.249±0.005	0.387±0.011
99	220	+01:34:34.84	+23:38:42.63	0.89±0.04	2.49±0.14	291.4±1.1	2565±3	410.6±1.1	131.5±1.7	0.160±0.003	0.596±0.017
100	221	+01:34:33.47	+23:38:21.99	0.53±0.02	3.09±0.18	150.8±1.6	1327±5	185.0±1.6	44±3	0.139±0.003	0.346±0.010
101	223	+01:34:33.89	+23:38:28.36	0.79±0.03	2.68±0.16	412.4±1.0	3629±3	353.5±1.2	160.6±1.5	0.097±0.002	0.659±0.018
102	224	+01:34:33.47	+23:38:21.99	0.133±0.005	0.69±0.04	6±8	50±20	3±14	35±3	0.0494±0.0010	0.306±0.009
103	225	+01:34:33.68	+23:38:25.17	0.62±0.03	1.12±0.06	108.8±1.9	958±6	91±2	244.0±1.2	0.0952±0.0019	0.81±0.02
104	226	+01:34:33.57	+23:38:23.53	0.191±0.008	0.80±0.05	20±4	174±13	6±9	87±2	0.0351±0.0007	0.486±0.014
105	227	+01:34:33.58	+23:38:23.64	···	0.76±0.04	3±12	20±40	···	13±5	···	0.184±0.005

Table C.1: **Table C.1 Continued:**

No.	MC ID	RA J2000	DEC J2000	Δv (km s^{-1})	R (pc)	$L_{^{12}CO(2-1)}$ K km s^{-1} pc^2	M_{lum} ($M_\odot$)	M_{vir} $M_\odot$)	Σ_{lum} $M_\odot$ pc^{-2}	α_{vir}	c
106	228	+01:34:33.68	+23:38:25.24	0.59±0.02	1.20±0.07	104.1±1.9	916±6	87±2	203.1±1.4	0.0950±0.0019	0.74±0.02
107	229	+01:34:33.57	+23:38:23.49	0.87±0.04	1.46±0.08	73±2	639±7	231.0±1.5	95±2	0.362±0.007	0.507±0.014
108	233	+01:34:33.68	+23:38:25.27	1.49±0.06	1.8±0.1	556.3±0.8	4895±2	835.2±0.8	485.5±0.9	0.171±0.003	1.15±0.03
109	234	+01:34:33.43	+23:38:21.50	0.65±0.03	1.17±0.07	282.9±1.2	2489±3	104±2	575.2±0.8	0.0418±0.0008	1.25±0.03
110	238	+01:34:33.28	+23:38:19.16	0.80±0.03	1.98±0.11	52±3	459±8	264.7±1.4	37±3	0.577±0.012	0.318±0.009
111	239	+01:34:33.12	+23:38:16.85	0.56±0.02	1.39±0.08	88±2	773±6	90±2	127.4±1.7	0.117±0.002	0.587±0.016
112	243	+01:34:34.80	+23:38:42.03	0.298±0.012	0.65±0.04	7±7	60±20	12±6	48±3	0.189±0.004	0.36±0.01
113	244	+01:34:33.58	+23:38:23.76	0.438±0.018	1.64±0.10	91±2	798±6	66±3	94±2	0.0830±0.0017	0.504±0.014
114	246	+01:34:33.62	+23:38:24.32	0.88±0.04	1.14±0.07	158.4±1.6	1394±5	186.6±1.6	344±1	0.134±0.003	0.96±0.03
115	247	+01:34:33.49	+23:38:22.42	1.20±0.05	0.87±0.05	60±3	529±7	263.0±1.4	221.9±1.3	0.50±0.01	0.77±0.02
116	248	+01:34:33.41	+23:38:21.21	0.70±0.03	0.47±0.03	23±4	203±12	49±3	295.1±1.1	0.240±0.005	0.89±0.02
117	249	+01:34:33.42	+23:38:21.29	1.63±0.07	1.67±0.10	1795.8±0.5	15803.2±1.4	925.7±0.7	1814.4±0.5	0.0586±0.0012	2.21±0.06
118	251	+01:34:33.56	+23:38:23.33	0.56±0.02	1.19±0.07	43±3	374±9	78±3	84±2	0.208±0.004	0.476±0.013
119	253	+01:34:33.77	+23:38:26.57	0.076±0.003	0.52±0.03	2±15	20±40	0±30	17±5	0.0423±0.0009	0.217±0.006
120	254	+01:34:34.56	+23:38:38.35	0.86±0.04	2.38±0.14	119.0±1.8	1047±5	368.8±1.2	59±3	0.352±0.007	0.399±0.011

Table C.1: **Table C.1 Continued:**

No.	MC ID	RA J2000	DEC J2000	Δv (km s^{-1})	R (pc)	$L_{^{12}CO(2-1)}$ K km s^{-1} pc^2	M_{lum} ($M_\odot$)	M_{vir} $M_\odot$)	Σ_{lum} $M_\odot$ pc^{-2}	α_{vir}	c
121	255	+01:34:34.85	+23:38:42.81	0.435±0.018	0.86±0.05	17±5	154±14	34±4	67±2	0.221±0.004	0.426±0.012
122	256	+01:34:33.02	+23:38:15.34	0.62±0.03	1.42±0.08	75±2	663±7	115±2	104.1±1.9	0.174±0.004	0.531±0.015
123	258	+01:34:34.04	+23:38:30.55	1.08±0.04	1.19±0.07	42±3	369±9	291.1±1.3	83±2	0.788±0.016	0.473±0.013
124	259	+01:34:33.32	+23:38:19.79	0.135±0.006	1.15±0.07	7±7	70±20	4±11	16±5	0.0674±0.0014	0.207±0.006
125	260	+01:34:34.24	+23:38:33.67	0.80±0.03	2.27±0.13	224.0±1.3	1971±4	305.4±1.3	122.2±1.8	0.155±0.003	0.575±0.016
126	261	+01:34:33.51	+23:38:22.63	0.341±0.014	1.48±0.09	26±4	228±11	36±4	33±3	0.160±0.003	0.298±0.008
127	262	+01:34:33.81	+23:38:27.15	1.37±0.06	1.51±0.09	165.2±1.5	1454±5	592.4±0.9	203.0±1.4	0.407±0.008	0.74±0.02
128	263	+01:34:34.98	+23:38:44.72	0.56±0.02	1.05±0.06	20±4	175±13	71±3	50±3	0.402±0.008	0.37±0.01
129	264	+01:34:34.80	+23:38:42.05	0.147±0.006	0.84±0.05	7±7	60±20	4±11	28±4	0.0604±0.0012	0.276±0.008
130	265	+01:34:33.46	+23:38:21.90	0.66±0.03	1.09±0.06	155.4±1.6	1367±5	101±2	363±1	0.0739±0.0015	0.99±0.03
131	269	+01:34:33.59	+23:38:23.87	0.62±0.03	1.10±0.06	23±4	204±12	89±2	53±3	0.436±0.009	0.380±0.011
132	270	+01:34:34.51	+23:38:37.64	0.118±0.005	0.76±0.04	5±9	40±30	2±15	23±4	0.0526±0.0011	0.251±0.007
133	271	+01:34:33.59	+23:38:23.90	0.135±0.006	0.86±0.05	7±7	60±20	3±12	27±4	0.0527±0.0011	0.270±0.008
134	272	+01:34:34.91	+23:38:43.64	0.099±0.004	0.75±0.04	3±11	30±30	2±18	15±5	0.0584±0.0012	0.201±0.006
135	273	+01:34:34.37	+23:38:35.48	0.53±0.02	0.85±0.05	18±5	161±14	50±3	70±2	0.312±0.006	0.436±0.012

Table C.1: **Table C.1 Continued:**

No.	MC ID	RA J2000	DEC J2000	Δv (km s^{-1})	R (pc)	$L_{^{12}CO(2-1)}$ K km s^{-1} pc^2	M_{lum} ($M_\odot$)	M_{vir} $M_\odot$)	Σ_{lum} $M_\odot$ pc^{-2}	α_{vir}	c
136	275	+01:34:32.94	+23:38:14.03	···	0.51±0.03	2±15	20±40	···	19±5	···	0.224±0.006
137	276	+01:34:33.75	+23:38:26.19	1.03±0.04	2.08±0.12	242.9±1.3	2137±4	467±1	157.4±1.5	0.218±0.004	0.652±0.018
138	277	+01:34:33.37	+23:38:20.60	0.428±0.017	0.83±0.05	15±5	129±15	32±4	60±3	0.246±0.005	0.403±0.011
139	279	+01:34:33.82	+23:38:27.29	0.433±0.018	1.08±0.06	45±3	393±9	43±3	107.8±1.9	0.108±0.002	0.540±0.015
140	281	+01:34:33.56	+23:38:23.41	0.48±0.02	1.04±0.06	53±3	465±8	51±3	136.1±1.7	0.110±0.002	0.607±0.017
141	282	+01:34:33.47	+23:38:22.05	0.450±0.018	0.54±0.03	27±4	238±11	23±5	259.0±1.2	0.0964±0.0019	0.84±0.02
142	286	+01:34:33.40	+23:38:20.93	0.68±0.03	1.18±0.07	51±3	451±8	116±2	103.3±1.9	0.256±0.005	0.528±0.015
143	287	+01:34:33.62	+23:38:24.36	0.361±0.015	0.58±0.03	16±5	139±15	16±6	132.2±1.7	0.114±0.002	0.598±0.017
144	288	+01:34:34.72	+23:38:40.81	0.357±0.015	1.35±0.08	30±4	264±11	36±4	46±3	0.137±0.003	0.354±0.010
145	290	+01:34:34.93	+23:38:43.99	0.91±0.04	1.88±0.11	116.4±1.8	1024±5	327.6±1.2	92±2	0.320±0.006	0.499±0.014
146	291	+01:34:33.76	+23:38:26.47	0.53±0.02	1.8±0.1	93±2	820±6	104±2	81±2	0.127±0.003	0.467±0.013
147	293	+01:34:33.61	+23:38:24.10	0.50±0.02	0.74±0.04	14±5	120±16	39±4	71±2	0.324±0.007	0.437±0.012
148	294	+01:34:34.92	+23:38:43.79	0.51±0.02	1.8±0.1	25±4	223±12	96±2	22±4	0.434±0.009	0.246±0.007
149	295	+01:34:34.33	+23:38:34.97	2.6±0.1	2.53±0.15	733.6±0.7	6455±2	3460.7±0.4	321.2±1.1	0.536±0.011	0.93±0.03
150	296	+01:34:33.48	+23:38:22.16	0.230±0.009	0.53±0.03	9±7	80±20	6±9	86±2	0.0775±0.0016	0.483±0.013

Table C.1: **Table C.1 Continued:**

No.	MC ID	RA	DEC	Δv	R	$L_{^{12}CO(2-1)}$	M_{lum}	M_{vir}	Σ_{lum}	α_{vir}	c
		J2000	J2000	(km s^{-1})	(pc)	K km s^{-1} pc^2	($M_\odot$)	$M_\odot$)	$M_\odot$ pc^{-2}		
151	297	+01:34:32.94	+23:38:14.04	···	0.47±0.03	1±18	10±50	···	16±5	···	0.207±0.006
152	299	+01:34:33.82	+23:38:27.37	0.59±0.02	0.81±0.05	14±5	119±16	59±3	58±3	0.496±0.010	0.396±0.011
153	300	+01:34:34.67	+23:38:40.01	1.24±0.05	2.25±0.13	171.6±1.5	1510±4	731.0±0.8	95±2	0.484±0.010	0.507±0.014
154	302	+01:34:33.42	+23:38:21.25	0.205±0.008	0.35±0.02	4±10	30±30	3±13	89±2	0.0903±0.0018	0.492±0.014
155	303	+01:34:34.41	+23:38:36.21	1.19±0.05	1.70±0.10	211.1±1.3	1858±4	505.5±1.0	204.8±1.4	0.272±0.005	0.74±0.02
156	304	+01:34:33.33	+23:38:19.89	0.077±0.003	0.60±0.03	1±18	10±50	0±30	9±7	0.0746±0.0015	0.155±0.004
157	305	+01:34:33.48	+23:38:22.25	0.206±0.008	0.63±0.04	15±5	129±15	6±9	104.7±1.9	0.0433±0.0009	0.532±0.015
158	306	+01:34:34.92	+23:38:43.75	0.134±0.005	1.62±0.09	4±10	40±30	6±9	4±9	0.166±0.003	0.110±0.003
159	307	+01:34:34.82	+23:38:42.31	0.179±0.007	1.04±0.06	6±8	50±20	7±8	16±5	0.132±0.003	0.206±0.006
160	310	+01:34:33.66	+23:38:24.90	0.074±0.003	0.76±0.04	10±6	86±19	0±20	48±3	0.0101±0.0002	0.359±0.010
161	311	+01:34:34.18	+23:38:32.75	0.186±0.008	1.01±0.06	13±5	113±16	7±8	35±3	0.0651±0.0013	0.309±0.009
162	313	+01:34:33.83	+23:38:27.43	0.78±0.03	1.8±0.1	130.2±1.7	1146±5	233.0±1.5	111.2±1.8	0.203±0.004	0.548±0.015
163	314	+01:34:33.67	+23:38:25.03	1.35±0.05	1.94±0.11	674.6±0.8	5936±2	741.3±0.8	499.9±0.9	0.125±0.003	1.16±0.03
164	315	+01:34:33.49	+23:38:22.34	0.67±0.03	0.90±0.05	152.5±1.6	1342±5	84±2	526.2±0.8	0.0625±0.0013	1.19±0.03
165	316	+01:34:33.63	+23:38:24.39	0.099±0.004	0.42±0.02	3±11	30±30	0±20	52±3	0.0300±0.0006	0.38±0.01

Table C.1: **Table C.1 Continued:**

No.	MC ID	RA J2000	DEC J2000	Δv (km s^{-1})	R (pc)	$L_{^{12}CO(2-1)}$ K km s^{-1} pc^2	M_{lum} ($M_\odot$)	M_{vir} $M_\odot$)	Σ_{lum} $M_\odot$ pc^{-2}	α_{vir}	c
166	317	+01:34:34.89	+23:38:43.30	1.01±0.04	0.96±0.06	28±4	246±11	206.5±1.5	85±2	0.839±0.017	0.479±0.013
167	318	+01:34:33.55	+23:38:23.32	0.55±0.02	0.83±0.05	24±4	211±12	52±3	98±2	0.249±0.005	0.515±0.014
168	319	+01:34:33.67	+23:38:25.05	0.434±0.018	0.68±0.04	34±3	302±10	27±4	207.4±1.3	0.0890±0.0018	0.75±0.02
169	320	+01:34:33.26	+23:38:18.97	0.77±0.03	1.43±0.08	50±3	438±8	177.4±1.7	69±2	0.405±0.008	0.430±0.012
170	321	+01:34:34.29	+23:38:34.36	0.80±0.03	1.43±0.08	40±3	351±9	194.3±1.6	55±3	0.554±0.011	0.385±0.011
171	322	+01:34:33.57	+23:38:23.50	0.275±0.011	0.57±0.03	9±7	80±20	9±7	74±2	0.119±0.002	0.448±0.012
172	323	+01:34:34.20	+23:38:32.97	0.209±0.009	0.89±0.05	6±8	50±20	8±8	20±4	0.160±0.003	0.235±0.007
173	324	+01:34:34.51	+23:38:37.58	0.48±0.02	1.02±0.06	23±4	205±12	49±3	63±2	0.240±0.005	0.411±0.011
174	325	+01:34:34.45	+23:38:36.79	0.67±0.03	1.68±0.10	57±3	498±8	160.4±1.8	56±3	0.322±0.006	0.389±0.011
175	327	+01:34:33.89	+23:38:28.38	0.53±0.02	1.39±0.08	34±3	300±10	80±2	50±3	0.267±0.005	0.37±0.01
176	328	+01:34:33.45	+23:38:21.68	0.435±0.018	0.56±0.03	11±6	95±18	22±5	97±2	0.233±0.005	0.513±0.014
177	330	+01:34:33.91	+23:38:28.62	0.79±0.03	1.60±0.09	103.2±1.9	908±6	208.2±1.5	112.5±1.8	0.229±0.005	0.552±0.015
178	331	+01:34:34.91	+23:38:43.59	0.397±0.016	1.11±0.06	7±7	70±20	37±4	17±5	0.561±0.011	0.214±0.006
179	333	+01:34:33.60	+23:38:24.01	0.56±0.02	1.00±0.06	44±3	388±9	66±3	124.0±1.7	0.170±0.003	0.579±0.016
180	334	+01:34:34.35	+23:38:35.18	0.162±0.007	0.59±0.03	2±16	10±50	3±12	13±5	0.237±0.005	0.184±0.005

Table C.1: **Table C.1 Continued:**

No.	MC ID	RA J2000	DEC J2000	Δv (km s^{-1})	R (pc)	$L_{^{12}CO(2-1)}$ K km s^{-1} pc^2	M_{lum} ($M_\odot$)	M_{vir} $M_\odot$)	Σ_{lum} $M_\odot$ pc^{-2}	α_{vir}	c
181	336	+01:34:33.89	+23:38:28.40	0.58±0.02	1.32±0.08	46±3	401±9	93±2	74±2	0.230±0.005	0.446±0.012
182	338	+01:34:33.93	+23:38:28.93	0.71±0.03	0.94±0.05	42±3	367±9	100±2	131.0±1.7	0.272±0.005	0.595±0.017
183	339	+01:34:33.26	+23:38:18.92	1.36±0.06	1.63±0.09	298.9±1.1	2630±3	634.4±0.9	313.5±1.1	0.241±0.005	0.92±0.03
184	342	+01:34:34.43	+23:38:36.52	0.73±0.03	2.75±0.16	129.4±1.7	1139±5	309.1±1.3	48±3	0.271±0.005	0.36±0.01
185	343	+01:34:33.35	+23:38:20.26	0.48±0.02	0.84±0.05	12±6	103±17	40±4	47±3	0.389±0.008	0.356±0.010
186	344	+01:34:33.49	+23:38:22.37	0.345±0.014	0.72±0.04	0±10	30±30	18±5	20±4	0.566±0.011	0.230±0.006
187	347	+01:34:33.77	+23:38:26.55	···	0.72±0.04	5±9	40±30	···	26±4	···	0.263±0.007
188	349	+01:34:33.49	+23:38:22.36	0.227±0.009	0.77±0.04	5±8	50±30	8±8	26±4	0.176±0.004	0.263±0.007
189	350	+01:34:33.54	+23:38:23.06	1.17±0.05	1.86±0.11	435.0±0.9	3828±3	530.8±1.0	351±1	0.139±0.003	0.97±0.03
190	351	+01:34:34.35	+23:38:35.22	0.185±0.008	0.50±0.03	2±13	20±40	4±12	26±4	0.173±0.003	0.267±0.007
191	352	+01:34:34.46	+23:38:36.83	1.54±0.06	1.88±0.11	199.4±1.4	1755±4	941.4±0.7	157.5±1.5	0.536±0.011	0.653±0.018
192	353	+01:34:35.02	+23:38:45.29	0.56±0.02	1.05±0.06	18±5	154±14	68±3	45±3	0.442±0.009	0.348±0.010
193	355	+01:34:34.24	+23:38:33.66	0.165±0.007	0.48±0.03	1±16	10±50	3±13	17±5	0.219±0.004	0.216±0.006
194	356	+01:34:34.49	+23:38:37.36	0.94±0.04	1.08±0.06	49±3	427±8	200.3±1.6	116.2±1.8	0.469±0.009	0.561±0.016
195	357	+01:34:33.85	+23:38:27.82	0.356±0.015	0.84±0.05	12±6	106±17	22±5	48±3	0.210±0.004	0.36±0.01

Table C.1: **Table C.1 Continued:**

No.	MC ID	RA J2000	DEC J2000	Δv (km s^{-1})	R (pc)	L$_{^{12}\mathrm{CO}(2-1)}$ K km s^{-1} pc^2	M$_{\mathrm{lum}}$ (M$_\odot$)	M$_{\mathrm{vir}}$ M$_\odot$)	Σ_{lum} M$_\odot$ pc^{-2}	α_{vir}	c
196	358	+01:34:33.47	+23:38:22.03	0.70±0.03	0.85±0.05	144.1±1.6	1268±5	88±2	558.6±0.8	0.0697±0.0014	1.23±0.03
197	359	+01:34:33.44	+23:38:21.53	0.438±0.018	0.60±0.03	18±5	156±14	24±5	136.1±1.7	0.156±0.003	0.607±0.017
198	360	+01:34:34.91	+23:38:43.60	2.18±0.09	1.8±0.1	125.6±1.7	1105±5	1757.2±0.5	114.1±1.8	1.59±0.03	0.556±0.015
199	361	+01:34:34.32	+23:38:34.73	0.392±0.016	1.46±0.08	17±5	147±14	47±3	22±4	0.320±0.006	0.244±0.007
200	362	+01:34:34.34	+23:38:35.15	0.26±0.01	0.40±0.02	2±13	20±40	5±10	42±3	0.266±0.005	0.336±0.009
201	363	+01:34:34.02	+23:38:30.28	2.17±0.09	1.92±0.11	411.1±1.0	3618±3	1904.7±0.5	311.0±1.1	0.526±0.011	0.92±0.03
202	364	+01:34:34.24	+23:38:33.62	0.66±0.03	0.55±0.03	9±6	82±19	50±3	86±2	0.618±0.012	0.483±0.013
203	366	+01:34:34.14	+23:38:32.06	0.64±0.03	1.13±0.07	33±3	290±10	98±2	72±2	0.338±0.007	0.441±0.012
204	367	+01:34:34.86	+23:38:42.96	1.34±0.05	2.97±0.17	306.5±1.1	2698±3	1115.9±0.7	98±2	0.414±0.008	0.514±0.014
205	369	+01:34:34.35	+23:38:35.22	0.283±0.012	0.77±0.04	9±7	80±20	13±6	42±3	0.167±0.003	0.335±0.009
206	370	+01:34:33.85	+23:38:27.68	0.54±0.02	1.36±0.08	16±5	143±14	83±2	25±4	0.579±0.012	0.258±0.007
207	372	+01:34:34.42	+23:38:36.33	0.54±0.02	1.47±0.08	19±4	169±13	91±2	25±4	0.536±0.011	0.260±0.007
208	374	+01:34:34.24	+23:38:33.62	0.54±0.02	1.30±0.08	25±4	216±12	80±2	41±3	0.371±0.007	0.332±0.009
209	375	+01:34:34.69	+23:38:40.28	0.306±0.012	1.03±0.06	10±6	91±18	20±5	28±4	0.221±0.004	0.273±0.008
210	376	+01:34:34.13	+23:38:31.96	0.95±0.04	1.34±0.08	36±3	319±10	256.5±1.4	56±3	0.803±0.016	0.390±0.011

Table C.1: **Table C.1 Continued:**

No.	MC ID	RA J2000	DEC J2000	Δv (km s^{-1})	R (pc)	$L_{^{12}CO(2-1)}$ K km s^{-1} pc^2	M_{lum} ($M_\odot$)	M_{vir} $M_\odot$)	Σ_{lum} $M_\odot$ pc^{-2}	α_{vir}	c
211	377	+01:34:33.86	+23:38:27.94	0.59±0.02	0.91±0.05	22±4	195±12	66±3	75±2	0.341±0.007	0.450±0.013
212	383	+01:34:34.36	+23:38:35.39	0.55±0.02	0.84±0.05	12±6	107±17	54±3	48±3	0.51±0.01	0.36±0.01
213	386	+01:34:34.49	+23:38:37.34	2.01±0.08	2.87±0.17	520.2±0.9	4578±3	2435.2±0.5	177.5±1.5	0.532±0.011	0.693±0.019
214	388	+01:34:34.59	+23:38:38.81	1.47±0.06	1.92±0.11	219.8±1.3	1935±4	875.9±0.8	166.4±1.5	0.453±0.009	0.671±0.019
215	389	+01:34:34.31	+23:38:34.67	1.07±0.04	1.30±0.08	90±2	794±6	311.0±1.3	150.3±1.6	0.392±0.008	0.638±0.018
216	390	+01:34:34.64	+23:38:39.66	0.358±0.015	0.94±0.05	18±5	155±14	25±4	56±3	0.163±0.003	0.390±0.011
217	391	+01:34:34.88	+23:38:43.19	0.377±0.015	0.88±0.05	7±8	60±20	26±4	24±4	0.456±0.009	0.253±0.007
218	392	+01:34:33.37	+23:38:20.48	0.138±0.006	0.74±0.04	7±7	60±20	3±13	38±3	0.0455±0.0009	0.320±0.009
219	393	+01:34:34.35	+23:38:35.26	0.221±0.009	0.76±0.04	5±9	40±30	8±8	25±4	0.175±0.004	0.258±0.007
220	395	+01:34:34.49	+23:38:37.36	0.69±0.03	1.07±0.06	30±4	262±11	108±2	73±2	0.411±0.008	0.444±0.012
221	397	+01:34:34.62	+23:38:39.33	0.50±0.02	1.09±0.06	22±4	192±12	58±3	52±3	0.301±0.006	0.37±0.01
222	399	+01:34:34.14	+23:38:32.10	0.364±0.015	1.13±0.07	15±5	134±15	31±4	34±3	0.234±0.005	0.301±0.008
223	401	+01:34:34.38	+23:38:35.71	0.289±0.012	0.91±0.05	8±7	70±20	16±6	27±4	0.225±0.005	0.271±0.008
224	402	+01:34:34.43	+23:38:36.40	0.218±0.009	1.00±0.06	4±10	40±30	10±7	12±6	0.275±0.006	0.177±0.005
225	408	+01:34:34.52	+23:38:37.78	0.66±0.03	1.59±0.09	68±2	600±7	144.0±1.9	75±2	0.240±0.005	0.451±0.013

Table C.1: **Table C.1 Continued:**

No.	MC ID	RA J2000	DEC J2000	Δv (km s^{-1})	R (pc)	$L_{^{12}CO(2-1)}$ K km s^{-1} pc^2	M_{lum} ($M_\odot$)	M_{vir} $M_\odot$)	Σ_{lum} $M_\odot$ pc^{-2}	α_{vir}	c
226	409	+01:34:34.19	+23:38:32.85	1.21±0.05	1.40±0.08	63±2	554±7	427.4±1.1	90±2	0.772±0.016	0.494±0.014
227	410	+01:34:34.72	+23:38:40.74	1.11±0.05	1.60±0.09	42±3	369±9	412.6±1.1	46±3	1.12±0.02	0.353±0.010
228	411	+01:34:33.92	+23:38:28.73	0.87±0.04	1.58±0.09	129.8±1.7	1143±5	252.3±1.4	145.3±1.6	0.221±0.004	0.627±0.017
229	412	+01:34:34.67	+23:38:40.07	0.50±0.02	1.97±0.11	37±3	329±9	103±2	27±4	0.313±0.006	0.270±0.008
230	413	+01:34:34.95	+23:38:44.27	0.51±0.02	1.19±0.07	30±4	262±11	65±3	59±3	0.247±0.005	0.401±0.011
231	414	+01:34:34.38	+23:38:35.67	0.68±0.03	2.27±0.13	56±3	495±8	221.3±1.5	31±4	0.447±0.009	0.288±0.008
232	417	+01:34:34.28	+23:38:34.25	0.96±0.04	1.34±0.08	70±2	618±7	259.1±1.4	110.1±1.9	0.419±0.008	0.546±0.015
233	418	+01:34:33.92	+23:38:28.77	0.76±0.03	2.64±0.15	133.0±1.7	1171±5	322.6±1.2	53±3	0.276±0.006	0.380±0.011
234	422	+01:34:33.95	+23:38:29.20	1.04±0.04	2.40±0.14	159.1±1.6	1400±5	547.3±1.0	78±2	0.391±0.008	0.458±0.013
235	423	+01:34:34.45	+23:38:36.68	1.18±0.05	1.39±0.08	64±2	567±7	408.1±1.1	93±2	0.720±0.014	0.502±0.014
236	424	+01:34:34.56	+23:38:38.46	0.93±0.04	1.69±0.10	78±2	685±7	307.5±1.3	76±2	0.449±0.009	0.454±0.013
237	425	+01:34:34.00	+23:38:29.96	0.74±0.03	1.71±0.10	42±3	366±9	194.7±1.6	40±3	0.533±0.011	0.328±0.009
238	426	+01:34:34.77	+23:38:41.58	0.76±0.03	1.51±0.09	52±3	454±8	182.0±1.7	63±2	0.401±0.008	0.414±0.012
239	427	+01:34:34.28	+23:38:34.19	0.48±0.02	1.85±0.11	34±3	299±10	89±2	28±4	0.299±0.006	0.275±0.008
240	428	+01:34:34.20	+23:38:33.02	0.72±0.03	0.99±0.06	37±3	328±10	108±2	107.6±1.9	0.328±0.007	0.539±0.015

Table C.1: **Table C.1 Continued:**

No.	MC ID	RA J2000	DEC J2000	Δv (km s^{-1})	R (pc)	$L_{^{12}CO(2-1)}$ K km s^{-1} pc^2	M_{lum} ($M_\odot$)	M_{vir} $M_\odot$)	Σ_{lum} $M_\odot$ pc^{-2}	α_{vir}	c
241	429	+01:34:34.00	+23:38:30.00	0.280±0.011	0.93±0.05	7±7	60±20	15±6	23±4	0.241±0.005	0.251±0.007
242	430	+01:34:34.09	+23:38:31.37	0.69±0.03	1.11±0.06	18±5	158±14	110±2	40±3	0.697±0.014	0.331±0.009
243	431	+01:34:33.93	+23:38:28.96	0.122±0.005	0.71±0.04	6±8	50±20	2±15	33±3	0.0430±0.0009	0.298±0.008
244	432	+01:34:34.84	+23:38:42.63	0.89±0.04	1.57±0.09	47±3	417±8	262.1±1.4	54±3	0.628±0.013	0.382±0.011
245	433	+01:34:34.85	+23:38:42.76	0.356±0.015	0.97±0.06	10±6	85±19	26±4	29±4	0.304±0.006	0.279±0.008
246	434	+01:34:34.57	+23:38:38.57	1.08±0.04	1.31±0.08	102.4±1.9	902±6	321.3±1.2	166.0±1.5	0.356±0.007	0.670±0.019
247	435	+01:34:34.06	+23:38:30.85	0.49±0.02	1.47±0.09	34±3	298±10	75±3	44±3	0.253±0.005	0.344±0.010
248	437	+01:34:34.69	+23:38:40.28	0.057±0.002	0.80±0.05	2±14	20±40	0±30	9±6	0.0302±0.0006	0.157±0.004
249	439	+01:34:34.31	+23:38:34.63	0.425±0.017	1.24±0.07	19±4	168±13	47±3	35±3	0.279±0.006	0.307±0.009
250	440	+01:34:34.23	+23:38:33.45	0.95±0.04	1.43±0.08	19±5	164±13	268.0±1.4	26±4	1.63±0.03	0.264±0.007
251	441	+01:34:35.00	+23:38:45.06	1.22±0.05	1.63±0.09	69±2	605±7	509.6±1.0	73±2	0.842±0.017	0.443±0.012
252	443	+01:34:34.70	+23:38:40.50	1.44±0.06	2.32±0.13	146.3±1.6	1288±5	1008.8±0.7	76±2	0.784±0.016	0.454±0.013
253	444	+01:34:34.29	+23:38:34.29	1.16±0.05	1.62±0.09	132.6±1.7	1167±5	455±1	141.6±1.6	0.390±0.008	0.619±0.017
254	448	+01:34:34.86	+23:38:42.95	1.42±0.06	1.64±0.09	77±2	677±7	699.1±0.8	80±2	1.03±0.02	0.465±0.013
255	449	+01:34:34.82	+23:38:42.26	0.96±0.04	2.30±0.13	116.6±1.8	1026±5	447.5±1.1	62±2	0.436±0.009	0.409±0.011

Table C.1: **Table C.1 Continued:**

No.	MC ID	RA J2000	DEC J2000	Δv (km s^{-1})	R (pc)	$L_{^{12}CO(2-1)}$ K km s^{-1} pc^2	M_{lum} ($M_\odot$)	M_{vir} $M_\odot$)	Σ_{lum} $M_\odot$ pc^{-2}	α_{vir}	c
256	450	+01:34:35.02	+23:38:45.30	0.81±0.03	1.21±0.07	22±4	191±12	168.5±1.7	41±3	0.884±0.018	0.334±0.009
257	455	+01:34:34.09	+23:38:31.31	0.371±0.015	1.04±0.06	13±5	114±16	30±4	33±3	0.265±0.005	0.300±0.008
258	456	+01:34:34.64	+23:38:39.61	0.84±0.03	1.33±0.08	65±2	575±7	199.7±1.6	103.0±1.9	0.348±0.007	0.528±0.015
259	458	+01:34:34.24	+23:38:33.63	0.98±0.04	1.84±0.11	144.2±1.6	1269±5	373.0±1.2	118.8±1.8	0.294±0.006	0.567±0.016
260	461	+01:34:34.43	+23:38:36.45	0.206±0.008	1.30±0.08	12±6	107±17	12±7	20±4	0.108±0.002	0.233±0.006
261	462	+01:34:34.65	+23:38:39.69	0.266±0.011	1.13±0.07	10±6	85±19	17±5	21±4	0.197±0.004	0.241±0.007
262	463	+01:34:34.92	+23:38:43.85	0.96±0.04	1.31±0.08	57±3	503±8	252.7±1.4	93±2	0.50±0.01	0.501±0.014
263	468	+01:34:34.88	+23:38:43.16	0.347±0.014	1.00±0.06	15±5	136±15	25±4	43±3	0.186±0.004	0.343±0.010
264	471	+01:34:34.50	+23:38:37.49	1.75±0.07	2.64±0.15	877.9±0.7	7725±2	1688.7±0.5	353±1	0.219±0.004	0.98±0.03
265	472	+01:34:34.43	+23:38:36.52	0.75±0.03	2.03±0.12	108.3±1.9	953±6	241.4±1.4	73±2	0.253±0.005	0.445±0.012
266	473	+01:34:34.32	+23:38:34.73	0.64±0.03	1.40±0.08	62±2	547±7	119±2	88±2	0.218±0.004	0.489±0.014
267	474	+01:34:34.51	+23:38:37.70	0.65±0.03	1.24±0.07	22±4	194±12	111±2	40±3	0.574±0.012	0.329±0.009
268	475	+01:34:34.69	+23:38:40.42	0.81±0.03	2.10±0.12	99±2	872±6	287.3±1.3	63±2	0.330±0.007	0.413±0.011
269	477	+01:34:34.58	+23:38:38.64	1.51±0.06	2.55±0.15	448.6±0.9	3948±3	1221.1±0.6	193.0±1.4	0.309±0.006	0.72±0.02
270	480	+01:34:34.35	+23:38:35.30	0.76±0.03	1.45±0.08	59±3	522±8	174.5±1.7	79±2	0.334±0.007	0.462±0.013

Table C.1: **Table C.1 Continued:**

No.	MC ID	RA	DEC	Δv	R	$L_{^{12}CO(2-1)}$	M_{lum}	M_{vir}	Σ_{lum}	α_{vir}	c
		J2000	J2000	(km s^{-1})	(pc)	K km s^{-1} pc^2	($M_\odot$)	$M_\odot$)	$M_\odot$ pc^{-2}		
271	482	+01:34:34.88	+23:38:43.18	0.188±0.008	1.03±0.06	15±5	136±15	8±8	41±3	0.0562±0.0011	0.333±0.009
272	483	+01:34:34.17	+23:38:32.53	0.135±0.006	0.50±0.03	7±7	60±20	2±16	76±2	0.0319±0.0006	0.452±0.013
273	484	+01:34:34.75	+23:38:41.21	0.135±0.006	0.92±0.05	6±8	50±20	4±12	19±4	0.0708±0.0014	0.225±0.006
274	485	+01:34:34.71	+23:38:40.67	1.63±0.07	1.72±0.10	79±2	698±7	954.8±0.7	75±2	1.37±0.03	0.450±0.013
275	487	+01:34:34.45	+23:38:36.70	0.277±0.011	1.29±0.07	17±5	150±14	21±5	29±4	0.138±0.003	0.279±0.008
276	490	+01:34:34.19	+23:38:32.92	0.425±0.017	0.76±0.04	30±4	260±11	29±4	143.6±1.6	0.110±0.002	0.623±0.017
277	491	+01:34:34.70	+23:38:40.55	0.152±0.006	1.95±0.11	22±4	190±12	9±7	16±5	0.050±0.001	0.208±0.006
278	492	+01:34:34.59	+23:38:38.78	0.100±0.004	0.53±0.03	1±18	10±50	0±20	12±6	0.110±0.002	0.177±0.005
279	493	+01:34:34.76	+23:38:41.36	0.109±0.004	0.81±0.05	4±10	40±30	2±16	18±5	0.0551±0.0011	0.219±0.006
280	494	+01:34:34.27	+23:38:34.05	1.10±0.05	1.05±0.06	61±2	540±7	268.7±1.4	155.7±1.6	0.50±0.01	0.649±0.018
281	495	+01:34:34.48	+23:38:37.27	0.229±0.009	1.30±0.08	17±5	151±14	14±6	28±4	0.0949±0.0019	0.277±0.008
282	497	+01:34:34.69	+23:38:40.28	0.271±0.011	2.70±0.16	57±3	499±8	42±3	22±4	0.0832±0.0017	0.243±0.007
283	499	+01:34:34.87	+23:38:43.04	0.100±0.004	0.87±0.05	5±8	50±30	2±17	20±4	0.0388±0.0008	0.230±0.006
284	500	+01:34:34.43	+23:38:36.47	0.114±0.005	1.37±0.08	16±5	137±15	4±12	23±4	0.0270±0.0005	0.251±0.007
285	501	+01:34:34.83	+23:38:42.40	0.236±0.010	1.15±0.07	7±7	60±20	13±6	15±5	0.215±0.004	0.202±0.006

Table C.1: **Table C.1 Continued:**

No.	MC ID	RA	DEC	Δv	R	$L_{^{12}CO(2-1)}$	M_{lum}	M_{vir}	Σ_{lum}	α_{vir}	c
		J2000	J2000	(km s^{-1})	(pc)	K km s^{-1} pc^2	($M_\odot$)	$M_\odot$)	$M_\odot$ pc^{-2}		
286	502	+01:34:34.71	+23:38:40.69	0.224±0.009	1.8±0.1	22±4	189±13	19±5	19±4	0.099±0.002	0.227±0.006
287	503	+01:34:34.35	+23:38:35.30	0.121±0.005	1.21±0.07	10±6	84±19	4±12	18±5	0.0442±0.0009	0.222±0.006
288	506	+01:34:34.45	+23:38:36.69	0.270±0.011	1.12±0.06	15±5	130±15	17±5	33±3	0.133±0.003	0.298±0.008
289	507	+01:34:34.09	+23:38:31.35	0.49±0.02	1.32±0.08	40±3	352±9	67±3	64±2	0.192±0.004	0.417±0.012
290	508	+01:34:34.80	+23:38:42.03	1.11±0.05	1.34±0.08	33±3	290±10	349.0±1.2	51±3	1.22±0.02	0.37±0.01
291	509	+01:34:34.64	+23:38:39.61	0.93±0.04	1.32±0.08	76±2	669±7	239.9±1.4	122.6±1.8	0.358±0.007	0.576±0.016
292	510	+01:34:34.72	+23:38:40.86	0.443±0.018	1.33±0.08	12±6	108±17	55±3	19±4	0.51±0.01	0.229±0.006
293	511	+01:34:34.69	+23:38:40.34	0.122±0.005	1.56±0.09	18±5	161±14	0±10	21±4	0.0301±0.0006	0.239±0.007
294	512	+01:34:34.05	+23:38:30.81	0.85±0.03	0.69±0.04	25±4	218±12	105±2	144.9±1.6	0.482±0.010	0.626±0.017
295	514	+01:34:34.69	+23:38:40.34	0.093±0.004	1.45±0.08	13±5	114±16	3±14	17±5	0.0232±0.0005	0.216±0.006
296	515	+01:34:34.09	+23:38:31.36	0.152±0.006	0.85±0.05	10±6	85±19	4±11	37±3	0.0484±0.0010	0.318±0.009
297	516	+01:34:34.45	+23:38:36.82	0.264±0.011	0.89±0.05	9±6	82±19	13±6	33±3	0.159±0.003	0.298±0.008
298	517	+01:34:34.65	+23:38:39.68	0.50±0.02	2.06±0.12	57±3	506±8	107±2	38±3	0.212±0.004	0.320±0.009
299	519	+01:34:34.39	+23:38:35.89	0.188±0.008	0.94±0.05	5±8	50±20	7±8	17±5	0.147±0.003	0.215±0.006
300	520	+01:34:34.66	+23:38:39.93	0.090±0.004	0.89±0.05	6±8	50±20	2±18	19±4	0.0316±0.0006	0.229±0.006

Table C.1: **Table C.1 Continued:**

No.	MC ID	RA J2000	DEC J2000	Δv (km s^{-1})	R (pc)	$L_{^{12}CO(2-1)}$ K km s^{-1} pc^{2}	M_{lum} ($M_{\odot}$)	M_{vir} $M_{\odot}$)	Σ_{lum} $M_{\odot}$ pc^{-2}	α_{vir}	c
301	521	+01:34:34.65	+23:38:39.78	$\cdots$	0.66±0.04	2±13	20±40	$\cdots$	14±5	$\cdots$	0.196±0.005

Table C.2: ^{12}CO catalogs for clumps in GMC 16

No.	MC ID	RA	DEC	Δv	R	$L_{^{12}CO(2-1)}$	M_{lum}	M_{vir}	Σ_{lum}	α_{vir}	c
		J2000	J2000	(km s^{-1})	(pc)	K km s^{-1} pc^2	($M_\odot$)	$M_\odot$)	$M_\odot$ pc^{-2}		
1	0	+01:33:58.66	+23:29:39.93	0.70±0.03	1.52±0.09	69±2	611±7	158.8±1.8	84±2	0.260±0.005	0.476±0.013
2	2	+01:33:58.68	+23:29:40.22	0.468±0.019	1.04±0.06	17±5	147±14	48±3	43±3	0.324±0.007	0.343±0.010
3	5	+01:33:59.18	+23:29:47.63	0.53±0.02	1.20±0.07	21±4	188±13	72±3	41±3	0.384±0.008	0.334±0.009
4	12	+01:33:59.90	+23:29:58.56	0.399±0.016	1.70±0.10	65±2	571±7	57±3	63±2	0.100±0.002	0.412±0.011
5	20	+01:33:59.92	+23:29:58.86	0.51±0.02	1.35±0.08	26±4	227±11	74±3	40±3	0.324±0.007	0.327±0.009
6	26	+01:33:59.93	+23:29:58.89	0.327±0.013	0.71±0.04	10±6	87±18	16±6	56±3	0.182±0.004	0.388±0.011
7	29	+01:34:00.30	+23:30:04.56	0.184±0.007	0.85±0.05	0±10	30±30	6±9	15±5	0.183±0.004	0.199±0.006
8	31	+01:33:59.31	+23:29:49.70	0.365±0.015	1.07±0.06	13±5	114±16	30±4	32±3	0.263±0.005	0.293±0.008
9	32	+01:34:00.04	+23:30:00.59	0.166±0.007	1.43±0.08	10±6	92±18	8±8	14±5	0.0901±0.0018	0.197±0.005
10	33	+01:33:59.13	+23:29:46.98	0.372±0.015	1.02±0.06	10±6	86±19	30±4	26±4	0.345±0.007	0.267±0.007
11	34	+01:33:59.04	+23:29:45.59	0.53±0.02	1.87±0.11	189.4±1.4	1666±4	109±2	151.3±1.6	0.0654±0.0013	0.640±0.018
12	37	+01:33:59.93	+23:29:58.88	0.244±0.010	0.82±0.05	13±5	116±16	10±7	55±3	0.0889±0.0018	0.384±0.011
13	39	+01:34:00.04	+23:30:00.55	0.56±0.02	2.12±0.12	71±2	629±7	137.6±1.9	44±3	0.219±0.004	0.346±0.010
14	44	+01:33:59.18	+23:29:47.69	0.80±0.03	3.07±0.18	65±2	570±7	409.8±1.1	19±4	0.720±0.014	0.228±0.006
15	45	+01:33:59.54	+23:29:53.06	0.173±0.007	1.07±0.06	8±7	70±20	7±9	20±4	0.0947±0.0019	0.230±0.006

Table C.2 Continued:

No.	MC ID	RA	DEC	Δv	R	$L_{^{12}CO(2-1)}$	M_{lum}	M_{vir}	Σ_{lum}	α_{vir}	c
		J2000	J2000	(km s^{-1})	(pc)	K km s^{-1} pc^2	($M_\odot$)	$M_\odot$)	$M_\odot$ pc^{-2}		
16	47	+01:34:00.11	+23:30:01.59	0.221±0.009	1.32±0.08	7±7	60±20	14±6	12±6	0.209±0.004	0.179±0.005
17	50	+01:33:59.35	+23:29:50.30	0.317±0.013	1.14±0.07	16±5	139±15	24±5	34±3	0.174±0.004	0.303±0.008
18	51	+01:33:59.80	+23:29:56.96	···	0.70±0.04	2±13	20±40	···	12±6	···	0.180±0.005
19	52	+01:33:59.93	+23:29:58.93	0.085±0.003	0.99±0.06	7±7	70±20	2±18	21±4	0.0230±0.0005	0.239±0.007
20	53	+01:33:59.92	+23:29:58.74	0.51±0.02	1.8±0.1	46±3	406±9	96±2	40±3	0.237±0.005	0.329±0.009
21	54	+01:33:59.51	+23:29:52.70	0.51±0.02	2.24±0.13	138.6±1.7	1220±5	121±2	77±2	0.100±0.002	0.457±0.013
22	57	+01:33:58.94	+23:29:44.09	0.61±0.02	1.25±0.07	86±2	759±6	96±2	155.5±1.6	0.127±0.003	0.648±0.018
23	59	+01:33:59.33	+23:29:49.92	1.12±0.05	3.02±0.17	580.5±0.8	5109±2	798.2±0.8	177.9±1.5	0.156±0.003	0.693±0.019
24	62	+01:33:59.94	+23:29:59.05	0.182±0.007	0.91±0.05	11±6	101±17	6±9	39±3	0.0627±0.0013	0.323±0.009
25	63	+01:34:00.12	+23:30:01.83	0.354±0.014	1.39±0.08	14±5	125±15	37±4	21±4	0.292±0.006	0.237±0.007
26	66	+01:33:59.87	+23:29:58.12	···	0.68±0.04	2±14	20±40	···	12±6	···	0.181±0.005
27	72	+01:33:58.75	+23:29:41.30	0.68±0.03	2.18±0.13	137.6±1.7	1211±5	210.7±1.5	81±2	0.174±0.004	0.468±0.013
28	78	+01:33:59.97	+23:29:59.54	0.148±0.006	0.92±0.05	5±8	50±30	4±11	18±5	0.0892±0.0018	0.219±0.006
29	79	+01:33:59.86	+23:29:57.84	0.124±0.005	0.82±0.05	0±10	30±30	3±14	15±5	0.0826±0.0017	0.203±0.006
30	84	+01:33:59.56	+23:29:53.39	0.56±0.02	1.42±0.08	34±3	299±10	93±2	47±3	0.311±0.006	0.358±0.010

Table C.2 Continued:

No.	MC ID	RA	DEC	Δv	R	$L_{^{12}CO(2-1)}$	M_{lum}	M_{vir}	Σ_{lum}	α_{vir}	c
		J2000	J2000	(km s^{-1})	(pc)	K km s^{-1} pc^2	($M_\odot$)	$M_\odot$)	$M_\odot$ pc^{-2}		
31	85	+01:33:59.45	+23:29:51.81	0.67±0.03	1.59±0.09	82±2	724±6	147.6±1.8	92±2	0.204±0.004	0.497±0.014
32	86	+01:33:59.02	+23:29:45.28	0.057±0.002	0.80±0.05	3±12	30±30	0±30	12±6	0.0215±0.0004	0.183±0.005
33	87	+01:33:59.62	+23:29:54.34	0.152±0.006	1.7±0.1	20±4	172±13	8±8	18±5	0.0489±0.0010	0.222±0.006
34	92	+01:33:59.00	+23:29:44.96	0.420±0.017	1.05±0.06	70±2	618±7	39±4	179.2±1.5	0.0629±0.0013	0.696±0.019
35	105	+01:33:59.36	+23:29:50.46	0.75±0.03	2.76±0.16	215.5±1.3	1896±4	325.0±1.2	79±2	0.171±0.003	0.464±0.013
36	106	+01:34:00.14	+23:30:02.08	0.66±0.03	2.09±0.12	41±3	360±9	192.5±1.6	26±4	0.535±0.011	0.266±0.007
37	107	+01:33:59.76	+23:29:56.45	0.62±0.03	2.49±0.14	74±2	649±7	198.0±1.6	33±3	0.305±0.006	0.300±0.008
38	108	+01:33:59.62	+23:29:54.26	0.197±0.008	1.96±0.11	34±3	303±10	16±6	25±4	0.0526±0.0011	0.260±0.007
39	111	+01:33:59.57	+23:29:53.56	0.236±0.010	1.07±0.06	9±7	79±19	13±6	22±4	0.158±0.003	0.244±0.007
40	115	+01:33:59.55	+23:29:53.22	0.72±0.03	2.41±0.14	44±3	386±9	264.8±1.4	21±4	0.686±0.014	0.239±0.007
41	116	+01:33:59.51	+23:29:52.60	0.69±0.03	1.95±0.11	80±2	702±6	194.8±1.6	59±3	0.277±0.006	0.399±0.011
42	123	+01:33:59.04	+23:29:45.58	0.81±0.03	1.8±0.1	66±2	580±7	247.9±1.4	57±3	0.427±0.009	0.393±0.011
43	124	+01:33:59.68	+23:29:55.26	···	0.88±0.05	3±12	20±30	···	10±6	···	0.164±0.005
44	125	+01:34:00.23	+23:30:03.41	0.294±0.012	2.54±0.15	29±4	258±11	46±3	13±5	0.179±0.004	0.185±0.005
45	126	+01:34:00.12	+23:30:01.75	···	0.75±0.04	2±16	10±50	···	8±7	···	0.146±0.004

Table C.2 Continued:

No.	MC ID	RA J2000	DEC J2000	Δv (km s^{-1})	R (pc)	$L_{^{12}CO(2-1)}$ K km s^{-1} pc^2	M_{lum} ($M_\odot$)	M_{vir} $M_\odot$)	Σ_{lum} $M_\odot$ pc^{-2}	α_{vir}	c
46	127	+01:33:59.02	+23:29:45.33	0.25±0.01	0.86±0.05	21±4	187±13	11±7	80±2	0.0582±0.0012	0.466±0.013
47	128	+01:33:59.72	+23:29:55.84	0.129±0.005	2.23±0.13	17±5	154±14	8±8	10±6	0.051±0.001	0.163±0.005
48	129	+01:33:59.84	+23:29:57.63	0.166±0.007	1.13±0.07	6±8	60±20	7±9	14±5	0.116±0.002	0.195±0.005
49	132	+01:33:59.57	+23:29:53.53	0.174±0.007	1.26±0.07	6±8	50±20	8±8	10±6	0.161±0.003	0.165±0.005
50	137	+01:33:59.01	+23:29:45.13	0.428±0.017	1.45±0.08	59±3	521±8	56±3	79±2	0.107±0.002	0.461±0.013
51	141	+01:33:59.27	+23:29:48.98	0.72±0.03	2.69±0.16	244.5±1.3	2152±4	290.2±1.3	95±2	0.135±0.003	0.506±0.014
52	142	+01:33:59.56	+23:29:53.37	0.76±0.03	3.01±0.17	333.7±1.1	2937±3	369.3±1.2	103.3±1.9	0.126±0.003	0.528±0.015
53	153	+01:33:59.54	+23:29:53.15	0.74±0.03	2.88±0.17	194.0±1.4	1707±4	335.0±1.2	65±2	0.196±0.004	0.421±0.012
54	158	+01:33:59.90	+23:29:58.52	0.57±0.02	2.18±0.13	79±2	697±7	149.1±1.8	46±3	0.214±0.004	0.355±0.010
55	159	+01:33:59.69	+23:29:55.41	0.259±0.011	2.58±0.15	47±3	412±8	36±4	20±4	0.0880±0.0018	0.231±0.006
56	160	+01:33:59.57	+23:29:53.61	0.305±0.012	1.34±0.08	11±6	101±17	26±4	18±5	0.260±0.005	0.220±0.006
57	163	+01:33:59.23	+23:29:48.52	0.60±0.02	1.63±0.09	84±2	743±6	121±2	89±2	0.163±0.003	0.491±0.014
58	164	+01:33:59.21	+23:29:48.20	···	0.65±0.04	2±16	10±50	···	10±6	···	0.166±0.005
59	166	+01:33:59.24	+23:29:48.60	0.77±0.03	2.70±0.16	197.7±1.4	1740±4	337.1±1.2	76±2	0.194±0.004	0.454±0.013
60	167	+01:33:58.87	+23:29:43.02	0.76±0.03	1.8±0.1	233.6±1.3	2056±4	213.4±1.5	212.0±1.3	0.104±0.002	0.76±0.02

Table C.2 Continued:

No.	MC ID	RA J2000	DEC J2000	Δv (km s^{-1})	R (pc)	$L_{^{12}CO(2-1)}$ K km s^{-1} pc^2	M_{lum} ($M_\odot$)	M_{vir} $M_\odot$)	Σ_{lum} $M_\odot$ pc^{-2}	α_{vir}	c
61	168	+01:33:59.76	+23:29:56.35	0.109±0.004	1.14±0.07	6±8	50±20	3±13	12±6	0.0582±0.0012	0.180±0.005
62	169	+01:33:59.11	+23:29:46.58	0.227±0.009	0.90±0.05	17±5	146±14	10±7	58±3	0.0663±0.0013	0.395±0.011
63	170	+01:33:58.90	+23:29:43.44	0.195±0.008	0.77±0.04	8±7	70±20	6±9	37±3	0.0897±0.0018	0.316±0.009
64	175	+01:33:59.15	+23:29:47.20	0.91±0.04	3.36±0.19	337.4±1.1	2969±3	587.3±0.9	84±2	0.198±0.004	0.476±0.013
65	176	+01:33:58.97	+23:29:44.52	0.146±0.006	0.90±0.05	10±6	86±19	4±11	34±3	0.0469±0.0009	0.302±0.008
66	177	+01:33:59.55	+23:29:53.22	···	0.75±0.04	1±19	10±60	···	5±8	···	0.119±0.003
67	178	+01:33:59.44	+23:29:51.59	0.372±0.015	0.94±0.05	19±5	164±13	27±4	59±3	0.166±0.003	0.400±0.011
68	179	+01:33:58.53	+23:29:37.97	0.25±0.01	0.82±0.05	4±10	30±30	10±7	16±5	0.303±0.006	0.209±0.006
69	180	+01:33:58.26	+23:29:33.86	···	0.75±0.04	3±11	30±30	···	15±5	···	0.203±0.006
70	182	+01:33:59.75	+23:29:56.30	0.25±0.01	1.41±0.08	15±5	129±15	18±5	21±4	0.138±0.003	0.237±0.007
71	183	+01:33:58.98	+23:29:44.64	0.78±0.03	2.59±0.15	557.2±0.8	4903±2	331.1±1.2	232.9±1.3	0.0675±0.0014	0.79±0.02
72	184	+01:33:59.10	+23:29:46.52	1.28±0.05	3.8±0.2	906.4±0.6	7976.4±1.9	1301.5±0.6	174.8±1.5	0.163±0.003	0.688±0.019
73	185	+01:33:59.63	+23:29:54.38	···	1.26±0.07	7±7	70±20	···	13±5	···	0.188±0.005
74	186	+01:33:58.26	+23:29:33.91	0.168±0.007	0.74±0.04	8±7	70±20	4±11	39±3	0.0649±0.0013	0.327±0.009
75	187	+01:33:59.63	+23:29:54.44	0.73±0.03	1.88±0.11	52±3	460±8	208.8±1.5	41±3	0.454±0.009	0.334±0.009

Table C.2 Continued:

No.	MC ID	RA	DEC	Δv	R	$L_{^{12}CO(2-1)}$	M_{lum}	M_{vir}	Σ_{lum}	α_{vir}	c
		J2000	J2000	(km s^{-1})	(pc)	K km s^{-1} pc^2	($M_\odot$)	$M_\odot$)	$M_\odot$ pc^{-2}		
76	188	+01:33:59.48	+23:29:52.16	0.407±0.017	1.23±0.07	22±4	190±13	43±3	40±3	0.225±0.005	0.329±0.009
77	190	+01:33:59.79	+23:29:56.89	0.68±0.03	2.34±0.14	124.0±1.8	1091±5	227.1±1.5	64±2	0.208±0.004	0.415±0.012
78	192	+01:33:59.70	+23:29:55.49	0.100±0.004	1.23±0.07	10±6	90±18	3±14	19±4	0.0287±0.0006	0.226±0.006
79	195	+01:33:59.16	+23:29:47.39	0.52±0.02	1.52±0.09	30±4	265±11	85±2	37±3	0.321±0.006	0.315±0.009
80	196	+01:33:59.72	+23:29:55.77	0.54±0.02	2.69±0.16	55±3	485±8	165.3±1.7	21±4	0.341±0.007	0.240±0.007
81	197	+01:33:59.41	+23:29:51.10	0.091±0.004	0.87±0.05	6±8	60±20	2±18	23±4	0.0276±0.0006	0.251±0.007
82	198	+01:33:58.26	+23:29:33.92	0.369±0.015	0.62±0.04	10±6	90±18	18±5	74±2	0.198±0.004	0.446±0.012
83	200	+01:33:59.29	+23:29:49.39	0.74±0.03	1.61±0.09	102.7±1.9	903±6	183.3±1.6	110.3±1.8	0.203±0.004	0.546±0.015
84	201	+01:33:59.91	+23:29:58.69	0.337±0.014	1.59±0.09	31±4	270±10	38±4	34±3	0.140±0.003	0.304±0.008
85	202	+01:33:59.69	+23:29:55.42	0.099±0.004	0.86±0.05	7±8	60±20	2±17	25±4	0.0304±0.0006	0.260±0.007
86	203	+01:33:59.33	+23:29:49.92	0.215±0.009	1.03±0.06	7±8	60±20	10±7	18±5	0.166±0.003	0.221±0.006
87	204	+01:33:58.94	+23:29:44.16	0.65±0.03	1.35±0.08	44±3	388±9	120±2	68±2	0.309±0.006	0.427±0.012
88	205	+01:33:59.49	+23:29:52.35	0.71±0.03	2.02±0.12	48±3	419±8	213.6±1.5	33±3	0.51±0.01	0.297±0.008
89	207	+01:33:59.85	+23:29:57.74	0.317±0.013	1.43±0.08	27±4	240±11	30±4	37±3	0.126±0.003	0.318±0.009
90	208	+01:33:59.19	+23:29:47.83	1.05±0.04	4.4±0.3	898.6±0.7	7907.9±1.9	1024.1±0.7	130.2±1.7	0.130±0.003	0.593±0.017

Table C.2 Continued:

No.	MC ID	RA J2000	DEC J2000	Δv (km s^{-1})	R (pc)	$L_{^{12}CO(2-1)}$ K km s^{-1} pc^{2}	M_{lum} ($M_\odot$)	M_{vir} $M_\odot$)	Σ_{lum} $M_\odot$ pc^{-2}	α_{vir}	c
91	210	+01:33:58.45	+23:29:36.71	0.064±0.003	1.00±0.06	2±12	20±40	0±20	7±7	0.0388±0.0008	0.137±0.004
92	211	+01:33:59.86	+23:29:57.89	0.211±0.009	0.92±0.05	7±8	60±20	9±8	22±4	0.150±0.003	0.242±0.007
93	213	+01:33:58.63	+23:29:39.42	0.55±0.02	0.69±0.04	82±2	719±6	43±3	481.0±0.9	0.0605±0.0012	1.14±0.03
94	217	+01:33:59.05	+23:29:45.81	0.64±0.03	4.2±0.2	202.0±1.4	1778±4	364.4±1.2	32±3	0.205±0.004	0.296±0.008
95	219	+01:33:58.68	+23:29:40.23	0.63±0.03	3.5±0.2	420.2±1.0	3698±3	294.9±1.3	94±2	0.0798±0.0016	0.504±0.014
96	221	+01:33:58.48	+23:29:37.24	0.437±0.018	1.40±0.08	36±3	313±10	56±3	51±3	0.180±0.004	0.37±0.01
97	222	+01:33:59.40	+23:29:50.98	0.58±0.02	2.61±0.15	136.6±1.7	1202±5	181.3±1.7	56±3	0.151±0.003	0.390±0.011
98	223	+01:33:59.21	+23:29:48.14	0.394±0.016	1.62±0.09	61±3	537±7	53±3	65±2	0.098±0.002	0.419±0.012
99	224	+01:33:58.76	+23:29:41.43	0.75±0.03	1.06±0.06	18±5	159±14	125±2	45±3	0.788±0.016	0.350±0.010
100	225	+01:33:59.20	+23:29:48.06	0.292±0.012	1.59±0.09	40±3	351±9	28±4	44±3	0.0811±0.0016	0.346±0.010
101	226	+01:33:59.36	+23:29:50.33	0.64±0.03	1.58±0.09	75±2	659±7	135.0±1.9	84±2	0.205±0.004	0.477±0.013
102	227	+01:34:00.00	+23:30:00.02	0.213±0.009	1.39±0.08	13±5	112±16	13±6	18±5	0.118±0.002	0.223±0.006
103	228	+01:33:59.83	+23:29:57.40	0.382±0.016	1.86±0.11	34±3	299±10	57±3	28±4	0.190±0.004	0.274±0.008
104	230	+01:33:58.90	+23:29:43.51	0.400±0.016	1.49±0.09	34±3	302±10	50±3	43±3	0.166±0.003	0.342±0.010
105	231	+01:33:59.46	+23:29:51.97	0.62±0.03	1.66±0.10	66±2	579±7	134.7±1.9	67±2	0.233±0.005	0.425±0.012

Table C.2 Continued:

No.	MC ID	RA	DEC	Δv	R	$L_{^{12}CO(2-1)}$	M_{lum}	M_{vir}	Σ_{lum}	α_{vir}	c
		J2000	J2000	(km s^{-1})	(pc)	K km s^{-1} pc^2	($M_\odot$)	$M_\odot$)	$M_\odot$ pc^{-2}		
106	234	+01:33:58.73	+23:29:40.89	0.49±0.02	1.39±0.08	32±3	280±10	71±3	46±3	0.250±0.005	0.354±0.010
107	236	+01:33:58.73	+23:29:41.01	0.83±0.03	1.67±0.10	199.5±1.4	1756±4	239.1±1.4	200.3±1.4	0.136±0.003	0.74±0.02
108	239	+01:33:58.76	+23:29:41.39	0.62±0.03	2.70±0.16	306.9±1.1	2701±3	218.8±1.5	118.0±1.8	0.0810±0.0016	0.565±0.016
109	240	+01:33:59.18	+23:29:47.72	0.96±0.04	3.4±0.2	205.7±1.4	1810±4	665.1±0.9	50±3	0.367±0.007	0.37±0.01
110	242	+01:33:58.51	+23:29:37.65	0.219±0.009	0.76±0.04	13±5	112±16	8±8	62±2	0.0680±0.0014	0.408±0.011
111	243	+01:33:58.62	+23:29:39.35	0.76±0.03	1.06±0.06	96±2	845±6	127±2	241.0±1.3	0.151±0.003	0.81±0.02
112	244	+01:33:58.49	+23:29:37.35	0.48±0.02	1.8±0.1	72±2	638±7	85±2	66±2	0.134±0.003	0.423±0.012
113	245	+01:33:58.58	+23:29:38.63	0.51±0.02	0.97±0.06	23±4	200±12	53±3	67±2	0.267±0.005	0.427±0.012
114	246	+01:33:58.26	+23:29:33.95	0.113±0.005	0.70±0.04	3±11	30±30	2±16	19±4	0.0632±0.0013	0.228±0.006
115	247	+01:33:58.72	+23:29:40.80	0.272±0.011	0.78±0.05	10±6	84±19	12±6	43±3	0.146±0.003	0.342±0.010
116	248	+01:33:58.64	+23:29:39.59	1.11±0.05	1.04±0.06	355±1	3120±3	268.2±1.4	926.9±0.6	0.0860±0.0017	1.58±0.04
117	249	+01:33:59.13	+23:29:46.88	0.77±0.03	2.01±0.12	209.8±1.4	1846±4	252.5±1.4	145.2±1.6	0.137±0.003	0.627±0.017
118	250	+01:33:58.52	+23:29:37.77	0.65±0.03	1.22±0.07	23±4	199±12	109±2	42±3	0.549±0.011	0.339±0.009
119	251	+01:33:58.58	+23:29:38.77	0.50±0.02	1.8±0.1	95±2	840±6	93±2	84±2	0.111±0.002	0.476±0.013
120	252	+01:33:58.19	+23:29:32.87	0.315±0.013	1.30±0.08	10±6	88±18	27±4	17±5	0.307±0.006	0.212±0.006

Table C.2 Continued:

No.	MC ID	RA	DEC	Δv	R	$L_{^{12}CO(2-1)}$	M_{lum}	M_{vir}	Σ_{lum}	α_{vir}	c
		J2000	J2000	(km s^{-1})	(pc)	K km s^{-1} pc^2	($M_\odot$)	$M_\odot$)	$M_\odot$ pc^{-2}		
121	253	+01:33:58.18	+23:29:32.68	0.48±0.02	0.99±0.06	14±5	123±16	48±3	40±3	0.388±0.008	0.330±0.009
122	254	+01:33:58.48	+23:29:37.27	0.312±0.013	1.04±0.06	25±4	223±12	21±5	65±2	0.0955±0.0019	0.420±0.012
123	260	+01:33:59.15	+23:29:47.23	1.00±0.04	2.70±0.16	247.0±1.2	2174±4	565.1±0.9	95±2	0.260±0.005	0.506±0.014
124	261	+01:33:58.40	+23:29:35.94	1.07±0.04	1.7±0.1	96±2	845±6	419.1±1.1	89±2	0.496±0.010	0.492±0.014
125	262	+01:33:58.91	+23:29:43.67	1.33±0.05	3.5±0.2	680.6±0.8	5989±2	1294.4±0.6	157.1±1.5	0.216±0.004	0.652±0.018
126	263	+01:33:59.03	+23:29:45.44	0.81±0.03	3.7±0.2	678.5±0.8	5971±2	514.1±1.0	136.7±1.7	0.0861±0.0017	0.608±0.017
127	264	+01:33:59.65	+23:29:54.70	0.54±0.02	1.8±0.1	29±4	257±11	108±2	27±4	0.419±0.008	0.269±0.007
128	266	+01:33:58.96	+23:29:44.45	0.63±0.03	2.67±0.15	186.8±1.4	1644±4	225.6±1.5	73±2	0.137±0.003	0.445±0.012
129	267	+01:33:58.30	+23:29:34.43	0.328±0.013	1.42±0.08	13±5	114±16	32±4	18±5	0.282±0.006	0.221±0.006
130	268	+01:33:59.40	+23:29:51.04	0.334±0.014	1.29±0.07	30±4	266±11	30±4	51±3	0.114±0.002	0.37±0.01
131	270	+01:33:58.59	+23:29:38.85	0.71±0.03	1.87±0.11	283.4±1.2	2494±3	200.3±1.6	226.0±1.3	0.0803±0.0016	0.78±0.02
132	271	+01:33:58.29	+23:29:34.34	0.58±0.02	1.83±0.11	143.4±1.6	1262±5	128±2	120.3±1.8	0.102±0.002	0.570±0.016
133	273	+01:33:58.72	+23:29:40.75	1.02±0.04	2.63±0.15	60±3	528±7	573.4±0.9	24±4	1.09±0.02	0.256±0.007
134	274	+01:33:58.61	+23:29:39.11	0.85±0.03	2.42±0.14	480.9±0.9	4232±3	369.4±1.2	230.9±1.3	0.0873±0.0018	0.79±0.02
135	275	+01:33:58.27	+23:29:34.02	0.314±0.013	1.52±0.09	38±3	335±9	31±4	46±3	0.0936±0.0019	0.354±0.010

Table C.2 Continued:

No.	MC ID	RA	DEC	Δv	R	$L_{^{12}CO(2-1)}$	M_{lum}	M_{vir}	Σ_{lum}	α_{vir}	c
		J2000	J2000	(km s^{-1})	(pc)	K km s^{-1} pc^2	($M_\odot$)	$M_\odot$)	$M_\odot$ pc^{-2}		
136	276	+01:33:58.62	+23:29:39.29	0.74±0.03	1.32±0.08	56±3	493±8	151.8±1.8	89±2	0.308±0.006	0.492±0.014
137	277	+01:33:58.73	+23:29:40.94	0.424±0.017	1.30±0.08	38±3	335±9	49±3	63±2	0.147±0.003	0.412±0.011
138	278	+01:33:58.72	+23:29:40.84	0.397±0.016	1.24±0.07	20±4	174±13	41±3	36±3	0.237±0.005	0.311±0.009
139	279	+01:33:58.70	+23:29:40.57	0.402±0.016	1.06±0.06	79±2	697±7	36±4	199.3±1.4	0.051±0.001	0.73±0.02
140	280	+01:33:58.40	+23:29:35.99	0.199±0.008	0.86±0.05	8±7	70±20	7±8	29±4	0.107±0.002	0.280±0.008
141	281	+01:33:58.45	+23:29:36.69	0.54±0.02	1.50±0.09	85±2	750±6	93±2	105.7±1.9	0.124±0.002	0.535±0.015
142	282	+01:34:00.15	+23:30:02.30	0.076±0.003	1.17±0.07	3±12	20±30	1±19	6±8	0.0588±0.0012	0.124±0.003
143	283	+01:33:58.43	+23:29:36.42	0.062±0.003	0.58±0.03	3±12	20±30	0±30	23±4	0.0191±0.0004	0.248±0.007
144	284	+01:33:58.45	+23:29:36.76	0.360±0.015	1.03±0.06	52±3	459±8	28±4	137.3±1.7	0.0612±0.0012	0.609±0.017
145	285	+01:33:58.58	+23:29:38.66	0.447±0.018	1.14±0.07	35±3	307±10	48±3	75±2	0.156±0.003	0.450±0.013
146	286	+01:33:58.90	+23:29:43.50	0.391±0.016	1.12±0.06	20±4	180±13	36±4	46±3	0.199±0.004	0.353±0.010
147	287	+01:33:59.42	+23:29:51.25	0.54±0.02	1.8±0.1	42±3	369±9	111±2	36±3	0.300±0.006	0.314±0.009
148	288	+01:33:58.53	+23:29:37.89	0.52±0.02	0.86±0.05	78±2	682±7	48±3	291.2±1.1	0.0705±0.0014	0.89±0.02
149	289	+01:33:58.54	+23:29:38.10	0.437±0.018	1.82±0.11	66±2	584±7	73±3	56±3	0.125±0.003	0.389±0.011
150	290	+01:33:58.14	+23:29:32.06	0.399±0.016	1.24±0.07	9±6	81±19	41±3	17±5	0.51±0.01	0.214±0.006

Table C.2 Continued:

No.	MC ID	RA J2000	DEC J2000	Δv (km s^{-1})	R (pc)	L$_{^{12}\mathrm{CO}(2-1)}$ K km s^{-1} pc^{2}	M$_{\mathrm{lum}}$ (M$_{\odot}$)	M$_{\mathrm{vir}}$ M$_{\odot}$)	Σ_{lum} M$_{\odot}$ pc^{-2}	α_{vir}	c
151	291	+01:33:58.42	+23:29:36.28	···	0.57±0.03	2±14	20±40	···	16±5	···	0.211±0.006
152	292	+01:33:58.27	+23:29:34.02	0.58±0.02	1.09±0.06	18±5	160±14	78±3	43±3	0.485±0.010	0.340±0.009
153	293	+01:33:58.53	+23:29:37.98	0.299±0.012	1.08±0.06	18±5	155±14	20±5	42±3	0.130±0.003	0.338±0.009
154	295	+01:33:58.43	+23:29:36.45	···	0.61±0.04	3±11	30±30	···	25±4	···	0.261±0.007
155	296	+01:33:58.71	+23:29:40.68	0.54±0.02	1.30±0.08	100.8±1.9	887±6	81±2	166.4±1.5	0.0913±0.0018	0.671±0.019
156	297	+01:33:58.62	+23:29:39.34	0.56±0.02	2.55±0.15	47±3	412±8	167.1±1.7	20±4	0.406±0.008	0.233±0.006
157	298	+01:33:58.27	+23:29:34.11	0.49±0.02	1.24±0.07	20±4	180±13	62±3	37±3	0.347±0.007	0.317±0.009
158	299	+01:33:58.73	+23:29:40.94	0.391±0.016	1.71±0.10	30±4	261±11	55±3	29±4	0.210±0.004	0.278±0.008
159	300	+01:33:58.34	+23:29:35.13	0.340±0.014	0.84±0.05	11±6	99±17	21±5	44±3	0.208±0.004	0.346±0.010
160	301	+01:33:58.34	+23:29:35.09	0.68±0.03	1.12±0.06	30±4	265±11	110±2	67±2	0.415±0.008	0.427±0.012
161	302	+01:33:59.06	+23:29:45.96	0.76±0.03	2.09±0.12	127.4±1.7	1121±5	255.6±1.4	81±2	0.228±0.005	0.469±0.013
162	303	+01:33:58.64	+23:29:39.64	0.243±0.010	0.81±0.05	6±8	60±20	10±7	27±4	0.178±0.004	0.272±0.008
163	304	+01:33:59.11	+23:29:46.72	0.58±0.02	1.28±0.07	52±3	462±8	89±2	90±2	0.194±0.004	0.493±0.014
164	305	+01:33:58.26	+23:29:33.97	0.360±0.015	0.80±0.05	8±7	70±20	22±5	34±3	0.320±0.006	0.303±0.008
165	306	+01:33:58.60	+23:29:38.96	0.411±0.017	1.90±0.11	70±2	620±7	67±3	55±3	0.109±0.002	0.384±0.011

Table C.2 Continued:

No.	MC ID	RA	DEC	Δv	R	$L_{^{12}CO(2-1)}$	M_{lum}	M_{vir}	Σ_{lum}	α_{vir}	c
		J2000	J2000	(km s^{-1})	(pc)	K km s^{-1} pc^2	($M_\odot$)	$M_\odot$)	$M_\odot$ pc^{-2}		
166	307	+01:33:58.44	+23:29:36.59	0.435±0.018	0.93±0.05	13±6	111±16	37±4	41±3	0.333±0.007	0.332±0.009
167	308	+01:33:58.92	+23:29:43.74	0.99±0.04	2.39±0.14	176.3±1.5	1552±4	489±1	87±2	0.315±0.006	0.484±0.013
168	309	+01:33:58.49	+23:29:37.37	0.48±0.02	1.29±0.07	17±5	152±14	63±3	29±4	0.418±0.008	0.280±0.008
169	310	+01:33:58.85	+23:29:42.79	0.088±0.004	0.80±0.05	3±11	30±30	0±20	14±5	0.0470±0.0009	0.192±0.005
170	313	+01:33:58.78	+23:29:41.64	0.61±0.02	0.82±0.05	14±5	124±15	63±3	59±3	0.51±0.01	0.398±0.011
171	314	+01:33:58.97	+23:29:44.59	0.405±0.017	1.66±0.10	46±3	407±9	57±3	47±3	0.140±0.003	0.356±0.010
172	315	+01:33:58.82	+23:29:42.27	0.228±0.009	1.52±0.09	38±3	335±9	17±5	46±3	0.0497±0.0010	0.353±0.010
173	316	+01:33:59.12	+23:29:46.76	0.58±0.02	1.38±0.08	43±3	374±9	96±2	63±2	0.257±0.005	0.412±0.011
174	318	+01:34:00.12	+23:30:01.75	0.318±0.013	1.64±0.10	12±6	109±16	35±4	13±5	0.321±0.006	0.186±0.005
175	319	+01:33:58.62	+23:29:39.28	0.69±0.03	1.30±0.07	46±3	401±9	131.2±1.9	76±2	0.327±0.007	0.453±0.013
176	320	+01:33:58.78	+23:29:41.65	0.414±0.017	1.8±0.1	43±3	381±9	65±3	37±3	0.171±0.003	0.316±0.009
177	322	+01:34:00.05	+23:30:00.73	0.50±0.02	2.04±0.12	47±3	418±8	108±2	32±3	0.258±0.005	0.294±0.008
178	323	+01:33:58.73	+23:29:41.02	0.204±0.008	1.14±0.07	12±6	110±16	10±7	27±4	0.0914±0.0018	0.269±0.007
179	324	+01:33:58.67	+23:29:40.03	0.56±0.02	1.31±0.08	37±3	328±10	87±2	61±2	0.265±0.005	0.407±0.011
180	325	+01:33:58.77	+23:29:41.52	0.220±0.009	1.53±0.09	22±4	189±13	16±6	26±4	0.0828±0.0017	0.263±0.007

Table C.2 Continued:

No.	MC ID	RA J2000	DEC J2000	Δv (km s^{-1})	R (pc)	$L_{^{12}CO(2-1)}$ K km s^{-1} pc^2	M_{lum} ($M_\odot$)	M_{vir} $M_\odot$)	Σ_{lum} $M_\odot$ pc^{-2}	α_{vir}	c
181	326	+01:33:59.70	+23:29:55.56	0.54±0.02	2.88±0.17	201.4±1.4	1772±4	173.0±1.7	68±2	0.098±0.002	0.430±0.012
182	327	+01:33:58.71	+23:29:40.70	0.445±0.018	1.59±0.09	54±3	472±8	66±3	59±3	0.140±0.003	0.401±0.011
183	329	+01:33:58.65	+23:29:39.70	0.285±0.012	1.23±0.07	15±5	128±15	21±5	27±4	0.163±0.003	0.270±0.008
184	330	+01:34:00.12	+23:30:01.85	0.160±0.007	1.15±0.07	5±9	40±30	6±9	11±6	0.141±0.003	0.169±0.005
185	331	+01:33:58.32	+23:29:34.75	0.61±0.02	1.08±0.06	15±5	136±15	83±2	37±3	0.614±0.012	0.316±0.009
186	332	+01:33:59.52	+23:29:52.80	0.344±0.014	1.92±0.11	35±3	310±10	48±3	27±4	0.154±0.003	0.269±0.007
187	333	+01:33:57.98	+23:29:29.75	0.53±0.02	1.25±0.07	20±4	175±13	74±3	35±3	0.421±0.008	0.310±0.009
188	334	+01:33:58.61	+23:29:39.17	0.134±0.005	0.81±0.05	0±10	30±30	3±13	15±5	0.0967±0.0019	0.204±0.006
189	335	+01:33:59.35	+23:29:50.31	0.397±0.016	1.7±0.1	60±3	532±7	58±3	55±3	0.108±0.002	0.387±0.011
190	336	+01:33:58.62	+23:29:39.32	0.50±0.02	1.32±0.08	63±2	552±7	69±3	101.1±1.9	0.125±0.003	0.523±0.015
191	337	+01:33:59.74	+23:29:56.12	0.437±0.018	1.71±0.10	37±3	327±10	69±3	36±3	0.210±0.004	0.310±0.009
192	339	+01:33:59.06	+23:29:45.84	0.297±0.012	1.54±0.09	17±5	145±14	29±4	20±4	0.197±0.004	0.230±0.006
193	340	+01:33:58.57	+23:29:38.62	0.60±0.02	0.80±0.05	16±5	138±15	61±3	68±2	0.443±0.009	0.428±0.012
194	341	+01:33:59.57	+23:29:53.61	0.388±0.016	1.66±0.10	16±5	145±14	52±3	17±5	0.362±0.007	0.213±0.006
195	342	+01:33:59.49	+23:29:52.33	0.340±0.014	1.31±0.08	13±6	111±16	32±4	21±4	0.287±0.006	0.236±0.007

Table C.2 Continued:

No.	MC ID	RA	DEC	Δv	R	$L_{^{12}CO(2-1)}$	M_{lum}	M_{vir}	Σ_{lum}	α_{vir}	c
		J2000	J2000	(km s^{-1})	(pc)	K km s^{-1} pc^2	($M_\odot$)	$M_\odot$)	$M_\odot$ pc^{-2}		
196	343	+01:33:59.65	+23:29:54.77	0.172±0.007	0.93±0.05	3±11	30±30	6±9	11±6	0.195±0.004	0.171±0.005
197	344	+01:33:59.50	+23:29:52.47	0.198±0.008	0.91±0.05	5±9	50±30	7±8	18±5	0.161±0.003	0.220±0.006

Table C.3: ^{12}CO catalogs for clumps in GMC 8

No.	MC ID	RA	DEC	Δv	R	$L_{^{12}CO(2-1)}$	M_{lum}	M_{vir}	Σ_{lum}	α_{vir}	c
		J2000	J2000	(km s^{-1})	(pc)	K km s^{-1} pc^2	(M$_\odot$)	M$_\odot$)	M$_\odot$ pc^{-2}		
1	4	+01:34:10.21	+23:32:33.14	0.459±0.019	2.58±0.15	72±2	631±7	114±2	30±4	0.181±0.004	0.285±0.008
2	6	+01:34:08.42	+23:32:06.33	0.52±0.02	2.73±0.16	45±3	394±9	158.1±1.8	17±5	0.402±0.008	0.213±0.006
3	8	+01:34:08.54	+23:32:08.09	0.87±0.04	2.99±0.17	93±2	818±6	471±1	29±4	0.576±0.012	0.280±0.008
4	19	+01:34:08.20	+23:32:02.97	0.216±0.009	1.12±0.06	7±8	60±20	11±7	15±5	0.189±0.004	0.199±0.006
5	23	+01:34:09.31	+23:32:19.64	1.94±0.08	7.4±0.4	1555.1±0.5	13685.1±1.5	5816.2±0.3	80±2	0.425±0.009	0.466±0.013
6	25	+01:34:10.00	+23:32:30.01	2.07±0.08	5.6±0.3	679.6±0.8	5981±2	5035.6±0.3	60±3	0.842±0.017	0.404±0.011
7	29	+01:34:08.37	+23:32:05.58	0.161±0.007	1.02±0.06	6±8	50±20	6±9	16±5	0.105±0.002	0.210±0.006
8	34	+01:34:10.29	+23:32:34.40	0.162±0.007	1.23±0.07	8±7	70±20	7±9	15±5	0.0959±0.0019	0.201±0.006
9	35	+01:34:10.42	+23:32:36.32	0.448±0.018	1.40±0.08	19±5	164±13	59±3	27±4	0.359±0.007	0.269±0.007
10	37	+01:34:10.36	+23:32:35.43	0.121±0.005	1.09±0.06	6±8	50±20	3±12	15±5	0.0623±0.0013	0.199±0.006
11	40	+01:34:10.30	+23:32:34.49	0.51±0.02	1.60±0.09	51±3	450±8	89±2	56±3	0.197±0.004	0.388±0.011
12	42	+01:34:08.95	+23:32:14.19	···	1.06±0.06	2±13	20±40	···	6±8	···	0.124±0.003
13	43	+01:34:08.98	+23:32:14.65	0.137±0.006	1.72±0.10	4±9	40±30	7±9	4±9	0.172±0.003	0.107±0.003
14	49	+01:34:10.37	+23:32:35.53	0.51±0.02	2.50±0.14	55±3	484±8	137.0±1.9	25±4	0.283±0.006	0.258±0.007
15	53	+01:34:08.33	+23:32:04.99	···	1.04±0.06	4±10	30±30	···	10±6	···	0.166±0.005

Table C.3 Continued:

No.	MC ID	RA	DEC	Δv	R	$L_{^{12}CO(2-1)}$	M_{lum}	M_{vir}	Σ_{lum}	α_{vir}	c
		J2000	J2000	(km s^{-1})	(pc)	K km s^{-1} pc^2	($M_\odot$)	$M_\odot$)	$M_\odot$ pc^{-2}		
16	54	+01:34:08.31	+23:32:04.70	0.113±0.005	1.19±0.07	7±8	60±20	3±12	13±5	0.0533±0.0011	0.191±0.005
17	56	+01:34:10.41	+23:32:36.19	0.357±0.015	1.35±0.08	19±4	168±13	36±4	29±4	0.216±0.004	0.281±0.008
18	57	+01:34:08.92	+23:32:13.79	0.476±0.019	1.91±0.11	37±3	328±10	91±2	29±4	0.278±0.006	0.278±0.008
19	58	+01:34:10.35	+23:32:35.21	0.56±0.02	1.41±0.08	14±5	128±15	93±2	20±4	0.726±0.015	0.235±0.007
20	59	+01:34:09.75	+23:32:26.31	0.67±0.03	2.76±0.16	185.9±1.4	1636±4	263.6±1.4	68±2	0.161±0.003	0.430±0.012
21	60	+01:34:09.24	+23:32:18.55	1.19±0.05	3.7±0.2	116.2±1.8	1023±5	1097.4±0.7	24±4	1.07±0.02	0.253±0.007
22	61	+01:34:08.98	+23:32:14.75	0.347±0.014	1.65±0.10	18±5	162±14	42±3	19±4	0.258±0.005	0.226±0.006
23	62	+01:34:10.18	+23:32:32.71	0.60±0.02	1.88±0.11	43±3	381±9	143.7±1.9	34±3	0.377±0.008	0.304±0.008
24	63	+01:34:08.92	+23:32:13.83	0.202±0.008	1.65±0.10	14±5	120±16	14±6	14±5	0.118±0.002	0.194±0.005
25	64	+01:34:10.46	+23:32:36.91	0.081±0.003	0.83±0.05	2±13	20±40	0±20	10±6	0.0556±0.0011	0.161±0.004
26	65	+01:34:08.98	+23:32:14.73	0.314±0.013	1.25±0.07	9±6	81±19	26±4	17±5	0.317±0.006	0.212±0.006
27	66	+01:34:10.43	+23:32:36.49	0.134±0.005	0.91±0.05	3±12	20±40	3±12	9±7	0.151±0.003	0.154±0.004
28	67	+01:34:10.26	+23:32:33.92	0.76±0.03	1.23±0.07	22±4	197±12	149.8±1.8	42±3	0.762±0.015	0.336±0.009
29	68	+01:34:08.93	+23:32:13.93	0.427±0.017	2.33±0.13	41±3	360±9	89±2	21±4	0.247±0.005	0.239±0.007
30	69	+01:34:09.26	+23:32:18.86	0.52±0.02	1.65±0.10	24±4	213±12	95±2	25±4	0.445±0.009	0.260±0.007

Table C.3 Continued:

No.	MC ID	RA	DEC	Δv	R	$L_{^{12}CO(2-1)}$	M_{lum}	M_{vir}	Σ_{lum}	α_{vir}	c
		J2000	J2000	(km s^{-1})	(pc)	K km s^{-1} pc^2	($M_\odot$)	$M_\odot$)	$M_\odot$ pc^{-2}		
31	70	+01:34:09.18	+23:32:17.74	0.0455±0.0019	1.25±0.07	0±10	30±30	0±30	7±7	0.0161±0.0003	0.136±0.004
32	71	+01:34:09.13	+23:32:16.94	0.62±0.03	1.53±0.09	36±3	317±10	123±2	43±3	0.389±0.008	0.342±0.010
33	74	+01:34:09.87	+23:32:28.11	0.223±0.009	1.37±0.08	9±6	80±19	14±6	14±5	0.179±0.004	0.191±0.005
34	75	+01:34:09.19	+23:32:17.88	0.98±0.04	2.46±0.14	45±3	399±9	499.4±1.0	21±4	1.25±0.03	0.238±0.007
35	76	+01:34:09.60	+23:32:24.07	2.38±0.10	5.3±0.3	342.0±1.1	3009±3	6231.0±0.3	35±3	2.07±0.04	0.306±0.009
36	77	+01:34:09.09	+23:32:16.42	0.355±0.014	2.43±0.14	28±4	251±11	64±3	14±5	0.257±0.005	0.191±0.005
37	80	+01:34:08.66	+23:32:09.90	1.42±0.06	3.6±0.2	407.1±1.0	3583±3	1496.8±0.6	90±2	0.418±0.008	0.494±0.014
38	81	+01:34:09.91	+23:32:28.72	0.074±0.003	0.96±0.06	2±13	20±40	0±20	7±8	0.0569±0.0011	0.135±0.004
39	84	+01:34:09.05	+23:32:15.79	0.83±0.03	2.02±0.12	65±2	568±7	293.7±1.3	44±3	0.52±0.01	0.346±0.010
40	85	+01:34:08.99	+23:32:14.78	0.51±0.02	1.38±0.08	20±4	175±13	76±3	29±4	0.431±0.009	0.281±0.008
41	89	+01:34:08.94	+23:32:14.09	0.129±0.005	1.29±0.07	8±7	70±20	0±10	13±5	0.0648±0.0013	0.191±0.005
42	90	+01:34:09.89	+23:32:28.35	0.55±0.02	1.56±0.09	28±4	249±11	101±2	32±3	0.405±0.008	0.296±0.008
43	94	+01:34:09.59	+23:32:23.90	1.26±0.05	3.8±0.2	243.1±1.3	2139±4	1267.5±0.6	47±3	0.593±0.012	0.358±0.010
44	95	+01:34:09.99	+23:32:29.78	0.377±0.015	1.71±0.10	29±4	255±11	51±3	28±4	0.200±0.004	0.275±0.008
45	102	+01:34:09.96	+23:32:29.39	0.55±0.02	1.92±0.11	32±3	280±10	123±2	24±4	0.440±0.009	0.255±0.007

Table C.3 Continued:

No.	MC ID	RA	DEC	Δv	R	$L_{^{12}CO(2-1)}$	M_{lum}	M_{vir}	Σ_{lum}	α_{vir}	c
		J2000	J2000	(km s^{-1})	(pc)	K km s^{-1} pc^2	($M_\odot$)	$M_\odot$)	$M_\odot$ pc^{-2}		
46	103	+01:34:09.90	+23:32:28.55	0.74±0.03	2.16±0.13	181.4±1.5	1596±4	251.3±1.4	108.8±1.9	0.157±0.003	0.542±0.015
47	105	+01:34:09.78	+23:32:26.76	0.416±0.017	2.11±0.12	34±3	300±10	77±3	21±4	0.256±0.005	0.241±0.007
48	106	+01:34:08.65	+23:32:09.82	0.91±0.04	3.8±0.2	208.0±1.4	1830±4	663.8±0.9	40±3	0.363±0.007	0.329±0.009
49	108	+01:34:09.05	+23:32:15.79	0.86±0.04	3.35±0.19	193.6±1.4	1704±4	524.3±1.0	48±3	0.308±0.006	0.36±0.01
50	113	+01:34:10.14	+23:32:32.06	1.07±0.04	5.2±0.3	611.8±0.8	5384±2	1250.1±0.6	63±2	0.232±0.005	0.412±0.011
51	114	+01:34:08.97	+23:32:14.51	1.32±0.05	3.8±0.2	199.9±1.4	1759±4	1379.6±0.6	39±3	0.784±0.016	0.325±0.009
52	115	+01:34:09.88	+23:32:28.17	0.372±0.015	2.86±0.17	30±4	265±11	83±2	10±6	0.315±0.006	0.167±0.005
53	118	+01:34:09.17	+23:32:17.52	1.48±0.06	4.3±0.2	442.2±0.9	3891±3	1962.3±0.5	69±2	0.50±0.01	0.430±0.012
54	119	+01:34:09.09	+23:32:16.28	0.365±0.015	1.18±0.07	14±5	121±16	33±4	28±4	0.271±0.005	0.275±0.008
55	120	+01:34:09.68	+23:32:25.26	0.0356±0.0015	0.95±0.05	2±12	20±40	0±40	8±7	0.0116±0.0002	0.144±0.004
56	121	+01:34:09.23	+23:32:18.45	0.184±0.008	1.44±0.08	9±6	81±19	10±7	12±6	0.127±0.003	0.183±0.005
57	122	+01:34:09.07	+23:32:16.07	0.405±0.017	1.96±0.11	28±4	249±11	68±3	21±4	0.271±0.005	0.236±0.007
58	123	+01:34:09.69	+23:32:25.37	0.156±0.006	1.93±0.11	12±6	107±17	10±7	9±6	0.0919±0.0018	0.158±0.004
59	125	+01:34:09.21	+23:32:18.17	0.332±0.014	2.29±0.13	23±4	205±12	53±3	12±6	0.259±0.005	0.183±0.005
60	126	+01:34:09.47	+23:32:21.99	1.19±0.05	1.86±0.11	77±2	675±7	550.7±0.9	62±2	0.816±0.016	0.410±0.011

Table C.3 Continued:

No.	MC ID	RA	DEC	Δv	R	$L_{^{12}CO(2-1)}$	M_{lum}	M_{vir}	Σ_{lum}	α_{vir}	c
		J2000	J2000	(km s^{-1})	(pc)	K km s^{-1} pc^2	($M_\odot$)	$M_\odot$)	$M_\odot$ pc^{-2}		
61	127	+01:34:09.47	+23:32:22.05	0.93±0.04	2.71±0.16	84±2	743±6	495±1	32±3	0.666±0.013	0.295±0.008
62	128	+01:34:09.00	+23:32:14.99	0.0296±0.0012	1.21±0.07	3±11	30±30	0±50	7±8	0.00731±0.00015	0.134±0.004
63	130	+01:34:09.68	+23:32:25.19	0.315±0.013	2.12±0.12	18±5	156±14	44±3	11±6	0.284±0.006	0.173±0.005
64	132	+01:34:08.25	+23:32:03.76	0.468±0.019	2.48±0.14	99±2	869±6	114±2	45±3	0.132±0.003	0.349±0.010
65	133	+01:34:09.77	+23:32:26.56	0.427±0.017	1.37±0.08	9±7	80±20	52±3	13±5	0.693±0.014	0.186±0.005
66	134	+01:34:10.04	+23:32:30.60	0.61±0.02	2.23±0.13	133.3±1.7	1173±5	175.8±1.7	75±2	0.150±0.003	0.450±0.013
67	135	+01:34:09.60	+23:32:23.96	0.68±0.03	1.24±0.07	37±3	328±10	120±2	68±2	0.365±0.007	0.429±0.012
68	138	+01:34:09.30	+23:32:19.53	0.57±0.02	2.06±0.12	47±3	413±8	142.3±1.9	31±3	0.345±0.007	0.289±0.008
69	139	+01:34:10.09	+23:32:31.29	0.367±0.015	0.82±0.05	10±6	89±18	23±5	43±3	0.259±0.005	0.339±0.009
70	142	+01:34:08.08	+23:32:01.16	0.62±0.03	2.23±0.13	69±2	612±7	178.5±1.7	39±3	0.292±0.006	0.326±0.009
71	144	+01:34:09.45	+23:32:21.82	1.49±0.06	3.4±0.2	406.9±1.0	3580±3	1601.8±0.6	97±2	0.447±0.009	0.513±0.014
72	145	+01:34:09.30	+23:32:19.47	0.94±0.04	2.60±0.15	65±2	573±7	478±1	27±4	0.833±0.017	0.271±0.008
73	146	+01:34:08.29	+23:32:04.36	0.84±0.03	2.87±0.17	256.9±1.2	2261±4	424.7±1.1	87±2	0.188±0.004	0.486±0.014
74	147	+01:34:09.68	+23:32:25.18	0.96±0.04	4.0±0.2	177.6±1.5	1562±4	763.7±0.8	32±3	0.489±0.010	0.292±0.008
75	149	+01:34:08.89	+23:32:13.39	0.092±0.004	0.84±0.05	3±11	30±30	1±18	12±6	0.0546±0.0011	0.183±0.005

Table C.3 Continued:

No.	MC ID	RA	DEC	Δv	R	$L_{^{12}CO(2-1)}$	M_{lum}	M_{vir}	Σ_{lum}	α_{vir}	c
		J2000	J2000	(km s^{-1})	(pc)	K km s^{-1} pc^2	($M_\odot$)	$M_\odot$)	$M_\odot$ pc^{-2}		
76	150	+01:34:09.54	+23:32:23.13	0.68±0.03	2.98±0.17	174.0±1.5	1531±4	288.1±1.3	55±3	0.188±0.004	0.385±0.011
77	152	+01:34:09.51	+23:32:22.59	0.169±0.007	2.02±0.12	10±6	89±18	12±6	7±7	0.135±0.003	0.137±0.004
78	153	+01:34:08.75	+23:32:11.27	0.64±0.03	2.13±0.12	50±3	436±8	185.2±1.6	31±4	0.425±0.009	0.288±0.008
79	154	+01:34:08.69	+23:32:10.42	1.37±0.06	3.9±0.2	220.7±1.3	1942±4	1560.9±0.6	40±3	0.804±0.016	0.328±0.009
80	156	+01:34:09.64	+23:32:24.55	0.84±0.03	6.7±0.4	144.9±1.6	1276±5	986.2±0.7	9±6	0.773±0.016	0.157±0.004
81	157	+01:34:09.71	+23:32:25.69	0.135±0.005	1.10±0.06	6±8	60±20	4±11	15±5	0.0754±0.0015	0.199±0.006
82	162	+01:34:09.58	+23:32:23.72	0.68±0.03	0.85±0.05	25±4	224±12	83±2	99±2	0.373±0.007	0.518±0.014
83	163	+01:34:09.67	+23:32:25.11	0.093±0.004	1.32±0.08	8±7	70±20	2±14	12±6	0.0355±0.0007	0.184±0.005
84	165	+01:34:09.55	+23:32:23.31	0.455±0.019	0.96±0.06	26±4	226±11	42±3	77±2	0.185±0.004	0.458±0.013
85	166	+01:34:09.18	+23:32:17.68	0.143±0.006	1.42±0.08	6±8	50±20	6±9	8±7	0.122±0.002	0.146±0.004
86	167	+01:34:08.07	+23:32:01.02	0.65±0.03	2.05±0.12	65±2	570±7	182.3±1.6	43±3	0.320±0.006	0.342±0.010
87	168	+01:34:10.14	+23:32:32.17	0.68±0.03	3.30±0.19	62±2	548±7	323.9±1.2	16±5	0.592±0.012	0.208±0.006
88	169	+01:34:09.02	+23:32:15.27	1.14±0.05	6.1±0.4	631.5±0.8	5558±2	1673.1±0.5	47±3	0.301±0.006	0.356±0.010
89	170	+01:34:08.97	+23:32:14.53	0.79±0.03	2.01±0.12	89±2	780±6	260.2±1.4	61±2	0.334±0.007	0.408±0.011
90	172	+01:34:09.29	+23:32:19.32	0.54±0.02	2.47±0.14	56±3	490±8	151.5±1.8	26±4	0.309±0.006	0.263±0.007

Table C.3 Continued:

No.	MC ID	RA J2000	DEC J2000	Δv (km s^{-1})	R (pc)	$L_{^{12}CO(2-1)}$ K km s^{-1} pc^2	M_{lum} ($M_\odot$)	M_{vir} $M_\odot$)	Σ_{lum} $M_\odot$ pc^{-2}	α_{vir}	c
91	173	+01:34:09.69	+23:32:25.37	0.476±0.019	1.51±0.09	41±3	357±9	72±3	50±3	0.200±0.004	0.37±0.01
92	174	+01:34:09.31	+23:32:19.70	0.94±0.04	2.78±0.16	88±2	776±6	513.3±1.0	32±3	0.662±0.013	0.294±0.008
93	176	+01:34:08.78	+23:32:11.69	1.03±0.04	3.21±0.19	97±2	854±6	713.0±0.8	26±4	0.835±0.017	0.267±0.007
94	177	+01:34:08.09	+23:32:01.35	0.277±0.011	0.70±0.04	5±9	50±30	11±7	30±4	0.243±0.005	0.284±0.008
95	178	+01:34:09.18	+23:32:17.65	0.327±0.013	1.33±0.08	8±7	70±20	30±4	13±5	0.419±0.008	0.186±0.005
96	180	+01:34:09.19	+23:32:17.83	0.86±0.04	1.58±0.09	70±2	616±7	246.9±1.4	79±2	0.401±0.008	0.462±0.013
97	181	+01:34:09.50	+23:32:22.45	1.13±0.05	1.7±0.1	126.6±1.7	1114±5	468±1	116.2±1.8	0.420±0.008	0.560±0.016
98	182	+01:34:09.22	+23:32:18.32	0.341±0.014	1.06±0.06	9±7	78±19	26±4	22±4	0.331±0.007	0.244±0.007
99	183	+01:34:08.75	+23:32:11.25	0.092±0.004	1.20±0.07	5±9	40±30	2±15	9±6	0.051±0.001	0.158±0.004
100	184	+01:34:09.01	+23:32:15.11	2.12±0.09	5.4±0.3	1956.6±0.4	17218.0±1.3	5057.2±0.3	189.2±1.4	0.294±0.006	0.72±0.02
101	186	+01:34:10.47	+23:32:37.06	···	1.01±0.06	2±14	20±40	···	5±8	···	0.119±0.003
102	187	+01:34:09.17	+23:32:17.54	0.474±0.019	2.15±0.12	21±4	182±13	101±2	13±5	0.557±0.011	0.185±0.005
103	188	+01:34:09.08	+23:32:16.27	1.02±0.04	2.62±0.15	170.4±1.5	1500±4	568.1±0.9	70±2	0.379±0.008	0.434±0.012
104	189	+01:34:09.54	+23:32:23.05	1.17±0.05	3.6±0.2	352±1	3102±3	1047.6±0.7	74±2	0.338±0.007	0.448±0.012
105	190	+01:34:10.53	+23:32:38.01	0.25±0.01	0.96±0.06	5±9	40±30	13±6	14±5	0.301±0.006	0.198±0.005

Table C.3 Continued:

No.	MC ID	RA	DEC	Δv	R	$L_{^{12}CO(2-1)}$	M_{lum}	M_{vir}	Σ_{lum}	α_{vir}	c
		J2000	J2000	(km s^{-1})	(pc)	K km s^{-1} pc^2	($M_\odot$)	$M_\odot$)	$M_\odot$ pc^{-2}		
106	191	+01:34:09.26	+23:32:18.91	0.338±0.014	1.72±0.10	30±4	268±11	41±3	29±4	0.153±0.003	0.280±0.008
107	192	+01:34:08.80	+23:32:11.97	0.50±0.02	0.90±0.05	16±5	139±15	47±3	54±3	0.336±0.007	0.383±0.011
108	193	+01:34:09.29	+23:32:19.33	1.65±0.07	4.9±0.3	613.6±0.8	5399±2	2776.5±0.4	72±2	0.51±0.01	0.442±0.012
109	194	+01:34:08.79	+23:32:11.83	0.91±0.04	3.35±0.19	64±2	559±7	583.1±0.9	16±5	1.04±0.02	0.207±0.006
110	196	+01:34:08.78	+23:32:11.74	0.80±0.03	1.35±0.08	49±3	431±8	180.0±1.7	75±2	0.417±0.008	0.451±0.013
111	198	+01:34:08.99	+23:32:14.83	0.58±0.02	3.7±0.2	207.1±1.4	1823±4	265.0±1.4	42±3	0.145±0.003	0.335±0.009
112	199	+01:34:08.77	+23:32:11.54	0.64±0.03	1.31±0.08	22±4	197±12	111±2	37±3	0.565±0.011	0.315±0.009
113	200	+01:34:08.74	+23:32:11.11	0.77±0.03	2.40±0.14	144.0±1.6	1267±5	295.6±1.3	70±2	0.233±0.005	0.435±0.012
114	201	+01:34:08.50	+23:32:07.43	0.61±0.02	2.09±0.12	123.6±1.8	1087±5	163.4±1.7	79±2	0.150±0.003	0.463±0.013
115	202	+01:34:09.11	+23:32:16.64	0.071±0.003	0.74±0.04	2±15	10±50	0±20	8±7	0.0565±0.0011	0.148±0.004
116	203	+01:34:08.36	+23:32:05.38	0.87±0.04	1.7±0.1	94±2	824±6	278.3±1.3	87±2	0.338±0.007	0.485±0.013
117	204	+01:34:09.50	+23:32:22.54	1.26±0.05	2.05±0.12	74±2	651±7	687.3±0.8	49±3	1.06±0.02	0.37±0.01
118	205	+01:34:09.19	+23:32:17.82	0.366±0.015	1.8±0.1	32±3	280±10	50±3	29±4	0.176±0.004	0.279±0.008
119	206	+01:34:09.94	+23:32:29.11	0.211±0.009	0.39±0.02	1±19	10±60	4±12	21±4	0.373±0.008	0.236±0.007
120	207	+01:34:09.03	+23:32:15.43	1.54±0.06	2.85±0.17	219.3±1.3	1930±4	1418.7±0.6	76±2	0.735±0.015	0.452±0.013

Table C.3 Continued:

No.	MC ID	RA J2000	DEC J2000	Δv (km s^{-1})	R (pc)	$L_{^{12}CO(2-1)}$ K km s^{-1} pc^2	M_{lum} ($M_\odot$)	M_{vir} $M_\odot$)	Σ_{lum} $M_\odot$ pc^{-2}	α_{vir}	c
121	208	+01:34:10.31	+23:32:34.59	0.76±0.03	2.12±0.12	53±3	463±8	255.0±1.4	33±3	0.550±0.011	0.298±0.008
122	210	+01:34:08.70	+23:32:10.46	0.146±0.006	1.07±0.06	6±8	50±20	0±10	14±5	0.0936±0.0019	0.197±0.005
123	211	+01:34:08.70	+23:32:10.50	0.060±0.002	0.89±0.05	3±12	20±40	0±30	9±6	0.0284±0.0006	0.160±0.004

Table C.4: ^{13}CO catalogs for clumps in NGC 604

No.	MC ID	RA	DEC	Δv	R	$L_{^{13}CO(2-1)}$	M_{lum}	M_{vir}	Σ_{lum}	α_{vir}	c
		J2000	J2000	(km s^{-1})	(pc)	K km s^{-1} pc^2	($M_\odot$)	$M_\odot$)	$M_\odot$ pc^{-2}		
1	0	+01:34:33.17	+23:38:17.60	0.100±0.004	0.88±0.05	1±18	10±50	2±16	4±9	0.180±0.004	0.107±0.003
2	5	+01:34:33.11	+23:38:16.62	0.097±0.004	0.71±0.04	2±13	20±40	1±19	13±5	0.0677±0.0014	0.189±0.005
3	6	+01:34:33.11	+23:38:16.72	0.091±0.004	0.92±0.05	3±11	30±30	2±18	10±6	0.0587±0.0012	0.167±0.005
4	8	+01:34:33.08	+23:38:16.27	0.337±0.014	1.25±0.07	8±7	70±20	30±4	14±5	0.449±0.009	0.192±0.005
5	10	+01:34:33.13	+23:38:17.01	0.404±0.016	1.20±0.07	5±9	40±30	41±3	9±7	1.02±0.02	0.155±0.004
6	11	+01:34:33.11	+23:38:16.70	0.25±0.01	1.17±0.07	11±6	97±18	15±6	23±4	0.156±0.003	0.247±0.007
7	12	+01:34:34.94	+23:38:44.17	0.060±0.002	0.74±0.04	0±20	10±60	0±30	4±9	0.0779±0.0016	0.107±0.003
8	13	+01:34:33.06	+23:38:15.95	0.083±0.003	1.05±0.06	2±16	10±50	2±18	4±10	0.111±0.002	0.104±0.003
9	17	+01:34:33.21	+23:38:18.14	0.266±0.011	1.17±0.07	6±8	50±20	17±5	13±5	0.318±0.006	0.186±0.005
10	19	+01:34:33.14	+23:38:17.04	···	0.59±0.03	0±30	0±80	···	5±9	···	0.111±0.003
11	20	+01:34:33.14	+23:38:17.17	0.190±0.008	1.37±0.08	3±11	30±30	10±7	5±9	0.373±0.008	0.113±0.003
12	21	+01:34:33.37	+23:38:20.56	0.406±0.017	1.70±0.10	12±6	107±17	59±3	12±6	0.548±0.011	0.179±0.005
13	22	+01:34:33.12	+23:38:16.81	0.113±0.005	0.99±0.06	4±10	40±30	3±14	12±6	0.0736±0.0015	0.178±0.005
14	23	+01:34:33.14	+23:38:17.08	0.459±0.019	1.33±0.08	12±6	106±17	59±3	19±4	0.553±0.011	0.228±0.006
15	24	+01:34:33.22	+23:38:18.35	0.049±0.002	1.35±0.08	2±13	20±40	0±30	0±10	0.0343±0.0007	0.097±0.003

Table C.4 Continued:

No.	MC ID	RA J2000	DEC J2000	Δv (km s^{-1})	R (pc)	$L_{^{13}CO(2-1)}$ K km s^{-1} pc^2	M_{lum} ($M_\odot$)	M_{vir} $M_\odot$)	Σ_{lum} $M_\odot$ pc^{-2}	α_{vir}	c
16	25	+01:34:33.12	+23:38:16.85	0.099±0.004	0.96±0.06	0±10	30±30	2±16	11±6	0.0601±0.0012	0.175±0.005
17	26	+01:34:33.24	+23:38:18.61	···	0.97±0.06	1±18	10±50	···	0±10	···	0.100±0.003
18	27	+01:34:34.61	+23:38:39.12	0.50±0.02	0.98±0.06	8±7	70±20	52±3	24±4	0.721±0.015	0.255±0.007
19	28	+01:34:33.39	+23:38:20.86	0.290±0.012	1.48±0.09	11±6	99±17	26±4	14±5	0.263±0.005	0.198±0.005
20	29	+01:34:33.12	+23:38:16.84	0.099±0.004	1.07±0.06	4±10	40±30	2±15	10±6	0.0616±0.0012	0.163±0.005
21	31	+01:34:33.65	+23:38:24.81	0.25±0.01	1.86±0.11	8±7	70±20	25±4	7±7	0.335±0.007	0.136±0.004
22	42	+01:34:33.33	+23:38:19.99	0.205±0.008	2.00±0.12	8±7	70±20	18±5	6±8	0.251±0.005	0.123±0.003
23	46	+01:34:33.20	+23:38:17.93	0.094±0.004	0.71±0.04	1±17	10±50	1±19	8±7	0.110±0.002	0.143±0.004
24	47	+01:34:33.63	+23:38:24.38	0.085±0.003	0.82±0.05	3±12	20±40	0±20	11±6	0.0525±0.0011	0.174±0.005
25	49	+01:34:33.14	+23:38:17.17	0.298±0.012	1.39±0.08	4±9	40±30	26±4	6±8	0.666±0.013	0.132±0.004
26	54	+01:34:33.46	+23:38:21.92	0.138±0.006	1.14±0.07	3±11	30±30	0±10	7±7	0.164±0.003	0.136±0.004
27	57	+01:34:33.72	+23:38:25.85	0.67±0.03	1.8±0.1	56±3	489±8	169.1±1.7	48±3	0.346±0.007	0.36±0.01
28	60	+01:34:33.29	+23:38:19.33	0.51±0.02	1.85±0.11	26±4	225±11	100±2	21±4	0.443±0.009	0.238±0.007
29	63	+01:34:33.28	+23:38:19.13	0.359±0.015	1.25±0.07	3±11	30±30	34±4	6±8	1.18±0.02	0.126±0.004
30	68	+01:34:33.83	+23:38:27.52	0.196±0.008	0.83±0.05	4±10	40±30	7±9	17±5	0.186±0.004	0.212±0.006

Table C.4 Continued:

No.	MC ID	RA J2000	DEC J2000	Δv (km s^{-1})	R (pc)	$L_{^{13}CO(2-1)}$ K km s^{-1} pc^2	M_{lum} ($M_\odot$)	M_{vir} $M_\odot$)	Σ_{lum} $M_\odot$ pc^{-2}	α_{vir}	c
31	70	+01:34:33.13	+23:38:17.02	0.330±0.013	1.49±0.09	11±6	93±18	34±4	13±5	0.367±0.007	0.190±0.005
32	73	+01:34:33.43	+23:38:21.48	0.266±0.011	0.36±0.02	0±20	10±70	5±10	15±5	0.875±0.018	0.200±0.006
33	77	+01:34:33.50	+23:38:22.48	0.412±0.017	1.02±0.06	9±6	82±19	36±4	25±4	0.444±0.009	0.261±0.007
34	78	+01:34:34.00	+23:38:29.97	1.03±0.04	1.35±0.08	48±3	421±8	299.5±1.3	73±2	0.711±0.014	0.445±0.012
35	79	+01:34:32.96	+23:38:14.41	0.049±0.002	0.95±0.06	1±16	10±50	0±30	5±9	0.0373±0.0008	0.111±0.003
36	80	+01:34:33.63	+23:38:24.38	0.146±0.006	0.82±0.05	0±10	30±30	4±12	16±5	0.111±0.002	0.206±0.006
37	81	+01:34:33.40	+23:38:20.93	0.0399±0.0016	0.88±0.05	2±13	20±40	0±40	8±7	0.0154±0.0003	0.145±0.004
38	87	+01:34:33.49	+23:38:22.36	0.49±0.02	1.36±0.08	8±7	70±20	67±3	12±6	0.938±0.019	0.183±0.005
39	89	+01:34:33.84	+23:38:27.55	0.099±0.004	0.94±0.05	0±10	30±30	2±16	11±6	0.0624±0.0013	0.175±0.005
40	90	+01:34:32.97	+23:38:14.58	···	1.21±0.07	3±12	20±40	···	5±9	···	0.114±0.003
41	95	+01:34:33.57	+23:38:23.58	0.164±0.007	0.84±0.05	3±11	30±30	0±10	13±5	0.164±0.003	0.188±0.005
42	97	+01:34:33.44	+23:38:21.54	0.361±0.015	1.36±0.08	9±7	79±19	37±4	14±5	0.472±0.009	0.192±0.005
43	103	+01:34:33.68	+23:38:25.21	0.050±0.002	1.06±0.06	3±11	30±30	0±30	8±7	0.0205±0.0004	0.144±0.004
44	105	+01:34:33.64	+23:38:24.55	0.099±0.004	0.89±0.05	5±9	50±30	2±16	18±5	0.0405±0.0008	0.222±0.006
45	106	+01:34:33.54	+23:38:23.15	0.416±0.017	1.82±0.11	12±6	109±16	66±3	10±6	0.608±0.012	0.168±0.005

Table C.4 Continued:

No.	MC ID	RA J2000	DEC J2000	Δv (km s^{-1})	R (pc)	$L_{^{13}CO(2-1)}$ K km s^{-1} pc^2	M_{lum} ($M_\odot$)	M_{vir} $M_\odot$)	Σ_{lum} $M_\odot$ pc^{-2}	α_{vir}	c
46	108	+01:34:34.12	+23:38:31.77	0.217±0.009	0.80±0.05	3±12	30±30	8±8	13±5	0.313±0.006	0.184±0.005
47	112	+01:34:33.57	+23:38:23.50	0.110±0.005	0.93±0.05	2±14	20±40	2±14	6±8	0.141±0.003	0.130±0.004
48	113	+01:34:33.46	+23:38:21.85	0.216±0.009	1.57±0.09	8±7	70±20	15±6	9±7	0.229±0.005	0.153±0.004
49	114	+01:34:33.13	+23:38:16.94	0.362±0.015	1.30±0.08	15±5	135±15	36±4	25±4	0.265±0.005	0.262±0.007
50	117	+01:34:33.89	+23:38:28.41	0.243±0.010	0.81±0.05	5±8	50±30	10±7	23±4	0.214±0.004	0.249±0.007
51	118	+01:34:34.68	+23:38:40.20	0.227±0.009	1.64±0.09	9±7	79±19	18±5	9±6	0.226±0.005	0.159±0.004
52	120	+01:34:33.28	+23:38:19.18	0.203±0.008	1.45±0.08	5±9	40±30	13±6	7±8	0.286±0.006	0.134±0.004
53	122	+01:34:33.47	+23:38:22.03	···	0.84±0.05	1±17	10±50	···	5±8	···	0.122±0.003
54	123	+01:34:34.11	+23:38:31.59	0.193±0.008	1.49±0.09	9±6	81±19	12±7	12±6	0.143±0.003	0.178±0.005
55	124	+01:34:33.50	+23:38:22.45	0.138±0.006	1.12±0.06	2±14	20±40	4±11	4±9	0.261±0.005	0.109±0.003
56	126	+01:34:33.74	+23:38:26.10	0.132±0.005	1.39±0.08	3±11	30±30	5±10	4±9	0.187±0.004	0.110±0.003
57	129	+01:34:33.67	+23:38:25.11	0.75±0.03	1.70±0.10	53±3	462±8	201.2±1.6	51±3	0.435±0.009	0.37±0.01
58	130	+01:34:33.22	+23:38:18.28	0.76±0.03	1.8±0.1	34±3	300±10	215.6±1.5	30±4	0.718±0.014	0.283±0.008
59	131	+01:34:33.52	+23:38:22.77	0.402±0.016	1.21±0.07	11±6	95±18	41±3	21±4	0.432±0.009	0.236±0.007
60	132	+01:34:34.72	+23:38:40.75	···	0.77±0.04	0±20	10±60	···	4±10	···	0.102±0.003

Table C.4 Continued:

No.	MC ID	RA	DEC	Δv	R	$L_{^{13}CO(2-1)}$	M_{lum}	M_{vir}	Σ_{lum}	α_{vir}	c
		J2000	J2000	(km s^{-1})	(pc)	K km s^{-1} pc^2	($M_\odot$)	$M_\odot$)	$M_\odot$ pc^{-2}		
61	133	+01:34:33.42	+23:38:21.35	0.190±0.008	1.15±0.07	12±6	105±17	9±8	25±4	0.0827±0.0017	0.262±0.007
62	136	+01:34:33.90	+23:38:28.47	0.242±0.010	0.75±0.04	5±9	40±30	9±7	23±4	0.228±0.005	0.249±0.007
63	137	+01:34:33.52	+23:38:22.73	0.063±0.003	1.19±0.07	3±11	30±30	0±20	6±8	0.0377±0.0008	0.126±0.003
64	138	+01:34:33.82	+23:38:27.33	···	0.99±0.06	1±16	10±50	···	4±10	···	0.105±0.003
65	139	+01:34:33.70	+23:38:25.52	0.187±0.008	1.31±0.08	4±9	40±30	10±7	7±7	0.249±0.005	0.139±0.004
66	141	+01:34:33.47	+23:38:21.99	0.474±0.019	1.40±0.08	13±5	113±16	66±3	18±5	0.588±0.012	0.222±0.006
67	142	+01:34:33.66	+23:38:24.86	0.457±0.019	0.99±0.06	25±4	221±12	43±3	71±2	0.197±0.004	0.439±0.012
68	144	+01:34:33.58	+23:38:23.69	0.224±0.009	1.04±0.06	6±8	60±20	11±7	16±5	0.199±0.004	0.210±0.006
69	145	+01:34:33.42	+23:38:21.23	0.127±0.005	1.39±0.08	5±9	40±30	0±10	7±7	0.112±0.002	0.137±0.004
70	147	+01:34:33.67	+23:38:25.06	0.364±0.015	1.15±0.07	13±5	112±16	32±4	27±4	0.285±0.006	0.270±0.008
71	148	+01:34:33.51	+23:38:22.59	0.439±0.018	0.86±0.05	7±7	70±20	35±4	28±4	0.533±0.011	0.276±0.008
72	149	+01:34:34.14	+23:38:32.13	0.222±0.009	2.11±0.12	9±7	80±20	22±5	6±8	0.281±0.006	0.122±0.003
73	150	+01:34:34.30	+23:38:34.45	0.132±0.005	0.82±0.05	0±10	30±30	3±13	15±5	0.0947±0.0019	0.201±0.006
74	152	+01:34:33.90	+23:38:28.54	0.094±0.004	0.92±0.05	2±14	20±40	2±17	7±7	0.0938±0.0019	0.136±0.004
75	153	+01:34:35.17	+23:38:47.59	0.204±0.008	1.25±0.07	2±14	20±40	11±7	0±10	0.622±0.013	0.098±0.003

Table C.4 Continued:

No.	MC ID	RA J2000	DEC J2000	Δv (km s^{-1})	R (pc)	$L_{^{13}CO(2-1)}$ K km s^{-1} pc^2	M_{lum} ($M_\odot$)	M_{vir} $M_\odot$)	Σ_{lum} $M_\odot$ pc^{-2}	α_{vir}	c
76	154	+01:34:33.43	+23:38:21.50	0.55±0.02	1.41±0.08	49±3	435±8	90±2	70±2	0.207±0.004	0.435±0.012
77	155	+01:34:34.13	+23:38:31.99	···	0.88±0.05	1±17	10±50	···	5±9	···	0.112±0.003
78	156	+01:34:33.90	+23:38:28.44	0.59±0.02	1.95±0.11	49±3	431±8	144.4±1.9	36±3	0.335±0.007	0.312±0.009
79	157	+01:34:33.02	+23:38:15.24	0.067±0.003	0.68±0.04	1±19	10±60	0±30	7±7	0.0651±0.0013	0.135±0.004
80	158	+01:34:33.40	+23:38:21.04	0.129±0.005	0.77±0.04	7±7	60±20	3±14	32±3	0.0448±0.0009	0.294±0.008
81	159	+01:34:33.62	+23:38:24.33	0.96±0.04	1.56±0.09	45±3	396±9	301.0±1.3	52±3	0.759±0.015	0.37±0.01
82	160	+01:34:33.00	+23:38:15.06	0.087±0.004	0.97±0.06	2±14	20±40	2±18	6±8	0.0906±0.0018	0.125±0.003
83	161	+01:34:32.97	+23:38:14.60	0.373±0.015	1.82±0.11	13±5	112±16	53±3	11±6	0.475±0.010	0.171±0.005
84	162	+01:34:33.78	+23:38:26.66	0.236±0.010	1.10±0.06	6±8	50±20	13±6	14±5	0.236±0.005	0.197±0.005
85	163	+01:34:34.29	+23:38:34.35	0.096±0.004	0.69±0.04	2±14	20±40	1±19	12±6	0.0730±0.0015	0.182±0.005
86	164	+01:34:33.75	+23:38:26.24	0.092±0.004	0.80±0.05	1±16	10±50	1±19	6±8	0.111±0.002	0.132±0.004
87	165	+01:34:33.67	+23:38:25.09	0.50±0.02	1.06±0.06	19±5	166±13	55±3	47±3	0.329±0.007	0.358±0.010
88	166	+01:34:33.52	+23:38:22.74	0.082±0.003	1.19±0.07	3±11	30±30	2±17	6±8	0.0653±0.0013	0.126±0.003
89	167	+01:34:33.56	+23:38:23.47	0.192±0.008	1.64±0.09	5±9	50±30	13±6	6±8	0.274±0.006	0.122±0.003
90	168	+01:34:33.41	+23:38:21.14	0.087±0.004	1.10±0.06	2±13	20±40	2±17	6±8	0.0823±0.0017	0.123±0.003

Table C.4 Continued:

No.	MC ID	RA	DEC	Δv	R	$L_{^{13}CO(2-1)}$	M_{lum}	M_{vir}	Σ_{lum}	α_{vir}	c
		J2000	J2000	(km s^{-1})	(pc)	K km s^{-1} pc^2	($M_{\odot}$)	$M_{\odot}$)	$M_{\odot}$ pc^{-2}		
91	169	+01:34:33.84	+23:38:27.61	0.059±0.002	0.73±0.04	0±20	10±60	0±30	5±9	0.0713±0.0014	0.111±0.003
92	170	+01:34:34.86	+23:38:42.84	0.442±0.018	1.60±0.09	13±5	112±16	66±3	14±5	0.585±0.012	0.194±0.005
93	172	+01:34:33.12	+23:38:16.73	0.116±0.005	1.16±0.07	3±11	30±30	3±12	7±7	0.112±0.002	0.136±0.004
94	173	+01:34:33.41	+23:38:21.22	1.31±0.05	1.71±0.10	357±1	3146±3	615.0±0.9	342.2±1.1	0.196±0.004	0.96±0.03
95	174	+01:34:33.68	+23:38:25.13	0.109±0.004	0.77±0.04	3±11	30±30	2±16	14±5	0.0741±0.0015	0.195±0.005
96	175	+01:34:33.74	+23:38:26.03	···	1.05±0.06	2±14	20±40	···	5±9	···	0.116±0.003
97	176	+01:34:33.66	+23:38:24.92	0.478±0.019	0.77±0.04	24±4	212±12	37±4	112.5±1.8	0.175±0.004	0.552±0.015
98	177	+01:34:33.49	+23:38:22.42	0.166±0.007	1.05±0.06	2±13	20±40	6±9	6±8	0.307±0.006	0.124±0.003
99	178	+01:34:33.52	+23:38:22.84	0.052±0.002	1.25±0.07	2±14	20±40	0±30	3±11	0.0445±0.0009	0.095±0.003
100	181	+01:34:33.41	+23:38:21.19	0.176±0.007	0.90±0.05	3±11	30±30	6±9	11±6	0.214±0.004	0.171±0.005
101	183	+01:34:33.31	+23:38:19.63	···	0.99±0.06	3±11	30±30	···	9±6	···	0.159±0.004
102	185	+01:34:33.58	+23:38:23.74	···	0.72±0.04	1±18	10±50	···	6±8	···	0.129±0.004
103	187	+01:34:33.78	+23:38:26.74	0.87±0.04	2.16±0.12	46±3	407±9	345.8±1.2	28±4	0.849±0.017	0.275±0.008
104	188	+01:34:33.35	+23:38:20.27	0.392±0.016	0.77±0.04	10±6	86±19	25±4	47±3	0.286±0.006	0.356±0.010
105	189	+01:34:33.77	+23:38:26.57	0.395±0.016	0.95±0.05	8±7	70±20	31±4	23±4	0.470±0.009	0.252±0.007

Table C.4 Continued:

No.	MC ID	RA	DEC	Δv	R	$L_{^{13}CO(2-1)}$	M_{lum}	M_{vir}	Σ_{lum}	α_{vir}	c
		J2000	J2000	(km s^{-1})	(pc)	K km s^{-1} pc^2	($M_\odot$)	$M_\odot$)	$M_\odot$ pc^{-2}		
106	190	+01:34:33.64	+23:38:24.59	0.383±0.016	1.8±0.1	10±6	88±18	56±3	9±7	0.637±0.013	0.152±0.004
107	191	+01:34:33.46	+23:38:21.86	0.59±0.02	1.28±0.07	44±3	390±9	93±2	76±2	0.240±0.005	0.452±0.013
108	192	+01:34:33.29	+23:38:19.32	0.076±0.003	1.06±0.06	0±10	30±30	0±20	9±7	0.0413±0.0008	0.154±0.004
109	193	+01:34:34.92	+23:38:43.74	···	0.78±0.04	0±20	10±60	···	4±10	···	0.103±0.003
110	194	+01:34:33.49	+23:38:22.37	0.25±0.01	0.80±0.05	3±12	20±40	10±7	11±6	0.464±0.009	0.174±0.005
111	196	+01:34:33.42	+23:38:21.23	0.222±0.009	0.80±0.05	3±11	30±30	8±8	14±5	0.288±0.006	0.197±0.005
112	197	+01:34:33.62	+23:38:24.36	0.51±0.02	1.18±0.07	31±4	270±10	65±3	63±2	0.238±0.005	0.411±0.011
113	198	+01:34:33.54	+23:38:23.16	0.078±0.003	0.90±0.05	2±13	20±40	0±20	8±7	0.0587±0.0012	0.145±0.004
114	199	+01:34:33.63	+23:38:24.50	0.318±0.013	1.51±0.09	13±5	115±16	32±4	16±5	0.278±0.006	0.209±0.006
115	201	+01:34:33.53	+23:38:22.94	0.25±0.01	0.92±0.05	2±13	20±40	12±6	8±7	0.587±0.012	0.145±0.004
116	202	+01:34:34.22	+23:38:33.28	0.53±0.02	1.19±0.07	13±5	116±16	70±3	26±4	0.600±0.012	0.264±0.007
117	204	+01:34:33.67	+23:38:24.98	0.179±0.007	1.46±0.08	15±5	134±15	10±7	20±4	0.0734±0.0015	0.233±0.006
118	205	+01:34:33.40	+23:38:21.02	0.151±0.006	0.84±0.05	2±13	20±40	4±11	9±6	0.200±0.004	0.157±0.004
119	206	+01:34:33.71	+23:38:25.69	0.54±0.02	0.93±0.05	24±4	213±12	56±3	79±2	0.264±0.005	0.462±0.013
120	207	+01:34:33.48	+23:38:22.23	0.215±0.009	1.28±0.07	3±11	30±30	12±6	6±8	0.431±0.009	0.124±0.003

Table C.4 Continued:

No.	MC ID	RA J2000	DEC J2000	Δv (km s^{-1})	R (pc)	$L_{^{13}CO(2-1)}$ K km s^{-1} pc^2	M_{lum} ($M_\odot$)	M_{vir} $M_\odot$)	Σ_{lum} $M_\odot$ pc^{-2}	α_{vir}	c
121	208	+01:34:33.29	+23:38:19.41	0.060±0.002	0.84±0.05	2±14	20±40	0±30	8±7	0.0365±0.0007	0.145±0.004
122	209	+01:34:33.75	+23:38:26.24	0.142±0.006	0.85±0.05	3±11	30±30	4±12	13±5	0.119±0.002	0.190±0.005
123	210	+01:34:33.49	+23:38:22.35	0.087±0.004	0.77±0.04	2±14	20±40	0±20	10±6	0.0660±0.0013	0.164±0.005
124	211	+01:34:33.42	+23:38:21.31	···	0.37±0.02	0±30	0±100	···	7±7	···	0.140±0.004
125	212	+01:34:33.75	+23:38:26.23	0.467±0.019	1.8±0.1	16±5	145±14	82±2	14±5	0.568±0.011	0.196±0.005
126	213	+01:34:33.65	+23:38:24.80	0.385±0.016	2.03±0.12	26±4	229±11	63±3	18±5	0.276±0.006	0.218±0.006
127	214	+01:34:33.77	+23:38:26.56	0.100±0.004	1.06±0.06	2±13	20±40	2±15	6±8	0.104±0.002	0.128±0.004
128	215	+01:34:33.39	+23:38:20.83	0.061±0.003	0.68±0.04	0±20	10±60	0±30	5±9	0.0756±0.0015	0.115±0.003
129	216	+01:34:33.47	+23:38:22.12	0.343±0.014	0.81±0.05	8±7	70±20	20±5	35±3	0.278±0.006	0.309±0.009
130	217	+01:34:33.35	+23:38:20.27	0.103±0.004	0.66±0.04	2±13	20±40	1±18	14±5	0.0750±0.0015	0.196±0.005
131	218	+01:34:33.49	+23:38:22.29	0.62±0.03	1.13±0.07	46±3	408±9	90±2	101.7±1.9	0.221±0.004	0.524±0.015
132	219	+01:34:33.77	+23:38:26.62	0.392±0.016	0.83±0.05	5±9	40±30	27±4	19±4	0.646±0.013	0.227±0.006
133	220	+01:34:33.42	+23:38:21.24	0.080±0.003	0.62±0.04	0±20	10±60	0±20	7±8	0.105±0.002	0.134±0.004
134	221	+01:34:33.75	+23:38:26.27	0.48±0.02	1.15±0.07	14±5	120±16	56±3	29±4	0.469±0.009	0.279±0.008
135	222	+01:34:33.62	+23:38:24.32	0.099±0.004	0.78±0.05	3±12	20±40	2±18	12±6	0.0691±0.0014	0.180±0.005

Table C.4 Continued:

No.	MC ID	RA J2000	DEC J2000	Δv (km s^{-1})	R (pc)	$L_{^{13}CO(2-1)}$ K km s^{-1} pc^2	M_{lum} ($M_\odot$)	M_{vir} $M_\odot$)	Σ_{lum} $M_\odot$ pc^{-2}	α_{vir}	c
136	223	+01:34:33.52	+23:38:22.84	0.143±0.006	0.47±0.03	0±20	10±60	2±16	11±6	0.279±0.006	0.169±0.005
137	224	+01:34:34.78	+23:38:41.69	···	0.64±0.04	0±20	10±70	···	4±9	···	0.110±0.003
138	225	+01:34:33.82	+23:38:27.26	0.418±0.017	0.92±0.05	0±10	30±30	34±4	12±6	1.03±0.02	0.183±0.005
139	226	+01:34:33.67	+23:38:25.02	0.100±0.004	1.13±0.07	6±8	50±20	2±15	13±5	0.0452±0.0009	0.187±0.005
140	227	+01:34:33.60	+23:38:23.95	0.338±0.014	1.32±0.08	9±6	81±19	32±4	15±5	0.391±0.008	0.200±0.006
141	228	+01:34:33.46	+23:38:21.83	0.077±0.003	0.99±0.06	2±14	20±40	0±20	6±8	0.0690±0.0014	0.125±0.003
142	229	+01:34:34.34	+23:38:35.10	0.216±0.009	1.32±0.08	5±9	40±30	13±6	8±7	0.313±0.006	0.143±0.004
143	230	+01:34:33.59	+23:38:23.84	0.082±0.003	1.30±0.08	2±13	20±40	2±16	4±10	0.0909±0.0018	0.101±0.003
144	232	+01:34:33.67	+23:38:25.07	0.053±0.002	0.93±0.05	3±11	30±30	0±30	10±6	0.0203±0.0004	0.164±0.005
145	234	+01:34:34.41	+23:38:36.18	0.473±0.019	1.24±0.07	7±7	60±20	58±3	13±5	0.945±0.019	0.186±0.005
146	235	+01:34:33.65	+23:38:24.80	···	0.72±0.04	2±14	20±40	···	10±6	···	0.167±0.005
147	236	+01:34:33.42	+23:38:21.33	0.187±0.008	0.55±0.03	0±20	10±70	4±11	7±7	0.608±0.012	0.138±0.004
148	237	+01:34:33.48	+23:38:22.20	0.391±0.016	0.76±0.04	13±5	112±16	24±5	62±2	0.217±0.004	0.408±0.011
149	238	+01:34:34.35	+23:38:35.29	0.365±0.015	1.38±0.08	7±7	60±20	39±4	11±6	0.609±0.012	0.170±0.005
150	240	+01:34:33.66	+23:38:24.89	0.182±0.007	0.59±0.03	0±10	30±30	4±11	30±4	0.128±0.003	0.283±0.008

Table C.4 Continued:

No.	MC ID	RA J2000	DEC J2000	Δv (km s^{-1})	R (pc)	$L_{^{13}CO(2-1)}$ K km s^{-1} pc^2	M_{lum} ($M_\odot$)	M_{vir} $M_\odot$)	Σ_{lum} $M_\odot$ pc^{-2}	α_{vir}	c
151	241	+01:34:33.42	+23:38:21.32	0.078±0.003	0.65±0.04	0±20	10±70	0±20	5±9	0.123±0.002	0.117±0.003
152	242	+01:34:34.43	+23:38:36.47	0.0365±0.0015	0.83±0.05	1±18	10±50	0±50	5±9	0.0225±0.0005	0.113±0.003
153	243	+01:34:33.47	+23:38:22.01	0.74±0.03	1.03±0.06	57±3	502±8	119±2	151.7±1.6	0.238±0.005	0.640±0.018
154	244	+01:34:33.66	+23:38:24.97	0.284±0.012	0.83±0.05	11±6	93±18	14±6	43±3	0.151±0.003	0.341±0.009
155	245	+01:34:34.57	+23:38:38.60	···	0.73±0.04	0±20	10±60	···	4±9	···	0.110±0.003
156	246	+01:34:33.53	+23:38:22.98	0.70±0.03	1.50±0.09	11±6	101±17	155.9±1.8	14±5	1.54±0.03	0.197±0.005
157	247	+01:34:33.44	+23:38:21.58	0.323±0.013	1.17±0.07	5±9	40±30	26±4	10±6	0.626±0.013	0.160±0.004
158	248	+01:34:34.33	+23:38:35.01	0.151±0.006	1.30±0.08	3±12	20±30	6±9	5±9	0.256±0.005	0.111±0.003
159	249	+01:34:33.27	+23:38:18.98	0.120±0.005	1.13±0.07	3±11	30±30	3±12	7±8	0.128±0.003	0.134±0.004
160	250	+01:34:33.26	+23:38:18.88	0.116±0.005	1.05±0.06	2±15	20±40	3±13	4±9	0.191±0.004	0.110±0.003
161	251	+01:34:33.53	+23:38:22.88	0.163±0.007	1.30±0.08	4±9	40±30	7±8	7±7	0.189±0.004	0.140±0.004
162	252	+01:34:32.96	+23:38:14.38	0.125±0.005	0.69±0.04	1±16	10±50	2±15	8±7	0.180±0.004	0.151±0.004
163	255	+01:34:33.91	+23:38:28.64	0.131±0.005	1.62±0.09	6±8	50±20	6±9	6±8	0.115±0.002	0.129±0.004
164	256	+01:34:33.92	+23:38:28.75	0.096±0.004	1.19±0.07	3±11	30±30	2±15	6±8	0.0830±0.0017	0.130±0.004
165	258	+01:34:33.93	+23:38:28.89	0.398±0.016	1.08±0.06	7±7	70±20	36±4	18±5	0.547±0.011	0.220±0.006

Table C.4 Continued:

No.	MC ID	RA J2000	DEC J2000	Δv (km s^{-1})	R (pc)	$L_{^{13}CO(2-1)}$ K km s^{-1} pc^2	M_{lum} ($M_\odot$)	M_{vir} $M_\odot$)	Σ_{lum} $M_\odot$ pc^{-2}	α_{vir}	c
166	259	+01:34:33.93	+23:38:28.90	0.169±0.007	0.65±0.04	2±15	10±40	4±11	11±6	0.260±0.005	0.174±0.005
167	260	+01:34:34.04	+23:38:30.66	0.163±0.007	1.34±0.08	3±11	30±30	7±8	5±9	0.284±0.006	0.113±0.003
168	269	+01:34:34.06	+23:38:30.88	0.084±0.003	0.68±0.04	1±18	10±50	0±20	7±7	0.0965±0.0019	0.139±0.004
169	272	+01:34:34.13	+23:38:32.02	0.169±0.007	1.41±0.08	0±10	30±30	8±8	5±8	0.256±0.005	0.119±0.003
170	273	+01:34:34.09	+23:38:31.31	0.122±0.005	1.25±0.07	5±9	40±30	4±11	8±7	0.0938±0.0019	0.151±0.004
171	276	+01:34:34.30	+23:38:34.47	0.0297±0.0012	1.14±0.07	2±14	20±40	0±50	4±10	0.0130±0.0003	0.104±0.003
172	278	+01:34:34.28	+23:38:34.17	0.192±0.008	0.94±0.05	2±12	20±40	7±8	8±7	0.333±0.007	0.146±0.004
173	282	+01:34:34.58	+23:38:38.74	···	0.77±0.04	0±20	10±60	···	5±9	···	0.111±0.003
174	283	+01:34:34.39	+23:38:35.90	0.184±0.008	1.8±0.1	8±7	70±20	13±6	7±7	0.186±0.004	0.135±0.004
175	285	+01:34:34.43	+23:38:36.45	0.74±0.03	1.90±0.11	28±4	250±11	217.1±1.5	22±4	0.867±0.017	0.244±0.007
176	286	+01:34:34.33	+23:38:34.96	0.143±0.006	0.91±0.05	2±13	20±40	4±11	8±7	0.191±0.004	0.146±0.004
177	287	+01:34:34.88	+23:38:43.19	0.302±0.012	1.92±0.11	14±5	122±16	37±4	11±6	0.299±0.006	0.169±0.005
178	288	+01:34:34.23	+23:38:33.52	0.277±0.011	1.52±0.09	12±6	109±16	24±5	15±5	0.224±0.005	0.202±0.006
179	289	+01:34:34.43	+23:38:36.42	0.191±0.008	1.01±0.06	3±12	20±40	8±8	7±7	0.326±0.007	0.141±0.004
180	290	+01:34:34.18	+23:38:32.69	0.283±0.012	1.33±0.08	16±5	137±15	22±5	25±4	0.163±0.003	0.258±0.007

Table C.4 Continued:

No.	MC ID	RA J2000	DEC J2000	Δv (km s^{-1})	R (pc)	$L_{^{13}CO(2-1)}$ K km s^{-1} pc^2	M_{lum} ($M_\odot$)	M_{vir} $M_\odot$)	Σ_{lum} $M_\odot$ pc^{-2}	α_{vir}	c
181	291	+01:34:34.29	+23:38:34.35	0.123±0.005	0.92±0.05	3±11	30±30	3±13	10±6	0.115±0.002	0.161±0.004
182	293	+01:34:34.72	+23:38:40.86	···	0.73±0.04	0±20	10±60	···	5±9	···	0.111±0.003
183	294	+01:34:34.31	+23:38:34.68	0.125±0.005	1.04±0.06	5±9	40±30	3±12	12±6	0.0850±0.0017	0.179±0.005
184	295	+01:34:34.22	+23:38:33.33	0.211±0.009	1.34±0.08	9±7	80±19	13±6	14±5	0.157±0.003	0.196±0.005
185	296	+01:34:34.48	+23:38:37.27	0.146±0.006	1.52±0.09	7±8	60±20	7±9	8±7	0.114±0.002	0.149±0.004
186	298	+01:34:34.75	+23:38:41.23	0.263±0.011	1.92±0.11	9±7	78±19	28±4	7±7	0.356±0.007	0.135±0.004
187	299	+01:34:34.38	+23:38:35.71	···	0.91±0.05	1±16	10±50	···	5±9	···	0.116±0.003
188	300	+01:34:34.89	+23:38:43.34	···	1.53±0.09	3±12	20±40	···	3±11	···	0.093±0.003
189	303	+01:34:34.50	+23:38:37.53	0.58±0.02	2.33±0.13	65±2	572±7	166.5±1.7	34±3	0.291±0.006	0.302±0.008
190	304	+01:34:34.21	+23:38:33.16	0.222±0.009	1.45±0.08	13±5	113±16	15±6	17±5	0.134±0.003	0.214±0.006
191	305	+01:34:34.48	+23:38:37.18	0.265±0.011	2.03±0.12	4±10	40±30	30±4	3±12	0.822±0.017	0.087±0.002
192	306	+01:34:34.42	+23:38:36.30	0.124±0.005	0.98±0.06	1±16	10±50	3±12	4±9	0.244±0.005	0.108±0.003
193	307	+01:34:34.43	+23:38:36.39	···	1.25±0.07	4±10	30±30	···	7±7	···	0.137±0.004
194	308	+01:34:34.72	+23:38:40.73	0.201±0.008	2.37±0.14	10±6	91±18	20±5	5±9	0.221±0.004	0.118±0.003
195	309	+01:34:34.09	+23:38:31.36	0.75±0.03	1.8±0.1	43±3	379±9	212.4±1.5	37±3	0.560±0.011	0.315±0.009

Table C.4 Continued:

No.	MC ID	RA J2000	DEC J2000	Δv (km s^{-1})	R (pc)	$L_{^{13}CO(2-1)}$ K km s^{-1} pc^2	M_{lum} ($M_\odot$)	M_{vir} $M_\odot$)	Σ_{lum} $M_\odot$ pc^{-2}	α_{vir}	c
196	311	+01:34:34.77	+23:38:41.53	0.092±0.004	0.94±0.05	2±15	10±50	2±17	5±9	0.117±0.002	0.118±0.003
197	312	+01:34:34.58	+23:38:38.76	0.401±0.016	1.72±0.10	14±5	123±15	58±3	13±5	0.472±0.010	0.189±0.005
198	313	+01:34:34.72	+23:38:40.75	0.403±0.016	2.42±0.14	15±5	136±15	82±2	7±7	0.606±0.012	0.141±0.004
199	315	+01:34:34.64	+23:38:39.59	0.073±0.003	0.79±0.05	1±18	10±50	0±20	5±9	0.0879±0.0018	0.118±0.003
200	316	+01:34:34.62	+23:38:39.33	0.312±0.013	1.25±0.07	8±7	70±20	26±4	13±5	0.385±0.008	0.191±0.005
201	317	+01:34:34.78	+23:38:41.65	0.084±0.003	0.73±0.04	0±20	10±60	0±20	5±9	0.139±0.003	0.112±0.003
202	318	+01:34:34.06	+23:38:30.93	0.54±0.02	1.65±0.10	12±6	103±17	100±2	12±6	0.97±0.02	0.180±0.005
203	319	+01:34:34.66	+23:38:39.97	0.059±0.002	0.97±0.06	1±17	10±50	0±30	4±10	0.0599±0.0012	0.104±0.003
204	320	+01:34:34.66	+23:38:39.92	0.287±0.012	2.80±0.16	13±5	115±16	49±3	5±9	0.422±0.008	0.112±0.003
205	322	+01:34:34.49	+23:38:37.32	0.080±0.003	1.07±0.06	2±13	20±40	1±19	5±8	0.0732±0.0015	0.121±0.003
206	324	+01:34:34.76	+23:38:41.46	0.096±0.004	0.71±0.04	0±20	10±60	1±19	5±9	0.185±0.004	0.112±0.003
207	326	+01:34:34.63	+23:38:39.48	0.100±0.004	1.20±0.07	2±15	10±40	3±14	3±11	0.171±0.003	0.094±0.003
208	327	+01:34:34.71	+23:38:40.61	0.110±0.004	1.38±0.08	4±9	40±30	4±12	6±8	0.0931±0.0019	0.130±0.004
209	328	+01:34:34.46	+23:38:36.89	0.094±0.004	1.00±0.06	2±15	20±40	2±16	5±9	0.116±0.002	0.117±0.003
210	329	+01:34:34.64	+23:38:39.59	0.160±0.007	1.92±0.11	6±8	60±20	10±7	5±9	0.183±0.004	0.114±0.003

Table C.4 Continued:

No.	MC ID	RA J2000	DEC J2000	Δv (km s^{-1})	R (pc)	$L_{^{13}CO(2-1)}$ K km s^{-1} pc^2	M_{lum} ($M_\odot$)	M_{vir} $M_\odot$)	Σ_{lum} $M_\odot$ pc^{-2}	α_{vir}	c
211	330	+01:34:34.53	+23:38:37.94	$\cdots$	0.66±0.04	0±20	10±70	$\cdots$	4±10	$\cdots$	0.103±0.003
212	332	+01:34:34.64	+23:38:39.65	0.25±0.01	1.35±0.08	3±11	30±30	17±5	5±9	0.580±0.012	0.118±0.003
213	333	+01:34:34.64	+23:38:39.65	0.073±0.003	0.91±0.05	1±16	10±50	0±20	5±9	0.0790±0.0016	0.116±0.003
214	334	+01:34:34.65	+23:38:39.72	$\cdots$	0.82±0.05	0±20	10±60	$\cdots$	4±10	$\cdots$	0.105±0.003
215	335	+01:34:34.71	+23:38:40.66	0.173±0.007	1.40±0.08	3±11	30±30	9±8	4±9	0.325±0.007	0.109±0.003
216	336	+01:34:33.64	+23:38:24.63	0.084±0.003	0.67±0.04	0±20	10±60	0±20	6±8	0.120±0.002	0.125±0.003

Table C.5: ^{13}CO catalogs for clumps in GMC 16

No.	MC ID	RA	DEC	Δv	R	$L_{^{13}CO(2-1)}$	M_{lum}	M_{vir}	Σ_{lum}	α_{vir}	c
		J2000	J2000	(km s^{-1})	(pc)	K km s^{-1} pc^2	($M_\odot$)	$M_\odot$)	$M_\odot$ pc^{-2}		
1	0	+01:33:58.91	+23:29:43.66	$\cdots$	0.80±0.05	0±20	10±60	$\cdots$	4±10	$\cdots$	0.102±0.003
2	3	+01:34:00.16	+23:30:02.39	$\cdots$	0.56±0.03	0±30	0±90	$\cdots$	4±10	$\cdots$	0.104±0.003
3	5	+01:33:59.04	+23:29:45.63	0.436±0.018	2.01±0.12	40±3	351±9	80±2	28±4	0.228±0.005	0.273±0.008
4	7	+01:33:59.51	+23:29:52.66	0.438±0.018	1.86±0.11	8±7	70±20	75±3	7±7	1.01±0.02	0.136±0.004
5	8	+01:33:59.81	+23:29:57.20	0.161±0.007	0.83±0.05	2±15	10±50	0±10	6±8	0.321±0.006	0.132±0.004
6	9	+01:33:58.91	+23:29:43.70	$\cdots$	0.79±0.05	2±16	10±50	$\cdots$	7±7	$\cdots$	0.138±0.004
7	11	+01:33:58.94	+23:29:44.03	0.188±0.008	1.46±0.08	13±5	113±16	11±7	17±5	0.0962±0.0019	0.213±0.006
8	12	+01:33:59.03	+23:29:45.42	$\cdots$	0.74±0.04	1±16	10±50	$\cdots$	7±7	$\cdots$	0.142±0.004
9	13	+01:33:58.97	+23:29:44.49	$\cdots$	1.01±0.06	1±16	10±50	$\cdots$	4±10	$\cdots$	0.103±0.003
10	16	+01:33:59.46	+23:29:51.87	0.220±0.009	1.39±0.08	4±9	40±30	14±6	6±8	0.379±0.008	0.129±0.004
11	17	+01:33:58.93	+23:29:43.98	0.156±0.006	0.90±0.05	5±8	50±20	0±10	19±4	0.0954±0.0019	0.225±0.006
12	18	+01:33:58.98	+23:29:44.77	0.177±0.007	0.94±0.05	3±12	20±40	6±9	8±7	0.276±0.006	0.148±0.004
13	20	+01:33:58.95	+23:29:44.29	0.121±0.005	0.92±0.05	1±16	10±50	3±13	5±9	0.219±0.004	0.114±0.003
14	22	+01:33:59.33	+23:29:49.92	0.51±0.02	2.27±0.13	49±3	435±8	123±2	27±4	0.284±0.006	0.270±0.007
15	24	+01:33:58.77	+23:29:41.53	0.094±0.004	1.07±0.06	3±12	20±40	2±16	6±8	0.0899±0.0018	0.129±0.004

Table C.5 Continued:

No.	MC ID	RA	DEC	Δv	R	$L_{^{13}CO(2-1)}$	M_{lum}	M_{vir}	Σ_{lum}	α_{vir}	c
		J2000	J2000	(km s^{-1})	(pc)	K km s^{-1} pc^2	($M_{\odot}$)	$M_{\odot}$)	$M_{\odot}$ pc^{-2}		
16	25	+01:33:59.53	+23:29:52.96	···	1.37±0.08	2±13	20±40	···	3±11	···	0.094±0.003
17	26	+01:33:59.00	+23:29:45.06	0.462±0.019	1.85±0.11	28±4	245±11	83±2	23±4	0.339±0.007	0.248±0.007
18	27	+01:33:58.73	+23:29:40.89	···	1.09±0.06	2±15	20±40	···	4±10	···	0.106±0.003
19	28	+01:33:59.55	+23:29:53.29	0.55±0.02	1.36±0.08	5±9	50±30	88±2	8±7	1.95±0.04	0.145±0.004
20	29	+01:33:58.36	+23:29:35.34	0.084±0.003	1.45±0.08	2±12	20±40	2±15	3±11	0.098±0.002	0.094±0.003
21	35	+01:33:59.49	+23:29:52.35	0.375±0.015	2.01±0.12	8±7	70±20	59±3	6±8	0.829±0.017	0.123±0.003
22	36	+01:33:59.45	+23:29:51.77	0.413±0.017	1.48±0.09	16±5	137±15	53±3	20±4	0.389±0.008	0.231±0.006
23	40	+01:33:59.37	+23:29:50.54	0.381±0.016	1.41±0.08	21±4	185±13	43±3	30±4	0.233±0.005	0.283±0.008
24	42	+01:33:59.67	+23:29:55.02	0.141±0.006	1.31±0.08	2±13	20±40	5±9	4±10	0.265±0.005	0.102±0.003
25	43	+01:33:59.60	+23:29:54.00	0.153±0.006	1.61±0.09	5±9	40±30	8±8	5±8	0.187±0.004	0.119±0.003
26	44	+01:33:59.71	+23:29:55.62	0.152±0.006	1.68±0.10	3±11	30±30	8±8	3±11	0.293±0.006	0.092±0.003
27	45	+01:33:59.02	+23:29:45.28	0.184±0.007	1.16±0.07	4±9	40±30	8±8	9±7	0.219±0.004	0.155±0.004
28	47	+01:33:59.57	+23:29:53.53	0.421±0.017	2.55±0.15	26±4	227±11	95±2	11±6	0.419±0.008	0.173±0.005
29	49	+01:33:59.10	+23:29:46.53	0.204±0.008	1.44±0.08	6±8	50±20	13±6	8±7	0.236±0.005	0.149±0.004
30	51	+01:33:59.34	+23:29:50.05	0.113±0.005	0.99±0.06	2±13	20±40	3±14	6±8	0.139±0.003	0.130±0.004

Table C.5 Continued:

No.	MC ID	RA J2000	DEC J2000	Δv (km s^{-1})	R (pc)	$L_{^{13}CO(2-1)}$ K km s^{-1} pc^2	M_{lum} ($M_\odot$)	M_{vir} $M_\odot$)	Σ_{lum} $M_\odot$ pc^{-2}	α_{vir}	c
31	53	+01:33:59.66	+23:29:54.86	0.096±0.004	1.40±0.08	3±11	30±30	3±13	4±9	0.101±0.002	0.109±0.003
32	60	+01:33:59.27	+23:29:49.02	0.222±0.009	1.89±0.11	8±7	70±20	20±5	7±8	0.263±0.005	0.133±0.004
33	62	+01:33:59.01	+23:29:45.11	⋯	0.77±0.04	1±17	10±50	⋯	6±8	⋯	0.130±0.004
34	63	+01:33:59.49	+23:29:52.34	0.258±0.011	1.7±0.1	5±9	40±30	24±5	5±9	0.559±0.011	0.111±0.003
35	64	+01:33:59.17	+23:29:47.59	⋯	0.78±0.04	0±20	10±60	⋯	5±9	⋯	0.111±0.003
36	67	+01:33:59.43	+23:29:51.45	0.139±0.006	1.94±0.11	9±6	83±19	8±8	7±7	0.0959±0.0019	0.137±0.004
37	68	+01:33:59.62	+23:29:54.23	⋯	0.87±0.05	1±19	10±60	⋯	4±10	⋯	0.105±0.003
38	71	+01:33:59.32	+23:29:49.87	0.352±0.014	1.70±0.10	19±4	169±13	44±3	19±4	0.261±0.005	0.225±0.006
39	73	+01:33:59.53	+23:29:52.91	0.212±0.009	1.91±0.11	9±7	80±20	18±5	7±8	0.239±0.005	0.133±0.004
40	77	+01:33:59.03	+23:29:45.49	⋯	1.25±0.07	2±13	20±40	⋯	4±10	⋯	0.105±0.003
41	79	+01:33:59.06	+23:29:45.95	0.108±0.004	1.29±0.07	3±11	30±30	3±13	5±9	0.121±0.002	0.116±0.003
42	80	+01:33:59.49	+23:29:52.35	0.238±0.010	1.8±0.1	7±8	60±20	21±5	6±8	0.372±0.007	0.124±0.003
43	82	+01:33:58.99	+23:29:44.92	0.0427±0.0017	1.29±0.07	2±13	20±40	0±30	4±10	0.0239±0.0005	0.104±0.003
44	91	+01:33:58.41	+23:29:36.17	0.060±0.002	1.02±0.06	1±17	10±50	0±30	3±11	0.0687±0.0014	0.096±0.003
45	92	+01:33:59.15	+23:29:47.20	⋯	0.59±0.03	0±30	0±80	⋯	4±10	⋯	0.102±0.003

Table C.5 Continued:

No.	MC ID	RA J2000	DEC J2000	Δv (km s^{-1})	R (pc)	$L_{^{13}CO(2-1)}$ K km s^{-1} pc^2	M_{lum} ($M_\odot$)	M_{vir} $M_\odot$)	Σ_{lum} $M_\odot$ pc^{-2}	α_{vir}	c
46	93	+01:33:59.25	+23:29:48.69	0.265±0.011	1.55±0.09	8±7	70±20	23±5	9±6	0.332±0.007	0.157±0.004
47	99	+01:33:59.52	+23:29:52.78	0.078±0.003	1.40±0.08	0±10	30±30	2±17	5±8	0.0536±0.0011	0.121±0.003
48	100	+01:33:58.87	+23:29:42.99	0.084±0.003	0.79±0.05	1±18	10±50	0±20	6±8	0.107±0.002	0.122±0.003
49	102	+01:33:58.88	+23:29:43.19	0.072±0.003	0.89±0.05	3±12	20±40	0±20	9±6	0.0426±0.0009	0.157±0.004
50	105	+01:33:58.96	+23:29:44.38	0.348±0.014	0.94±0.05	12±6	109±17	24±5	39±3	0.220±0.004	0.326±0.009
51	106	+01:33:59.63	+23:29:54.46	0.071±0.003	0.84±0.05	1±18	10±50	0±20	5±9	0.0893±0.0018	0.111±0.003
52	107	+01:33:59.23	+23:29:48.39	0.50±0.02	1.82±0.11	42±3	366±9	95±2	35±3	0.261±0.005	0.308±0.009
53	108	+01:33:59.52	+23:29:52.79	···	0.79±0.05	1±18	10±50	···	5±9	···	0.118±0.003
54	109	+01:33:59.05	+23:29:45.80	···	0.69±0.04	0±20	10±60	···	5±8	···	0.120±0.003
55	110	+01:33:58.99	+23:29:44.87	···	0.68±0.04	2±14	20±40	···	12±6	···	0.179±0.005
56	112	+01:33:58.87	+23:29:43.07	0.105±0.004	0.86±0.05	3±11	30±30	2±16	11±6	0.0773±0.0016	0.172±0.005
57	113	+01:33:59.16	+23:29:47.44	0.240±0.010	1.66±0.10	17±5	148±14	20±5	17±5	0.136±0.003	0.215±0.006
58	114	+01:33:59.29	+23:29:49.34	0.146±0.006	0.73±0.04	3±12	30±30	3±12	15±5	0.131±0.003	0.201±0.006
59	115	+01:33:59.04	+23:29:45.56	0.416±0.017	1.82±0.11	7±7	60±20	66±3	6±8	1.07±0.02	0.127±0.004
60	117	+01:33:58.69	+23:29:40.42	0.175±0.007	1.59±0.09	7±7	60±20	10±7	8±7	0.161±0.003	0.147±0.004

Table C.5 Continued:

No.	MC ID	RA	DEC	Δv	R	$L_{^{13}CO(2-1)}$	M_{lum}	M_{vir}	Σ_{lum}	α_{vir}	c
		J2000	J2000	(km s^{-1})	(pc)	K km s^{-1} pc^2	($M_\odot$)	$M_\odot$)	$M_\odot$ pc^{-2}		
61	118	+01:33:59.08	+23:29:46.25	0.64±0.03	2.21±0.13	128.2±1.7	1128±5	188.3±1.6	73±2	0.167±0.003	0.445±0.012
62	119	+01:33:58.87	+23:29:43.10	0.163±0.007	1.05±0.06	3±11	30±30	6±9	8±7	0.220±0.004	0.144±0.004
63	120	+01:33:59.10	+23:29:46.46	0.166±0.007	1.30±0.08	3±11	30±30	7±8	6±8	0.250±0.005	0.123±0.003
64	122	+01:33:59.22	+23:29:48.35	0.365±0.015	1.51±0.09	7±7	60±20	42±3	9±7	0.670±0.013	0.154±0.004
65	123	+01:33:58.96	+23:29:44.36	0.100±0.004	0.59±0.03	2±13	20±40	0±20	18±5	0.0622±0.0013	0.221±0.006
66	124	+01:33:58.63	+23:29:39.52	0.99±0.04	1.13±0.07	106.9±1.9	941±6	230.7±1.5	236.4±1.3	0.245±0.005	0.80±0.02
67	125	+01:33:59.29	+23:29:49.35	0.200±0.008	0.96±0.06	5±9	50±30	8±8	16±5	0.179±0.004	0.205±0.006
68	126	+01:33:59.06	+23:29:45.85	0.071±0.003	1.15±0.07	2±15	20±40	0±20	0±10	0.0783±0.0016	0.100±0.003
69	127	+01:33:58.67	+23:29:40.09	···	0.83±0.05	0±20	10±60	···	4±10	···	0.105±0.003
70	129	+01:33:58.67	+23:29:40.06	0.262±0.011	1.57±0.09	11±6	97±18	23±5	12±6	0.234±0.005	0.183±0.005
71	130	+01:33:58.50	+23:29:37.45	0.140±0.006	1.63±0.09	5±9	40±30	7±9	5±9	0.160±0.003	0.116±0.003
72	132	+01:33:58.83	+23:29:42.40	0.186±0.008	1.00±0.06	3±12	20±30	7±8	8±7	0.297±0.006	0.145±0.004
73	133	+01:33:58.58	+23:29:38.66	0.52±0.02	1.7±0.1	19±4	171±13	97±2	18±5	0.571±0.011	0.221±0.006
74	134	+01:33:58.76	+23:29:41.35	0.394±0.016	2.70±0.16	26±4	229±11	88±2	10±6	0.385±0.008	0.164±0.005
75	136	+01:33:59.11	+23:29:46.72	0.456±0.019	2.12±0.12	21±4	183±13	93±2	13±5	0.50±0.01	0.187±0.005

Table C.5 Continued:

No.	MC ID	RA J2000	DEC J2000	Δv (km s^{-1})	R (pc)	$L_{^{13}CO(2-1)}$ K km s^{-1} pc^2	M_{lum} ($M_\odot$)	M_{vir} $M_\odot$)	Σ_{lum} $M_\odot$ pc^{-2}	α_{vir}	c
76	137	+01:33:59.30	+23:29:49.44	0.293±0.012	1.27±0.07	0±10	30±30	23±5	6±8	0.720±0.014	0.130±0.004
77	141	+01:33:58.62	+23:29:39.24	0.111±0.005	0.70±0.04	3±11	30±30	2±16	17±5	0.0710±0.0014	0.211±0.006
78	143	+01:33:59.03	+23:29:45.47	0.210±0.009	2.83±0.16	19±5	164±13	26±4	7±8	0.159±0.003	0.133±0.004
79	144	+01:33:59.22	+23:29:48.29	0.094±0.004	1.13±0.07	3±11	30±30	2±15	7±7	0.0727±0.0015	0.139±0.004
80	145	+01:33:59.15	+23:29:47.19	0.118±0.005	0.73±0.04	1±18	10±50	2±15	7±8	0.197±0.004	0.133±0.004
81	146	+01:33:58.56	+23:29:38.47	0.0429±0.0018	1.41±0.08	2±12	20±40	0±30	0±10	0.0251±0.0005	0.097±0.003
82	148	+01:33:58.48	+23:29:37.23	0.294±0.012	1.07±0.06	2±13	20±40	19±5	6±8	0.947±0.019	0.124±0.003
83	149	+01:33:59.52	+23:29:52.76	0.125±0.005	1.03±0.06	1±17	10±50	3±12	3±11	0.299±0.006	0.096±0.003
84	151	+01:33:58.74	+23:29:41.06	0.125±0.005	1.05±0.06	2±15	10±40	3±12	4±9	0.232±0.005	0.108±0.003
85	152	+01:33:58.60	+23:29:39.04	0.72±0.03	1.85±0.11	99±2	871±6	198.2±1.6	81±2	0.228±0.005	0.469±0.013
86	153	+01:33:58.64	+23:29:39.65	0.88±0.04	1.86±0.11	19±5	165±13	299.2±1.3	15±5	1.81±0.04	0.203±0.006
87	154	+01:33:58.81	+23:29:42.09	0.205±0.008	1.15±0.07	2±13	20±40	10±7	5±9	0.531±0.011	0.112±0.003
88	155	+01:33:58.73	+23:29:41.00	0.216±0.009	1.04±0.06	5±9	40±30	10±7	12±6	0.250±0.005	0.180±0.005
89	156	+01:33:59.05	+23:29:45.75	0.50±0.02	1.21±0.07	11±6	93±18	62±3	20±4	0.672±0.014	0.234±0.007
90	157	+01:33:59.14	+23:29:47.03	0.082±0.003	0.77±0.04	1±18	10±50	0±20	6±8	0.098±0.002	0.126±0.004

Table C.5 Continued:

No.	MC ID	RA J2000	DEC J2000	Δv (km s^{-1})	R (pc)	$L_{^{13}CO(2-1)}$ K km s^{-1} pc^2	M_{lum} ($M_\odot$)	M_{vir} $M_\odot$)	Σ_{lum} $M_\odot$ pc^{-2}	α_{vir}	c
91	160	+01:33:58.99	+23:29:44.90	0.55±0.02	2.32±0.13	46±3	409±9	147.7±1.8	24±4	0.361±0.007	0.256±0.007
92	161	+01:33:59.20	+23:29:47.98	0.384±0.016	2.03±0.12	15±5	134±15	63±3	10±6	0.469±0.009	0.167±0.005
93	163	+01:33:59.05	+23:29:45.70	0.097±0.004	0.89±0.05	3±11	30±30	2±17	11±6	0.0673±0.0014	0.169±0.005
94	166	+01:33:58.71	+23:29:40.58	0.209±0.009	1.66±0.10	16±5	139±15	15±6	16±5	0.109±0.002	0.209±0.006
95	167	+01:33:58.37	+23:29:35.48	···	0.47±0.03	0±30	0±100	···	4±10	···	0.106±0.003
96	168	+01:33:58.59	+23:29:38.81	0.169±0.007	0.81±0.05	4±10	40±30	0±10	18±5	0.134±0.003	0.218±0.006
97	170	+01:33:59.14	+23:29:47.04	···	0.78±0.05	0±20	10±60	···	4±9	···	0.107±0.003
98	171	+01:33:58.78	+23:29:41.72	0.091±0.004	1.01±0.06	3±12	30±30	2±17	8±7	0.0692±0.0014	0.147±0.004
99	172	+01:33:58.70	+23:29:40.56	0.134±0.005	1.8±0.1	7±7	60±20	7±8	6±8	0.108±0.002	0.129±0.004
100	173	+01:33:58.71	+23:29:40.58	0.49±0.02	1.14±0.07	22±4	193±12	57±3	48±3	0.295±0.006	0.359±0.010
101	176	+01:33:58.73	+23:29:40.93	0.163±0.007	1.14±0.07	3±11	30±30	6±9	7±7	0.213±0.004	0.141±0.004
102	178	+01:33:58.29	+23:29:34.37	0.25±0.01	1.47±0.09	10±6	89±18	19±5	13±5	0.216±0.004	0.188±0.005
103	180	+01:33:58.61	+23:29:39.09	0.151±0.006	0.96±0.06	7±8	60±20	0±10	20±4	0.0790±0.0016	0.234±0.006
104	182	+01:33:58.53	+23:29:37.93	···	0.77±0.04	1±18	10±50	···	6±8	···	0.124±0.003
105	183	+01:33:59.02	+23:29:45.34	0.308±0.013	3.21±0.19	33±3	290±10	64±3	9±7	0.223±0.004	0.155±0.004

Table C.5 Continued:

No.	MC ID	RA	DEC	Δv	R	$L_{^{13}CO(2-1)}$	M_{lum}	M_{vir}	Σ_{lum}	α_{vir}	c
		J2000	J2000	(km s^{-1})	(pc)	K km s^{-1} pc^2	($M_\odot$)	$M_\odot$)	$M_\odot$ pc^{-2}		
106	184	+01:33:58.94	+23:29:44.07	0.112±0.005	1.60±0.09	2±13	20±40	4±11	3±12	0.206±0.004	0.083±0.002
107	185	+01:33:58.51	+23:29:37.62	0.126±0.005	0.96±0.06	5±9	40±30	3±12	14±5	0.0783±0.0016	0.196±0.005
108	186	+01:33:58.28	+23:29:34.14	0.132±0.005	1.7±0.1	5±9	50±30	6±9	5±9	0.138±0.003	0.115±0.003
109	187	+01:33:58.57	+23:29:38.48	0.095±0.004	0.83±0.05	3±11	30±30	2±18	13±5	0.0542±0.0011	0.190±0.005
110	188	+01:33:58.52	+23:29:37.86	0.442±0.018	1.05±0.06	18±5	156±14	43±3	45±3	0.275±0.006	0.351±0.010
111	189	+01:33:58.89	+23:29:43.38	0.215±0.009	1.21±0.07	6±8	50±20	12±7	11±6	0.241±0.005	0.169±0.005
112	190	+01:33:58.60	+23:29:39.04	0.308±0.013	1.83±0.11	25±4	221±12	36±4	21±4	0.165±0.003	0.239±0.007
113	191	+01:33:58.72	+23:29:40.79	0.075±0.003	1.13±0.07	2±14	20±40	1±19	4±10	0.0827±0.0017	0.105±0.003
114	192	+01:33:58.60	+23:29:39.04	0.095±0.004	1.11±0.06	6±8	60±20	2±15	14±5	0.0380±0.0008	0.196±0.005
115	193	+01:33:58.61	+23:29:39.12	0.365±0.015	1.85±0.11	20±4	180±13	52±3	17±5	0.288±0.006	0.212±0.006
116	194	+01:33:58.28	+23:29:34.19	0.130±0.005	1.25±0.07	4±10	40±30	4±11	8±7	0.120±0.002	0.143±0.004
117	195	+01:33:58.54	+23:29:38.15	0.155±0.006	1.29±0.07	4±10	40±30	6±9	7±7	0.176±0.004	0.138±0.004
118	196	+01:33:58.21	+23:29:33.18	0.147±0.006	1.38±0.08	5±9	40±30	6±9	7±7	0.140±0.003	0.142±0.004
119	197	+01:33:58.53	+23:29:37.88	0.436±0.018	1.8±0.1	16±5	137±15	71±3	14±5	0.52±0.01	0.193±0.005
120	198	+01:33:58.91	+23:29:43.63	0.48±0.02	1.62±0.09	14±5	124±15	78±3	15±5	0.633±0.013	0.201±0.006

Table C.5 Continued:

No.	MC ID	RA J2000	DEC J2000	Δv (km s^{-1})	R (pc)	$L_{^{13}CO(2-1)}$ K km s^{-1} pc^2	M_{lum} ($M_\odot$)	M_{vir} $M_\odot$)	Σ_{lum} $M_\odot$ pc^{-2}	α_{vir}	c
121	200	+01:33:58.78	+23:29:41.75	0.360±0.015	1.47±0.08	14±5	123±16	40±4	18±5	0.324±0.007	0.222±0.006
122	202	+01:33:58.64	+23:29:39.63	0.25±0.01	0.50±0.03	5±9	40±30	6±9	58±3	0.142±0.003	0.395±0.011
123	203	+01:33:58.87	+23:29:43.01	···	0.79±0.05	1±19	10±60	···	5±9	···	0.111±0.003
124	204	+01:33:59.04	+23:29:45.59	0.299±0.012	1.39±0.08	7±7	70±20	26±4	11±6	0.396±0.008	0.172±0.005
125	205	+01:33:58.91	+23:29:43.63	0.092±0.004	0.76±0.04	0±20	10±60	1±19	4±9	0.176±0.004	0.107±0.003
126	206	+01:33:59.19	+23:29:47.87	0.0460±0.0019	0.78±0.04	0±20	10±70	0±40	0±10	0.0524±0.0011	0.097±0.003
127	207	+01:33:58.72	+23:29:40.75	0.55±0.02	1.67±0.10	44±3	388±9	106±2	44±3	0.272±0.005	0.346±0.010
128	208	+01:33:58.65	+23:29:39.68	···	1.06±0.06	3±11	30±30	···	8±7	···	0.147±0.004
129	209	+01:33:58.90	+23:29:43.57	0.130±0.005	1.12±0.06	3±11	30±30	4±11	8±7	0.132±0.003	0.144±0.004
130	210	+01:33:59.02	+23:29:45.28	0.097±0.004	1.00±0.06	3±11	30±30	2±16	9±6	0.0674±0.0014	0.158±0.004
131	211	+01:33:58.84	+23:29:42.57	0.136±0.006	1.01±0.06	3±11	30±30	4±11	8±7	0.149±0.003	0.149±0.004
132	212	+01:33:58.77	+23:29:41.49	0.055±0.002	1.14±0.07	2±14	20±40	0±30	4±9	0.0409±0.0008	0.108±0.003
133	214	+01:33:58.62	+23:29:39.31	0.236±0.010	1.8±0.1	16±5	142±14	21±5	14±5	0.146±0.003	0.198±0.006
134	215	+01:33:58.88	+23:29:43.24	0.52±0.02	2.16±0.12	23±4	201±12	121±2	14±5	0.598±0.012	0.193±0.005
135	217	+01:33:59.04	+23:29:45.63	0.264±0.011	1.72±0.10	8±7	70±20	25±4	8±7	0.336±0.007	0.147±0.004

Table C.5 Continued:

No.	MC ID	RA	DEC	Δv	R	$L_{^{13}CO(2-1)}$	M_{lum}	M_{vir}	Σ_{lum}	α_{vir}	c
		J2000	J2000	(km s^{-1})	(pc)	K km s^{-1} pc^2	($M_\odot$)	$M_\odot$)	$M_\odot$ pc^{-2}		
136	218	+01:33:58.86	+23:29:42.93	0.0332±0.0014	1.03±0.06	1±16	10±50	0±50	4±10	0.0188±0.0004	0.101±0.003
137	219	+01:33:58.79	+23:29:41.85	· · ·	0.79±0.05	2±15	10±50	· · ·	7±7	· · ·	0.139±0.004
138	220	+01:33:58.78	+23:29:41.71	0.302±0.012	2.93±0.17	14±5	120±16	56±3	4±9	0.469±0.009	0.110±0.003
139	221	+01:33:58.69	+23:29:40.36	0.095±0.004	0.99±0.06	2±14	20±40	2±16	5±8	0.115±0.002	0.120±0.003
140	224	+01:33:58.89	+23:29:43.39	0.357±0.015	1.69±0.10	18±5	157±14	45±3	17±5	0.288±0.006	0.217±0.006
141	225	+01:33:59.11	+23:29:46.69	0.071±0.003	1.25±0.07	2±14	20±40	1±19	4±10	0.0711±0.0014	0.101±0.003
142	226	+01:33:58.23	+23:29:33.38	· · ·	0.99±0.06	1±16	10±50	· · ·	4±10	· · ·	0.105±0.003
143	227	+01:33:58.98	+23:29:44.66	0.48±0.02	2.22±0.13	24±4	215±12	109±2	14±5	0.50±0.01	0.194±0.005
144	228	+01:33:58.89	+23:29:43.30	0.098±0.004	1.01±0.06	4±10	40±30	2±16	12±6	0.0557±0.0011	0.177±0.005
145	230	+01:33:58.74	+23:29:41.16	0.52±0.02	2.78±0.16	17±5	149±14	156.3±1.8	6±8	1.05±0.02	0.129±0.004
146	231	+01:33:58.80	+23:29:42.07	0.275±0.011	1.55±0.09	8±7	70±20	25±4	10±6	0.344±0.007	0.160±0.004
147	232	+01:33:59.10	+23:29:46.48	0.25±0.01	1.07±0.06	5±9	40±30	14±6	11±6	0.332±0.007	0.175±0.005
148	233	+01:33:58.95	+23:29:44.22	0.149±0.006	1.8±0.1	8±7	70±20	8±8	7±7	0.116±0.002	0.139±0.004
149	234	+01:33:58.78	+23:29:41.76	0.177±0.007	1.27±0.07	0±10	30±30	8±8	6±8	0.264±0.005	0.130±0.004
150	235	+01:33:59.68	+23:29:55.26	0.172±0.007	1.30±0.08	3±11	30±30	8±8	6±8	0.264±0.005	0.125±0.003

Table C.5 Continued:

No.	MC ID	RA	DEC	Δv	R	$L_{^{13}CO(2-1)}$	M_{lum}	M_{vir}	Σ_{lum}	α_{vir}	c
		J2000	J2000	(km s^{-1})	(pc)	K km s^{-1} pc^2	($M_\odot$)	$M_\odot$)	$M_\odot$ pc^{-2}		
151	236	+01:33:59.10	+23:29:46.53	0.080±0.003	1.01±0.06	2±14	20±40	1±19	5±8	0.0796±0.0016	0.121±0.003
152	237	+01:33:59.01	+23:29:45.21	0.330±0.013	1.30±0.08	5±8	50±30	30±4	9±7	0.632±0.013	0.155±0.004
153	238	+01:34:00.07	+23:30:01.02	0.060±0.002	0.71±0.04	0±20	10±60	0±30	4±9	0.0775±0.0016	0.110±0.003

Table C.6: ^{13}CO catalogs for clumps in GMC 8

No.	MC ID	RA	DEC	Δv	R	$L_{^{13}CO(2-1)}$	M_{lum}	M_{vir}	Σ_{lum}	α_{vir}	c
		J2000	J2000	(km s^{-1})	(pc)	K km s^{-1} pc^2	($M_\odot$)	$M_\odot$)	$M_\odot$ pc^{-2}		
1	0	+01:34:08.45	+23:32:06.75	0.097±0.004	0.76±0.04	0±20	10±60	2±18	4±10	0.215±0.004	0.102±0.003
2	1	+01:34:10.50	+23:32:37.43	0.0365±0.0015	1.05±0.06	1±17	10±50	0±40	3±11	0.0263±0.0005	0.093±0.003
3	2	+01:34:09.41	+23:32:21.20	···	0.65±0.04	0±30	10±80	···	4±10	···	0.103±0.003
4	3	+01:34:08.17	+23:32:02.58	0.129±0.005	0.99±0.06	3±12	20±40	3±12	8±7	0.147±0.003	0.144±0.004
5	4	+01:34:09.32	+23:32:19.76	0.133±0.005	0.77±0.04	2±15	10±50	3±13	8±7	0.201±0.004	0.143±0.004
6	5	+01:34:10.16	+23:32:32.40	0.0412±0.0017	0.76±0.04	0±20	10±60	0±40	4±9	0.0347±0.0007	0.108±0.003
7	6	+01:34:08.03	+23:32:00.38	0.0297±0.0012	1.18±0.07	2±14	20±40	0±50	0±10	0.0135±0.0003	0.100±0.003
8	7	+01:34:10.16	+23:32:32.42	0.087±0.004	1.21±0.07	2±13	20±40	2±16	4±10	0.100±0.002	0.106±0.003
9	9	+01:34:10.17	+23:32:32.62	0.257±0.011	1.42±0.08	5±8	50±20	20±5	8±7	0.413±0.008	0.143±0.004
10	10	+01:34:09.84	+23:32:27.59	0.099±0.004	1.20±0.07	2±15	20±40	2±14	0±10	0.159±0.003	0.096±0.003
11	11	+01:34:08.53	+23:32:07.94	···	0.48±0.03	0±30	0±100	···	4±9	···	0.107±0.003
12	12	+01:34:09.56	+23:32:23.47	···	0.98±0.06	1±17	10±50	···	4±10	···	0.103±0.003
13	13	+01:34:09.58	+23:32:23.73	···	0.78±0.04	0±20	10±70	···	3±11	···	0.096±0.003
14	14	+01:34:09.03	+23:32:15.51	0.118±0.005	1.36±0.08	0±10	30±30	4±11	5±8	0.128±0.003	0.120±0.003
15	15	+01:34:10.32	+23:32:34.77	0.090±0.004	0.81±0.05	1±17	10±50	1±19	6±8	0.119±0.002	0.124±0.003

Table C.6 Continued:

No.	MC ID	RA	DEC	Δv	R	$L_{^{13}CO(2-1)}$	M_{lum}	M_{vir}	Σ_{lum}	α_{vir}	c
		J2000	J2000	(km s^{-1})	(pc)	K km s^{-1} pc^2	(M$_\odot$)	M$_\odot$)	M$_\odot$ pc^{-2}		
16	16	+01:34:10.36	+23:32:35.40	0.096±0.004	1.22±0.07	2±15	20±40	2±14	3±11	0.156±0.003	0.094±0.003
17	17	+01:34:09.35	+23:32:20.29	0.55±0.02	1.61±0.09	19±5	163±13	102±2	20±4	0.625±0.013	0.233±0.006
18	18	+01:34:09.65	+23:32:24.80	0.094±0.004	0.79±0.05	1±16	10±50	1±18	6±8	0.115±0.002	0.132±0.004
19	19	+01:34:09.22	+23:32:18.35	···	0.54±0.03	0±30	0±90	···	4±10	···	0.102±0.003
20	20	+01:34:09.33	+23:32:19.93	0.54±0.02	1.99±0.12	17±5	149±14	121±2	12±6	0.813±0.016	0.180±0.005
21	21	+01:34:08.93	+23:32:13.92	0.074±0.003	0.99±0.06	1±17	10±50	0±20	0±10	0.102±0.002	0.100±0.003
22	22	+01:34:10.20	+23:32:33.02	···	0.65±0.04	0±30	10±70	···	4±10	···	0.105±0.003
23	23	+01:34:09.44	+23:32:21.55	0.083±0.003	0.77±0.04	0±20	10±70	0±20	0±10	0.168±0.003	0.098±0.003
24	25	+01:34:09.89	+23:32:28.36	0.72±0.03	2.29±0.13	86±2	761±6	247.9±1.4	46±3	0.326±0.007	0.353±0.010
25	27	+01:34:09.78	+23:32:26.64	0.473±0.019	2.22±0.13	12±6	106±17	104±2	7±7	0.98±0.02	0.136±0.004
26	29	+01:34:09.50	+23:32:22.50	0.198±0.008	1.61±0.09	0±10	30±30	13±6	4±10	0.392±0.008	0.106±0.003
27	30	+01:34:09.01	+23:32:15.13	0.107±0.004	0.77±0.04	1±19	10±60	2±16	5±9	0.205±0.004	0.114±0.003
28	31	+01:34:09.69	+23:32:25.30	0.77±0.03	3.22±0.19	54±3	476±8	400.1±1.1	15±5	0.841±0.017	0.199±0.006
29	33	+01:34:10.22	+23:32:33.30	0.317±0.013	1.09±0.06	0±10	30±30	23±5	8±7	0.754±0.015	0.149±0.004
30	34	+01:34:10.14	+23:32:32.03	0.099±0.004	1.20±0.07	2±14	20±40	2±14	4±10	0.135±0.003	0.104±0.003

Table C.6 Continued:

No.	MC ID	RA	DEC	Δv	R	$L_{^{13}CO(2-1)}$	M_{lum}	M_{vir}	Σ_{lum}	α_{vir}	c
		J2000	J2000	(km s^{-1})	(pc)	K km s^{-1} pc^2	($M_\odot$)	$M_\odot$)	$M_\odot$ pc^{-2}		
31	35	+01:34:08.96	+23:32:14.43	0.141±0.006	1.24±0.07	0±10	30±30	5±10	7±8	0.164±0.003	0.133±0.004
32	36	+01:34:10.04	+23:32:30.66	0.390±0.016	1.98±0.11	23±4	201±12	63±3	16±5	0.314±0.006	0.210±0.006
33	37	+01:34:10.09	+23:32:31.32	0.271±0.011	0.81±0.05	0±10	30±30	12±6	15±5	0.402±0.008	0.201±0.006
34	38	+01:34:09.80	+23:32:27.00	0.138±0.006	1.08±0.06	2±14	20±40	4±11	5±9	0.239±0.005	0.115±0.003
35	39	+01:34:10.20	+23:32:32.99	0.272±0.011	2.08±0.12	8±7	70±20	32±4	5±9	0.462±0.009	0.118±0.003
36	40	+01:34:09.79	+23:32:26.84	0.080±0.003	0.47±0.03	0±30	0±90	0±30	6±8	0.157±0.003	0.126±0.003
37	41	+01:34:09.61	+23:32:24.14	0.208±0.008	1.53±0.09	5±9	40±30	14±6	5±8	0.352±0.007	0.121±0.003
38	42	+01:34:08.95	+23:32:14.32	0.383±0.016	1.43±0.08	7±8	60±20	44±3	9±6	0.747±0.015	0.157±0.004
39	44	+01:34:09.59	+23:32:23.91	0.64±0.03	1.98±0.11	20±4	179±13	172.6±1.7	14±5	0.964±0.019	0.198±0.006
40	45	+01:34:09.54	+23:32:23.17	0.96±0.04	2.27±0.13	26±4	229±11	439.9±1.1	14±5	1.92±0.04	0.196±0.005
41	46	+01:34:10.49	+23:32:37.36	0.134±0.005	1.00±0.06	3±12	20±40	4±11	7±7	0.165±0.003	0.140±0.004
42	47	+01:34:08.97	+23:32:14.56	0.188±0.008	1.15±0.07	3±11	30±30	9±8	7±7	0.288±0.006	0.139±0.004
43	48	+01:34:09.02	+23:32:15.30	0.229±0.009	1.72±0.10	5±9	40±30	19±5	5±9	0.431±0.009	0.113±0.003
44	49	+01:34:08.26	+23:32:03.84	0.441±0.018	1.82±0.11	11±6	96±18	74±3	9±6	0.773±0.016	0.158±0.004
45	50	+01:34:10.03	+23:32:30.40	0.131±0.005	0.80±0.05	2±15	20±40	3±13	8±7	0.188±0.004	0.144±0.004

Table C.6 Continued:

No.	MC ID	RA	DEC	Δv	R	$L_{^{13}CO(2-1)}$	M_{lum}	M_{vir}	Σ_{lum}	α_{vir}	c
		J2000	J2000	(km s^{-1})	(pc)	K km s^{-1} pc^2	($M_\odot$)	$M_\odot$)	$M_\odot$ pc^{-2}		
46	51	+01:34:10.17	+23:32:32.55	0.275±0.011	2.12±0.12	7±7	60±20	34±4	4±9	0.535±0.011	0.110±0.003
47	52	+01:34:09.01	+23:32:15.20	0.363±0.015	2.40±0.14	16±5	138±15	67±3	8±7	0.484±0.010	0.143±0.004
48	53	+01:34:09.57	+23:32:23.55	0.268±0.011	1.95±0.11	16±5	138±15	29±4	12±6	0.213±0.004	0.177±0.005
49	54	+01:34:09.13	+23:32:17.02	0.71±0.03	2.58±0.15	28±4	242±11	270.4±1.4	12±6	1.12±0.02	0.177±0.005
50	56	+01:34:10.10	+23:32:31.46	0.298±0.012	1.55±0.09	6±8	50±20	29±4	7±7	0.571±0.011	0.135±0.004
51	57	+01:34:09.68	+23:32:25.19	0.0375±0.0015	0.87±0.05	1±19	10±60	0±40	4±10	0.0263±0.0005	0.106±0.003
52	58	+01:34:09.22	+23:32:18.29	0.422±0.017	2.29±0.13	12±6	104±17	85±2	6±8	0.823±0.017	0.131±0.004
53	59	+01:34:09.02	+23:32:15.29	0.316±0.013	2.37±0.14	14±5	120±16	50±3	7±7	0.415±0.008	0.135±0.004
54	60	+01:34:09.03	+23:32:15.38	0.232±0.009	1.41±0.08	5±9	40±30	16±6	7±8	0.384±0.008	0.134±0.004
55	61	+01:34:08.12	+23:32:01.81	0.091±0.004	1.05±0.06	2±15	20±40	2±16	5±9	0.117±0.002	0.111±0.003
56	62	+01:34:09.52	+23:32:22.84	0.086±0.004	0.85±0.05	1±19	10±60	1±19	4±10	0.143±0.003	0.105±0.003
57	63	+01:34:09.98	+23:32:29.73	0.094±0.004	0.77±0.04	1±18	10±50	1±19	5±8	0.139±0.003	0.122±0.003
58	64	+01:34:10.39	+23:32:35.90	0.069±0.003	0.48±0.03	0±30	0±100	0±30	4±9	0.152±0.003	0.109±0.003
59	65	+01:34:09.94	+23:32:29.05	···	1.7±0.1	3±12	20±40	···	2±13	···	0.081±0.002
60	66	+01:34:08.16	+23:32:02.33	0.213±0.009	0.81±0.05	2±14	20±40	8±8	8±7	0.442±0.009	0.151±0.004

Table C.6 Continued:

No.	MC ID	RA J2000	DEC J2000	Δv (km s^{-1})	R (pc)	$L_{^{13}CO(2-1)}$ K km s^{-1} pc^2	M_{lum} (M$_\odot$)	M_{vir} M$_\odot$)	Σ_{lum} M$_\odot$ pc^{-2}	α_{vir}	c
61	67	+01:34:08.13	+23:32:01.90	···	0.77±0.04	0±20	10±70	···	3±11	···	0.095±0.003
62	68	+01:34:09.62	+23:32:24.26	···	0.73±0.04	0±20	10±60	···	4±9	···	0.109±0.003
63	69	+01:34:10.50	+23:32:37.51	0.096±0.004	0.74±0.04	1±19	10±60	1±19	5±8	0.154±0.003	0.120±0.003
64	70	+01:34:08.97	+23:32:14.58	0.76±0.03	2.27±0.13	35±3	304±10	275.1±1.3	19±4	0.905±0.018	0.226±0.006
65	71	+01:34:09.14	+23:32:17.11	0.59±0.02	2.07±0.12	27±4	242±11	149.3±1.8	18±5	0.617±0.012	0.220±0.006
66	72	+01:34:08.50	+23:32:07.44	0.298±0.012	1.24±0.07	4±10	40±30	23±5	7±7	0.639±0.013	0.142±0.004
67	73	+01:34:09.32	+23:32:19.74	···	0.75±0.04	0±20	10±60	···	4±9	···	0.108±0.003
68	74	+01:34:10.38	+23:32:35.69	···	0.95±0.06	1±19	10±60	···	0±10	···	0.096±0.003
69	75	+01:34:09.94	+23:32:29.09	···	0.72±0.04	0±20	10±70	···	4±9	···	0.107±0.003
70	76	+01:34:08.37	+23:32:05.52	0.315±0.013	1.41±0.08	7±7	60±20	29±4	10±6	0.457±0.009	0.167±0.005
71	77	+01:34:09.48	+23:32:22.15	···	1.00±0.06	1±17	10±50	···	4±10	···	0.101±0.003
72	78	+01:34:10.19	+23:32:32.81	0.064±0.003	0.68±0.04	0±20	10±60	0±30	5±9	0.0789±0.0016	0.117±0.003
73	79	+01:34:09.02	+23:32:15.31	0.473±0.019	1.95±0.11	11±6	97±17	92±2	8±7	0.943±0.019	0.148±0.004
74	81	+01:34:09.42	+23:32:21.35	0.100±0.004	0.81±0.05	2±14	20±40	2±17	8±7	0.098±0.002	0.150±0.004
75	82	+01:34:09.01	+23:32:15.21	···	0.65±0.04	0±30	0±80	···	3±11	···	0.096±0.003

Table C.6 Continued:

No.	MC ID	RA	DEC	Δv	R	$L_{^{13}CO(2-1)}$	M_{lum}	M_{vir}	Σ_{lum}	α_{vir}	c
		J2000	J2000	(km s^{-1})	(pc)	K km s^{-1} pc^2	($M_\odot$)	$M_\odot$)	$M_\odot$ pc^{-2}		
76	83	+01:34:09.07	+23:32:16.11	···	0.72±0.04	0±20	10±70	···	0±10	···	0.097±0.003
77	84	+01:34:10.44	+23:32:36.61	0.092±0.004	1.07±0.06	3±12	20±40	2±16	6±8	0.0834±0.0017	0.131±0.004
78	85	+01:34:08.84	+23:32:12.53	···	0.70±0.04	0±20	10±70	···	4±9	···	0.106±0.003
79	86	+01:34:08.42	+23:32:06.25	0.081±0.003	0.88±0.05	1±18	10±50	0±20	5±9	0.110±0.002	0.111±0.003
80	87	+01:34:09.35	+23:32:20.29	0.103±0.004	1.38±0.08	0±10	30±30	3±13	5±8	0.0968±0.0019	0.120±0.003
81	88	+01:34:10.35	+23:32:35.30	0.111±0.005	1.06±0.06	2±14	20±40	3±13	5±9	0.150±0.003	0.118±0.003
82	89	+01:34:08.53	+23:32:07.90	···	0.73±0.04	0±20	10±70	···	4±10	···	0.102±0.003
83	90	+01:34:09.07	+23:32:16.03	0.084±0.003	0.83±0.05	1±18	10±50	0±20	5±9	0.120±0.002	0.113±0.003
84	91	+01:34:09.65	+23:32:24.79	···	0.77±0.04	0±20	10±60	···	4±9	···	0.108±0.003
85	92	+01:34:09.77	+23:32:26.48	0.132±0.005	1.44±0.08	4±10	40±30	5±10	5±8	0.148±0.003	0.121±0.003
86	93	+01:34:09.10	+23:32:16.51	0.126±0.005	1.25±0.07	2±13	20±40	4±11	4±9	0.198±0.004	0.108±0.003
87	94	+01:34:10.44	+23:32:36.66	0.099±0.004	0.64±0.04	1±19	10±60	1±19	7±7	0.139±0.003	0.141±0.004
88	95	+01:34:08.37	+23:32:05.56	···	0.70±0.04	0±20	10±70	···	4±10	···	0.103±0.003

Appendix D

ALMA ^{13}CO(J = 1–0) observations of NGC 604 in M33: physical properties of molecular clouds

Monthly Notices of the ROYAL ASTRONOMICAL SOCIETY

MNRAS **504,** 4511–4521 (2021)
Advance Access publication 2021 May 4

doi:10.1093/mnras/stab1251

ALMA ^{13}CO(J = 1–0) observations of NGC 604 in M33: physical properties of molecular clouds

S. P. Phiri,[1★] J. M. Kirk,[1★] D. Ward-Thompson,[1★] A. E. Sansom[1] and G. J. Bendo[2]

[1]*Jeremiah Horrocks Institute, School of Natural Sciences, University of Central Lancashire, Preston, Lancashire PR1 2HE, UK*
[2]*UK ALMA Regional Centre Node, Jodrell Bank Centre for Astrophysics, Department of Physics and Astronomy, The University of Manchester, Oxford Road, Manchester M13 9PL, UK*

Accepted 2021 April 19. Received 2021 March 26; in original form 2020 October 8

ABSTRACT

We present Atacama Large Millimeter/submillimeter Array (ALMA) observations of ^{13}CO(J = 1–0) line and 104 GHz continuum emission from NGC 604, a giant H II region (GHR) in the nearby spiral galaxy M33. Our high spatial resolution images (3.2 arcsec × 2.4 arcsec, corresponding to 13 × 10 pc physical scale) allow us to detect 15 molecular clouds. We find spatial offsets between the ^{13}CO and 104 GHz continuum emission and also detect continuum emission near the centre of the GHR. The identified molecular clouds have sizes ranging from 5–21 pc, linewidths of 0.3–3.0 km s^{-1} and luminosity-derived masses of (0.4–80.5) × 10^3 M$_\odot$. These molecular clouds are in near virial equilibrium, with a spearman correlation coefficient of 0.98. The linewidth–size relationship for these clouds is offset from the corresponding relations for the Milky Way and for NGC 300, although this may be an artefact of the dendrogram process.

Key words: ISM: clouds – ISM: individual objects (NGC 604) – galaxies: individual (M33) – molecules: ISM.

1 INTRODUCTION

Star formation occurs within cold, dense Giant Molecular Clouds (GMCs) embedded within the interstellar medium (ISM). GMCs show turbulent internal motions and are predominantly comprised of molecular hydrogen. Observations of GMCs within our own Galaxy have shown they have spatial scales of up to a hundred parsec, large-scale velocity dispersions which are supersonic, and masses up to 10^6 solar masses (Heyer & Dame 2015). Three key empirical GMC scaling relations, which have become officially accepted diagnostics for the physical conditions and structure, were first identified by Larson (1981). Later studies by other authors (e.g. Solomon et al. 1987; Rice et al. 2016, and references therein) have demonstrated the ubiquity of these scaling relations, commonly called Larson's relations, for Milky Way clouds. The first scaling relation is the size–linewidth relation, where the velocity line width of giant molecular clouds is proportional to the 0.5 power of the size, $\Delta v \propto R^{0.5}$. The second relation deals with GMC's virial equilibrium, where gravitational potential energy and kinetic energy are in approximate equilibrium (Larson 1981; Solomon et al. 1987; Heyer et al. 2009; Heyer & Dame 2015). This equilibrium manifests as a direct correlation between the masses estimated from related methods, e.g. the virial mass (M_vir) and the luminous mass (e.g. from ^{13}CO in our case). A final implication of the Larson scaling relationships is that the surface density of molecular is approximately constant (e.g. $\Sigma \propto M/R^2 \propto \rho R$). This proceeds from the third law which showed that $\rho \propto 1/R$ where R is an estimate of its physical size of the cloud and ρ is its mass volume density (Larson 1981). This clear universality in cloud structure was verified in other Galactic studies (Solomon et al. 1987; Heyer et al. 2009). Some extragalactic studies have also found correlations between GMC size and mass (Bolatto et al. 2008; Hughes et al. 2010). However, Faesi, Lada & Forbrich (2018) note that these extragalactic observations have low sensitivities, with the majority of pixels in GMCs near the sensitivity threshold, so the correlations may or may not be physically meaningful.

In as much as Milky Way GMCs have been the foundation of GMC studies, observations of these sources are affected by a number of challenging phenomena, mainly the blending of emission from multiple clouds along the line of sight. External galaxies offer an opportunity to study GMCs and star formation in different environments, including different metallicities and different galaxy types, and to make comparisons with our own Galaxy. With the emergence of modern (sub)millimeter interferometers and large single-dish telescopes, it has become possible to resolve individual GMCs in nearby galaxies (Schruba et al. 2017).

GMCs are traced by emission from the low rotational (J) states of the CO molecules, which are excited via collisions at temperatures ranging from 5 to 20 K (van Dishoeck & Black 1988). A number of high-resolution CO observations have been done in external galaxies, including M33 (Engargiola et al. 2003; Rosolowsky et al. 2003, 2007; Gratier et al. 2012) and NGC 300 (Faesi et al. 2018). More recently, the Physics at High Angular resolution in Nearby GalaxieS project has mapped CO(2–1) emission from multiple galaxies, resolving the molecular gas reservoir into individual GMCs across the full disc (Schinnerer et al. 2019).

M33 is a flocculent spiral galaxy in the Local Group. It is metal poor but gas rich and has a metallicity of $12 + \log(\frac{O}{H}) = 8.36 \pm 0.04$ (Rosolowsky & Simon 2008). It is at a distance of 840 kpc (Freedman,

★ E-mail: spphiri@uclan.ac.uk (SPP); jmkirk@uclan.ac.uk (JMK); DWard-Thompson@uclan.ac.uk (DW-T)

Wilson & Madore 1991; Kam et al. 2015) and an inclination of 56° (Kam et al. 2015), which allows us to resolve gas components with minimum contamination along the line of sight and to map their inner structure of GMCs. Earlier studies of GMCs in this galaxy include those by Wilson, Walker & Thornley (1997), Rosolowsky et al. (2007), Tosaki et al. (2007), Miura et al. (2010), Gratier et al. (2010, 2012), and Tabatabaei et al. (2014).

The giant H II region (GHR) NGC 604 is located in the northern arm of M33. This region has attracted interest because it has the highest star formation rate in the entire galaxy (Miura et al. 2012). The GHR has been observed in radio emission (Viallefond et al. 1992; Wilson & Scoville 1992; Churchwell & Goss 1999; Tosaki et al. 2007; Miura et al. 2010), optical emission (Drissen, Moffat & Shara 1993) and X-ray emission (Tüllmann et al. 2008). Based on these previous studies, the H α nebula has a core–halo structure extending out to 200–400 pc. It contains more than 200 O-type stars that are surrounded by photoionized filaments and shells (Relaño & Kennicutt 2009).

Faesi et al. (2018) note that determining true physical signatures in extragalactic studies is made difficult due to the wide range of source finding techniques and deferring observational characteristics (angular, spectral, and sensitivity) used. Hence, new analysis techniques are needed to overcome these problems and to understand the universality of Larson's relations.

In this work, we present a dendrogram analysis of ALMA observations of ^{13}CO(J = 1–0) and 104 GHz continuum emission from NGC 604. These observations have better resolutions and sensitivities compared to prior observations, which helps to overcome many of the issues highlighted by Faesi et al. (2018). We look at whether the ^{13}CO emission from NGC 604 obey Larson's relations in the same way as the ^{12}CO emission from the same region as presented by Wilson & Scoville (1992, hereafter WS92). Using these new data, we measure the properties of the clouds and examine the state of the star formation in the region, and we compare to results presented earlier by Miura et al. (2010). We present the observations and data reduction process in Section 2, the structure decomposition analysis and measurements of the cloud properties in Section 3, and the results in Section 4. We discuss our results in Section 5 and summarize our results in Section 6.

2 OBSERVATIONS AND DATA REDUCTION

We use archival ALMA Band 3 observations of the ^{13}CO(J = 1–0) (110.27 GHz) line emission from NGC 604 obtained during Cycle 2 (project code 2013.1.00639.S; PI: T. Tosaki). The target was observed with the ALMA 12-m array on 18 January 2015 for a total of 60 min on-source. ALMA was in configuration C34-2/1 with 34 antennas (although two are flagged as unusable) arranged with baselines ranging from 15 to 349 m, which yields a minimum beam angular resolution of 2.2 arcsec and a maximum recoverable scale of 29 arcsec (at 110.27 GHz). This corresponds to physical scales of 9–116 pc at the distance of 840 kpc to M33. The observed field of view is 43 arcsec. J2258−2758 was used as a bandpass calibrator, Mars as a flux calibrator and J0237+2848 as a phase calibrator.

Four spectral windows were used in the observations. Three of the spectral windows cover the ^{13}CO (J = 1–0) at 110.2 GHz, C^{18}CO(J = 1–0) at 109.8 GHz and CH3OH at 96.7 GHz lines; each of these spectral windows contained 180 channels with widths of 244.14 kHz, covering a bandwidth of 117.2 MHz. The fourth spectral window covered continuum emission from 98.56 to 99.50 GHz using 3840 channels with widths of 244.14 kHz (∼ 0.664 km s^{-1}). Only the ^{13}CO (J = 1–0) and continuum emission are detected in this data.

The Common Astronomy Software Application package (CASA; McMullin et al. 2007) version 5.6.1 was used to process the data. We first performed the standard pipeline calibration on the visibility data and then produced line cubes and continuum images using TCLEAN. We set the pixel scale for both the continuum and line images to 0.36 arcsec. The channel width for the ^{13}CO image was set to 0.664 km s^{-1}. We used Briggs weighting with the robust parameter set to 0.5 to improve the angular resolution of the final images without severely compromising the image sensitivity. The synthesized beam sizes are 3.2 × 2.4 arcsec for the line data and 3.9 × 2.8 arcsec for the continuum data. The achieved rms sensitivity in the line data is 2.6 mJy beam^{-1} and continuum is 0.04 mJy beam^{-1}. The calibration uncertainty is expected to be 5 per cent (Braatz, Impellizzeri & Biggs 2020).

The ^{13}CO(J = 1–0) integrated intensity map and the 104 GHz continuum map are shown in Fig. 1. As an additional visualization aid, the ^{13}CO(J = 1–0) emission is overlaid as contours on the continuum image in Fig. 2.

The 104-GHz continuum emission detected in NGC 604 (as shown in the bottom right panel of Fig. 1) is believed to be dominated by free–free emission [as indicated by the spectral energy distribution analyses of other galaxies by Peel et al. (2011) and Bendo et al. (2015, 2016)] that originates from OB stars within NGC 604. We find spatial offsets between ^{13}CO line and 104-GHz continuum emission as shown in Fig. 2. See Section 5 for more details on their distribution.

3 STRUCTURE DECOMPOSITION AND CLOUD PROPERTIES

To identify structures within the ^{13}CO(J = 1–0) image cube, we used the ASTRODENDRO package, which decomposes emission into a hierarchy of nested structures (Rosolowsky et al. 2008; Colombo et al. 2015). This dendrogram technique provides a precise representation of the topology of star-forming complexes. Parameters were chosen so that the algorithm could identify local maxima in the cube above the 4$\sigma_{\rm rms}$ level that were also 3$\sigma_{\rm rms}$ above the merge level with adjacent structures. Isorsurfaces surrounding the local maxima were categorized as trunks, branches, or leaves based on whether they were the largest contiguous structures (trunks), intermediate in scale (branches) or had no resolved substructure (leaves). The resulting dendrogram for ^{13}CO(J = 1–0) in NGC 604 is shown in Fig. 3. We identified 20 structures in the entire dendrogram, consisting of 15 leaves and 4 branches, using the above parameters. Spectra for the peak brightness pixels, for each leaf, are presented in Appendix A1. We use letter **L** to represent the leaf number in our labels for the structures. From now onwards, we shall refer to these leaves as molecular clouds.

We compared our results with the results from Miura et al. (2010), who show observations of ^{12}CO(J = 1–0) line emission from NGC 604 as observed by the Nobeyama Millimeter Array. We detected and resolved the clouds that they labelled NMA 4, 7, 8, 9, 10. We, however, are not able to detect NMA 1, 3, 6, 11, and 12 above our 4$\sigma_{\rm rms}$ noise level. This is because Miura et al. (2012) used a lower detection threshold of 3σ. If we lower our detection threshold to 3σ, we can detect these sources, but we also detect additional spurious noise in the maps. Given this situation, we chose to use only sources detected at the higher threshold. NMA 2 and 5 are outside of our field of view. We proceed to determine the basic properties of the identified structures at this point.

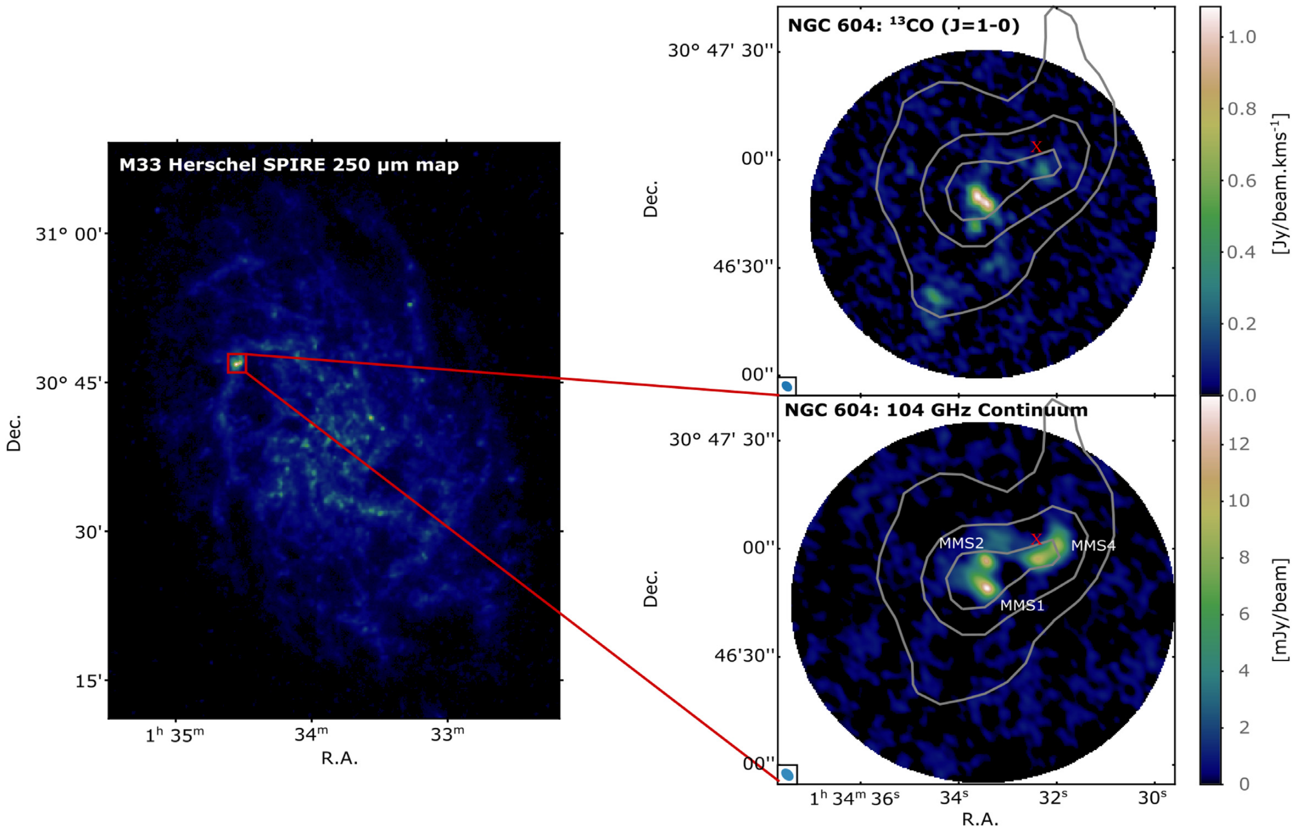

Figure 1. *Left-hand panel:* A 250 μm image of M33 tracing cold interstellar dust emission. *Right top panel:* The ^{13}CO(J = 1–0) emission in NGC 604 as observed by ALMA. *Right bottom panel:* The ALMA 104-GHz continuum emission in NGC 604 resolved into three sources, which we call millimeter sources (MMS). The grey contours in both right-hand panels show the 250 μm emission, and the red cross symbol shows the centre of the GHR.

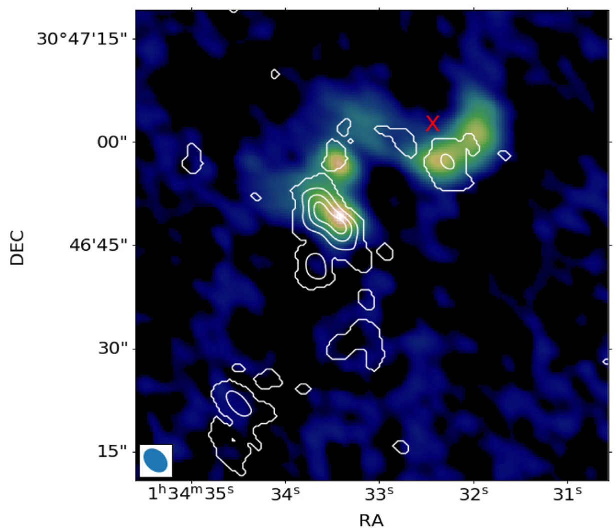

Figure 2. The ALMA 104-GHz continuum image of NGC 604 in colour with the integrated ^{13}CO(J = 1–0) emission overlaid as white contours. The contour levels represent 20, 40, 60, and 80 per cent of the peak emission. The angular resolution is 3.″9 × 2.″8 for ALMA 104-GHz continuum. The continuum emission is seen only near the centre of the GHR, and some regions with ^{13}CO(J = 1–0) emission do not have continuum emission. The colour bar is the same as the bottom right panel of Fig 1.

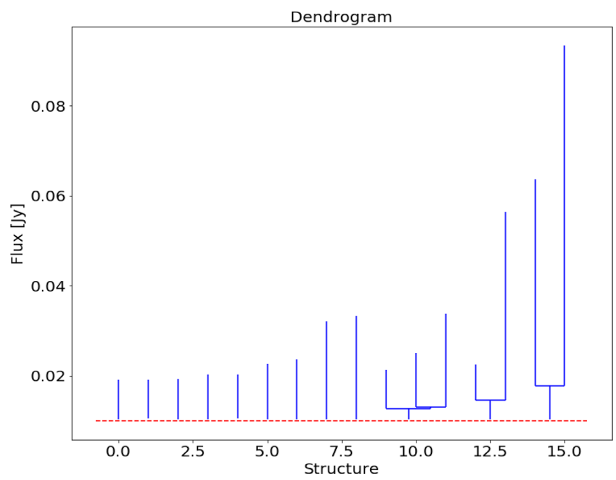

Figure 3. The dendrogram of the ALMA ^{13}CO(J = 1–0) structures in NGC 604. The top of each vertical line indicates a leaf node, which we assume to be a molecular cloud. The horizontal red dotted line represents the minimum value of the tree, which is at 4σ noise level.

The basic properties of the identified structures are also determined by ASTRODENDRO using the bijection approach (Rosolowsky et al. 2008). We extracted the molecular cloud properties using the approach described by Wong et al. (2017). These properties include spatial and velocity centroids ($\bar{x}$, $\bar{y}$, $\bar{v}$), the integrated flux F, the rms

Table 1. Cloud properties derived from ^{13}CO(J = 1–0) in NGC 604 using dendrogram analysis. See Section 3 for the details on how the properties were derived.

MC ID	RA J2000	Dec. J2000	V_{LSR} (km s^{-1})	Δv (km s^{-1})	$L_{^{13}CO}$ K km s^{-1} pc^2	R (pc)	M_{mol} (10^3 M$_\odot$)	M_{vir} 10^3 M$_\odot$)	α_{vir}	Σ_{lum} M$_\odot$ pc^{-2}
L1	01^{h}34^{m}32^s.28	+ 30:46:57.07	−245.7	2.4 ± 0.3	498 ± 60	9.8 ± 0.9	11.0 ± 1.0	10.5 ± 2.8	1.0 ± 0.25	36 ± 7
L2	01^{h}34^{m}32^s.73	+ 30:46:59.84	−249.1	0.3 ± 0.01	20 ± 3	4.2 ± 0.6	0.4 ± 0.06	0.1 ± 0.0	0.22 ± 0.04	6 ± 2
L3	01^{h}34^{m}33^s.39	+ 30:47:01.85	−243.8	0.7 ± 0.1	60 ± 7	5.7 ± 0.5	1.3 ± 0.2	0.6 ± 0.2	0.42 ± 0.12	13 ± 2
L4	01^{h}34^{m}33^s.46	+ 30:46:57.98	−244.4	1.3 ± 0.1	78 ± 13	6.9 ± 0.5	1.7 ± 0.2	2.1 ± 0.4	1.2 ± 0.24	11 ± 2
L5	01^{h}34^{m}33^s.54	+ 30:46:48.88	−243.1	2.9 ± 0.3	3660 ± 520	13.4 ± 1.2	80.5 ± 11.1	21.3 ± 4.8	0.3 ± 0.06	143 ± 26
L6	01^{h}34^{m}33^s.67	+ 30:46:41.92	−241.1	1.9 ± 0.2	672 ± 97	8.1 ± 0.6	14.8 ± 2.0	5.7 ± 1.3	0.4 ± 0.1	72 ± 11
L7	01^{h}34^{m}33^s.13	+ 30:46:37.09	−252.0	1.4 ± 0.1	122 ± 17	8.5 ± 0.7	2.7 ± 0.3	3.0 ± 0.5	1.1 ± 0.2	12 ± 2
L8	01^{h}34^{m}33^s.16	+ 30:46:31.80	−247.1	1.7 ± 0.2	412 ± 51	13.5 ± 1.2	9.1 ± 0.9	7.1 ± 1.8	0.8 ± 0.2	16 ± 3
L9	01^{h}34^{m}33^s.37	+ 30:46:30.44	−252.4	0.8 ± 0.1	47 ± 5	5.3 ± 0.5	1.0 ± 0.1	0.7 ± 0.2	0.7 ± 0.17	12 ± 2
L10	01^{h}34^{m}34^s.18	+ 30:46:25.48	−219.2	0.3 ± 0.03	21 ± 3	5.1 ± 0.5	0.5 ± 0.06	0.1 ± 0.02	0.2 ± 0.04	6 ± 1.1
L11	01^{h}34^{m}34^s.49	+ 30:46:21.91	−220.5	2.2 ± 0.3	1076 ± 158	15.5 ± 1.8	23.7 ± 4.0	13.6 ± 3.6	0.6 ± 0.17	31 ± 7
L12	01^{h}34^{m}34^s.57	+ 30:46:14.66	−217.9	0.5 ± 0.06	32 ± 4	5.0 ± 0.4	0.7 ± 0.1	0.2 ± 0.1	0.3 ± 0.09	9 ± 1.4
L13	01^{h}34^{m}35^s.30	+ 30:46:46.12	−223.2	0.4 ± 0.07	40 ± 6	6.3 ± 0.6	0.9 ± 0.1	0.2 ± 0.1	0.25 ± 0.08	7 ± 1.4
L14	01^{h}34^{m}34^s.98	+ 30:46:57.35	−229.8	0.8 ± 0.1	114 ± 17	6.6 ± 0.5	2.5 ± 0.3	0.8 ± 0.2	0.31 ± 0.08	18 ± 3
L15	01^{h}34^{m}35^s.80	+ 30:46:58.45	−226.5	0.6 ± 0.08	42 ± 6	8.3 ± 0.7	0.9 ± 0.1	0.6 ± 0.2	0.7 ± 0.19	4 ± 1

linewidth Δv (defined as the intensity-weighted second moment of the structure along the velocity axis), the position angle of the major axis ϕ, and the scaling terms along the major and minor axes, σ_{maj} and σ_{min}. From these basic quantities, we calculated additional cloud properties; these are listed in Table 1. The rms spatial size σ_r is given by the geometric mean of σ_{maj} and σ_{min}. The spherical radius R is set to 1.91 σ_r following Solomon et al. (1987) and Rosolowsky & Leroy (2006). The luminosity-based mass for ^{13}CO(J = 1–0) is computed using

$$\frac{M_{lum}}{M_\odot} = \frac{X_{^{13}CO}}{2\times 10^{20}[\mathrm{cm^{-2}/(K\ km\ s^{-1})}]} \times 4.4 \frac{L_{^{13}CO}}{\mathrm{K\ km\ s^{-1}\ pc^2}} = 4.4 X_2 L_{^{13}CO} \tag{1}$$

from Rosolowsky et al. (2008), where $X_{^{13}CO}$ is the assumed ^{13}CO(1 − 0) − to − H_2 conversion factor. This calculation includes a factor of 1.36 to account for the mass of helium. Changes to the first term or conversion factor are represented with the parameter X_2. We have adopted $X_2 = 5$ based on the average ^{13}CO(1 − 0) − to − H_2 conversion factor of 1.0×10^{21}cm^{-2}/(K km s^{-1}) for nearby disc spiral galaxies found by Cormier et al. (2018). This average is equivalent to what would be expected for the conversion factor for a galaxy with 12 + log(O/H) = 8.4. This is close to the abundance of 12 + log(O/H) = 8.45 ± 0.04 measured for NGC 604 (Esteban et al. 2009). The scatter in $X_{^{13}CO}$ value is 0.3 dex (Cormier et al. 2018). This uncertainty means that masses will have a systematic error of about a factor of 2.

The virial mass of molecular clouds derived assuming virial equilibrium is

$$M_{vir} = 189 \Delta v^2 R \qquad [M_\odot], \tag{2}$$

where Δv is the linewidth in km s^{-1} and R is the spherical radius in pc. This formulation assumes a truncated power-law density distribution of $\rho \propto R^{-\beta}$ with $\beta = 1$ and with the assumption that magnetic fields and external pressure are negligible (Solomon et al. 1987). In this equation, M_{vir} is only defined for finite clouds with resolved radii.

The average molecular gas surface density Σ_{lum} is defined as

$$\Sigma_{lum} = \frac{M_{lum}}{\pi R^2} \qquad [M_\odot\ \mathrm{pc}^{-2}] \tag{3}$$

where M_{lum} is the luminosity-based mass.

The dynamic state of a cloud is described by the virial parameter α_{vir} which is given by

$$\alpha_{vir} = \frac{189 \Delta v^2 R}{M_{lum}}. \tag{4}$$

Allowing for uncertainties in measured parameters, a virtual ratio of ≤2 is generally taken to mean that a cloud is gravitational bound. However, a cloud with an α_{vir} ratio significantly lower than this would need additional internal support (e.g. magnetic fields) to survive for longer than the usual dynamical time-scale (Faesi et al. 2018).

The uncertainties in the molecular clouds properties R, Δv, $L_{^{13}CO}$, and M_{lum} are computed using a bootstrap method with 50 iterations. The bootstrapping determines errors by generating several trial clouds from the original cloud data. The properties are measured for each trial cloud, and the uncertainties are estimated from the variance of properties derived from these resampled and remeasured data sets. The final uncertainty in each property is the standard deviation of the bootstrapped values scaled by the square root of the oversampling rate. The bootsrap method is described in detail by Rosolowsky & Leroy (2006) and Rosolowsky et al. (2008). Other uncertainties in derived properties presented in this work are calculated using the standard propagation of errors.

4 RESULTS

The properties of the 15 molecular clouds (leaves) identified by our dendrogram analysis are presented in Table 1, and the left-hand panel of Fig. 4 shows the the locations of these clouds. The two right-hand panels in Fig. 4 show magnified versions of the NMA-8 region. Miura et al. (2010) only detected a single object in this region, but we detected four separate sources and resolved the structure in the brightest source. We discuss this more in Section 5.

4.1 Scaling relations

Fig. 5 shows the size–linewidth relation for our sources. The clouds in blue are the 15 clouds identified as unresolved substructure (leaves) by our analysis technique, and those in red are the branches which harbour resolved substructures. To investigate whether our molecular clouds are in virial equilibrium, we plotted molecular mass versus virial mass in Fig. 6. In the absence of other forces, the virial parameter, which is the ratio of kinetic to gravitational potential energies, indicates the level of boundedness. The *unbound* ones are

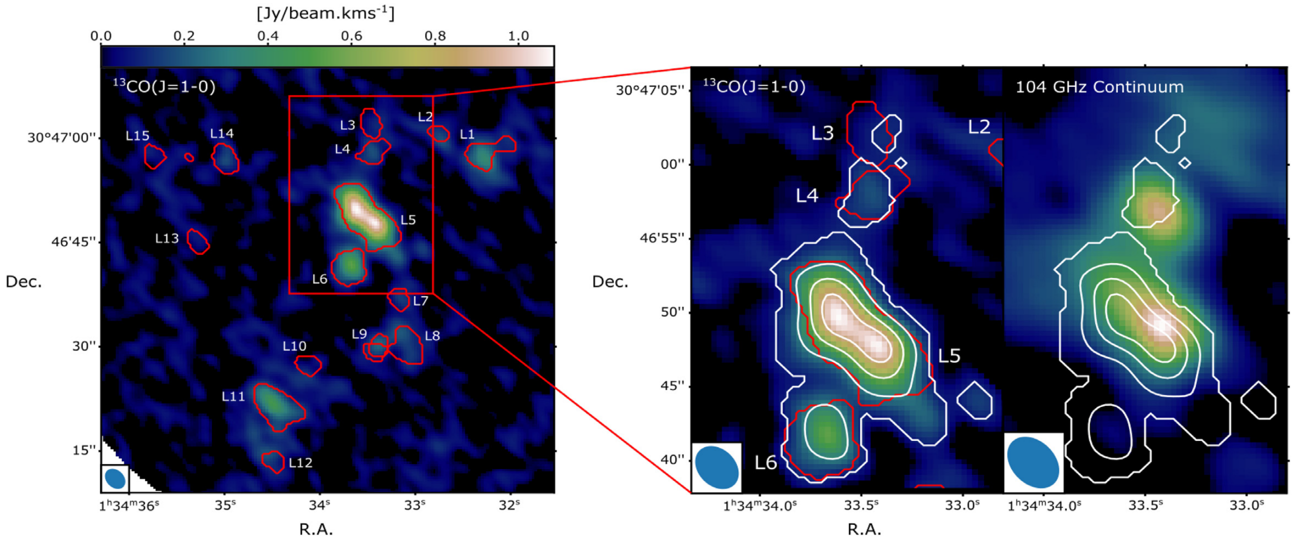

Figure 4. The left-hand panel shows the ^{13}CO(J = 1–0) emission from NGC 604 with the red contours demarcating the clouds identified by astrodendro. The red box shows the NMA-8 region, which is shown in detail in the two right-hand zoomed panels. The right-hand zoomed panel shows the ^{13}CO(J = 1–0) emission from the four resolved molecular clouds (details as the larger amp), while the left-hand zoomed panel shows the 104-GHz continuum emission. White contours showing the ^{13}CO(J = 1–0) line emission are overlaid on both zoomed panels. The contour levels represent 20, 40, 60, and 80 per cent of the peak emission.

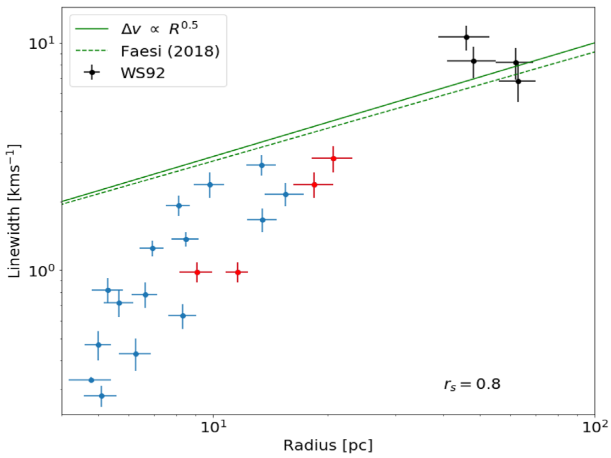

Figure 5. Size–linewidth relation of resolved molecular clouds in NGC 604. The green solid and dashed lines are the power-law slopes of Milky Way (Solomon et al. 1987) and extragalactic (Faesi et al. 2018) giant molecular clouds, respectively. The blue and red points represent the molecular clouds identified as leaves and branches in dendrogram tree, respectively. The black points are WS92 molecular clouds of NGC 604. There is a correlation with spearman rank of, $r_{\rm s} = 0.8$.

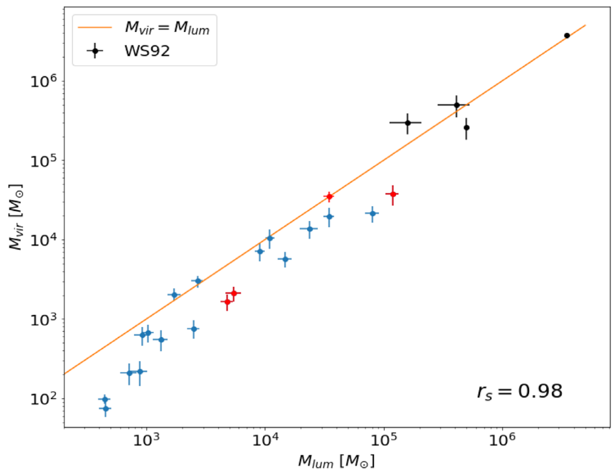

Figure 6. Luminosity mass plotted against virial mass. We see a strong correlation between these two parameters with a spearman coefficient of $r_{\rm s} = 0.98$ indicated in the bottom right corner. The yellow line indicates a one-to-one relation. Despite being correlated most clouds fall below the one-to-one relation. The red, blue, and black points are the same as in Fig. 5.

those with $\alpha_{\rm vir} > 2$, while the *bound* are those with $\alpha_{\rm vir}$ between 1 and 2, and the ones with $\alpha_{\rm vir} \leq 1$ are in a state of forming stars.

4.1.1 Size–line width relation

The size–linewidth relation is commonly known as Larson's first law. The $\Delta v \propto R^{0.5}$ relates the linewidth in km s^{-1} to the radius in parsecs (Wong et al. 2017). Large CO linewidths seen at parsec scales are evidence that these clouds are turbulent. It then follows from the size–linewidth relationship that there is a turbulent cascade of energy through the ISM (Faesi et al. 2018) and that the form of this turbulence is described by its power-law slope [1/2 for compressible, 1/3 for incompressible, (McKee & Ostriker 2007)].

Fig. 5 shows the size–linewidth relation for our GMCs. We see that there is a clear trend, with larger clouds having larger linewidths, as is found in Milky Way clouds. The Spearman correlation coefficient for these data has the value of $r_{\rm s} = 0.8$, which indicates that there is a correlation between size and linewidths of GMCs in NGC 604. We also show in Fig. 5 the Milky Way power-law slope (green solid line) from Solomon et al. (1987) and the extragalactic slope (green dashed line) from Faesi et al. (2018) for NGC 300. The relation for the NGC 604 clouds does not match the Milky Way and NGC 300 slopes; the linewidths at small radii for the NGC 604 data fall below the Milky Way and NGC 300 relations. In the figure, we plot results done by Wilson & Scoville (1992) (black points). Despite their results having considerable poor resolution, (8 arcsec × 7 arcsec) compared to our ALMA 3.2 arcsec × 2.4 arcsec). There is consistency between the two results on large sizes having large linewidths (WS92 results) and smaller sizes having smaller linewidths (our clouds). The features are a typical characteristics of a turbulent spectrum which has a range of scales with increasing kinetic energy at large scales. We find their results to be in agreement with both the Milky Way and NGC 300 relations. Wong et al. (2017, 2019) found a similar offset in the size–linewidth relationship between Milky Way and Large Magellanic Cloud data. They ascribed the discrepancy to two factors. The first was the limitations in resolution of the Large Magellanic Cloud observations. The second was the bijection approach in dendrogram analysis. The rms linewidths in the dendrogram analysis tend to be underestimated for structures which are defined by high isocontour levels such as leaves because the full width of the spectral line is truncated by the isosurface boundary (Rosolowsky 2005; Rosolowsky et al. 2008). NGC 604 and 30 Dor, one of the region Wong et al. (2017) studied, are both sites of massive star formation surrounding giant H II regions and would both be places with high isocontour levels, so both of these locations could plausibly be affected by this truncation bias. It is worth noting that other extragalactic studies have found no strong correlation between size and linewidth (Colombo et al. 2014; Maeda et al. 2020).

4.1.2 *Molecular mass–virial mass relations*

The Milky Way observations have shown that the majority of GMCs are in self-gravitational equilibrium (e.g. Larson 1981; Solomon et al. 1987; Heyer et al. 2009; Heyer & Dame 2015). This leads to a direct correlation between $M_{\rm vir}$ and the mass measured through other independent method (in our case the ^{13}CO luminosity). Recent extragalactic studies of NGC 300 by Faesi et al. (2018) and NGC 1300 by Maeda et al. (2020) have found a strong correlation between $M_{\rm vir}$ and $M_{\rm lum}$ and a low scatter in $\alpha_{\rm vir}$ near unity. We show in Fig. 6 that the clouds in NGC 604 are in near virial equilibrium and that the data are strongly correlated, with a Spearman coefficient of $r_s = 0.98$. Most of the clouds are lying below a one-to-one relation, illustrating that the masses estimated from the luminosities are slightly higher than the virial masses, which is a direct consequence of underestimating linewidths as discussed in the previous section. These clouds have virial parameters ranging from 0.2 to 1.1, indicating that some clouds are in virial equilibrium while others could be in a state of forming stars. The Wilson & Scoville (1992) data, which are also shown in Fig. 6, largely seem consistent with the results from NGC 604.

5 DISCUSSION

As seen in Fig. 2, both continuum and ^{13}CO(J = 1–0) emission are detected near the centre of the H II region, although at locations further from the centre of the H II region, we found a few locations with only ^{13}CO(J = 1–0) emission. The regions that are associated with continuum emission are actively forming stars. We have labelled the three continuum sources with the abbreviation MMS (millimetre source), with MMS1 corresponding to L5, MMS2 corresponding to L4, and MMS4 corresponding to L1 as seen in the bottom right panel of Fig. 1. Muraoka et al. (2020) also identified three sources in this region. Our MMS2 corresponds to their MMS2, but they were able to resolve the brighter source, which we labelled as MMS1, into two sources labelled MMS1 and MMS3 (which is why we labelled our third source as MMS4).

Regions only detected in ^{13}CO(J = 1–0) emission are dense molecular clouds with no active star formation. In these regions, atomic hydrogen (H I) could be forming H_2, and these clouds may form stars as the H II expands. Previous studies in this region have found similar results and suggested that GMCs in NGC 604 are at different evolutionary stages, which would lead to sequential star formation induced by the expansion of GHR (Tosaki et al. 2007; Miura et al. 2010). To make comparison to the work done previously by Miura et al. (2010), we use the nomenclature for their clouds and identify how many clouds we have resolved in each major GMC.

5.1 NMA-8

We have resolved NMA-8, the largest GMC in NGC 604 found by Miura et al. (2010), into four individual molecular clouds that we labelled L3, L4, L5, and L6. It is possible that L5 contains two or more smaller clouds, but we could not separate them into smaller clouds when applying ASTRODENDRO to the ^{13}CO data. Based on the ^{12}CO(J = 1–0) observations, NMA-8 is known to be the most massive (7.4 ± 2.8 × 10^5 M$_\odot$) GMC in the GHR (Miura et al. 2010, and references therein). Using ^{13}CO(J = 1–0), we estimate a virial mass of 0.8 ± 0.3 × 10^5 M$_\odot$ and a molecular mass of 1.2 ± 0.2 × 10^5 M$_\odot$ in NMA-8, which is a factor of 5 less than the ^{12}CO(J = 1–0) molecular mass presented by Miura et al. (2010). This is attributed to ^{13}CO(J = 1–0) only tracing the dense gas, hence, resolving away diffuse gas which make up large-scale structure and also to the underestimation of linewidths. Our computed ^{13}CO molecular mass for NMA-8 is comparable to the Orion A GMC, which has an estimated ^{12}CO molecular mass of 1.1 × 10^5 M$_\odot$ (Wilson et al. 2005). The NMA-8 molecular mass estimate from ^{13}CO is higher than the virial mass estimated from the linewidths and the spherical radius but agree within the errors. The estimated molecular mass of 0.8 ± 0.1 × 10^5 M$_\odot$ in L5 is comparable to Orion B in the Milky Way, which has a mass of 0.82 × 10^5 M$_\odot$ (Wilson et al. 2005).

The association of L4 and L5 with 104-GHz continuum sources, which is expected to be dominated by free–free emission (e.g. Peel et al. 2011; Bendo et al. 2015, 2016), clearly indicates that they are undergoing star formation. However, the peaks in the ^{13}CO emission from these sources do no coincide exactly with the continuum peaks, as seen in the right zoomed panel of Fig. 4. The continuum peaks lie closer to the centre of the H II region than the ^{13}CO peaks. This misalignment in this region has been reported previously by Miura et al. (2010). The spatial offset between these peaks is an indication that these two tracers do trace different regions. The centre has photoionizing stars which photoionize the gas surrounding which we trace by continuum in turn. The ^{13}CO(1–0) line, being the lowest J-transition with a very low excitation temperature, preferentially traces cold dense molecular gas away from the centre. It is thus insensitive to the warm gas traced by the continuum emission. Earlier studies in NGC 604 by Muraoka et al. (2012) also found a temperature gradient in the NGC 604 clouds.

5.2 Other GMCs in NGC 604

We have for the first time resolved NMA-7 into three sources (L10, L11, and L12) and NMA-9 into three sources (L7, L8, and L9). Other than L1, these other GMCs are not associated with continuum sources and are not associated with ongoing star formation. NMA-9 is the second massive and second largest complex in the imaged area, with a molecular mass of about 0.6 ± 0.1 × 10^5 M$_\odot$. As we indicated before, the clouds without continuum emission could be places where the atomic gas is currently forming molecular gas, but when the GHR expands, these clouds may form stars.

Generally, NGC 604 molecular clouds indicate that they are at different evolutionary stages within the H II region, with some being associated with both continuum and line emission while others only line emission. Additional dendrogram analyses with higher resolution data will be necessary to explore these phenomena in more detail.

6 CONCLUSIONS

We have presented ALMA ^{13}CO(1–0) and 104-GHz continuum observations of NGC 604. Using the ASTRODENDRO algorithm, we identified 15 molecular clouds. The main results are given as follows:

(1) The identified molecular clouds have sizes R ranging from 5 to 21 pc, linewidths Δv, of 0.3–3.0 km s^{-1} and luminosity-derived masses $M_{\rm lum}$, of (0.4–80.5) $\times$ 10^3 M$_\odot$. These sizes, linewidths, and masses are comparable to typical Milky Way molecular clouds.

(2) For the first time, this work has resolved NMA-8, the most massive GMC, into four molecular clouds named L3, L4, L5, and L6, with L5 showing two clear peaks. We detect 104-GHz continuum emission from L5, although it is offset from the ^{13}CO emission.

(3) We only detect 104-GHz continuum emission near the centre of GHR. Further out of the centre, only ^{13}CO line emission is detected. This indicates that the GMCs in NGC 604 are in different evolutionary stages as previously suggested by Tosaki et al. (2007) and Miura et al. (2010). Additionally, we find a spatial misalignment between ^{13}CO and 104-GHz continuum in NGC 604. The centre has photoionizing stars which photoionize the gas surrounding which we trace by continuum in turn while the ^{13}CO(1–0) line, being the lowest J-transition with a very low excitation temperature, preferentially traces cold dense molecular gas away from the centre. It is thus insensitive to the warm gas traced by the continuum emission. This is a confirmation of what previous studies found in the same region.

(4) We have found that the sizes and linewidths are correlated for the NGC 604 GMCs but that the relationship is offset from the Milky Way scaling relation. This may be a consequence of the limited resolution of our data or artefact of the dendrogram analysis as applied to bright sources. The relation for the clouds in NGC 604 is consistent with the idea of compressible hierarchical turbulence in the ISM within this region.

(5) We find a clear one-to-one relationship between virial mass and luminous mass indicating that the clouds in NGC 604 are in virial equilibrium. This relation is consistent with the earlier relation published by WS92.

(6) The virial parameter ranges from 0.2 to 1.1. This result entails that some of the molecular clouds are below $\alpha_{\rm vir} = 1$ which means that not only are they in a state of forming stars but photoionizing stars have been formed. Other clouds have $\alpha_{\rm vir}$ values near unity, which means that they are in virial equilibrium.

ACKNOWLEDGEMENTS

We thank the anonymous referee for the helpful comments in improving this manuscript. Research reported in this publication was supported by a Newton Fund project, DARA (Development in Africa with Radio Astronomy), and awarded by the UK's Science and Technology Facilities Council (STFC) - grant reference ST/R001103/1. This work makes use of the following ALMA data: ADS/JAO.ALMA2013.1.00639.S. ALMA is a partnership of ESO (representing its member states), NSF (USA) and NINS (Japan), together with NRC (Canada), MOST and ASIAA (Taiwan), and KASI (Republic of Korea), in cooperation with the Republic of Chile. The Joint ALMA Observatory is operated by ESO, AUI/NRAO and NAOJ. This research made use of ASTRODENDRO, a PYTHON package to compute dendrograms of Astronomical data.[1] This research made use of ASTROPY,[2] a community-developed core PYTHON package for Astronomy (Astropy Collaboration 2013, 2018).

DATA AVAILABILITY

The raw data underlying this article is available on the ALMA archive: ADS/JAO.ALMA2013.1.00639.S. The calibrated image data generated for this research will be shared on reasonable request to the corresponding author.

REFERENCES

Astropy Collaboration, 2013, A&A, 558, A33
Astropy Collaboration, 2018, AJ, 156, 123
Bendo G. J., Beswick R. J., D'Cruze M. J., Dickinson C., Fuller G. A., Muxlow T. W. B., 2015, MNRAS, 450, L80
Bendo G. J., Henkel C., D'Cruze M. J., Dickinson C., Fuller G. A., Karim A., 2016, MNRAS, 463, 252
Bolatto A. D., Leroy A. K., Rosolowsky E., Walter F., Blitz L., 2008, ApJ, 686, 948
Braatz J., Impellizzeri V., Biggs A. P. S., 2020, ALMA Cycle 8 Proposer's Guide, version 1.0. Joint ALMA Observatory, Santiago
Churchwell E., Goss W. M., 1999, ApJ, 514, 188
Colombo D. et al., 2014, ApJ, 784, 3
Colombo D., Rosolowsky E., Ginsburg A., Duarte-Cabral A., Hughes A., 2015, MNRAS, 454, 2067
Cormier D. et al., 2018, MNRAS, 475, 3909
Drissen L., Moffat A. F. J., Shara M. M., 1993, in Cassinelli J. P., Churchwell E. B., eds, ASP Conf. Ser. Vol. 35, Massive Stars: Their Lives in the Interstellar Medium. Astron. Soc. Pac., San Francisco, p. 528
Engargiola G., Plambeck R. L., Rosolowsky E., Blitz L., 2003, ApJS, 149, 343
Esteban C., Bresolin F., Peimbert M., García-Rojas J., Peimbert A., Mesa-Delgado A., 2009, ApJ, 700, 654
Faesi C. M., Lada C. J., Forbrich J., 2018, ApJ, 857, 19
Freedman W. L., Wilson C. D., Madore B. F., 1991, ApJ, 372, 455
Gratier P. et al., 2010, A&A, 522, A3
Gratier P. et al., 2012, A&A, 542, A108
Heyer M., Dame T. M., 2015, ARA&A, 53, 583
Heyer M., Krawczyk C., Duval J., Jackson J. M., 2009, ApJ, 699, 1092
Hughes A. et al., 2010, MNRAS, 406, 2065
Kam Z. S., Carignan C., Chemin L., Amram P., Epinat B., 2015, MNRAS, 449, 4048
Larson R. B., 1981, MNRAS, 194, 809
Maeda F., Ohta K., Fujimoto Y., Habe A., 2020, MNRAS, 493, 5045
McKee C. F., Ostriker E. C., 2007, ARA&A, 45, 565
McMullin J. P., Waters B., Schiebel D., Young W., Golap K., 2007, in Shaw R. A., Hill F., Bell D. J., eds, ASP Conf. Ser. Ser. Vol. 376, Astronomical Data Analysis Software and Systems XVI, Astron. Soc. Pac., San Francisco, p. 127
Miura R. et al., 2010, ApJ, 724, 1120
Miura R. E. et al., 2012, ApJ, 761, 37
Muraoka K., Tosaki T., Miura R., Onodera S., Kuno N., Nakanishi K., Kaneko H., Komugi S., 2012, PASJ, 64, 3

[1] http://www.dendrograms.org/
[2] http://www.astropy.org

Muraoka K. et al., 2020, ApJ, 903, 94
Peel M. W., Dickinson C., Davies R. D., Clements D. L., Beswick R. J., 2011, MNRAS, 416, L99
Relaño M., Robert C. K. Jr, 2009, ApJ, 699, 1125
Rice T. S., Goodman A. A., Bergin E. A., Beaumont C., Dame T. M., 2016, ApJ, 822, 52
Rosolowsky E., 2005, PASP, 117, 1403
Rosolowsky E., Leroy A., 2006, PASP, 118, 590
Rosolowsky E., Simon J. D., 2008, ApJ, 675, 1213
Rosolowsky E., Engargiola G., Plambeck R., Blitz L., 2003, ApJ, 599, 258
Rosolowsky E., Keto E., Matsushita S., Willner S. P., 2007, ApJ, 661, 830
Rosolowsky E. W., Pineda J. E., Kauffmann J., Goodman A. A., 2008, ApJ, 679, 1338
Schinnerer E. et al., 2019, ApJ, 887, 49
Schruba A. et al., 2017, ApJ, 835, 278
Solomon P. M., Rivolo A. R., Barrett J., Yahil A., 1987, ApJ, 319, 730
Tabatabaei F. S. et al., 2014, A&A, 561, A95
Tosaki T., Miura R., Sawada T., Kuno N., Nakanishi K., Kohno K., Okumura S. K., Kawabe R., 2007, ApJ, 664, L27
Tüllmann R. et al., 2008, ApJ, 685, 919
van Dishoeck E. F., Black J. H., 1988, ApJ, 334, 771
Viallefond F., Boulanger F., Cox P., Lequeux J., Perault M., Vogel S. N., 1992, A&A, 265, 437
Wilson C. D., Scoville N., 1992, ApJ, 385, 512 (WS92)
Wilson C. D., Walker C. E., Thornley M. D., 1997, ApJ, 483, 210
Wilson B. A., Dame T. M., Masheder M. R. W., Thaddeus P., 2005, A&A, 430, 523
Wong T. et al., 2017, ApJ, 850, 139
Wong T. et al., 2019, ApJ, 885, 50

APPENDIX A: PEAK SPECTRA FOR THE SOURCES

Presented here in Fig. A1 are the spectra (as measured at the peak of the emission) for each of the molecular clouds identified in our dendrogram analysis.

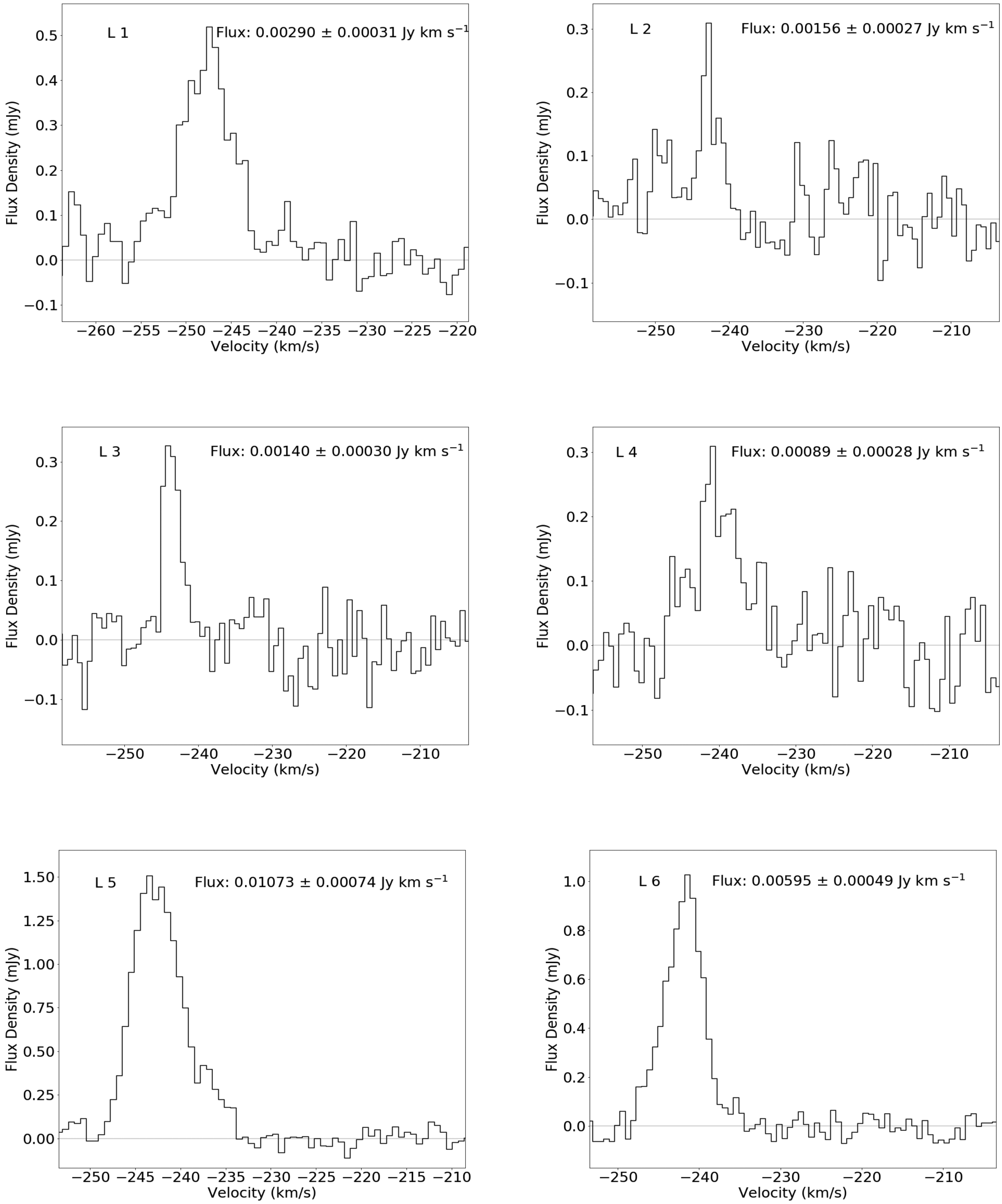

Figure A1. NGC 604 GMC spectra as measured at the peak of the emission from each source.

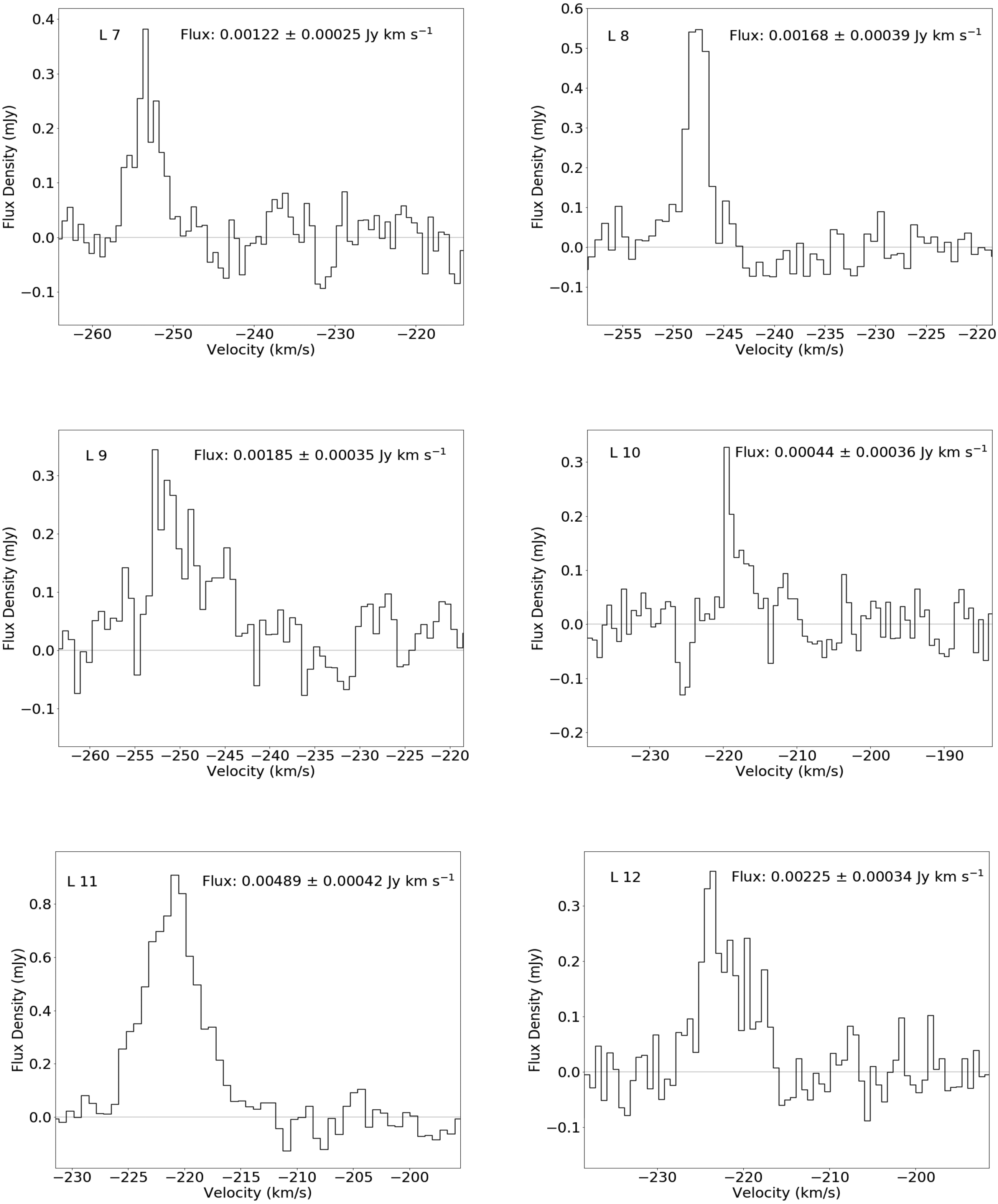

Figure A1. continued.

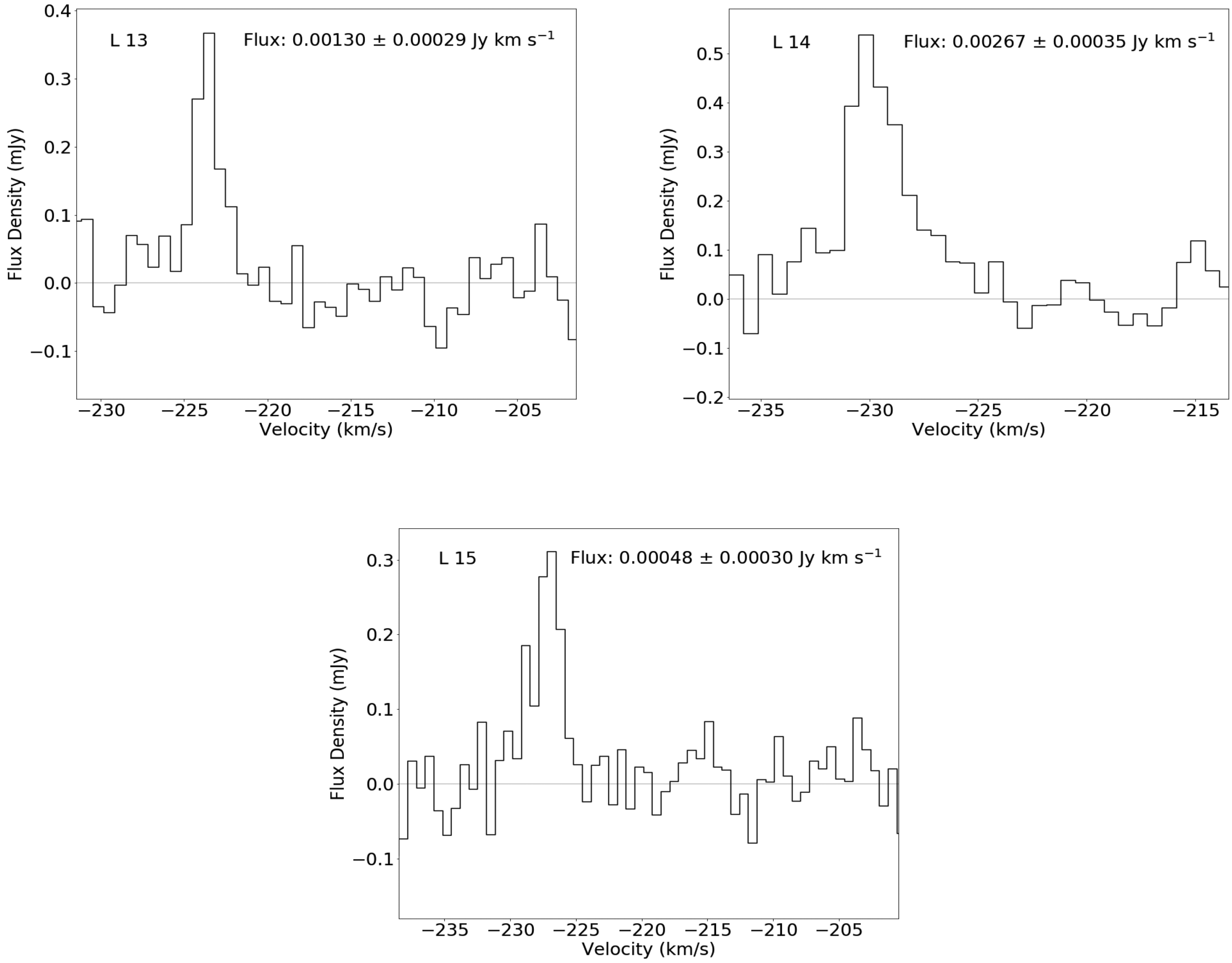

Figure A1. continued.

This paper has been typeset from a TEX/LATEX file prepared by the author.